# A DISPLACEMENT POTENTIAL-BASED NUMERICAL SOLUTION
# FOR ORTHOTROPIC COMPOSITE PANELS
# UNDER END MOMENT AND SHEAR LOADING

S. K. Deb Nath and S. Reaz Ahmed

The elastic behavior of an orthotropic composite panel is analyzed under the influence of an end moment as well as shear loading. The panel is rigidly fixed at one of its ends, and the fibers are assumed to be directed along its length. An efficient finite difference computational scheme, based on the displacement potential formulation, is used to analyze the present mixed boundary value elastic problem. The effects of several important issues, for example, the panel aspect ratio, edge stiffening, and fiber reinforcement, on the elastic field are investigated. Solutions are presented mainly in the form of graphs and the predicted deformed shape. Finally, the reliability and superiority of the present computational scheme is discussed in comparison to the corresponding finite element predictions.

*A list of symbols can be found on page 1003.*

## 1. Introduction

The strength-to-weight ratio of a fiber reinforced composite material is usually higher than that of the corresponding isotropic material. The use of composite materials is increasing day by day, particularly to satisfy the demand for lightweight structures. The use of composite panels in the construction of engineering structures, for example, aircraft, is quite extensive. It is known that the mechanical properties, such as strength and toughness of a fiber reinforced composite, differ significantly from those of an isotropic material and eventually play an important role in defining the state of stress and deformation of the structural component under loading.

Stress analysis has now become a classical subject in the field of solid mechanics. However, stress analysis problems are still being examined with improved sophistication with respect to the methods of analysis [Conway et al. 1951; Chow et al. 1953; Krishna Murty 1984; Suzuki 1986; Durelli and Ranganayakamma 1989; Hardy and Pipelzadeh 1991]. Elasticity problems are usually formulated either in terms of deformation parameters or stress parameters. Among the existing mathematical models of plane boundary value stress problems, the stress function approach and the displacement formulation are notable [Timoshenko and Goodier 1979]. Application of the stress function formulation in conjunction with the finite difference technique has been reported for the solution for plane elastic problems in which all boundary conditions are described in terms of stresses only [Chow et al. 1953; Chapel and Smith 1968]. Further, Conway [1953] extended the stress function formulation in the form of Fourier integrals to the case in which the material was orthotropic, and obtained analytical solutions for a number of ideal problems. The shortcomings of the stress function approach are that it accepts boundary conditions only

in terms of loadings. Boundary restraints that are specified in terms of displacement components cannot be satisfactorily imposed on the stress function. Because most practical problems of elasticity are of mixed boundary value type, the stress function approach fails to provide an explicit understanding of the state of stresses at the critical support and stiffener components. Here, a 'mixed boundary value problem' refers to one in which the displacement components are described over part of the boundary surface and the stress components over the remainder of the boundary surface. The boundary conditions may also be specified as a mixture of boundary restraints and boundary loadings, as realized in the cases of stiffeners, guided edges, etc.

Reliable and accurate prediction of stresses, especially at the surfaces of engineering structures, is of great importance with respect to reliability, safety, and economic design. The uncertainties associated with the prediction of surface stresses by standard computational approaches (for example, the finite element method, FEM) have been pointed out by several researchers [Richards and Daniels 1987; Smart 1987; Dow et al. 1990]. On the other hand, introducing a new boundary modeling approach for finite difference applications of the displacement formulation of solid mechanics [Dow et al. 1990] solved the problem of a uniformly loaded cantilever beam and reported that the accuracy of the finite difference method (FDM), with respect to reproducing the state of stresses along the bounding surfaces, was much higher than the accuracy of FE analysis. However, the computational efforts of the FD analysis, under the new boundary modeling approach, were somewhat greater than the efforts required for FE analysis. Recently, Ranzi et al. [2006] reported a comparative study of the performances of available modeling approaches for the analysis of composite beams with partial shear interactions. Comparing the performances with exact analytical solutions, the FDM was determined to be an adequate numerical tool for describing the composite behavior of beams, and the corresponding FD solutions were shown to be more accurate when compared with the usual eight degree-of-freedom FEM solutions, even when finer discretization was used for the FEM solutions.

The recent research and the developments with respect to using the displacement potential approach [Ahmed et al. 1996; 1998; 2005b; Akanda et al. 2002] have generated renewed interest in the fields of both analytical and numerical solutions for practical stress problems. In this boundary modeling approach, the plane elastic problem is formulated in terms of a potential function of space variables, defined in terms of two displacement components that must satisfy a single differential equation of equilibrium. Moreover, the present computational approach permits the reduction of the number of dependent variables that must be evaluated at each nodal point to one. This is an advantage over the standard solution methods, which use at least two unknowns at each nodal point for solving plane problems. As a result, the total number of simultaneous equations that must be solved in the present approach is reduced to half of those required in usual approaches, which eventually leads to a drastic reduction in computational effort as well as increased overall accuracy of the solution [Ahmed et al. 2005a]. The present modeling approach also enables us to very efficiently manage the mixed mode of boundary conditions as well as their zones of transition. Recently, Ahmed et al. [2005a] proposed a general displacement potential formulation for the solution for anisotropic composite structures. Further, Nath et al. extended the use of the formulation to the problems of orthotropic composite materials, and obtained analytical solutions for a number of composite structures under various types of loading and supporting conditions [Nath et al. 2006; 2007; 2009].

A new analysis of the elastic field of composite panels subjected to an end moment as well as a shear loading is the subject of the present paper. The panels are assumed to be rigidly fixed at one end,

and the fibers are situated along the longitudinal axis of the panel. The solutions are obtained using the displacement potential formulation in conjunction with FDM, and the corresponding distributions of stress and displacements are presented mainly in the form of graphs as well as the predicted deformed shape. Some of the issues of interest, for example, the effects of the aspect ratio, edge stiffening, and fiber reinforcement, etc. on the elastic field are also investigated. Finally, a comprehensive comparative analysis is presented in an attempt to check the appropriateness as well as superiority of the present numerical solutions. More specifically, the reliable prediction of stresses at the critical sections of the panel, especially at the regions of transition between physical conditions, is discussed in comparison to the stresses predicted by standard FEM.

## 2. Displacement potential formulation

The two differential equations for equilibrium in plane stress problems describing orthotropic elastic bodies of Hookean materials, with respect to a rectangular coordinate system, in the absence of body forces, and in terms of the displacement components, are as follows [Jones 1975; Timoshenko and Goodier 1979]:

$$\left(\frac{E_1^2}{E_1 - v_{12}^2 E_2}\right)\frac{\partial^2 u_x}{\partial x^2} + \left(\frac{v_{12} E_1 E_2}{E_1 - v_{12}^2 E_2} + G_{12}\right)\frac{\partial^2 u_y}{\partial x \partial y} + G_{12}\frac{\partial^2 u_x}{\partial y^2} = 0, \tag{1}$$

$$\left(\frac{E_1 E_2}{E_1 - v_{12}^2 E_2}\right)\frac{\partial^2 u_y}{\partial y^2} + \left(\frac{v_{12} E_1 E_2}{E_1 - v_{12}^2 E_2} + G_{12}\right)\frac{\partial^2 u_x}{\partial x \partial y} + G_{12}\frac{\partial^2 u_y}{\partial x^2} = 0, \tag{2}$$

where $E_1$ and $E_2$ are the elastic moduli of the material in the $x$- and $y$-directions, respectively, $v_{12}$ is the major Poisson's ratio, and $G_{12}$ is the in-plane shear modulus. Instead of solving the above two elliptic partial differential equations simultaneously, the existence of a new potential function of space variables is investigated in an attempt to reduce the problem to the determination of a single variable from a single differential equation of equilibrium. In the present approach, a new potential function $\psi(x, y)$ is thus defined in terms of the two displacement components as follows [Ahmed et al. 2005a]:

$$u_x = \alpha_1 \frac{\partial^2 \psi}{\partial x^2} + \alpha_2 \frac{\partial^2 \psi}{\partial x \partial y} + \alpha_3 \frac{\partial^2 \psi}{\partial y^2}, \qquad u_y = \alpha_4 \frac{\partial^2 \psi}{\partial x^2} + \alpha_5 \frac{\partial^2 \psi}{\partial x \partial y} + \alpha_6 \frac{\partial^2 \psi}{\partial y^2}. \tag{3}$$

Here, the $\alpha$s are unknown material constants. For a unidirectional orthotropic composite lamina, in which the fibers are directed along the $x$-axis, the values of these constants are

$$\alpha_1 = \alpha_3 = \alpha_5 = 0, \quad \alpha_2 = 1, \quad \alpha_4 = -\frac{E_1^2}{Z_{11}}, \quad \alpha_6 = -\frac{G_{12}(E_1 - v_{12}^2 E_2)}{Z_{11}} \tag{4}$$

(see [Ahmed et al. 2005a]), where

$$Z_{11} = v_{12} E_1 E_2 + G_{12}(E_1 - v_{12}^2) E_2.$$

Substitution of (3) into the first equilibrium condition, (1), shows that the latter is automatically satisfied. Therefore, $\psi$ must satisfy the second equilibrium condition, (2), only. Expressing (2) in terms of

the potential function $\psi$, for the case of orthotropic plane stress problems, $\psi$ must satisfy the condition

$$E_1 G_{12} \frac{\partial^4 \psi}{\partial x^4} + E_2(E_1 - 2v_{12}G_{12})\frac{\partial^4 \psi}{\partial x^2 \partial y^2} + E_2 G_{12}\frac{\partial^4 \psi}{\partial y^4} = 0; \tag{5}$$

see [Ahmed et al. 2005a; Nath et al. 2007].

Because the present approach considers a single dependent variable for solving the panel problem, all of the equations associated with the normal and the tangential components of stress and displacement are expressed in terms of the function $\psi$. The expressions for the displacement components for the plane stress orthotropic composite materials are restated here:

$$u_x(x, y) = \frac{\partial^2 \psi}{\partial x \partial y}, \tag{6}$$

$$u_y(x, y) = -\frac{1}{Z_{11}}\left[E_1^2 \frac{\partial^2 \psi}{\partial x^2} + G_{12}(E_1 - v_{12}^2 E_2)\frac{\partial^2 \psi}{\partial y^2}\right]. \tag{7}$$

The differential equations associated with the stress components are obtained by substituting Equations (6) and (7) into the stress–displacement relations of plane stress problems. The resulting expressions for the stress components in terms of the function $\psi$ are as follows [Ahmed et al. 2005a]:

$$\sigma_{xx}(x, y) = \frac{E_1 G_{12}}{Z_{11}}\left[E_1 \frac{\partial^3 \psi}{\partial x^2 \partial y} - v_{12}E_2 \frac{\partial^3 \psi}{\partial y^3}\right], \tag{8}$$

$$\sigma_{yy}(x, y) = \frac{E_1 E_2}{Z_{11}}\left[(v_{12}G_{12} - E_1)\frac{\partial^3 \psi}{\partial x^2 \partial y} - G_{12}\frac{\partial^3 \psi}{\partial y^3}\right], \tag{9}$$

$$\sigma_{xy}(x, y) = -\frac{E_1 G_{12}}{Z_{11}}\left[E_1 \frac{\partial^3 \psi}{\partial x^3} - v_{12}E_2 \frac{\partial^3 \psi}{\partial x \partial y^2}\right]. \tag{10}$$

## 3. Geometries and loadings of the panel

Two cases of an orthotropic panel are considered (Figure 1). Case I is a composite panel with a rectangular cross section that is supported at its left lateral end ($x/b = 0$) and subjected to a bending moment at its right lateral end ($x/b = 1$). The normal stress on the right lateral end, causing the bending moment,
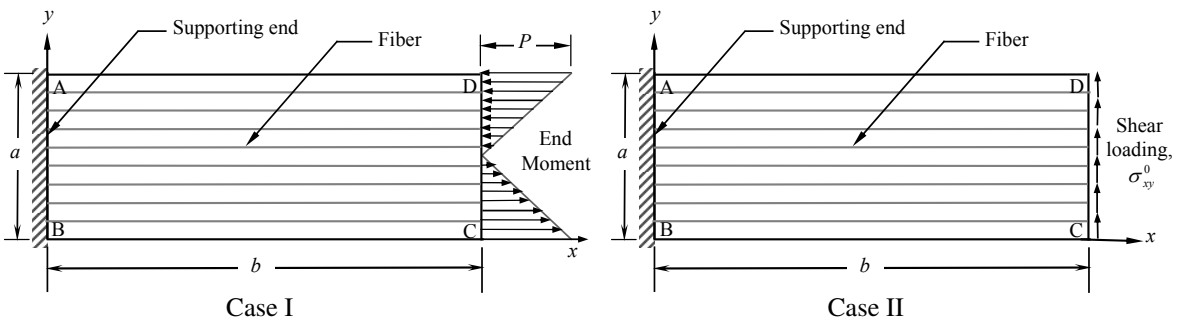


**Figure 1.** Model of orthotropic composite panels subjected to an end moment (Case I) or to shear loading (Case II).

is distributed according to a simple linear relationship given by $\sigma_n = P[1 - 2(y/a)]$, where $P$ is the maximum intensity of the stress.

Case II is also a panel with a rectangular cross section that is supported at its left lateral end and is subjected to a uniform shear loading (intensity $\sigma_{xy}^0$) at the right lateral end. The supporting ends of the panels are considered to be rigidly fixed, and the fibers are assumed to be situated along the panel length. In both cases, $b/a$ ratios of 1, 2, and 3 are considered.

## 4. Numerical solution to the problem

The FDM is used to discretize the governing differential equation (5) as well as the differential equations associated with the boundary conditions (6)–(10). The discrete values of the potential function $\psi(x, y)$, at the mesh points of the domain concerned, are solved from the system of linear algebraic equations resulting from the application of the governing equation and the boundary conditions by the use of a direct method of solution.

*Discretization of the domain.* The region of interest is divided into the desired number of mesh points, and the values of the dependent function $\psi(x, y)$ are sought only at these points. Depending upon the type of differential equations involved and on the geometry of the panel, a uniform rectangular mesh network is used. The error of the computational approach is of the order $h^2$, and a mesh network of around 450 nodal points would be sufficient for an accurate and stable numerical solution [Akanda et al. 2000]. The discretization scheme of the panel is schematically illustrated in Figure 2. The governing differential equation, which is used to evaluate the function $\psi(x, y)$ only at the internal mesh points, is expressed in difference form using central difference operators as

$$F_1\big(\psi(i-2, j) + \psi(i+2, j)\big) - F_2\big(\psi(i-1, j) + \psi(i+1, j)\big) - F_3\big(\psi(i, j+1) + \psi(i, j-1)\big)$$
$$+ F_4\psi(i, j) + F_5\big(\psi(i+1, j+1) + \psi(i+1, j-1) + \psi(i-1, j+1) + \psi(i-1, j-1)\big)$$
$$+ F_6\big(\psi(i, j-2) + \psi(i, j+2)\big) = 0, \quad (11)$$

where

$$F_1 = (k/h)^4, \quad F_2 = 4(k/h)^4 + 2M(k/h)^2, \quad F_3 = 2M(k/h)^2 + 4\frac{E_2}{E_1},$$

$$F_4 = 6(k/h)^4 + 4M(k/h)^2 + 6\frac{E_2}{E_1}, \quad F_5 = M(k/h)^2, \quad F_6 = \frac{E_2}{E_1}, \quad M = \frac{E_2}{G_{12}} - \frac{2\nu_{12}E_2}{E_1},$$

Here $h, k$ are the mesh lengths in the $x$- and $y$-directions, respectively.

The corresponding grid structure of the difference equation, Equation (11), for any internal mesh point $(i, j)$ is shown in Figure 2. The pivotal point $(i, j)$ in the grid structure is the point of application of the governing equation. As far as the present central-difference grid structure of the governing equation is concerned, when the point of application $(i, j)$ becomes an immediate neighbor to the physical boundary, it will involve mesh points both interior and exterior to the physical boundary of the panel. Thus, an imaginary boundary, exterior to the physical boundary, as shown in Figure 2, is introduced such that the application of the governing equation (11), especially to the points in the immediate neighborhood of the
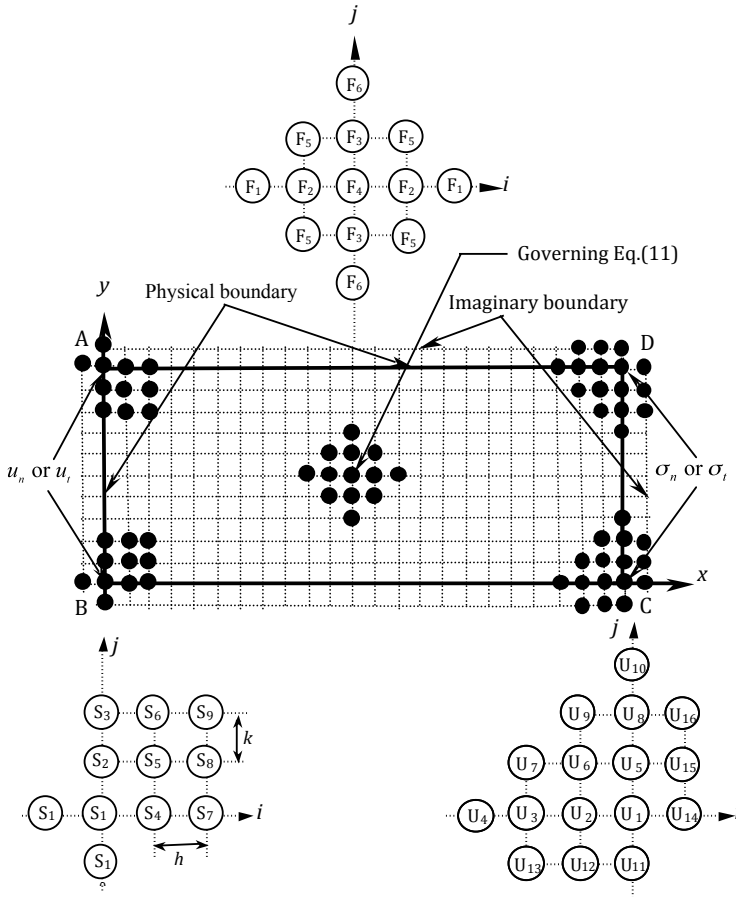
**Figure 2.** Finite-difference mesh network used to describe the panel, and the application of FD stencils of the governing equation and boundary conditions.

physical boundary, involves no points exterior to the model boundary (imaginary one), thereby causing no difficulties in developing a straightforward program.

*Management of boundary conditions.* The physical conditions at any point on a boundary are usually visualized in terms of normal and tangential components of displacement and stress. The expressions for the normal and tangential components of displacement in terms of the function $\psi$ are

$$u_n(x, y) = lu_x(x, y) + mu_y(x, y), \qquad u_t(x, y) = lu_y(x, y) - mu_x(x, y), \tag{12}$$

where $l$ and $m$ are the direction cosines of a point on the boundary. Similarly, the expressions for the normal and tangential components of stress for points on the body are

$$\sigma_n(x, y) = l^2\sigma_{xx}(x, y) + 2lm\sigma_{xy}(x, y) + m^2\sigma_{yy}(x, y), \tag{13}$$

$$\sigma_t(x, y) = (l^2 - m^2)\sigma_{xy}(x, y) + lm[\sigma_{yy}(x, y) - \sigma_{xx}(x, y)]. \tag{14}$$

Expressions (12)–(14) can be found in [Akanda et al. 2002].

Because the differential equations associated with the boundary conditions contain second and third order derivatives of the function $\psi$, the use of central difference expressions is not practical because most of the time it leads to the inclusion of points exterior to the imaginary boundary. The derivatives of the boundary expressions are thus replaced by their corresponding backward or forward difference formulas, keeping the order of the local truncation error the same, $O(h^2)$. In order to avoid the inclusion of points exterior to the imaginary boundary, four different sets of finite difference expressions for each of the boundary conditions are developed for the points at different regions of the boundary. These four sets of algebraic equations are derived by adopting different combinations of forward and backward difference schemes. The choice of the appropriate set of expressions for a point on the boundary is determined by the point's position on the boundary, which avoids the introduction of additional mesh points external to the imaginary boundary. Some of the difference equations derived for the boundary conditions are shown below.

For example, the finite difference form of the normal or tangential component of displacement ($i$-forward, $j$-forward) for the bottom left boundary is expressed as follows:

$$u_n(i, j) = S_1\psi(i, j) + S_2\psi(i, j+1) + S_3\psi(i, j+2)$$
$$+ S_4\psi(i+1, j) + S_5\psi(i+1, j+1) + S_6\psi(i+1, j+2) + S_7\psi(i+2, j)$$
$$+ S_8\psi(i+2, j+1) + S_9\psi(i+2, j+2) + S_{10}\psi(i, j-1) + S_{11}\psi(i-1, j). \quad (15)$$

Similarly, the finite difference form of the normal or tangential component of stress ($i$-backward, $j$-forward) for the bottom right boundary is expressed as follows:

$$\sigma_n(i, j) = U_1\psi(i, j) + U_2\psi(i-1, j) + U_3\psi(i-2, j) + U_4\psi(i-3, j) + U_5\psi(i, j+1)$$
$$+ U_6\psi(i-1, j+1) + U_7\psi(i-2, j+1) + U_8\psi(i, j+2) + U_9\psi(i-1, j+2)$$
$$+ U_{10}\psi(i, j+3) + U_{11}\psi(i, j-1) + U_{12}\psi(i-1, j-1) + U_{13}\psi(i-2, j-1)$$
$$+ U_{14}\psi(i+1, j) + U_{15}\psi(i+1, j+1) + U_{16}\psi(i+1, j+2), \quad (16)$$

where the coefficients $S_i$ and $U_i$ are functions of elastic constants, direction cosines, and mesh lengths. The corresponding FD grid structures of the difference equations, (15) and (16), are also shown in Figure 2. The structures of the normal and tangential components are found to be identical in form, but they differ in the sense of the nodal coefficients.

*Placement of boundary conditions and evaluation of stresses and displacements.* There are two conditions to be satisfied at a point on the physical boundary of the rectangular panel, therefore, two difference equations corresponding to the respective boundary conditions are applied to the same point on the boundary. Of these two equations, one is used to evaluate the function $\psi$ at the physical boundary point, and the remaining equation is used to evaluate $\psi$ at the corresponding point on the imaginary boundary. Special treatments are adopted for the four corner mesh points, which are generally the points of transition for the boundary conditions. The program is organized in such a fashion that it will satisfy three out of the available four boundary conditions for each corner point. As a result, the outer corner points of the imaginary boundary are not taken into consideration for the present solution, as illustrated in the FD mesh network

of Figure 2. Therefore, the application of the governing equation as well as the necessary boundary conditions ensures that every mesh point of the computational domain will have a single algebraic equation in terms of the function $\psi$ for its evaluation. Finally, in order to evaluate the stress and displacement components, four sets of finite difference expressions for each of the displacement and stress components (6)–(10) are developed in a fashion similar to that adopted in the case of the boundary conditions. Because all of the stress and displacement components are expressed in terms of the function $\psi$, the parameters of interest are readily calculated from the $\psi$ values obtained at the mesh points of the domain.

In the present computational approach, the number of algebraic equations is equal to the number of field nodal points, and for each nodal point, there is only one unknown. Thus an $(n \times n)$ matrix of coefficients is generated for a total of $n$ active field nodal points. It was shown that the present displacement potential-based FDM can save a tremendous amount of computational effort (approximately 87%) for the solution for a two-dimensional problem in comparison with the effort required for the usual computational approaches [Ahmed et al. 2005a].

## 5. Results and discussion

The results of the finite difference solution for the composite panel subjected to two different types of loading, as described in Section 3, are presented in this section. The results are presented mainly in the form of the calculated deformed shape and the distribution of the various stress and displacement components of interest. In all cases, displacements are normalized with respect to panel width ($a$), and stresses are normalized with respect to the maximum intensity of the applied loading ($P$ and $\sigma_{xy}^0$, see Figure 1). The details of the boundary conditions used to obtain the FD solutions, as they relate to the bounding edges, are given in Table 1, while Table 2 presents the boundary conditions associated with the corner points. For most of the results, the panel material is considered to be a boron/epoxy composite for which the effective mechanical properties, together with the properties of glass/epoxy and graphite/epoxy, are listed in Table 3. For the panel subjected to the end moment (Case I), solutions are obtained for different panel aspect ratios ($b/a$). The solutions for the elastic field of the panel (Case II) are presented mainly in a comparative fashion with the corresponding FEM solutions. The magnitude of

| boundary segment | given boundary conditions | correspondence between mesh points and given boundary conditions | |
|---|---|---|---|
| | | mesh point on the physical boundary conditions | mesh point on the imaginary boundary conditions |
| AB | $(u_n, u_t)$ | $u_n = 0$ | $u_t = 0$ |
| BC | $(\sigma_n, \sigma_t)$ | $\sigma_n = 0$ | $\sigma_t = 0$ |
| DA | $(\sigma_n, \sigma_t)$ | $\sigma_n = 0$ | $\sigma_t = 0$ |
| CD (Case I) | $(\sigma_n, \sigma_t)$ | $\sigma_n = P[1 - 2(y/a)]$ | $\sigma_t = 0$ |
| CD (Case II) | $(\sigma_n, \sigma_t)$ | $\sigma_t = \sigma_{xy}^0$ | $\sigma_n = 0$ |

**Table 1.** Boundary conditions used for different boundary segments of the panels, Case I and Case II (see Figure 1).

| corner points | given boundary conditions | used boundary conditions | correspondence between mesh points and given boundary conditions | |
|---|---|---|---|---|
| | | | mesh point on the physical boundary conditions | mesh point on the imaginary boundary conditions |
| A | $[(u_n, u_t), (\sigma_n, \sigma_t)]$ | $[u_n, u_t, \sigma_n]$ | $\sigma_n = 0$ | $u_n = 0, u_t = 0$ |
| B | $[(u_n, u_t), (\sigma_n, \sigma_t)]$ | $[u_n, u_t, \sigma_n]$ | $\sigma_n = 0$ | $u_n = 0, u_t = 0$ |
| C (Case II) | $[(\sigma_n, \sigma_t), (\sigma_n, \sigma_t)]$ | $[\sigma_n, \sigma_t, \sigma_n]$ | $\sigma_t = \sigma_{xy}^0$ | $\sigma_n = 0, \sigma_t = 0$ |
| C (Case I) | $[(\sigma_n, \sigma_t), (\sigma_n, \sigma_t)]$ | $[\sigma_n, \sigma_t, \sigma_n]$ | $\sigma_n = P$ | $\sigma_n = 0, \sigma_t = 0$ |
| D (Case II) | $[(\sigma_n, \sigma_t), (\sigma_n, \sigma_t)]$ | $[\sigma_n, \sigma_t, \sigma_n]$ | $\sigma_t = \sigma_{xy}^0$ | $\sigma_n = 0, \sigma_t = 0$ |
| D (Case I) | $[(\sigma_n, \sigma_t), (\sigma_n, \sigma_t)]$ | $[\sigma_n, \sigma_t, \sigma_n]$ | $\sigma_n = -P$ | $\sigma_n = 0, \sigma_t = 0$ |

**Table 2.** Boundary conditions used for corner points of the panels, Case I and Case II (see Figure 1).

| material | property | boron/epoxy | graphite/epoxy | glass/epoxy |
|---|---|---|---|---|
| composite | $V_f$ | 0.50 | 0.70 | 0.45 |
| | $E_1$ ($10^6$ psi) | 29.59 | 26.25 | 5.60 |
| | $E_2$ ($10^6$ psi) | 2.68 | 1.49 | 1.20 |
| | $G_{12}$ ($10^6$ psi) | 0.81 | 1.04 | 0.60 |
| | $\nu_{12}$ | 0.23 | 0.28 | 0.26 |
| epoxy | $E$ ($10^6$ psi) | 0.50 | | |
| | $\nu$ | 0.35 | | |

**Table 3.** Mechanical properties of composites used.

the maximum intensity of loading per unit area for the two cases of the panel ($P$ and $\sigma_{xy}^0$, respectively) is arbitrarily assumed to be 6000 psi (41.4 MPa). The FD mesh network used to model the panels with different aspect ratios contains nodal points (24–56 × 19) in the direction of $x$ and $y$, respectively.

**5.1.** *Orthotropic panel under application of an end moment (Case I).* The numerical results obtained for the relevant displacement and stress components at different sections of the panel under the end moment are analyzed and presented in this section. Figure 3, top, shows the predicted deformed shape of the boron/epoxy panel with $b/a = 2$, in which the displacements are magnified by a factor of 100. The overall deformation pattern of the panel is found to be in good agreement with the physical model of the panel. From the distribution of axial displacement components ($u_x$) at different longitudinal sections of a panel, it is observed that the displacement varies linearly and antisymmetrically with respect to the panel width. At the right lateral end, the displacement takes its highest value and decreases gradually towards the supporting end. For a particular longitudinal section, the lateral displacement ($u_y$) is found to remain constant over the panel width, the magnitude of which, however, gradually decreases as we move towards the supporting end. Furthermore, the displacement field of the orthotropic panel is analyzed in
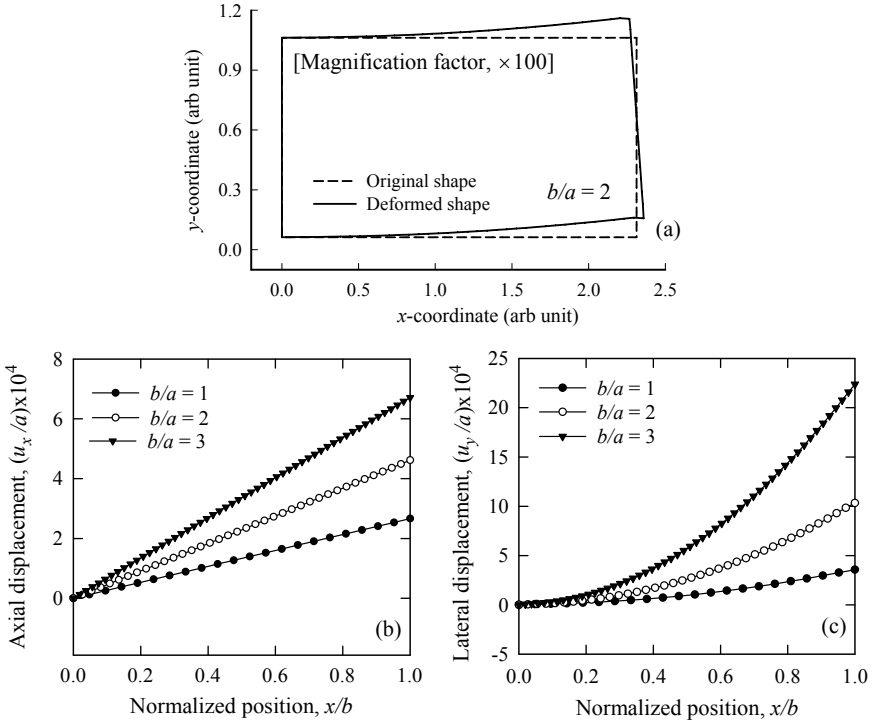
**Figure 3.** Deformed shape (top) and distributions of axial (bottom left) and lateral (bottom right) displacements at section $y/a = 0$ of boron/epoxy panels (Case I).

the perspective of panel aspect ratio. The axial and lateral displacements along the lower longitudinal edge ($y/a = 0$) of the panel are presented with respect to the normalized axial position, as a function of aspect ratio, in Figure 3, bottom. The axial displacement varies linearly with respect to the panel length, whereas the lateral displacement varies nonlinearly. As far as the magnitude is concerned, the lateral displacements are found to take much higher values than the axial displacements.

Figure 4 illustrates the distribution of axial stress components at different sections of the orthotropic
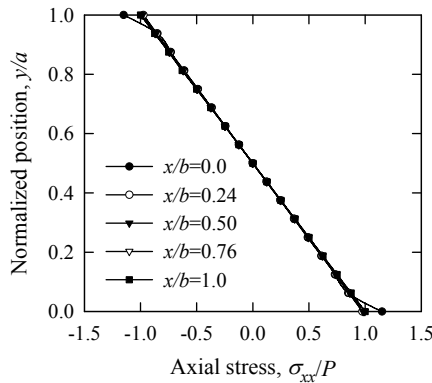


**Figure 4.** Distribution of the axial stress component at different sections of the boron/epoxy panel (Case I, $b/a = 2$).

panel, $b/a = 2$. It is observed from the solution that the distribution of axial stress is identical for all longitudinal sections of the panel, and varies linearly from its maximum to minimum value with respect to panel width. The maximum and minimum values of the normalized axial stress are found to occur at the two opposing edges, the magnitudes of which are 1 and $-1$. As far as the applied moment loading is concerned, the FD solution for the axial stress component is completely in agreement with the expected solution, both in terms of magnitude and nature of variation. The axial stress distributions are found to be independent of the panel aspect ratio, that is, at a particular section of $x/b$, the distribution remains identical for different $b/a$ ratios both in terms of magnitude and shape. Other components of stress are found to be insignificant when their magnitudes are compared with the magnitude of the axial stress.

**5.2.** *Orthotropic panel subjected to shear loading (Case II).* In this section, the FD solutions for the composite panel (Case II) are presented mainly in the form of a comparison with the corresponding solutions from the FEM. Note that no reliable theoretical solution for the present composite panel problem is available in the literature. The reliability and accuracy of the present numerical solutions is, therefore, verified by comparison with a numerical solution that is based on a completely different philosophy. Therefore, the same panel problem was solved by FEM using the standard commercial software ANSYS with two different aspect ratios, $b/a = 2$ and 3. Considering the rectangular shape of the panel, four-noded rectangular plane elements (orthotropic) are used to construct the corresponding mesh network. All elements have the same aspect ratio, and their distribution is kept uniform all over the domain. The total number of finite elements used to discretize the panel is 800 ($40 \times 20$). The convergence as well as accuracy of the solution is verified by varying the element mesh density.

Figure 5 presents the distributions of displacement components at the mid-longitudinal section of the composite panels having different aspect ratios. For this particular loading on the panel, the lateral stress distributions at the mid-longitudinal section are found to be straight vertical lines when analyzed from the perspective of the panel width. The corresponding FE predictions of displacements are also included in the same graphs. In general, the two solutions for displacements are very close to each other. A critical comparison of the axial displacements reveals that the discrepancy between the two solutions is almost negligible for panels with higher aspect ratios, but for shorter panels, FEM predicts slightly higher displacements, especially in the regions near the two opposing longitudinal edges. Unlike the constant lateral
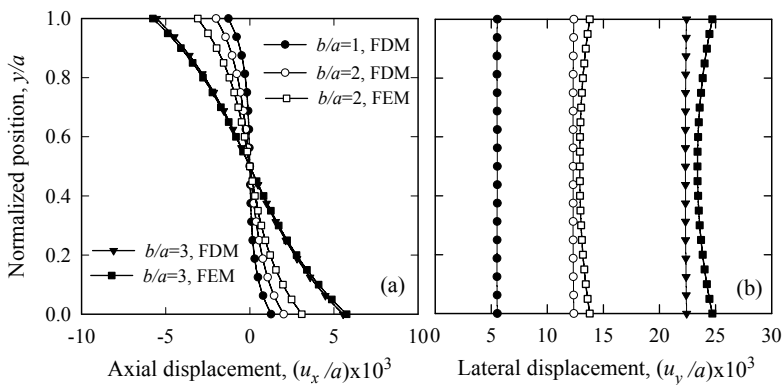


**Figure 5.** Distributions of (a) axial and (b) lateral displacements at section $x/b = 0.5$ of boron/epoxy panels (Case II).

displacements predicted by the present numerical approach, FEM predicts a nonlinear distribution of the displacement component, in which the case of axial displacement similarly shows a slight increase in lateral displacement in the neighborhood of the opposing longitudinal edges. As far as the physical characteristics of the panel are concerned, it may be difficult to verify that the FEM solution is reliable, especially around the two opposing longitudinal edges where the displacements are found to assume higher values than those at the interior region of the same section, $x/b = 0.5$. Results also show that the aspect ratio has a significant influence on the displacement field of an orthotropic panel subjected to a shear loading.

Figure 6 presents the axial stress distributions at the support, $x/b = 0$ and at section $x/b = 0.1$ of the panels for which $b/a = 2$ and 3. Along with the present FD solutions, the results of FEM are included for the convenience of direct comparison. Sections near the supporting end have been chosen here for consideration because the fixed end of the panel is identified to be the most critical section in terms of stresses. For both panels, the two numerical solutions for axial stress are in excellent agreement. Slight discrepancies between the solutions are observed, particularly at the corner points of the supporting end. For the corner points of the supporting end, which are, in fact, the points of singularity by design, FE results show higher nonlinearity, and, thus, a higher value of the axial stress compared to the nonlinearity of FD solutions. The FD predictions at the section $x/b = 0.1$ are found to be identical to those of FE solutions both at the edges and in the interior region. In general, the stress level is found to increase with increased aspect ratio, and the nonlinearity of the distribution decreases as the panel becomes longer.
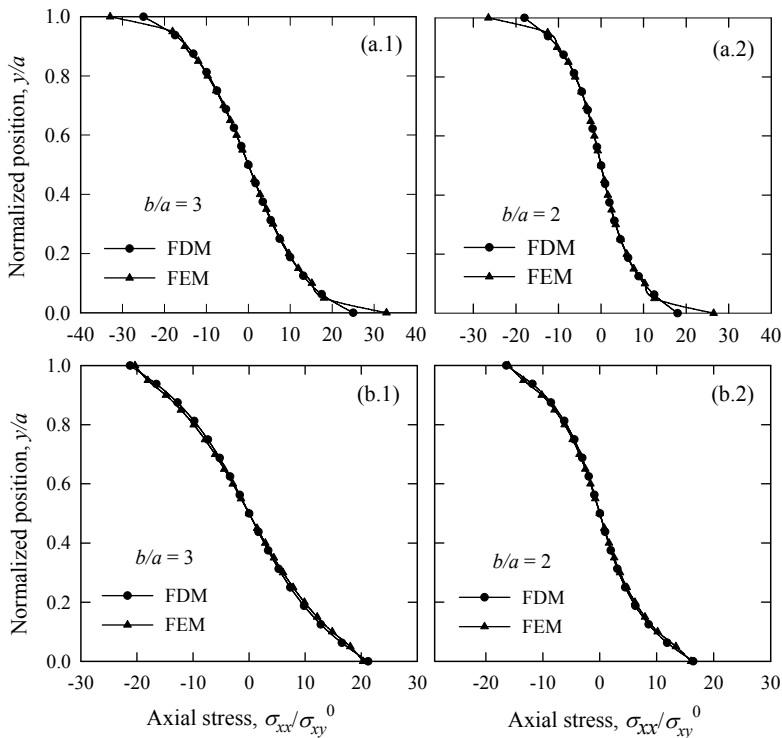


**Figure 6.** Distributions of the axial stress component at the supporting end (top row) and at the section $x/b = 0.1$ (bottom row) of boron/epoxy panels under shear loading (Case II).
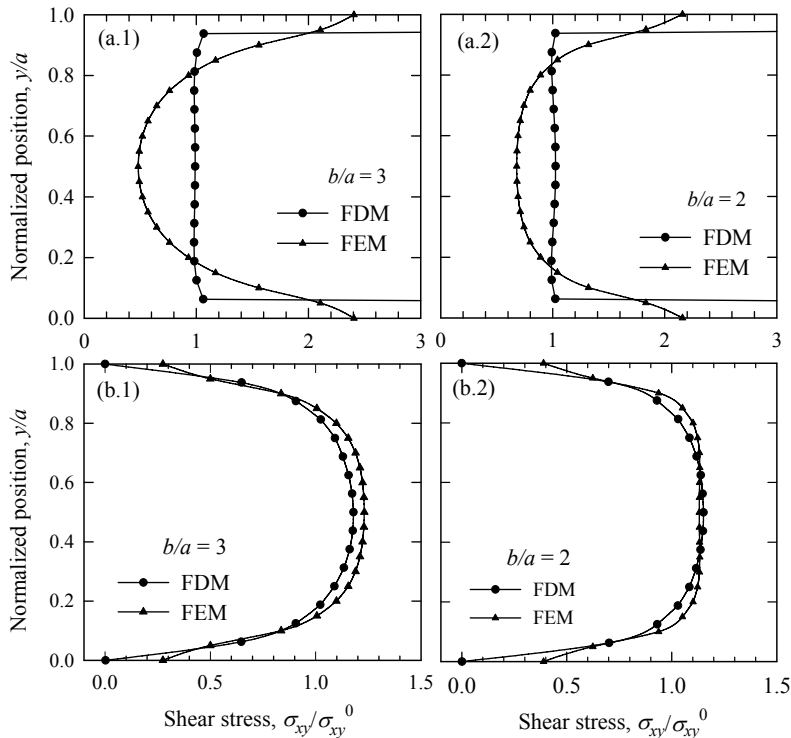
**Figure 7.** Distributions of the shear stress component at the supporting end (top row) and at the section $x/b = 0.1$ (bottom row) of boron/epoxy panels under shear loading (Case II).

The nonlinear distribution of the stress at the support is found to approach linearity as the section under consideration is moved away from the supporting end.

The distributions of shear stress along the panel width, particularly for sections $x/b = 0$ and 0.1, are shown in Figure 7 for the panels with $b/a = 2$ and 3. The corresponding FE predictions of shear stress are also included in the same figures. The top row of Figure 7 compares the two solutions for the shear stress at the supporting edges of the two panels $b/a = 2$ and 3. The two solutions for the shear stress at the fixed support are found to differ quite substantially in terms of both magnitude and shape. The present $\psi$-formulation predicts a constant shear stress at the supporting end, the associated magnitude of which is found to be identical to that applied at the right lateral end. In addition, for the present orthotropic panel under shear loading, the shear stress at the support is found to be independent of panel aspect ratio. However, the FEM predicts a highly nonlinear distribution for the shear stress at the support. The maximum stress is observed at the upper and lower corners of the support, whereas the mid-region experiences the minimum stress. This particular shape of the distribution is found to be the reverse of the distributions obtained for the remaining longitudinal sections of the panel, in which the maximum stress is observed at the mid-region and the stress vanishes at the upper and lower edges. The effect of the singularity at the two corner points of the support is clearly reflected in the solutions from the FDM, because the stresses predicted at the two corner points are found to be higher than those at the remaining points of the support. Because the modeling of the boundary conditions for the corner points

in standard FE simulations does not take into account the effect of the singularity, the predictions near the corner regions may be unreliable. On the other hand, the transition of the boundary conditions in our FD modeling is handled in a more efficient way; for example, for each of the corner points of the panel, a total of three conditions out of the available four are satisfied appropriately (see Table 2). As a result, the present solutions are claimed to be closer to the actual states of the stresses. Note that the effect of the singularity in our FD solution is found to be highly localized, because the uniformity of the shear stress distribution at the supporting end remains unaffected except for the two corner points; see Figure 7, top. For sections away from the support, the shear stress distributions are significantly different from the distributions at the support, where the maximum stress at a particular section develops at the mid-width position, and the stress vanishes at the opposing longitudinal edges. The solutions at section $x/b = 0.1$ are presented in the bottom row of Figure 7. The two numerical solutions are found to be almost identical except for the small discrepancies at the two longitudinal surfaces. More specifically, the comparison of solutions in these two graphs shows that the FEM predictions of shear stress at the upper and lower surfaces are not reliable, even though the section concerned is free from singularities. The present FDM is, however, found to be free from the drawbacks of standard computational methods, and is able to predict the actual state of stresses at the surfaces.

Figure 8 shows the distribution of the lateral stress $\sigma_{yy}$ at the sections $x/b = 0$ and 0.1 of the panel with different aspect ratios. Figure 8, top left, shows the solutions from the FDM at the supporting end
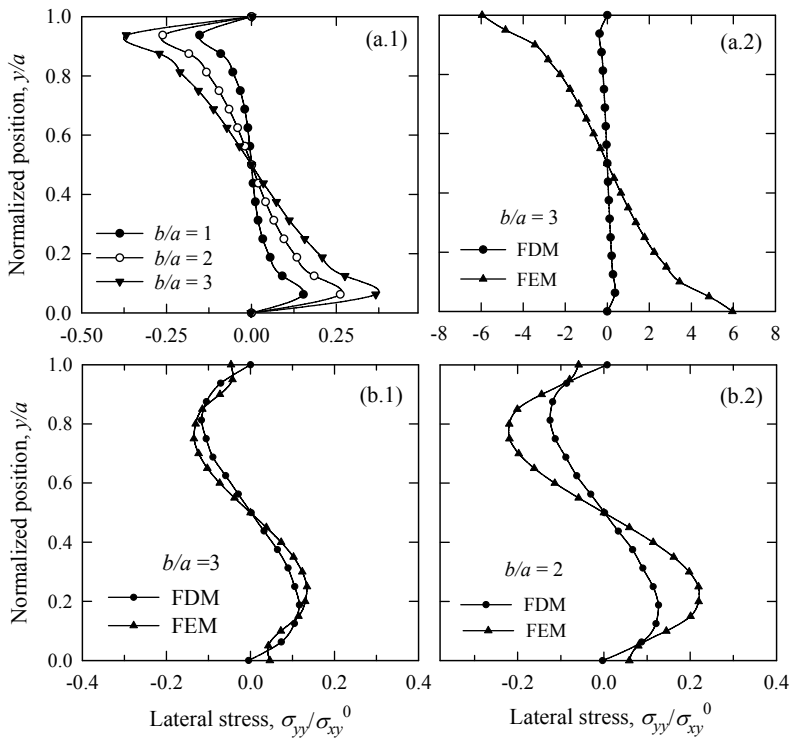


**Figure 8.** Distributions of the lateral stress component at the supporting end (top row) and at the section $x/b = 0.1$ (bottom row) of boron/epoxy panels under shear loading (Case II).

of the panels having $b/a = 1$, 2, and 3. Stresses at the support are found to increase with increasing panel aspect ratio, although the magnitude of the stress is lowest, compared to the magnitudes of shear and axial stresses, at the support. Stresses at the two corner points of the supporting end are found to be zero, which agrees with the physical conditions of the panels (see Table 2). Figure 8, top right, compares the solutions for the stress at the support obtained by FDM and FEM. As shown in the figure, the two solutions differ quite significantly from each other. The maximum normal stress at the support of the panel, $b/a = 3$, predicted by FEM, is found to be around 15 times higher than that predicted by FDM, which is in contrast with the stresses predicted for other sections of the panel. The bottom row of Figure 8 compares the solutions at section $x/b = 0.1$ for the two panels. From the figure, the two solutions at section $x/b = 0.1$ are found to be comparable with minor deviations, especially in the regions of the top and bottom surfaces. The FE solution for $\sigma_{yy}$ does not reflect the physical characteristics of the panel, because the stresses do not vanish on the top and bottom surfaces, even when the section concerned is free from singularities. This inaccuracy of the FEM solution is found to be more pronounced as we approach the section containing the points of singularity, calling into question the reliability of the solution at the supporting end. The FD solution for the lateral stress $\sigma_{yy}$ conforms appropriately to the physical model of the panel for all regions of interest at or away from the surfaces.

The superiority of the present FDM in reproducing the stresses at the bounding surfaces is further illustrated in Figure 9. The figure describes the distributions of axial stresses obtained by FDM and FEM at the right lateral end of the panel with $b/a = 2$, subjected to a uniform shear loading only. The boundary is basically free from any normal loading, and the corresponding state of stress is modeled exactly by the present method. However, the FEM solution is found to assume a peculiar antisymmetric distribution of the axial stress at the right end, which is highly unlikely. The effect of the singularity on the FEM solution is very prominent; quantitative analysis shows that the region over which the effect of singularity is prominent is more than 20% of the width, from both surfaces $y/a = 0$ and 1. On the other hand, the present computational method allows one to exactly satisfy the condition that $\sigma_n = 0$ at the corner points of the right end (see Table 2), and, additionally, the condition is reflected appropriately in the solution.

The present computational scheme is extended to investigate the effects of stiffeners on the elastic field of the orthotropic panels. A maximum in the panel's axial stress (Case II) develops at the fixed support $(y/a = 0)$ when the panel is free from the stiffeners. However, the stress at the support is found to vanish
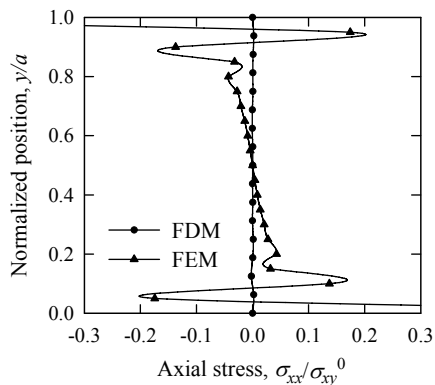


**Figure 9.** Comparison of two solutions for the axial stress distribution at the right lateral end of boron/epoxy panel ($b/a = 2$) under shear loading (Case II).
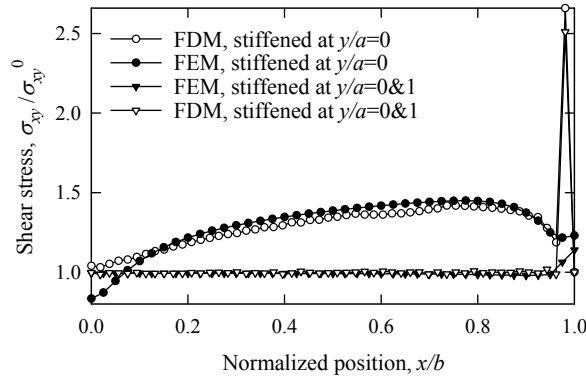
**Figure 10.** Distributions of the shear stress component along the stiffened edge, $y/a = 0$, of the boron/epoxy panel ($b/a = 3$) under shear loading (Case II).

when both opposing longitudinal edges ($y/a = 0$ and 1) are stiffened. We note that the physical condition of the stiffeners is modeled here by restraining the tangential displacements ($u_x$) of the longitudinal edges, while they are kept free from normal loading [Nath and Ahmed 2009]. The greatest impact of the stiffeners on the elastic field is realized in the shearing stress that develops along the stiffened edges, which is presented comparatively in Figure 10. The figure shows results for two cases of stiffened panels: (a) one of the longitudinal edges ($y/a = 0$) is stiffened; and (b) both longitudinal edges ($y/a = 0$ and 1) are stiffened. When the two opposing edges are stiffened, a uniform shearing stress develops along the stiffened edges, which is, with respect to magnitude, identical to the magnitude of the applied loading, $\sigma_{xy}^0$. However, when only the edge, $y/a = 0$, is stiffened, a gradually increasing shearing stress is observed along the edge, the magnitude of which varies approximately within $1.0 \leq (\sigma_{xy}/\sigma_{xy}^0) < 1.5$ (see Figure 10). Similar to the previous cases, the FDM and FEM solutions are found to be nearly identical for almost all regions, except for the two extreme regions of the longitudinal edge. The maximum shearing stress predicted by the present FDM at the stiffened edge is $[\sigma_{xy}]_{\max} \approx 2.6\sigma_{xy}^0$, which is found on the stiffened edge immediately adjacent to the bottom-right corner; the corresponding FEM prediction is only 1.23 times the applied stress, $\sigma_{xy}^0$, which is found at the bottom-right corner of the stiffened edge. Because the point of maximum stress, identified by the present FDM, is free from singularities, and, additionally, the method reproduces the stress at the bottom corner point of the right lateral end exactly, the FD prediction of the maximum shear stress appears to be highly reliable, even though it is not supported by FEM. Moreover, the stress predicted by FEM near the left corner region of the stiffened edge is questionable, because it assumes a value less than that of the applied one, $\sigma_{xy}^0$.

Figure 11 presents the distribution of the lateral stress component at the fixed support of a panel composed of different composites. The distribution, therefore, describes the effect of fiber reinforcement in epoxy resin on the elastic field that develops under shear loading (Case II). The analysis presented shows that the effect of fiber reinforcement on the lateral stress, especially at the supporting end, is quite significant, whereas the effect on the axial and shearing stresses is not significant. Figure 11 reveals that the highest lateral stress develops when the epoxy resin is free from fibers, that is, the panel is composed of an isotropic epoxy resin. The stress level is found to decrease significantly as the longitudinal fibers are inserted into the resin. Among the composites, the maximum lateral stress at the support is found for the case of glass/epoxy. The general trend of the results suggests that at the supporting end of the shear
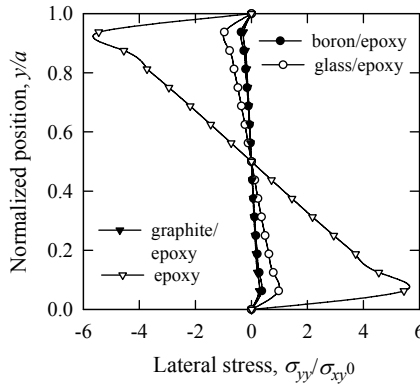
**Figure 11.** Effect of fiber reinforcement on the lateral stress at the supporting end of the boron/epoxy panel ($b/a = 3$) under shear loading (Case II).

loaded panel, where displacements in both directions are restrained, the magnitude of the lateral stress decreases with increased elastic moduli of the panel material (see Table 3).

## 6. Conclusions

The elastic behavior of an orthotropic composite panel with mixed boundary conditions is analyzed using an efficient numerical method. The special advantages of the method over existing approaches are its ability to satisfy and reproduce the boundary conditions appropriately, whether they are specified in terms of loading, restraints, or any combination thereof. Moreover, the present displacement potential-based computational method requires less computational effort to solve a problem compared to the effort required by standard computational approaches. Results of the present analysis show that critical stresses at the panel support are significantly influenced by the aspect ratio as well as edge stiffening, particularly when the panel is subjected to shear loading. Comparative analysis to the standard finite element method verifies the superiority of the present displacement potential formulation in conjunction with the finite difference method for predicting accurate and reliable stresses at any critical section of the panel, specially at the regions of transition of boundary conditions.

## Index of notation

| | | | |
|---|---|---|---|
| $E_1$ | Elastic modulus of the material in $x$-direction | $\sigma_{xx}, \sigma_{yy}$ | Axial and lateral stress components |
| $E_2$ | Elastic modulus of the material in $y$-direction | $\sigma_{xy}$ | Shearing stress component in the $xy$ plane |
| $\nu_{12}, \nu_{21}$ | Major and minor Poisson's ratios | $u_n, u_t$ | Normal and tangential displacement |
| $G_{12}$ | In-plane shear modulus in the 1-2 plane | $\sigma_n, \sigma_t$ | Normal and tangential stress |
| $E$ | Elastic modulus of isotropic material | $\psi$ | Displacement potential function |
| $G$ | Shear modulus of isotropic material | $a, b$ | Dimensions of the panel in $x$- and $y$-directions |
| $l, m$ | Direction cosines of the normal to a boundary | $P$ | Maximum intensity of normal stress in Case I |
| $u_x, u_y$ | Displacement components | $\sigma_{xy}^0$ | Intensity of applied shear stress in Case II |

## References

[Ahmed et al. 1996] S. R. Ahmed, A. B. M. Idris, and M. W. Uddin, "Numerical solution of both ends fixed deep beams", *Comput. Struct.* **61**:1 (1996), 21–29.

[Ahmed et al. 1998] S. R. Ahmed, M. R. Khan, K. M. S. Islam, and M. W. Uddin, "Investigation of stresses at the fixed end of deep cantilever beams", *Comput. Struct.* **69**:3 (1998), 329–338.

[Ahmed et al. 2005a] S. R. Ahmed, M. Z. Hossain, and M. W. Uddin, "A general mathematical formulation for finite-difference solution of mixed-boundary-value problems of anisotropic materials", *Comput. Struct.* **83**:1 (2005), 35–51.

[Ahmed et al. 2005b] S. R. Ahmed, S. K. D. Nath, and M. W. Uddin, "Optimum shapes of tire-treads for avoiding lateral slippage between tires and roads", *Int. J. Numer. Methods Eng.* **64**:6 (2005), 729–750.

[Akanda et al. 2000] M. A. S. Akanda, S. R. Ahmed, M. R. Khan, and M. W. Uddin, "A finite-difference scheme for mixed boundary-value problems of arbitrary-shaped elastic bodies", *Adv. Eng. Software* **31**:3 (2000), 173–184.

[Akanda et al. 2002] M. A. S. Akanda, S. R. Ahmed, and M. W. Uddin, "Stress analysis of gear teeth using displacement potential function and finite differences", *Int. J. Numer. Methods Eng.* **53**:7 (2002), 1629–1640.

[Chapel and Smith 1968] R. E. Chapel and H. W. Smith, "Finite-difference solutions for plane stresses", *AIAA J.* **6**:6 (1968), 1156–1157.

[Chow et al. 1953] L. Chow, H. D. Conway, and G. Winter, "Stresses in deep beams", *Trans. ASCE* **118**:2557 (1953), 686–708.

[Conway 1953] H. D. Conway, "Some problems of orthotropic plane stress", *J. Appl. Mech.* (*ASME*) **20**:1 (1953), 72–76.

[Conway et al. 1951] H. D. Conway, L. Chow, and G. W. Morgan, "Analysis of deep beams", *J. Appl. Mech.* (*ASME*) **18** (1951), 163–172.

[Dow et al. 1990] J. O. Dow, M. S. Jones, and S. A. Harwood, "A new approach to boundary modelling for finite difference applications in solid mechanics", *Int. J. Numer. Methods Eng.* **30**:1 (1990), 99–113.

[Durelli and Ranganayakamma 1989] A. J. Durelli and B. Ranganayakamma, "Parametric solution of stresses in beams", *J. Eng. Mech.* (*ASCE*) **115**:2 (1989), 401–414.

[Hardy and Pipelzadeh 1991] S. J. Hardy and M. K. Pipelzadeh, "Static analysis of short beams", *J. Strain Anal. Eng. Des.* **26**:1 (1991), 15–29.

[Jones 1975] R. M. Jones, *Mechanics of composite materials*, McGraw-Hill, New York, 1975.

[Krishna Murty 1984] A. V. Krishna Murty, "Towards a consistent beam theory", *AIAA J.* **22**:6 (1984), 811–816.

[Nath and Ahmed 2009] S. K. D. Nath and S. R. Ahmed, "Displacement potential solution of stiffened composite struts subjected to eccentric loading", *Appl. Math. Model.* **33**:3 (2009), 1761–1775.

[Nath et al. 2006] S. K. D. Nath, S. R. Ahmed, and A. M. Afsar, "Displacement potential solution of short stiffened flat composite bars under axial loadings", *Int. J. Appl. Mech. Eng.* **11**:3 (2006), 557–575.

[Nath et al. 2007] S. K. D. Nath, A. M. Afsar, and S. R. Ahmed, "Displacement potential solution of a deep stiffened cantilever beam of orthotropic composite material", *J. Strain Anal. Eng. Des.* **42**:7 (2007), 529–541.

[Ranzi et al. 2006] G. Ranzi, F. Gara, G. Leoni, and M. A. Bradford, "Analysis of composite beams with partial shear interaction using available modelling techniques: a comparative study", *Comput. Struct.* **84**:13–14 (2006), 930–941.

[Richards and Daniels 1987] T. H. Richards and M. J. Daniels, "Enhancing finite element surface stress predictions: a semi-analytic technique for axisymmetric solids", *J. Strain Anal. Eng. Des.* **22**:2 (1987), 75–86.

[Smart 1987] J. Smart, "On the determination of boundary stresses in finite elements", *J. Strain Anal. Eng. Des.* **22**:2 (1987), 87–96.

[Suzuki 1986] S. Suzuki, "Stress analysis of short beams", *AIAA J.* **24**:8 (1986), 1396–1398.

[Timoshenko and Goodier 1979] S. Timoshenko and V. N. Goodier, *Theory of elasticity*, 3rd ed., McGraw-Hill, New York, 1979.

S. K. DEB NATH: sankar_20005@yahoo.com
*Department of Mechanical Engineering, International University of Business, Agriculture and Technology, Dhaka-1230, Bangladesh*

S. REAZ AHMED: reaz207@yahoo.com
*Department of Mechanical Engineering, Bangladesh University of Engineering and Technology, BUET, Dhaka-1000, Bangladesh*

# ANISOTROPY IN HYPOELASTIC SOFT-TISSUE MECHANICS II: SIMPLE EXTENSIONAL EXPERIMENTS

ALAN D. FREED

Isochoric, hypoelastic, material models are employed to describe the passive response of isotropic and anisotropic soft tissues, using experimental data that have been taken from the literature. The isotropic tissues modeled are elastin and fat, and the anisotropic tissue modeled is tendon. A graphical technique is provided for estimating the material parameters of the anisotropic model, whose values are contrasted with maximum likelihood estimates. All numerical integrations were made with a new 4(3) Runge–Kutta integrator whose quadratures and weights are motivated by finite-element theory.

## 1. Introduction

Part I of this paper [Freed 2008] departed from longstanding tradition by considering a *hypoelastic* construction for soft tissues, instead of adopting a more conventional *hyperelastic* formulation. In this second part, we extend and apply this theory to a variety of axially loaded, soft-tissue experiments that have been published in the literature.

*Hyperelastic materials* establish stress via a potential function in strain [Ogden 1984]. Such potentials have their origin in thermodynamics. They produce theories where the value of stress depends only on the current state of strain, and not on the path traversed to reach that state. *Hypoelastic materials* establish stress-rate via a linear function in strain-rate [Truesdell 1955], and have the ability to reach states of stress that are path dependent, in accordance with recent experimental observations [Criscione et al. 2003]. In [Freed 2008], a special class of hypoelastic materials was introduced where stress-rate is given by a potential function in strain-rate. Such potentials must be quadratic in strain-rate so as to remain compatible with Truesdell's general definition of a hypoelastic material. The definition for hypoelastic materials given here is similar in mathematical structure to the classic construct of hyperelastic materials, it is just that the independent and dependent variables are now in rate form.

What motivated this researcher to consider hypoelasticity over hyperelasticity for describing the passive response of soft tissues is the fact that ever since Fung's pioneering work [1967], we have known that the stress/strain response of soft tissues is, to a good approximation, exponential. For the ensuing forty years, tissue mechanicians have proposed numerous ways to incorporate this exponential property into their hyperelastic frameworks. All of these seem rather ad hoc to me; whereas, hypoelasticity, being a rate theory, has the exponential character of its solution built in, so to speak (the characteristic solution of a first-order differential equation is an exponential). Consequently, the hypoelastic viewpoint should allow for a more satisfying theory to be constructed. This paper is but a step in that direction.

An application of hypoelastic models requires solving systems of ordinary differential equations (ODEs) satisfying initial conditions (ICs). Analytic solutions are available for only the simplest boundary conditions (BCs). Most BCs will require numerical solutions, with the more complex problems requiring finite-element (FE) analysis. Such BCs may describe an experiment whose purpose is to establish the parameters of a model, or they may specify a more challenging problem, like the interaction between neighboring tissues and a bioprosthetic implant. The method of solution that one chooses will be BC dependent. In this paper, the sole purpose for solving BCs is to acquire parameter estimates for models. For this purpose, the optimization strategy and the Runge–Kutta integrator of Appendices A and B, respectively, have been employed.

Hypoelastic models present a new set of challenges over traditional hyperelastic models in their implementation into FE codes. The consistent tangent matrix for a material model is typically required by codes designed to analyze solid bodies [Holzapfel 2000]. Their construction is more amenable to the stress/strain relations of hyperelastic materials than it is to the stress-rate/strain-rate relations of hypoelastic materials. In the case of the latter, an efficient integration algorithm, local at the Gauss point, must also accompany the model. It is often the efficiency of such an integrator that determines whether or not a particular rate-model is viable. Fluids codes, being rate codes, and hypoelasticity, being a rate theory, suggest a different avenue. Computational fluid dynamics (CFD) codes may be the better choice for implementing a hypoelastic material model. This is speculation at this time, and will be the topic of future research.

This paper begins with a synopsis of the isochoric, hypoelastic, constitutive model for isotropic soft tissues derived in [Freed 2008]. Solutions for this material model are provided for the BCs of uniaxial, equibiaxial, laterally constrained, and pure-shear extensions. There are no off-diagonal components in the deformation gradients that describe these experiments. It is shown that for isochoric hypoelastic materials, the BC for laterally-constrained extension does not reproduce the stress state caused by the BC for pure shear, like occurs with isochoric hyperelastic models.

The next section extends our isotropic theory to one that is suitable for anisotropic materials through the introduction of an anisotropy tensor, which is a material tensor that was given a geometric interpretation in [Freed 2008]. Invariant theory is called upon to construct a potential function, through which an anisotropic, isochoric, hypoelastic, constitutive equation is derived. Physical arguments are used to reduce the numbers-of and combinations-between pertinent invariants. A tensor function is introduced to address the physical observations that: collagen fibrils do not support compressive or hydrostatic states of stress, and their response becomes linear after their crimp has stretched straight. The resulting constitutive equation has been solved for the BCs of: uniaxial and laterally-constrained extensions stretched in the fiber direction, uniaxial extensions stretched normal to the fiber direction, and equibiaxial extensions where the fibers align with one of the two loading axes. The anisotropy considered here describes a single-fiber family with a fiber dispersion that projects onto the transverse plane in the reference state as a circular disk.

This theoretical discussion is followed by a results section where numerical solutions are presented for these two, hypoelastic, material models. Elastin and the calcaneal fat pad are modeled as isotropic hypoelastic materials, while tendon (fascia lata) is modeled as an anisotropic hypoelastic material. The paper concludes with a discussion of the hypoelastic models presented, along with some of the results obtained.

A maximum likelihood algorithm is outlined in the Appendix A, with an emphasis toward acquiring parameter estimates for models described by ODEs satisfying an IC, like hypoelastic material models. Also presented in Appendix B is a new, embedded, Runge–Kutta method that has proved to be both accurate and reliable for solving nonstiff systems of nonlinear ODEs.

*Preliminaries.* Scalars are typeset in italics, for example, $y$. Vectors are typeset in lower-case bold italics, for example, $\boldsymbol{y} = y_i \boldsymbol{e}_i$. Tensors are typeset in upper-case bold italics, for example, $\boldsymbol{Y} = Y_{ij} \boldsymbol{e}_i \otimes \boldsymbol{e}_j$, where $\otimes$ is the tensor product. Components $y_i$ and $Y_{ij}$ are also typeset in italics, and are quantified in a rectangular Cartesian basis $\{\boldsymbol{e}_1, \boldsymbol{e}_2, \boldsymbol{e}_3\}$. Exceptions to this notation are minimal, but they do arise, typically for historical reasons.

Polar tensors, like $\bar{\boldsymbol{Y}}$, relate to their Eulerian counterparts, in this case $\boldsymbol{Y}$, via the mapping $\bar{\boldsymbol{Y}} = \boldsymbol{R}^T \boldsymbol{Y} \boldsymbol{R}$, where $\boldsymbol{R}$ is the rotation tensor from a polar decomposition of the deformation gradient tensor $\boldsymbol{F}$. The material derivative of a polar field $\dot{\bar{\boldsymbol{Y}}}$ maps into the Eulerian frame as $\dot{\bar{\boldsymbol{Y}}} = \boldsymbol{R}^T \hat{\boldsymbol{Y}} \boldsymbol{R}$, where $\hat{\boldsymbol{Y}}$ denotes the polar rate of $\boldsymbol{Y}$ defined by $\hat{\boldsymbol{Y}} = \dot{\boldsymbol{Y}} - \Omega \boldsymbol{Y} + \boldsymbol{Y} \Omega$ [Dienes 1987], which is the objective rate of [Green and Naghdi 1965], with tensor $\Omega = \dot{\boldsymbol{R}} \boldsymbol{R}^T$ defining spin, or the rate of rigid-body rotation (compare [Dienes 1979]).

## 2. Isotropic hypoelastic model

Most biological tissues are anisotropic, but there are a few tissues that are essentially isotropic, of which elastin and fat are examples, and are modeled in Section 4.1.

In [Freed 2008] we derived the constitutive equation for an isotropic hypoelastic tissue from the potential equation

$$\dot{\bar{\boldsymbol{T}}} = \frac{\partial \Psi(\bar{\boldsymbol{T}}, \dot{\bar{\boldsymbol{E}}})}{\partial \dot{\bar{\boldsymbol{E}}}}, \tag{1}$$

where tensor $\boldsymbol{T}$ is the Kirchhoff stress, and tensor $\hat{\boldsymbol{E}}$ is the polar rate of strain (it is synonymous with the stretching tensor $\boldsymbol{D} = \operatorname{sym} \boldsymbol{L}$, where $\boldsymbol{L} = \dot{\boldsymbol{F}} \boldsymbol{F}^{-1}$ is the velocity gradient tensor). Polar equivalents to these Eulerian fields, which are used above, are gotten through standard mappings; in particular, $\bar{\boldsymbol{T}} = \boldsymbol{R}^T \boldsymbol{T} \boldsymbol{R}$, $\dot{\bar{\boldsymbol{T}}} = \boldsymbol{R}^T \hat{\boldsymbol{T}} \boldsymbol{R}$ and $\dot{\bar{\boldsymbol{E}}} = \boldsymbol{R}^T \hat{\boldsymbol{E}} \boldsymbol{R} \equiv \boldsymbol{R}^T \boldsymbol{D} \boldsymbol{R}$.

Because the two arguments $\bar{\boldsymbol{T}}$ and $\dot{\bar{\boldsymbol{E}}}$ of the scalar potential $\Psi$ are symmetric tensor fields, they can be replaced with ten scalar invariants [Rivlin and Smith 1969]. This number can be reduced by imposing Truesdell's [1955] definition for a hypoelastic solid, which requires each term in $\Psi$ to be quadratic in strain-rate; by imposing Fung's law [1967], which restricts each term in $\Psi$ to be at most linear in stress; and by imposing an isochoric constraint, $\operatorname{tr} \dot{\bar{\boldsymbol{E}}} = 0$. From these restrictions, one arrives at the most general form that potential $\Psi$ can have; it being [Freed 2008]

$$\Psi = \mu \operatorname{tr}(\dot{\bar{\boldsymbol{E}}} \dot{\bar{\boldsymbol{E}}}) + \alpha \tfrac{1}{3} \operatorname{tr}(\bar{\boldsymbol{T}}) \operatorname{tr}(\dot{\bar{\boldsymbol{E}}} \dot{\bar{\boldsymbol{E}}}) + \beta \operatorname{tr}(\bar{\boldsymbol{T}} \dot{\bar{\boldsymbol{E}}} \dot{\bar{\boldsymbol{E}}}) - \wp (\operatorname{tr} \dot{\bar{\boldsymbol{E}}} - 0). \tag{2}$$

where scalar $\dot{\wp}$ is a Lagrange multiplier forcing an isochoric (constant volume) response, and $\alpha$, $\beta$ and $\mu$ are material constants: $\mu$ has units of stress, it being the small-strain shear modulus, while parameters $\alpha$ and $\beta$ are both dimensionless, governing the rate of exponential growth in stress with increasing strain, with $\alpha$ accounting for the response due to hydrostatic pressure. Substituting this potential into (1) gives

the constitutive equation for an isotropic, isochoric, hypoelastic tissue, which is

$$\dot{\bar{T}} + \dot{\wp}\bar{I} = 2(\mu - \alpha p)\dot{\bar{E}} + \beta(\bar{T}\dot{\bar{E}} + \dot{\bar{E}}\bar{T}), \tag{3}$$

where scalar $p = -\frac{1}{3}\,\mathrm{tr}\,T$ is the hydrostatic pressure, which is distinct from the Lagrange multiplier $\wp$. This is an advantage over isochoric hyperelastic models, which cannot distinguish $p$ from $\wp$ in their constructs. ODE (3) is subject to an IC of $\bar{T}(0) = \bar{T}_0$.

*Classic boundary value problems.* Three experiments are commonly employed to estimate the material parameters of isotropic, isochoric, hyperelastic solids used to model rubbery materials; they are: uniaxial extension, equibiaxial extension, and pure shear [Treloar 1975], of which any two are sufficient for a complete characterization. Unlike hyperelastic models, hypoelastic models can respond to the presence of hydrostatic pressure. Consequently, as shown below, stress states from the BC of a laterally-constrained extension does not reproduce the stress state from the BC of pure shear in hypoelastic materials, as they do in hyperelastic materials.

*Uniaxial and equibiaxial extensions.* For the isotropic, isochoric, hypoelastic material described by (3), the BC for uniaxial extension is quantified by the ODE[1]

$$\frac{d\tau}{d\lambda} = \frac{3\mu + (\alpha + 2\beta)\tau}{\lambda}, \tag{4}$$

while the BC for equibiaxial extension is governed by

$$\frac{d\tau}{d\lambda} = 2\frac{3\mu + (2\alpha + \beta)\tau}{\lambda}, \tag{5}$$

wherein $\tau$ is the Kirchhoff (true or Cauchy) stress, and $\lambda$ is the applied stretch, with a typical IC being $\tau(1) = 0$. Equations (4) and (5), satisfying this IC, have an analytic solution of the form $\tau = \frac{a}{b}\left(e^{b\ln\lambda} - 1\right)$, where $a = 3\mu$ and $b = \alpha + 2\beta$ for uniaxial extension, and $a = 6\mu$ and $b = 4\alpha + 2\beta$ for equibiaxial extension. This solution is expressed in terms of the natural (true or Hencky) strain.

In the small-strain limit, uniaxial extension has a modulus of $3\mu$, while equibiaxial extension has a modulus of $6\mu$, which agree with predictions from the classic theory for rubber elasticity [Treloar 1975]. Whenever $\alpha = \beta$, the same ratio of 3:6 exists between their tangent moduli throughout the nonlinear region. However, whenever $\alpha \neq \beta$, hypoelasticity is capable of predicting different, nonlinear, stress/strain responses for these two experiments. This is because, unlike isochoric hyperelastic models, the affect of hydrostatic pressure is handled by isochoric hypoelastic models. This is apparent in (4) and (5), where equibiaxial extension has twice the pressure content of uniaxial extension, and four times the effect.

Either experiment, by itself, is incapable of delineating $\alpha$ from $\beta$. As a minimum, two excursions into stretch/stress space, whose deformations extend well into the nonlinear region, and that possess different hydrostatic states, like uniaxial and equibiaxial extensions, are needed in order to be able to acquire a complete characterization of all three parameters in this simple material model.

---

[1] Equation (4) is nearly, but not exactly, equal to Fung's law [1967] $d\sigma/d\lambda = E + \gamma\sigma$, where $\sigma = \tau/\lambda$ is the engineering stress and $E$ and $\gamma$ are material constants. In his paper, Fung spent a lot of effort addressing what is, effectively, the correct initial condition to impose, from the experimentalist's point of view, and how it manifests itself in the integrated solution of his law.

An application of the chain rule allowed stretch to replace time as the independent variable in (4) and (5); hence, hypoelasticity can be used to model quasistatic experiments.

*Pure shear.* A state of pure shear is achieved by extending a block of material in one direction by some amount $\lambda$, while simultaneously compressing it in a lateral direction by $\lambda^{-1}$, with the third orthogonal direction remaining fixed in length and free from traction. This is a difficult BC to achieve experimentally. For the isotropic, isochoric, hypoelastic material of (3), the pure shear BC is described by the ODEs

$$\frac{\mathrm{d}\tau_i}{\mathrm{d}\lambda_i} = \pm 2\frac{\mu + \beta\tau_i}{\lambda_i}, \quad i = 1, 2, \tag{6}$$

which are independent of pressure — the hallmark of pure shear — as parameter $\alpha$ is not present. Here $i = 1$ associates with the plus sign, and that direction where stretch is $\lambda$; while $i = 2$ associates with the minus sign, and that direction where stretch is $\lambda^{-1}$. Mohr's circle is centered at the origin, with its two circumscribed circles having equal diameters, and as such, this stress state is free from hydrostatic pressure.

*Laterally constrained axial extensions.* Pure-shear experiments done on elastomers typically apply an axial extension to a short but very wide sheet of material, relying on the lateral constraint of the grips to effectively keep the lateral principal stretch fixed at one (compare [Treloar 1975]). An indirect consequence of the isochoric constraint, when applied to hyperelastic solids, is that any translation of Mohr's circle is nonphysical, because these models cannot distinguish between hydrostatic pressure and their isochoric Lagrange multiplier. Consequently, because the two circumscribed Mohr's circles have the same diameter for both the laterally constrained and pure shear BCs, these BCs produce equivalent states of stress when imposed on isochoric hyperelastic materials.

In contrast, the BC of laterally constrained axial extension does not produce a stress state that is akin to pure shear when applied to an isochoric hypoelastic solid, because hypoelastic materials can support hydrostatic pressures, so translations of Mohr's circle remain physical in hypoelastic models. For the isotropic, isochoric, hypoelastic tissues obeying (3), the stretching of a short wide sheet is described by the ODEs

$$\frac{\mathrm{d}\tau_1}{\mathrm{d}\lambda} = 2\frac{2\mu + \frac{2}{3}\alpha(\tau_1 + \tau_2) + \beta\tau_1}{\lambda} \quad \text{and} \quad \frac{\mathrm{d}\tau_2}{\mathrm{d}\lambda} = \frac{2\mu + \frac{2}{3}\alpha(\tau_1 + \tau_2)}{\lambda}, \tag{7}$$

where $\tau_1$ is the stress in the applied stretch direction, $\tau_2$ is the stress in the lateral direction along the grips, and $\lambda$ is the applied stretch. These formulæ are distinct from those that govern pure shear in (6).

## 3. Anisotropic hypoelastic model

The potential equation (1) describing an isotropic hypoelastic tissue can be extended straightaway for anisotropic tissues by introducing a structural tensor $\bar{A}$ [Freed 2008; Freed et al. 2005; Gasser et al. 2006] into its argument list so that

$$\dot{\bar{T}} = \frac{\partial\Psi(\bar{A}, \bar{T}, \dot{\bar{E}})}{\partial\dot{\bar{E}}}, \tag{8}$$

where tensor $\bar{A}$ is a physical constant in the sense of [Oldroyd 1950]. This is the anisotropy tensor, and it is normalized so that $\|\bar{A}\|_2 = 1$ for geometric reasons [Freed 2008].

The three symmetric tensors that are the arguments of $\Psi$ can be replaced with twenty-eight scalar invariants [Rivlin and Smith 1969]. By applying the same reasoning used to reduce the set of invariants that lead to (2); by imposing our geometric restriction that the anisotropy tensor $\bar{A}$ attenuates deformations, not loads, and is a material constant [Freed 2008]; by introducing a mechanism to account for the fact that collagen fibrils are one-dimensional structures in soft tissues that do not support compressive or hydrostatic loads (these are handled by the surrounding matrix); and finally, by introducing another mechanism to provide for a smooth transition between the nonlinear and linear regions in a typical stress-stretch curve for soft tissue, which is caused by the stretching of crimped collagen; one is eventually lead to the potential

$$\Psi = \mu \operatorname{tr}(\dot{\bar{E}}\bar{A}\dot{\bar{E}}) + \alpha \tfrac{1}{3} \operatorname{tr}(\bar{T}) \operatorname{tr}(\dot{\bar{E}}\bar{A}\dot{\bar{E}}) + \beta \operatorname{tr}(\overline{\mathcal{T}}\dot{\bar{E}}\bar{A}\dot{\bar{E}}) - \wp(\operatorname{tr} \dot{\bar{E}} - 0), \tag{9}$$

which produces the following constitutive equation for an anisotropic, isochoric, hypoelastic tissue[2]

$$\dot{\bar{T}} + \dot{\wp}\,\bar{I} = (\mu - \alpha p)\left(\dot{\bar{E}}\bar{A} + \bar{A}\dot{\bar{E}}\right) + \beta\left(\overline{\mathcal{T}}\dot{\bar{E}}\bar{A} + \bar{A}\dot{\bar{E}}\,\overline{\mathcal{T}}\right), \tag{10}$$

where, in addition to the material parameters $\mu$, $\alpha$ and $\beta$ of the isotropic model, one has to also quantify the five independent components of $\bar{A}$ that describe the tissue's anisotropy, recalling that $\|\bar{A}\|_2 = 1$, and to establish a mathematical structure for the symmetric tensor function $\overline{\mathcal{T}}$.

The polar stress $\bar{T}$ has been replaced by a tensor valued function $\overline{\mathcal{T}} = R^T \mathcal{T} R$ in the $\beta$ term of (9) and (10). This function is introduced into the phenomenological relationship to address the physical restrictions that collagen fibrils are tension-only structures with helical geometries in their unloaded state, and that these helices stretch straight under deformation [Freed and Doehring 2005]. The tensor function considered is

$$\mathcal{T}(T) = Q^T \widetilde{\mathcal{T}}\, Q \quad \text{wherein} \quad \widetilde{\mathcal{T}} = \begin{bmatrix} f(\tau_1) & 0 & 0 \\ 0 & f(\tau_2) & 0 \\ 0 & 0 & f(\tau_3) \end{bmatrix} \quad \text{and} \quad Q_{ij} = \tilde{e}_i \cdot e_j, \tag{11}$$

so that $\overline{\mathcal{T}} = R^T Q^T \widetilde{\mathcal{T}} Q R$, where the eigenvalues $\tau_i$ and eigenvectors $\tilde{e}_i$ arise from a spectral representation of the Kirchhoff stress $T$, and are normalized so that $I = \tilde{e}_i \otimes \tilde{e}_j$ ($i, j = 1, 2, 3$). Orthogonal tensor $Q$ is a mapping between the spectral $\{\tilde{e}_1, \tilde{e}_2, \tilde{e}_3\}$ and spatial $\{e_1, e_2, e_3\}$ base vectors, while orthogonal tensor $R$ is a mapping between the polar $\{\bar{e}_1, \bar{e}_2, \bar{e}_3\}$ and spatial $\{e_1, e_2, e_3\}$ base vectors. The dimensionless function $f$ is taken to be the ramped step

$$f(\tau) = \begin{cases} 1 & \text{if} \quad \tau > \tau^\star, \\ \tau/\tau^\star & \text{if} \ 0 \le \tau \le \tau^\star, \\ 0 & \text{if} \quad \tau < 0, \end{cases} \tag{12}$$

with $\tau^\star$ establishing a threshold stress beyond which collagen crimp is stretched straight. This choice of stress function, in conjunction with our hypoelastic formulation, will enable stress/stretch curves typical of many tissues to be modeled; specifically, those where there is a shallow sloped toe region followed

---

[2]Proposition 1 in [Freed 2008] is not employed here. It was found during the process of writing this document that the decoupling of strain rate into separate fiber and matrix constituents, defined according to that hypothesis, lead to constitutive formulæ that could not accommodate the large difference in shear moduli present in the data for human fascia lata from [1994] that are modeled here.

by a heel that transitions into a linear true stress/strain response that, in a stress/stretch plot, will have slight curvature. If the tissue of interest does not have this type of stress/strain behavior, then a different function for $\mathscr{T}$ will be needed.

In accordance with the above definition for $\mathscr{T}$, the material constants in the anisotropic constitutive equation (10) have slightly different physical interpretations from those of the isotropic constitutive equation (3); specifically, $\mu$ is the tissue modulus when collagen is behaving like a helical spring, while $\beta$ is the tissue modulus at those stresses $\tau_i > \tau^\star$ where collagen has stretched straight. These ideas have been developed in [Freed and Doehring 2005] and works cited therein, to model the response of collagen fibrils. The parameters $\mu$, $\beta$ and $\tau^\star$ all have units of stress, while $\alpha$ remains dimensionless and retains its prior physical interpretation.

***Uniform extensions.*** There is a versatility in the present theory in that any, admissible, anisotropy tensor $\bar{A}$ can be incorporated into the above constitutive framework without altering its construction. Various $\bar{A}$ tensors belonging to the class of single-fiber families with elliptic projections onto the transverse plane of the reference configuration can be found in [Freed 2008].

It has been demonstrated, for example, that fiber branching is physiologically necessary to stabilize the left ventricle wall, thereby ensuring proper heart function [Niederer et al. 2004]. In their study, splay was described as a single-fiber family with an elliptic projection onto the transverse plane.

The formulæ that follow are applications of the anisotropic, hypoelastic, isochoric tissue given by (10) to four separate BCs that are extensional loadings. In each case, anisotropy is considered to belong to a single-fiber family where the geometric arrangement of fiber orientation at a mass point is encased by a cone in the polar frame, and whose matrix representation is

$$\bar{A} = \begin{bmatrix} 1 & 0 & 0 \\ 0 & \delta & 0 \\ 0 & 0 & \delta \end{bmatrix}, \tag{13}$$

where the angle of mean fiber orientation has been chosen to align with the 1-direction. The scalar $\delta$, which satisfies $0 \leq \delta \leq 1$, has a statistical origin [Freed et al. 2005; Gasser et al. 2006]. It is the dispersion parameter quantifying the extent of fiber splay.

Other tissues, like arteries [Holzapfel et al. 2002], will require orthotropic anisotropy tensors that belong to material classes with two or more fiber families. Such tissues are not addressed in this paper.

***Extensions in the mean fiber direction.*** Here a specimen is loaded in the fiber- or 1-direction by a stretch of $\lambda$. Given that the tissue has an anisotropy described by (13), the constitutive equation (10) produces the matrix equation

$$\begin{bmatrix} \dot{\tau} & 0 & 0 \\ 0 & 0 & 0 \\ 0 & 0 & 0 \end{bmatrix} + \begin{bmatrix} \dot{\wp} & 0 & 0 \\ 0 & \dot{\wp} & 0 \\ 0 & 0 & \dot{\wp} \end{bmatrix} = 2\left(\mu + \alpha\frac{\tau}{3}\right) \begin{bmatrix} \dot{\lambda}/\lambda & 0 & 0 \\ 0 & -\delta\dot{\lambda}/2\lambda & 0 \\ 0 & 0 & -\delta\dot{\lambda}/2\lambda \end{bmatrix} + 2\beta \begin{bmatrix} f(\tau)\dot{\lambda}/\lambda & 0 & 0 \\ 0 & 0 & 0 \\ 0 & 0 & 0 \end{bmatrix}. \tag{14}$$

Substituting the equation for the Lagrange multiplier $\dot{\wp}$ (the equations associated with the second or third rows) into the equation for the Kirchhoff stress, and multiplying through by $dt/d\lambda$, one arrives at the governing ODE for this BC, which is

$$\frac{d\tau}{d\lambda} = \frac{2+\delta}{3}\frac{3\mu + \alpha\tau}{\lambda} + 2\beta\frac{f(\tau)}{\lambda}, \tag{15}$$

a typical IC being $\tau(1) = 0$.

*Extensions normal to the mean fiber direction.* Here a specimen is loaded normal to the fiber alignment, or in the 2-direction, by a stretch of $\lambda$. Given that the tissue has an anisotropy described by (13), the constitutive equation (10) produces the matrix equation

$$\begin{bmatrix} 0 & 0 & 0 \\ 0 & \dot{\tau} & 0 \\ 0 & 0 & 0 \end{bmatrix} + \begin{bmatrix} \dot{\wp} & 0 & 0 \\ 0 & \dot{\wp} & 0 \\ 0 & 0 & \dot{\wp} \end{bmatrix} = 2\left(\mu + \alpha\frac{\tau}{3}\right)\begin{bmatrix} -\nu\dot{\lambda}/\lambda & 0 & 0 \\ 0 & \delta\dot{\lambda}/\lambda & 0 \\ 0 & 0 & \delta(\nu-1)\dot{\lambda}/\lambda \end{bmatrix} + 2\beta\begin{bmatrix} 0 & 0 & 0 \\ 0 & \delta f(\tau)\dot{\lambda}/\lambda & 0 \\ 0 & 0 & 0 \end{bmatrix}, \tag{16}$$

where $\nu$ accommodates variations in the Poisson contraction between the directions that are parallel-with and transverse-to the mean fiber direction. Equating the two equations for the Lagrange multiplier $\dot{\wp}$ leads to the relationship $\delta = \nu/(1-\nu)$, which inverts as $\nu = \delta/(1+\delta)$; consequently, because $0 \le \delta \le 1$, it follows that $0 \le \nu \le 1/2$. The ODE governing Kirchhoff stress for this BC is

$$\frac{d\tau}{d\lambda} = \frac{2\delta(2+\delta)}{3(1+\delta)}\frac{3\mu + \alpha\tau}{\lambda} + 2\delta\beta\frac{f(\tau)}{\lambda}, \tag{17}$$

which also has a typical IC of $\tau(1) = 0$.

*Laterally constrained extensions in the mean fiber direction.* This is basically the same experiment as axial extension, except that Poisson contraction in the 2-direction is not allowed. Given that the tissue has an anisotropy described by (13), the constitutive equation (10) produces the matrix equation

$$\begin{bmatrix} \dot{\tau}_1 & 0 & 0 \\ 0 & \dot{\tau}_2 & 0 \\ 0 & 0 & 0 \end{bmatrix} + \begin{bmatrix} \dot{\wp} & 0 & 0 \\ 0 & \dot{\wp} & 0 \\ 0 & 0 & \dot{\wp} \end{bmatrix} = 2\left(\mu + \alpha\frac{\tau_1+\tau_2}{3}\right)\begin{bmatrix} \dot{\lambda}/\lambda & 0 & 0 \\ 0 & 0 & 0 \\ 0 & 0 & -\delta\dot{\lambda}/\lambda \end{bmatrix} + 2\beta\begin{bmatrix} f(\tau_1)\dot{\lambda}/\lambda & 0 & 0 \\ 0 & 0 & 0 \\ 0 & 0 & 0 \end{bmatrix}, \tag{18}$$

where $\tau_1$ is the Kirchhoff stress in the direction of applied traction, and $\tau_2$ is the Kirchhoff stress in the lateral direction of constraint, which is usually not measured in these experiments. Substituting the equation for the Lagrange multiplier $\dot{\wp}$ into the two equations for the principal Kirchhoff stresses results in two ODEs that describe this BC, they being

$$\frac{d\tau_1}{d\lambda} = \frac{2(1+\delta)}{3}\frac{3\mu + \alpha(\tau_1+\tau_2)}{\lambda} + 2\beta\frac{f(\tau_1)}{\lambda} \quad \text{and} \quad \frac{d\tau_2}{d\lambda} = \frac{2\delta}{3}\frac{3\mu + \alpha(\tau_1+\tau_2)}{\lambda}, \tag{19}$$

which have typical ICs of $\tau_1(1) = \tau_2(1) = 0$. The presence of parameter $\alpha$ indicates that this deformation contains a hydrostatic pressure, and is therefore not a pure-shear deformation.

*Equibiaxial extensions.* For isotropic materials, it makes no difference whether the traction or the stretches are maintained equal in an equibiaxial experiment; it does, however, make a difference for anisotropic materials. Here we consider the case where the two orthogonal stretches are maintained equal, with fiber alignment being in the 1-direction. Given that the tissue has an anisotropy that is described by (13), the constitutive equation (10) produces the matrix equation

$$\begin{bmatrix} \dot{\tau}_1+\dot{\wp} & 0 & 0 \\ 0 & \dot{\tau}_2+\dot{\wp} & 0 \\ 0 & 0 & \dot{\wp} \end{bmatrix} = 2\left(\mu + \alpha\frac{\tau_1+\tau_2}{3}\right)\begin{bmatrix} \dot{\lambda}/\lambda & 0 & 0 \\ 0 & \delta\dot{\lambda}/\lambda & 0 \\ 0 & 0 & -2\delta\dot{\lambda}/\lambda \end{bmatrix} + 2\beta\begin{bmatrix} f(\tau_1)\dot{\lambda}/\lambda & 0 & 0 \\ 0 & f(\tau_2)\delta\dot{\lambda}/\lambda & 0 \\ 0 & 0 & 0 \end{bmatrix}. \tag{20}$$

Substituting the equation for the Lagrange multiplier $\dot{\wp}$ into the two equations for the principal Kirchhoff stresses results in the governing ODEs for this BC, they being

$$\frac{d\tau_1}{d\lambda} = \frac{2(1+\delta)}{3} \frac{3\mu + \alpha(\tau_1 + \tau_2)}{\lambda} + 2\beta \frac{f(\tau_1)}{\lambda} \quad \text{and} \quad \frac{d\tau_2}{d\lambda} = \delta \frac{3\mu + \alpha(\tau_1 + \tau_2)}{\lambda} + 2\delta\beta \frac{f(\tau_2)}{\lambda}, \quad (21)$$

which have typical ICs of $\tau_1(1) = \tau_2(1) = 0$. There is only a slight difference in the formulæ for $d\tau_2/d\lambda$ between (19) and (21), while their formulæ for $d\tau_1/d\lambda$ are identical.

## 4. Results

Our hypoelastic theory is now applied to a few examples where experimental data have been taken from the literature. Purified elastin and the calcaneal fat pad are modeled as isotropic materials, while the fascia lata tendon is modeled as an anisotropic material. The numerical optimization and integration algorithms used to obtain estimates for the material parameters are outlined in two appendices.

**4.1. *Elastin and fat.*** The author is not aware of a single, published, experimental, data set for an isotropic soft tissue that is sufficient to unambiguously quantify all three material parameters associated with (3). In the examples that follow, either $\alpha$ or $\beta$ is assigned to be zero, a priori; specifically, it is supposed that $\alpha = 0$ for fibrous tissues, and that $\beta = 0$ for nonfibrous tissues. This is conjecture until such time when experimental data become available to test its validity.

Aaron and Gosline [1981] performed uniaxial quasistatic experiments on purified elastin fibers (5–8 $\mu$m in diameter) extracted from the bovine ligamentum nuchae. They were tested in distilled water at 24°C. Because fibers are one-dimensional structures, it is expected that they cannot support hydrostatic states, and as such, we set $\alpha = 0$ in this case. Figure 1 shows a fitting of (4) to the experimental data of [Aaron and Gosline 1981], and yields material constants with 90% confidence intervals of $\mu = 0.210 \pm 0.048$ MPa and $\beta = 1.53 \pm 0.19$, with a coefficient of determination of $R^2 = 0.976$.



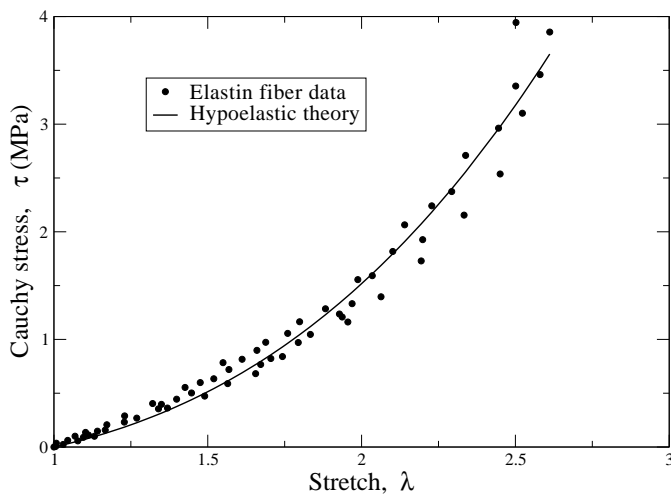**Figure 1.** Hypoelastic theory contrasted with experimental data for elastin fibers (5–8 $\mu$m in diameter) tested in simple extension, where $\mu = 0.21$ MPa and $\beta = 1.5$, taking $\alpha = 0$. The data are from [Aaron and Gosline 1981, Figure 2a].
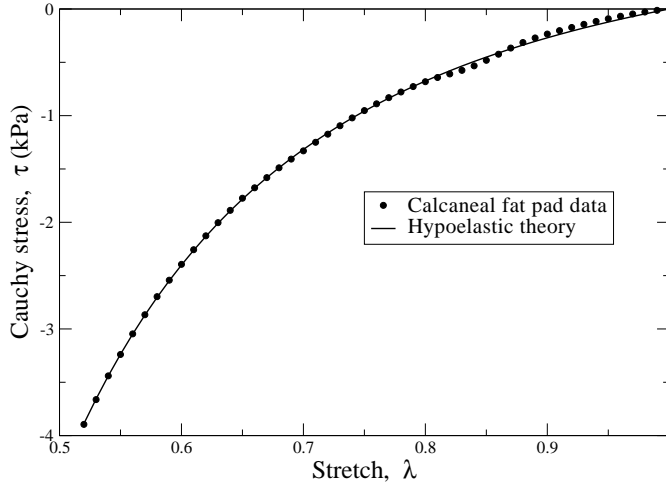
**Figure 2.** Hypoelastic theory contrasted with experimental data for the human, calcaneal, fat pad ($N = 10$) tested in simple compression, where $\mu = 0.74$ kPa and $\alpha = -2.64$, taking $\beta = 0$. The data are from [Miller-Young et al. 2002, Figure 3].

Miller-Young et al. [2002] performed compression experiments on the human, calcaneal, fat pad excised from the feet of cadavers. They were tested in air at ambient temperature. Because the calcaneal fat pad operates predominantly in a hydrostatic environment, one would expect parameter $\alpha$ to dominate over $\beta$, and as such, we have set $\beta = 0$ in this case. A fitting of (4) to the mean curve constructed from averaging ten quasistatic experiments, each from an individual specimen, yields material constants with 90% confidence intervals of $\mu = 0.741 \pm 0.016$ kPa and $\alpha = -2.638 \pm 0.063$, with a coefficient of determination of $R^2 = 0.999$. (See Figure 2.) The averaging of data over ten experiments contributed to the high $R^2$ value obtained here. The reported standard deviation for experimental variability around the mean stress for these ten experiments was about $\pm 10\%$ at the point of maximum compression [Miller-Young et al. 2002].

**4.2.** *Algorithm for graphical estimation of model parameters.* Hypoelastic constitutive equations are rate models. This suggests that estimates for its material constants could be tangents to specific response curves, located at specific points along them, which could be obtained graphically from experimental data. This point of departure is adopted in the following algorithm.

**Algorithm 1.** Whenever axial and transverse, uniaxial experiments are available for a material whose anisotropy is described by a single-fiber family with fiber dispersion being enclosed by a cone, that is, whenever constitutive equations (15) and (17) apply, then measure the following four slopes, and record the necessary stretches and stresses of their tangent points.

    i. From a stretch vs. true-stress diagram constructed from a uniaxial experiment whose loading axis was aligned with the fiber direction, measure

- $E_a$, which is the slope at $\lambda = 1$;
- $E_f$, which is the slope midway through the linear region, and
  - $\lambda_f$, the stretch at this tangent point;

- $E_h$, which is the slope halfway up the heel in the nonlinear region, and
  - $\lambda_h$ and $\tau_h$, the stretch and stress at this tangent point.
ii. From a stretch vs. true-stress diagram constructed from a uniaxial experiment whose loading axis was normal to the fiber direction, measure
  - $E_t$, which is the slope at $\lambda = 1$.

With these data in hand, estimates for the material constants come from the formulæ

$$\delta = \frac{E_t}{2E_a - E_t}, \quad \mu = E_a \frac{2E_a - E_t}{4E_a - E_t}, \quad \beta = \frac{\lambda_f E_f - E_a}{2}, \quad \tau^\star = \tau_h \frac{\lambda_f E_f - E_a}{\lambda_h E_h - E_a}.$$

We assume here that $\alpha = 0$, as these two experiments lack sensitivity to discriminate $\alpha$ from $\beta$.

In this algorithm we chose to plot Cauchy stress $\tau$ versus stretch $\lambda$. This was a conscious decision, made because it requires minimal messaging of the raw data. Therefore, these data can be easily mapped into another stress/strain pair that may be of interest to someone else, i.e., the data have archival value. Without simultaneous knowledge of the deformation gradient, it is difficult, and often impossible, to convert data from one stress/strain format into another when they are only made available as curves in figures.

Having said this, an alternative method for graphically determining parameters in hypoelastic models undergoing simple extensions, which does manipulate the raw data, would be to plot true stress $\tau$ versus the tangent modulus $\lambda d\tau/d\lambda$, similar to what's done in [Fung 1967]. However, because methods for numeric differentiation magnify noise in their data streams, and because such data streams tend to be noisy to begin with, it is useful, if not essential, that a smoothing function be used to represent these raw data, from which rates are gotten by differentiating the smoothing function instead of the raw data themselves. The generalized cross-validatory method [Woltring 1986] has been used by the author for this purpose with good effect in other studies, but it was not used here.

**4.3. Tendon.** Algorithm 1 applies to experimental data sets where uniaxial extensions have been done on two samples: one where axial extension is in the mean fiber direction, and the other where axial extension is normal to the fiber direction. The experimental data of [Weiss 1994] acquired from human fascia lata belong to this classification.

Figure 3 illustrates how to apply step (i) of Algorithm 1 to the data of [Weiss 1994], where the sample was loaded in the direction of the fibers. Modulus $E_a$ is the tangent to the curve at $\lambda = 1$, which has a measured value of 120 MPa. Modulus $E_f$ is a tangent to the curve at $\lambda_f$, which was placed roughly midway along the linear portion of the curve, and has a measured value of 675 MPa at a stretch of 1.06. The critical part in an application of this algorithm is to select the next tangent point. Here we seek a location where the tangent modulus is roughly half that of $E_f$. Drawing this tangent establishes $E_h$, which has a measured value of 325 MPa ($\sim 675/2$) at the tangent point $\lambda_h = 1.0112$ and $\tau_h = 2.26$ MPa. This completes step (i) of Algorithm 1.

Step (ii) of Algorithm 1 is much less involved. Here all that is required is to acquire the tangent modulus at $\lambda = 1$ from an experiment where the sample was loaded normal to the fiber direction. Figure 4 presents data from [Weiss 1994]; the tangent modulus $E_t$ has a measured value of 30 MPa. Although the initial tangent moduli only differ by a factor of four between Figures 3 and 4, their local tangent moduli at stretches exceeding 1.03 differ by a factor of well over twenty.
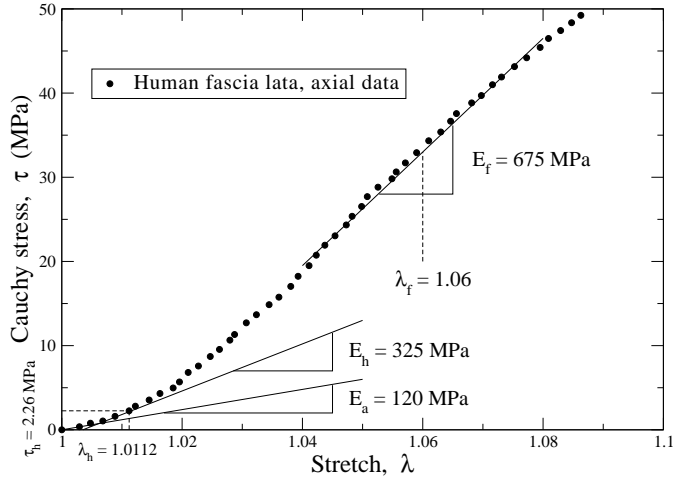
**Figure 3.** The slopes and their locations pertaining to part (i) of Algorithm 1. The data are from [Weiss 1994, Figure 6.7].
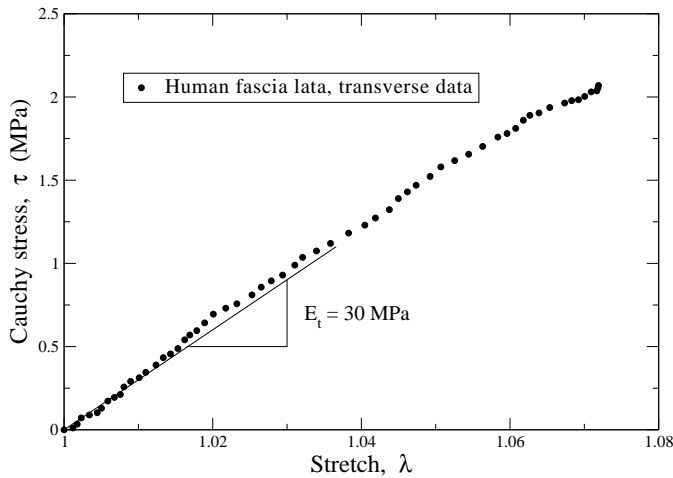


**Figure 4.** The slope pertaining to part (ii) of Algorithm 1. The data are from in [Weiss 1994, Figure 6.6].

An application of Algorithm 1 to the acquisition of estimates for the model parameters present in (15) and (17) produced the values listed in Table 1, and the dashed response curves displayed in Figures 5 and 6. (Note the different vertical scales.) The parameters listed in this table are the outcome of our first

| Parameters | $\delta$ | $\mu$/MPa | $\beta$/MPa | $\tau^{\star}$/MPa | $R^2$ |
|---|---|---|---|---|---|
| Graphical estimates | $0.14\pm0.07$ | $56\pm62$ | $300\pm68$ | $6.5\pm5.0$ | 0.743 |
| Optimized estimates | $0.06\pm0.018$ | $120\pm41$ | $225\pm41$ | $13\pm5.7$ | 0.996 |

**Table 1.** Parameter estimates with 90% confidence intervals for the anisotropic, iso-choric, hypoelastic, tissue model (10), obtained by the graphical method of Algorithm 1, and by the numerical method of Appendix B. The parameter $\alpha$ was set to 0 in both cases.
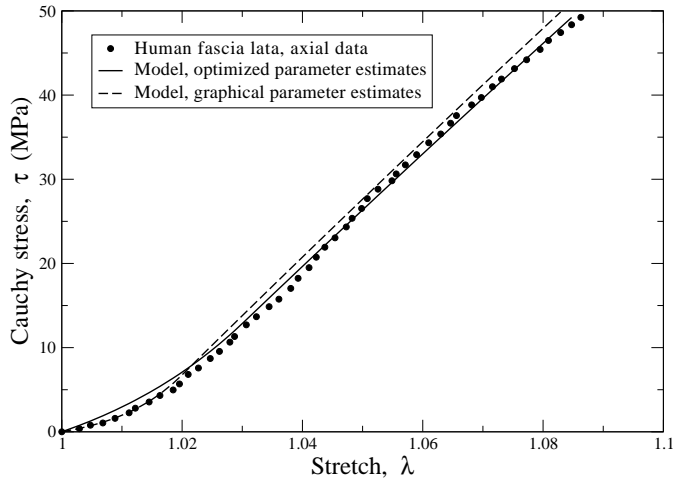
**Figure 5.** Comparisons between experimental data and values from (15), where the parameters were estimated using the graphical method of Algorithm 1 and the maximum likelihood method of Appendix B. The data are from [Weiss 1994, Figure 6.7].
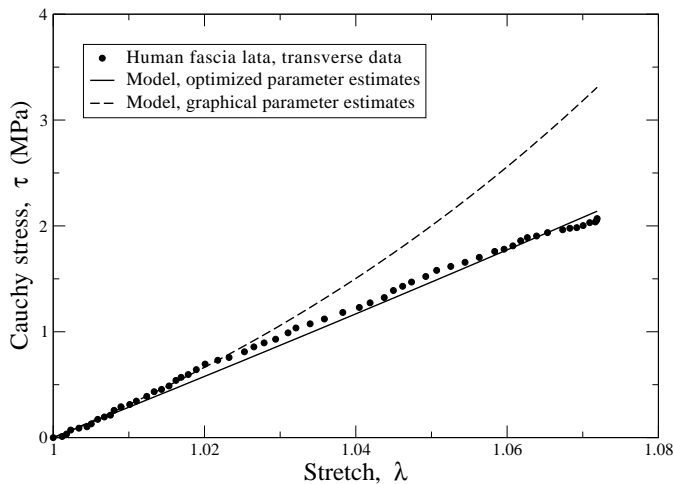


**Figure 6.** Comparisons between experimental data and (17), where parameters were estimated from the graphical method of Algorithm 1, and the maximum likelihood method of Appendix B. The data are from [Weiss 1994, Figure 6.6].

and only attempt to graphically quantify the tangent moduli utilized by the formulæ in Algorithm 1. The 90% confidence intervals for the graphical estimates were obtained by constructing a covariance matrix for their residuals, as described in Appendix A. Improvements, based on visual inspection, could have likely been obtained by iterating on one's choice of parameters, but that was not done here.

Using these graphical estimates as initial guesses for the parameters, maximum likelihood estimates were then obtained whose values are also listed in Table 1, along with their 90% confidence intervals, and whose responses are plotted as the solid curves in Figures 5 and 6.

## 5. Discussion

To gain sensitivity between parameters $\alpha$ and $\beta$ in the hypoelastic tissue models during a parameter estimation will require at least two experiments, each loaded into the nonlinear region of their response, and each with a different hydrostatic state. Experimental data with sufficient sensitivity to discriminate $\alpha$ from $\beta$ are rare. A document where such a data set will be considered is now being written.

Parameters $\alpha$ and $\beta$ are confounded in the parameter estimates of this paper, because experiments with the same hydrostatic state have been used for model correlations. We have dealt with this confounding by assigning one or the other of the nonlinear parameters to be zero, based on physical arguments. Consequently, care should be exercised if any of the parameters derived herein are to be used in an actual three-dimensional analysis, as the data sets used to quantify the models, by themselves, are incapable of providing complete sensitivity for all parameters during an optimization.

*Isotropic case.* The Fung-like parameters $\alpha$ and $\beta$ are associated with stress/strain responses that grow exponentially in stress with increasing stretch, and because of this, they do not produce responses with tension/compression symmetry. As a general observation, the soft tissues that nature has created to support compressive loads are poor at supporting tensile loads, and vice versa. This is consistent with the influence that parameters $\alpha$ and $\beta$ have on the overall material response. Hence, one might expect $\alpha$ to be restricted to taking on negative values, and $\beta$ to be restricted to taking on positive values, as is the case here, but this is only conjecture at this time.

The correlation between theory and experimental data is quite good in Figure 1, with an $R^2$ statistic of 0.976, and it is exceptional in Figure 2, with an $R^2$ statistic of 0.999, especially since there are only two adjustable parameters available to the model, due to the fact that the experimental data sets that were fit against belong to just one type of boundary-value problem; namely, simple extension.

*Anisotropic case.* An advantage of our constitutive equation (10) for describing soft tissues over most models published in the open literature is the relative ease by which it can be applied to tissues with different anisotropic structures. This is because anisotropy is handled through a single, symmetric, material tensor $\bar{A}$ whose independent components establish the relative directional strengths of the anisotropy. Anisotropy tensors for splayed fiber architectures belonging to a single-fiber family with an elliptic projection onto the transverse plane in the reference configuration have been reviewed in [Freed 2008].

The particular relationship between the angle of fiber dispersion $\angle$ and the dispersion parameter $\delta$ itself, as it appears in (13), will depend upon the probability distribution function that one selects. Curiously, the mathematical structure of matrix $\bar{A}$ is independent of that choice [Gasser et al. 2006], which is remarkable result. One such possible mapping is given in Table 2.

At first glance, when comparing the two estimated values for the dispersion parameter $\delta$ listed in

| angle | 0° | 5° | 10° | 15° | 20° | 25° | 30° | 35° | 40° | 45° | 60° | 90° | 180° |
|-------|-----|------|------|------|------|------|------|------|------|------|------|------|------|
| $\delta$ | 0 | 0.02 | 0.06 | 0.13 | 0.23 | 0.34 | 0.45 | 0.54 | 0.61 | 0.67 | 0.78 | 0.90 | 1 |

**Table 2.** Dispersion parameter $\delta$ at various angles of fiber splay for a fiber fan with Gaussian distribution [Freed et al. 2005], where 0° is the limiting case of transverse isotropy and 180° is the other limiting case of planar isotropy.
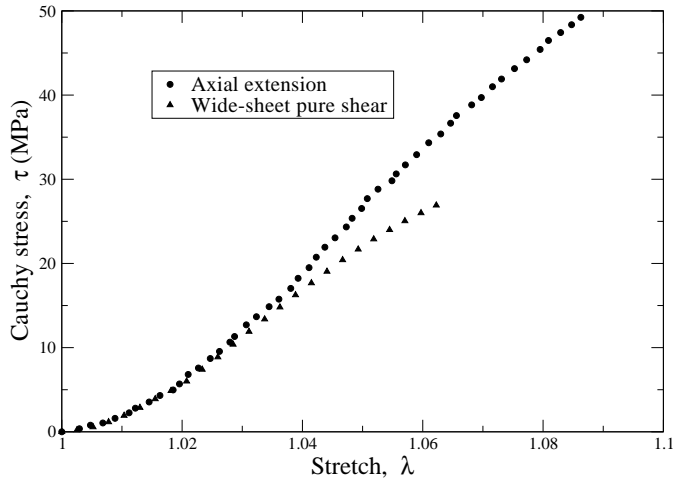
**Figure 7.** Data for human fascia lata tested in axial extension, and laterally constrained (wide sheet) axial extension, often referred to as pure shear in the rubber literature. The data are from [Weiss 1994, Figures 6.7 and 6.8].

Table 1, obtained from the two different estimation procedures, one might be inclined to think that these estimates are significantly different. However, when viewed through Table 2, we see that these differences correspond to fiber dispersion angles of roughly 10° and 15° (or 5° and 7.5° off the mean) which, from this vantage point, is a rather small difference. Both of these angles seem reasonable for tendon.

Differences between the BCs (19) for laterally-constrained axial extensions and the BCs (15) for simple axial extensions in the strong direction diminish in the neighborhood of transverse isotropy, that is, as $\delta \to 0$. This agrees with the experimental data of Weiss [1994] presented in Figure 7; his experiments were done on human fascia lata. They are plotted together here, and lie one atop the other up to stretches of about 1.03. Beyond this point they begin to diverge because of experimental difficulties, as Weiss states: "The most likely cause of this systematic error is a problem in satisfying the constraint that the lateral stretch was maintained at a value of 1.0." Because these experimental curves are coincident, the laterally-constrained axial experiment brings little added value to the overall process of parameter estimation for tissues whose fiber alignment is fairly strong.

An inspection of Figure 5 for the axial response suggests that the two methods of parameter estimation are equally good. The graphical method does slightly better for stretches below 1.02, while the maximum likelihood method does slightly better for stretches beyond 1.02. Examining the estimates for the shear modulus $\mu$ given in Table 1, which controls the response around $\lambda = 1$, one finds a factor of two difference between them. This disparity is exasperated by the relatively short toe region that is present in these data.

An inspection of Figure 6 for the transverse response may lead one to want to draw a different conclusion, but one should not be too hasty. The absolute differences in predicted stresses are less here than they are in Figure 5; the relative differences are, however, significantly greater, which is why the small coefficient of determination reported in Table 1 for the graphical method. Certainly, the correlations are good below a stretch of 1.02 in Figure 6. Above that, the correlation that used estimates from the graphical method starts to pick up an exponential contribution that is not present in the correlation that

used maximum likelihood estimates. The reason for this is the factor of two difference between the values of their dispersion parameters $\delta$. Because their $\delta$s differ by a factor of two, the graphical correlation has twice the contribution that the numerical correlation has in the nonlinear region, introduced through the term $2\delta\beta f(\tau)/\lambda$ in (17). This effect is countered in the linear region by a like difference between the estimates for their shear moduli $\mu$.

A close examination of the theoretical curves in the linear response region of Figure 5 finds that they are not exactly linear. There is a small degree of concavity in them with increasing stretch, as there is in the experimental data. This effect is not large, and theory and experiment are consistent in this regard. If fact, theory implies a linear response beyond the toe region only in true stress/strain plots. Also, if one back calculates from the optimized parameters listed in Table 1 to get the fiber modulus $E_f$, one obtains 650 MPa, which is very close to the graphical value of 675 MPa.

## 6. Concluding remarks

As a general observation, hypoelasticity seems to be well suited for describing the passive elastic response of soft tissues. The modeling put forward in this paper supports this conclusion, but it is just a first step towards model verification. Many other tissues and boundary-value problems, including FE analyses, need to be modeled with this theory to determine its domain of applicability and its overall usefulness.

## Appendix A. Parameter estimation

Here we describe how to obtain maximum likelihood estimates for parameters in models that are described in terms of a system of ODEs, like hypoelasticity. The text [Bard 1974] is somewhat old, but remains an excellent reference for nonlinear parameter estimation techniques. All numerical integrations done in this paper were obtained using the Runge–Kutta integrator introduced in Appendix B.

Assign $I$ to be the number of measured/modeled variables, $J$ to be the number of internal state variables, $K$ to be the number of unknown parameters to be estimated, and $N$ to be the number of experimental observations to be fit against. Let scalar $x_n$ denote the control (or independent) variable at datum point $n$ — for example, stretch — where $n$ ranges from 1 to $N$. Let the one-dimensional vectors $\boldsymbol{y}_n$ and $\boldsymbol{\mathcal{Y}}(\boldsymbol{\theta}, x_n)$ contain the experimental and theoretical response (or dependent) variables, respectively, at each datum point $n$, for example, stresses, while $\bar{\boldsymbol{y}} = \frac{1}{N}\sum_{n=1}^{N} \boldsymbol{y}_n$ denotes their experimental mean. And let the $K$-dimensional vector $\boldsymbol{\theta}$ contain parameters for the model whose values are being sought. This algorithm requires that $N \geq I$ and that $N > K$.

Adopting a standard reduced model for assessing error, let the $I$-dimensional residual vector $\boldsymbol{r}_n$ at datum point $n$ be defined by

$$\boldsymbol{r}_n(\boldsymbol{\theta}) = \boldsymbol{y}_n - \boldsymbol{\mathcal{Y}}(\boldsymbol{\theta}, x_n) \quad \text{with components} \quad r_{n,i}(\boldsymbol{\theta}) = y_{n,i} - \mathcal{Y}_i(\boldsymbol{\theta}, x_n), \tag{22}$$

in which $r_{n,i}$ denotes the $i$-th row element of column vector $\boldsymbol{r}_n$, $i = 1, 2, \ldots, I$. Vector $\boldsymbol{r}_n(\boldsymbol{\vartheta})$ is the experimental error at state $n$ whenever $\boldsymbol{\vartheta}$ represents the actual parameters from a model that is 'truth'. The $I \times I$ matrix

$$\boldsymbol{M}(\boldsymbol{\theta}) = \sum_{n=1}^{N} \boldsymbol{r}_n(\boldsymbol{\theta}) \otimes \boldsymbol{r}_n(\boldsymbol{\theta}) \quad \text{with components} \quad M_{ij}(\boldsymbol{\theta}) = \sum_{n=1}^{N} r_{n,i}(\boldsymbol{\theta}) r_{n,j}(\boldsymbol{\theta}) \tag{23}$$

defines the moment of residuals, which will be symmetric positive-definite whenever $\|\boldsymbol{r}_n\| > 0$ for at least $I$ of the $N$ measurements, as each $\boldsymbol{r}_n \otimes \boldsymbol{r}_n$ is at most a rank-1 matrix.

Whenever the residuals $\boldsymbol{r}_n$ from each of the $N$ datum points are independent of one another, and whenever they are normally distributed with the same covariance matrix $\boldsymbol{V}$, then the likelihood $\mathscr{L}$ of $\boldsymbol{\theta}$ being the actual set of parameters $\boldsymbol{\vartheta}$ for a given model $\mathscr{Y}$ is the product of its $N$ probability density functions

$$
\begin{aligned}
\mathscr{L}[\boldsymbol{r}(\boldsymbol{\theta})|\boldsymbol{V}] = \mathscr{L}(\boldsymbol{\theta}) &= \prod_{n=1}^{N} \frac{1}{\sqrt{(2\pi)^I \det \boldsymbol{V}}} \exp\left(-\tfrac{1}{2}\boldsymbol{r}_n(\boldsymbol{\theta}) \cdot \boldsymbol{V}^{-1}\boldsymbol{r}_n(\boldsymbol{\theta})\right) \\
&= \left(\frac{1}{(2\pi)^I \det \boldsymbol{V}}\right)^{N/2} \exp\left(-\frac{1}{2} \sum_{n=1}^{N} \boldsymbol{r}_n(\boldsymbol{\theta}) \cdot \boldsymbol{V}^{-1}\boldsymbol{r}_n(\boldsymbol{\theta})\right) \\
&= \left(\frac{1}{(2\pi)^I \det \boldsymbol{V}}\right)^{N/2} \exp\left(-\tfrac{1}{2}\operatorname{tr}(\boldsymbol{V}^{-1}\boldsymbol{M}(\boldsymbol{\theta}))\right).
\end{aligned}
\tag{24}
$$

For those cases where the covariance matrix of the residuals $\boldsymbol{V}$ is not known in advance, as is our situation, the natural logarithm of this likelihood function simplifies (24) to [Bard 1974]

$$
\ln(\mathscr{L}(\boldsymbol{\theta})) = \frac{N}{2}\left(I\left(\ln\left(\frac{N}{2\pi}\right) - 1\right) - \ln \det \boldsymbol{M}(\boldsymbol{\theta})\right),
\tag{25}
$$

whose bias-corrected covariance matrix can be determined post-analysis as $\boldsymbol{V} = \frac{I}{IN-K}\boldsymbol{M}(\boldsymbol{\vartheta})$. From this matrix, one can acquire confidence intervals for the parameter estimates, and one can ascertain whether or not the parameters act independent of one another (compare [Bard 1974]).

The Akaike information criterion (AIC) is a powerful tool that blends information theory with statistics for the purpose of objectively selecting the best model from a pool of candidate models [Burnham and Anderson 2002]. A model's log-likelihood, computed by (25), quantifies one of the two terms that make up the AIC statistic; in particular, $\text{AIC} = 2\left(NK/(N-K-1) - \ln \mathscr{L}(\boldsymbol{\vartheta})\right)$, where $K$ varies between models. What AIC brings to the table when modeling soft tissues is discussed in more detail in [Freed and Diethelm 2006].

Maximizing the log-likelihood function of (25) is equivalent to minimizing the objective function

$$
\Phi(\boldsymbol{\theta}) = \frac{N}{2} \ln \det \boldsymbol{M}(\boldsymbol{\theta}).
\tag{26}
$$

The minimization of this objective function can be cast as a linear equation $\boldsymbol{H}\Delta\boldsymbol{\theta} = -\boldsymbol{q}$ that can in turn be solved iteratively via Newton–Raphson iteration[3] so that $\boldsymbol{\theta}_{\nu+1} = \boldsymbol{\theta}_\nu - \boldsymbol{H}_\nu^{-1}\boldsymbol{q}_\nu$, with $\boldsymbol{\theta}_{\nu+1} \to \boldsymbol{\vartheta}$ at convergence. Gauss' approximation for the Hessian $\boldsymbol{H}$ insures that the $K \times K$ matrix $\boldsymbol{H}$ is symmetric positive-definite in that

$$
\boldsymbol{H} = \frac{\partial^2 \Phi(\boldsymbol{\theta})}{\partial\boldsymbol{\theta}\,\partial\boldsymbol{\theta}} = 2\sum_{n=1}^{N} \boldsymbol{B}_n^T \boldsymbol{G}\boldsymbol{B}_n \quad \text{with} \quad \boldsymbol{q} = \frac{\partial\Phi(\boldsymbol{\theta})}{\partial\boldsymbol{\theta}} = -2\sum_{n=1}^{N} \boldsymbol{B}_n^T \boldsymbol{G}\boldsymbol{r}_n,
\tag{27}
$$

---

[3]Newton–Raphson iteration was actually the genius of Thomas Simpson; see for example [O'Connor and Robertson 2005].

whose embedded metric and gradient matrices, for maximum likelihood estimates, are defined by

$$G = \frac{\partial \Phi(M(\theta))}{\partial M} = \frac{N}{2} M^{-1}(\theta) \quad \text{and} \quad B_n = -\frac{\partial r_n(\theta)}{\partial \theta} = \frac{\partial \mathcal{Y}(\theta, x_n)}{\partial \theta}. \tag{28}$$

Different choices for the objective function lead to different constructions for metric $G$; for example, $G = I$ associates with the method of least squares [Bard 1974]. For the optimizations done in this paper, the moment of residuals $M$ was always a fully populated matrix; therefore, least-squares regression is not appropriate here.

***Dynamic models.*** In dynamic models, like hypoelasticity, the $I$ response variables $\mathcal{Y}_i(\theta, s, x)$, $i = 1, 2, \ldots, I$, depend on a set of $J$ internal state variables $s_j(\theta, x)$, $j = 1, 2, \ldots, J$, that are in turn governed by a system of first-order ODEs so that[4]

$$\frac{ds}{dx} = f(\theta, s, x) \quad \text{with IC} \quad s(\theta, x_0) = s_0, \tag{29}$$

implying that there are now $N + 1$ experimental datum points, with the model being calibrated at the initial state $\mathcal{Y}(\theta, s_0, x_0) = y_0$. It therefore follows from the chain rule that gradient $B_n$ now becomes

$$B_n = \frac{\partial \mathcal{Y}(\theta, s_n, x_n)}{\partial \theta} + \frac{\partial \mathcal{Y}(\theta, s_n, x_n)}{\partial s_n} \frac{\partial s_n}{\partial \theta}, \tag{30}$$

whose unknown matrix of coefficients $\partial s_n / \partial \theta$ is a solution to an ODE called the sensitivity equation

$$\frac{d}{dx} \frac{\partial s}{\partial \theta} = \frac{\partial f}{\partial \theta} + \frac{\partial f}{\partial s} \frac{\partial s}{\partial \theta} \quad \text{with IC} \quad \frac{\partial s(\theta, x_0)}{\partial \theta} = \frac{\partial s_0}{\partial \theta}, \tag{31}$$

that needs to be integrated simultaneously with (29), as they constitute a coupled system. The writing of (31) requires $s$ to be continuous and sufficiently differentiable in $x$ and $\theta$ so that the left-hand side $\frac{\partial}{\partial \theta} \frac{ds}{dx}$ can be reordered to read as $\frac{d}{dx} \frac{\partial s}{\partial \theta}$.

Dynamic models also differ from static ones in that the sums to $N$ in (27) for the Hessian $H$ and gradient $q$ now start at 0, instead of 1, so that the initial conditions can be accounted for. This is essential whenever initial conditions are to be amongst the parameters being estimated in an optimization.

***Coefficient of determination.*** The $R^2$ statistic is not uniquely defined for nonlinear optimizations, and many schemes have been proposed in the literature. The $R^2$ statistic chosen for use here was derived in [Buse 1973] for the method of generalized least squares, and is selected because of its relative ease in application, once log-likelihood estimates $\vartheta$ are in hand, and because of its applicability to the maximum likelihood method. It is defined by

$$R^2 = 1 - \sum_{n=1}^{N} \frac{r_n(\theta) \cdot M(\theta)^{-1} r_n(\theta)}{\sum_{\nu=1}^{N} (y_\nu - \bar{y}) \cdot M(\theta)^{-1} (y_\nu - \bar{y})} \Bigg|_{\theta = \vartheta}, \tag{32}$$

---

[4]In some models, like those in (3) and (10), there is no difference between the response and internal state variables. In other models, there is a difference; for example, in the fiber-matrix theory presented in [Freed 2008], the fiber and matrix stresses $T^f$ and $T^m$ are internal state variables that relate to the response variable, stress $T$, via an equation of state known as the rule of mixtures.

where the covariance matrix for the residuals $V$ has been replaced by the moment of residuals $M$, because they become proportional whenever $M(\theta)$ is evaluated with the maximum likelihood estimates $\hat{\vartheta}$.

## Appendix B. A new 4(3) Runge–Kutta integrator

Integrations done in this paper were achieved using the explicit 4(3) Runge–Kutta integrator whose coefficients are given in Table 3. This fourth-order Runge–Kutta method in five stages with an embedded third-order method solves the nonlinear ODE $d\boldsymbol{y}/dx = \boldsymbol{f}(x, \boldsymbol{y})$ with IC $\boldsymbol{y}(x_0) = \boldsymbol{y}_0$ via the formulæ

$$
\begin{aligned}
\boldsymbol{k}_1 &= \boldsymbol{f}(x_i, \boldsymbol{y}_i), \\
\boldsymbol{k}_2 &= \boldsymbol{f}(x_i + c_2 h, \boldsymbol{y}_i + h a_{21} \boldsymbol{k}_1), \\
\boldsymbol{k}_3 &= \boldsymbol{f}(x_i + c_3 h, \boldsymbol{y}_i + h(a_{31} \boldsymbol{k}_1 + a_{32} \boldsymbol{k}_2)), \\
\boldsymbol{k}_4 &= \boldsymbol{f}(x_i + c_4 h, \boldsymbol{y}_i + h(a_{41} \boldsymbol{k}_1 + a_{42} \boldsymbol{k}_2 + a_{43} \boldsymbol{k}_3)), \\
\boldsymbol{k}_5 &= \boldsymbol{f}(x_i + c_5 h, \boldsymbol{y}_i + h(a_{51} \boldsymbol{k}_1 + a_{52} \boldsymbol{k}_2 + a_{53} \boldsymbol{k}_3 + a_{54} \boldsymbol{k}_4)), \\
\boldsymbol{y}_{i+1} &= \boldsymbol{y}_i + h(b_1 \boldsymbol{k}_1 + b_2 \boldsymbol{k}_2 + b_3 \boldsymbol{k}_3 + b_4 \boldsymbol{k}_4 + b_5 \boldsymbol{k}_5), \\
\hat{\boldsymbol{y}}_{i+1} &= \boldsymbol{y}_i + h(\hat{b}_1 \boldsymbol{k}_1 + \hat{b}_2 \boldsymbol{k}_2 + \hat{b}_3 \boldsymbol{k}_3 + \hat{b}_4 \boldsymbol{k}_4 + \hat{b}_5 \boldsymbol{k}_5),
\end{aligned} \tag{33}
$$

where $h = x_{i+1} - x_i$ is the step size. We derived the coupling coefficients (the $a_{ij}$ in the center tableau of Table 3) for this integrator from the four order conditions for a third-order Runge–Kutta method, and from the eight order conditions for a fourth-order method [Hairer et al. 1993]. This integrator combines the quadrature points (the $c_i$) and weights (the $b_j$) from Kutta's three-eights rule [1901], which is fourth-order accurate, with those from Simpson's rule[5] (establishing $c_3$ and the $\hat{b}_j$), which is third-order accurate. These quadrature/weight schemes arise from Lagrange interpolation, and are manifest in FE theory whenever discrete nodal forces are used to represent uniform, external, pressure loadings that in turn produce uniform states of stress within an element [Cook et al. 2002]. It is this continuity of a

| | | | | | | | | | | | | | | | | | |
|---|---|---|---|---|---|---|---|---|---|---|---|---|---|---|---|---|---|
| 0 | | | | | | 0 | | | | | | | 0 | | | | |
| $c_2$ | $a_{21}$ | | | | | 1/3 | 1/3 | | | | | | 1/3 | 1/3 | | | |
| $c_3$ | $a_{31}$ | $a_{32}$ | | | | 1/2 | 0 | 1/2 | | | | | 1/2 | 0 | 1/2 | | |
| $c_4$ | $a_{41}$ | $a_{42}$ | $a_{43}$ | | | 2/3 | $-x/3$ | $x$ | $2(1-x)/3$ | | | | 2/3 | $-2/9$ | 2/3 | 2/9 | |
| $c_5$ | $a_{51}$ | $a_{52}$ | $a_{53}$ | $a_{54}$ | | 1 | $x$ | $2-3x$ | $2(x-1)$ | 1 | | | 1 | 2/3 | 0 | $-2/3$ | 1 |
| $\boldsymbol{y}$ | $b_1$ | $b_2$ | $b_3$ | $b_4$ | $b_5$ | $\boldsymbol{y}$ | 1/8 | 3/8 | 0 | 3/8 | 1/8 | | $\boldsymbol{y}$ | 1/8 | 3/8 | 0 | 3/8 | 1/8 |
| $\hat{\boldsymbol{y}}$ | $\hat{b}_1$ | $\hat{b}_2$ | $\hat{b}_3$ | $\hat{b}_4$ | $\hat{b}_5$ | $\hat{\boldsymbol{y}}$ | 1/6 | 0 | 2/3 | 0 | 1/6 | | $\hat{\boldsymbol{y}}$ | 1/6 | 0 | 2/3 | 0 | 1/6 |

**Table 3.** The Butcher tableau for a generic, five-stage, Runge–Kutta method is given on the left. The Butcher tableau for a new, embedded, 4(3) Runge–Kutta method in 5 stages is presented in the middle, where $x$ has been set to 2/3 in the right tableau, which is near optimum.

---

[5]"Simpson's rule had been used by Johannes Kepler in the construction of an approximate method for computing the volume of wine casks. This work of Kepler's was published in 1615, almost 100 years before Simpson was born, in his treatise with the title *Nova stereometria doliorum vinariorum* (A new stereometry [i.e. method for the computation of the volume] for wine casks). Hence, at least in the German speaking literature, Simpson's rule is sometimes called 'Kepler's cask rule'." (Private communication, Prof. Kai Diethelm, Technische Universität Braunschweig.)

uniform input producing a uniform output through a discretized interface that motivated the development of this integrator.

With the quadrature points and weights established a priori, the resulting twelve order conditions, several being satisfied trivially by the preassigned quadrature points and weights, require that the unknown elements in the bottom two rows of the coupling matrix be described in terms of a single parameter, as shown in the middle tableau. The selected value for this parameter, $x = 2/3$, yields the simple set of coupling coefficients listed in the rightmost tableau of Table 3, which roughly minimize the error coefficients of this integrator. These error coefficients are measures of how far the order conditions are from being satisfied for the next higher-order set. For this integrator, they are $(-1/54, 1/36, -1/9, 119/144, -1/9, -23/27, -1/9, 1/36, 2/9)$ for solution $y$, and $(0, 0, 1/9, 1/9)$ for solution $\hat{y}$.

The PI (proportional integral) controller of [Gustafsson et al. 1988] was used to dynamically adjust the step size of integration. This controller is driven by a local error estimate $y - \hat{y}$ that, for the integrator in Table 3, has contributions arising from each of the five quadrature locations, which is another desirable feature of our integrator.

## Acknowledgement

## References

[Aaron and Gosline 1981] B. B. Aaron and J. M. Gosline, "Elastin as a random-network elastomer: a mechanical and optical analysis of single elastin fibers", *Biopolymers* **20**:6 (1981), 1247–1260.

[Bard 1974] Y. Bard, *Nonlinear parameter estimation*, Academic Press, New York, 1974.

[Burnham and Anderson 2002] K. P. Burnham and D. R. Anderson, *Model selection and multimodel inference: a practical information-theoretic approach*, 2nd ed., Springer, New York, 2002.

[Buse 1973] A. Buse, "Goodness of fit in generalized least squares estimation", *Am. Stat.* **27**:3 (1973), 106–108.

[Cook et al. 2002] R. D. Cook, D. S. Malkus, M. E. Plesha, and R. J. Witt, *Concepts and applications of finite element analysis*, 4th ed., Wiley, New York, 2002.

[Criscione et al. 2003] J. C. Criscione, M. S. Sacks, and W. C. Hunter, "Experimentally tractable, pseudo-elastic constitutive law for biomembranes, II: Application", *J. Biomech. Eng.* (*ASME*) **125**:1 (2003), 100–105.

[Dienes 1979] J. K. Dienes, "On the analysis of rotation and stress rate in deforming bodies", *Acta Mech.* **32**:4 (1979), 217–232.

[Dienes 1987] J. K. Dienes, "Theory of deformation, 1: Kinematics", Technical Report LA–11063–MS, Vol. 1, Los Alamos National Laboratory, December 1987.

[Freed 2008] A. D. Freed, "Anisotropy in hypoelastic soft-tissue mechanics, I: Theory", *J. Mech. Mater. Struct.* **3**:5 (2008), 911–928.

[Freed and Diethelm 2006] A. D. Freed and K. Diethelm, "Fractional calculus in biomechanics: a 3D viscoelastic model using regularized fractional derivative kernels with application to the human calcaneal fat pad", *Biomech. Model. Mechanobiol.* **5**:4 (2006), 203–215.

[Freed and Doehring 2005] A. D. Freed and T. C. Doehring, "Elastic model for crimped collagen fibrils", *J. Biomech. Eng.* (*ASME*) **127**:4 (2005), 587–593.

[Freed et al. 2005] A. D. Freed, D. R. Einstein, and I. Vesely, "Invariant formulation for dispersed transverse isotropy in aortic heart valves: an efficient means for modeling fiber splay", *Biomech. Model. Mechanobiol.* **4**:2–3 (2005), 100–117.

[Fung 1967] Y. C. Fung, "Elasticity of soft tissues in simple elongation", *Am. J. Physiol.* **213**:6 (1967), 1532–1544.

[Gasser et al. 2006] T. C. Gasser, R. W. Ogden, and G. A. Holzapfel, "Hyperelastic modelling of arterial layers with distributed collagen fibre orientations", *J. R. Soc. Interface* **3**:6 (2006), 15–35.

[Green and Naghdi 1965] A. E. Green and P. M. Naghdi, "A general theory of an elastic-plastic continuum", *Arch. Ration. Mech. An.* **18**:4 (1965), 251–281.

[Gustafsson et al. 1988] K. Gustafsson, M. Lundh, and G. Söderlind, "A PI stepsize control for the numerical solution of ordinary differential equations", *BIT* **28**:2 (1988), 270–287.

[Hairer et al. 1993] E. Hairer, S. P. Nørsett, and G. Wanner, *Solving ordinary differential equations, I: Nonstiff problems*, 2nd ed., Springer Series in Computational Mathematics **8**, Springer, Berlin, 1993.

[Holzapfel 2000] G. A. Holzapfel, *Nonlinear solid mechanics: a continuum approach for engineering*, Wiley, Chichester, 2000.

[Holzapfel et al. 2002] G. A. Holzapfel, T. C. Gasser, and M. Stadler, "A structural model for the viscoelastic behavior of arterial walls: continuum formulation and finite element analysis", *Eur. J. Mech. A Solids* **21**:3 (2002), 441–463.

[Kutta 1901] W. Kutta, "Beitrag zur näherungsweisen Integration totaler Differentialgleichungen", *Z. Math. Phys.* **46** (1901), 435–453.

[Miller-Young et al. 2002] J. E. Miller-Young, N. A. Duncan, and G. Baroud, "Material properties of the human calcaneal fat pad in compression: experiment and theory", *J. Biomech.* **35**:12 (2002), 1523–1531.

[Niederer et al. 2004] P. F. Niederer, P. P. Lunkenheimer, and C. W. Cryer, "On the significance of fiber branching in the human myocardium", *Biomech. Model. Mechanobiol.* **3**:1 (2004), 1–5.

[O'Connor and Robertson 2005] J. J. O'Connor and E. F. Robertson, "Thomas Simpson", online biography in the *MacTutor History of Mathematics*, 2005, Available at http://www-history.mcs.st-and.ac.uk/Biographies/Simpson.html.

[Ogden 1984] R. W. Ogden, *Non-linear elastic deformations*, Wiley, New York, 1984. Republished by Dover, Mineola, NY, 1997.

[Oldroyd 1950] J. G. Oldroyd, "On the formulation of rheological equations of state", *Proc. R. Soc. Lond. A* **200**:1063 (1950), 523–541.

[Rivlin and Smith 1969] R. S. Rivlin and G. F. Smith, "Orthogonal integrity basis for *N* symmetric matrices", pp. 121–141 in *Contributions to mechanics*, edited by D. Abir, Pergamon, New York, 1969.

[Treloar 1975] L. R. G. Treloar, *The physics of rubber elasticity*, 3rd ed., Clarendon, Oxford, 1975.

[Truesdell 1955] C. Truesdell, "Hypo-elasticity", *Indiana Univ. Math. J.* **4**:1 (1955), 83–133.

[Weiss 1994] J. A. Weiss, *A constitutive model and finite element representation for transversely isotropic soft tissues*, Ph.D. thesis, University of Utah, December 1994.

[Woltring 1986] H. J. Woltring, "A Fortran package for generalized, cross-validatory spline smoothing and differentiation", *Adv. Eng. Software* **8**:2 (1986), 104–113.

ALAN D. FREED: adfreed@svsu.edu
*Saginaw Valley State University, 202 Pioneer Hall, 7400 Bay Road, University Center, MI 48710, United States*

# DYNAMICS OF A LIGHT HOOP WITH AN ATTACHED HEAVY DISK: INSIDE AN INTERACTION PULSE

VLADO A. LUBARDA

An analysis of motion of a light hoop with a heavy circular disk attached to the inner side of its rim over a rough horizontal surface is presented. When the radius of the disk is small relative to the radius of the hoop, the motion is characterized by the sequence of sharp interaction pulses between the hoop and the horizontal surface, during which a complex transition between stick, slip, and reversed slip takes place. This is accompanied by the corresponding changes in the frictional force, which include abrupt reversal of its direction, and rapid increase and discontinuous changes of the normal component of the reactive force. The intensity of the interaction rapidly diminishes with an increase of the radius of the disk or the mass of the hoop. The effects of the coefficient of friction on the dynamic interactions, stick and slip transitions, and the energy dissipation are discussed.

## 1. Introduction

This paper is an analysis of motion of a light hoop with a heavy circular disk attached to the inner side of its rim released to move on a rough horizontal surface. This seemingly simple problem in dynamics is characterized by a surprising complexity of the involved kinematics and kinetics of motion, which reveals a variety of information of a possible interest for the mechanics of frictional impact. When the radius of the disk is small relative to the radius of a light hoop, the motion is characterized by the sequence of sharp interaction pulses between the hoop and the horizontal surface during which a complex transition between stick, slip, and reversed slip takes place. The sharp interaction pulses arise in response to large angular velocity and angular acceleration of the hoop built in a short interval of time during which the disk passes above the horizontal surface. The motion is also characterized by the corresponding sudden changes in the velocity components of the center of the disk. The intensity of the sharp interactions between the hoop and the horizontal surface as well as the overall complexity of motion (transitions from one type of motion to another) diminish with the increasing size of the disk or the mass of the hoop. For sufficiently large disks, the rolling without transition to sliding prevails throughout the motion. The analysis demonstrates that for light hoops and very small disks, the time integral of the tangential component of the interaction pulse is in general different from the product of the coefficient of kinetic friction and the time integral of the normal component of the interaction pulse (referred to in the mechanics of frictional impact as the Whittaker [1961] or Kane and Levinson [1985] assumption for the impulse components).

The presented analysis resulted from the study of a puzzling dynamics problem of motion of a massless hoop with an attached point mass, which is mentioned in the books by Littlewood [1986] and Kilmister
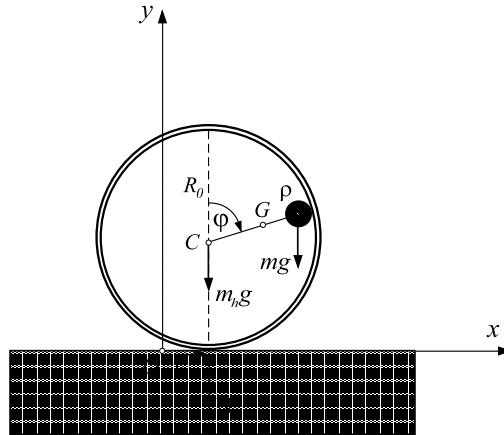
**Figure 1.** Rolling/sliding motion of a thin light hoop of mass $m_h$ with the inner and outer radii $R_0$ and $R = r R_0$, respectively. The attached disk has radius $\rho$ and mass $m$. The mass center of the system is at the point $G$ such that $\overline{CG} = \vartheta R_0$, where $\vartheta = (1-k)m/M$, $k = \rho/R_0$, and $M = m + m_h$ is the total mass of the system.

and Reeve [1966], and which has been a subject of several recent publications addressing the question of whether the hoop lifts off the horizontal surface during its motion [Tokieda 1997; Butler 1999; Pritchett 1999; Theron 2000; 2002; Theron and du Plessis 2001; Liu and Yun 2004]. This hopping of the hoop dilemma was associated with the uncertainties in the description of motion of a hypothetical dynamic system which engages in rotation but does not possess any rotational inertia, which can become dynamically indeterminate. In the process of elaborating on this dynamic indeterminacy, the analysis unveiled another interesting aspect of the problem, namely the description of sharp interaction pulses between the hoop and the horizontal surface as the disk passes just above the horizontal surface. This resembles some features of the interactions occurring during the frictional impact of colliding bodies, which can be treated only by additional considerations or assumptions about the deformation in the contact region [Johnson 1985; Brogliato 1999; Stronge 2000]. The analysis presented in this paper may thus help to better understand the impulsive interactions and the stick/slip transitions in the latter problems.

## 2. Motion of a light hoop with an attached circular disk

The dynamics of motion of a light hoop with an attached disk was studied in detail in [Pritchett 1999; Theron 2000; Theron and du Plessis 2001], with the goal of addressing the question of possible hopping of the hoop and the dynamic indeterminacy in some stages of motion of an idealized system of a massless hoop with an attached point mass. In this and the subsequent section we extend this analysis to describe the interaction pulses and the stick/slip transitions throughout the motion of the hoop, for various mass ratios and the geometric and friction parameters. We adopt the model in which the mass $m$ is uniformly distributed within a circular disk of radius $\rho$, which is attached to the inner side of a thin hoop with inner radius $R_0$, outer radius $R$, and a uniformly distributed mass $m_h$ (Figure 1).

**2.1.** *Rolling motion.* If the coefficient of friction between the hoop and the horizontal surface is sufficiently high, as specified in the sequel by (9), the hoop begins its motion by rolling, such that the

coordinates of the mass center of the system are

$$x = x_C + \vartheta R_0 \sin \varphi, \qquad y = R + \vartheta R_0 \cos \varphi. \tag{1}$$

Here, $x_C = R(\varphi - \varphi_0)$ is the horizontal coordinate of the center of the hoop, $\vartheta = (1-k)m/M$, $k = \rho/R_0$, and $M = m + m_h$ is the mass of the moving system. With this notation, the distance between the center of the hoop and the mass center of the system is $\overline{CG} = \vartheta R_0$. The corresponding equations of motion (ignoring the coefficient of rolling resistance and the associated rolling resistance moment) are

$$M\ddot{x} = F, \qquad M\ddot{y} = N - Mg, \qquad J\ddot{\varphi} = N\vartheta R_0 \sin \varphi - F(R + \vartheta R_0 \cos \varphi). \tag{2}$$

The moment of inertia of the hoop/disk system for its mass center $G$ is

$$J = \eta^2 M R_0^2, \qquad \eta^2 = \frac{m_h}{2M}(1 + r^2) + \frac{m_h}{m}\vartheta^2 + \frac{m}{2M}k^2, \tag{3}$$

where $r = R/R_0$ (so that $\eta R_0$ is the radius of gyration of the hoop/disk system). When (1) is substituted into the first two equations of (2), the normal and friction force can be expressed as

$$N = M\big[g - \vartheta R_0(\cos \varphi \dot{\varphi}^2 + \sin \varphi \ddot{\varphi})\big], \qquad F = M\big[R\ddot{\varphi} - \vartheta R_0(\sin \varphi \dot{\varphi}^2 - \cos \varphi \ddot{\varphi})\big]. \tag{4}$$

The differential equation for $\varphi$ then follows from the third equation in (2) as

$$[\varsigma + 2(1 + \cos \varphi)]\ddot{\varphi} - \sin \varphi \dot{\varphi}^2 = \frac{g}{R} \sin \varphi, \tag{5}$$

with the initial conditions $\varphi(0) = \varphi_0$ and $\dot{\varphi}(0) = 0$ at time $t = 0$. The nondimensional parameter $\varsigma$ is defined by

$$\varsigma = \frac{3k^2 + 4k(r-1) + 2(r-1)^2 + (1 + 3r^2)m_h/m}{2r(1-k)}. \tag{6}$$

Since $2\ddot{\varphi} = d(\dot{\varphi}^2)/d\varphi$, (5) can be solved for $\dot{\varphi}^2$ to obtain

$$\dot{\varphi}^2 = \frac{2g}{R} \frac{\cos \varphi_0 - \cos \varphi}{\varsigma + 2(1 + \cos \varphi)}. \tag{7}$$

Alternatively, the expression for the square of the angular velocity follows directly from the energy conservation during the rolling motion, which requires that $2Mg(y_0 - y) = M(\dot{x}^2 + \dot{y}^2) + J\dot{\varphi}^2$. Upon the time-differentiation of (7), or by substituting (7) back into (5), the angular acceleration is found to be

$$\ddot{\varphi} = \frac{g \sin \varphi}{R} \frac{\varsigma + 2(1 + \cos \varphi_0)}{[\varsigma + 2(1 + \cos \varphi)]^2}. \tag{8}$$

Having determined $\dot{\varphi}^2$ and $\ddot{\varphi}$ as the functions of $\varphi$, the normal and friction forces can be calculated from (4). The rolling motion proceeds as long as $|F| \le \mu_s N$ and $N > 0$. The minimum coefficient of static friction needed for rolling to begin at the inception of motion is

$$\mu_s^{\min} = \frac{F(\varphi_0)}{N(\varphi_0)} = \frac{[r + \vartheta \cos \varphi_0] \sin \varphi_0}{r[\varsigma + 2(1 + \cos \varphi_0)] - \vartheta \sin^2 \varphi_0}. \tag{9}$$

The larger the disk radius, the smaller the minimum coefficient of static friction required for rolling.

If $k = 0$, $m_{\text{h}} = 0$, and $r = 1$ then $\mu_{\text{s}}^{\min} = \tan(\varphi_0/2)$. For $\mu_{\text{s}}^{\min} < \tan(\varphi_0/2)$, a massless hoop with an attached point mass released from rest with a point mass at an angle $\varphi_0$ skims the surface without interaction with it ($N = F = 0$, $\ddot{x} = 0$, $\ddot{y} = -g$) until the impact of the point mass with the surface at $\varphi = \pi$ [Theron and du Plessis 2001]. For $\mu_{\text{s}}^{\min} > \tan(\varphi_0/2)$, the rolling stage of the motion of a massless hoop with an attached point mass is specified by (5) with $\varsigma = 0$, which has a closed form solution $\sin(\varphi/2) = \sin(\varphi_0/2) \cosh[(g/4R)^{1/2}t]$, with the corresponding normal force $N = mg[2\cos^2(\varphi/2) - \cos^2(\varphi_0/2)]$.

**2.2. Combined rolling/sliding motion.** If $\varphi_1$ is the angle at which $|F| = \mu_{\text{s}}N$, the hoop will engage in a combined rolling/sliding motion, which continues in alternating cycles of decreasing amplitude, until the hoop comes to rest with the disk at its bottom. The analysis has to be performed sequentially following each stage of motion by checking the direction of the relative slip between the hoop and the horizontal surface, which is forward or backward depending on the sign of ($\dot{x}_C - R\dot{\varphi}$). During a forward slip ($\dot{x}_C - R\dot{\varphi} > 0$), the velocity of the contact point of the hoop with the horizontal surface is directed toward the right, and the friction force toward the left. The opposite is true in the case of backward slip ($\dot{x}_C - R\dot{\varphi} < 0$). Theron [2000] refers to a forward slip as skidding and to a backward slip as spinning. This terminology will be used for the rest of the paper. Each time the relative slip between the hoop and the horizontal surface changes from spinning to skidding, or vice versa, the force of friction reverses its direction. There could also be intervals of resumed rolling and depending on the ratios $\rho/R_0$ and $m/M$ the hoop may settle in an oscillating rolling motion around $\varphi = \pi$.

Assuming that $N \geq 0$ throughout the motion, so that there is no hopping of the hoop ($y_C = R$), which is verified and confirmed by calculations a posteriori, the coordinates of the center of the disk during the rolling/sliding stage of motion are given by (1) with $x_C \neq R(\varphi - \varphi_0)$. Denoting by $\mu < \mu_{\text{s}}$ the coefficient of kinetic friction, the frictional force is

$$F = -\hat{\mu}N, \qquad \hat{\mu} = \mu \, \text{sign}(\dot{x}_C - R\dot{\varphi}), \tag{10}$$

and the equations of motion become

$$\ddot{x}_C + \vartheta R_0(-\sin\varphi \dot{\varphi}^2 + \cos\varphi \ddot{\varphi}) = -\hat{\mu}(N/M),$$
$$-\vartheta R_0(\cos\varphi \dot{\varphi}^2 + \sin\varphi \ddot{\varphi}) = (N/M) - g, \tag{11}$$
$$\eta^2 R_0 \ddot{\varphi} = [\vartheta \sin\varphi + \hat{\mu}(r + \vartheta \cos\varphi)](N/M).$$

When the second equation in (11) is substituted into the third equation to eliminate $N/M$, the differential equation for $\dot{\varphi}^2$ is found to be

$$\frac{1}{2}[\sin\varphi + \alpha z(\varphi)]\frac{d\dot{\varphi}^2}{d\varphi} + \cos\varphi \dot{\varphi}^2 = \frac{g}{\vartheta R_0}, \tag{12}$$

where

$$\alpha = \frac{\eta^2}{\vartheta} = \frac{m_{\text{h}}}{2m}\frac{r^2+1}{1-k} + \frac{m_{\text{h}}}{m+m_{\text{h}}}(1-k) + \frac{k^2}{2(1-k)}, \tag{13}$$

and

$$z(\varphi) = [\vartheta(\sin\varphi + \hat{\mu}\cos\varphi) + r\hat{\mu}]^{-1}. \tag{14}$$

The associated initial condition is specified by the continuity of $\dot{\varphi}^2$ at the transition from rolling to rolling/sliding at $\varphi = \varphi_1$.

Equation (12) does not have an explicit closed form solution but can be solved numerically. Once $\dot\varphi^2$ is determined, the angular acceleration follows from

$$\ddot\varphi = \left[\sin\varphi + \alpha z(\varphi)\right]^{-1}\left(\frac{g}{\vartheta R_0} - \cos\varphi\dot\varphi^2\right). \tag{15}$$

The force $N$ is then calculated from the second equation in (11). The velocity of the center of the disk $\dot x_C$ is determined by integrating the first equation in (11). Since $\ddot x_C = \dot\varphi\, dx_C/d\varphi$, this becomes

$$\frac{d\dot x_C}{d\varphi} = \left\{-g\hat\mu + \vartheta R_0\left[(\sin\varphi + \hat\mu\cos\varphi)\dot\varphi^2 - (\cos\varphi - \hat\mu\sin\varphi)\ddot\varphi\right]\right\}/\dot\varphi, \tag{16}$$

with the initial condition $\dot x_C(\varphi_1) = R\dot\varphi(\varphi_1)$. The integration of the differential equations (12) and (16) proceeds in parallel to check the nature of the relative slip determined by the $\mathrm{sign}(\dot x_C - R\dot\varphi)$. Care must also be taken to calculate $\dot\varphi$ from the square root of $\dot\varphi^2$ with the appropriate sign before it is used in (16) depending whether the rotation of the hoop is clockwise or counterclockwise. Furthermore, as the small disk passes above the horizontal surface, the angular acceleration $\ddot\varphi$, and thus $d\dot\varphi^2/d\varphi$, experiences a rapid (nearly discontinuous) change, while $\dot\varphi^2$ attains its maximum value. Hence there is a change of the slip direction near $\varphi = \pi$ (unless rolling takes the hoop through the state of the maximum angular velocity).

**2.3. Resumption of rolling.** If the rolling resumes after the rolling/sliding phase of the motion then $|F| < \mu_s N$, $N > 0$, and $R\dot\varphi = \dot x_C$. Denote by $\varphi_3$ the angle at the end of the rolling/sliding phase and let $\dot\varphi_3$ and $\dot x_{C_3} = R\dot\varphi_3$ denote the corresponding angular velocity of the hoop and the velocity of its center. During the subsequent pure rolling motion, one has

$$x = x_{C_3} + R(\varphi - \varphi_3) + \vartheta R_0\sin\varphi, \qquad y = R + \vartheta R_0\cos\varphi, \tag{17}$$

and it readily follows that

$$\dot\varphi^2 = \frac{2g}{R}\frac{\cos\varphi_3 - \cos\varphi + c_3}{\varsigma + 2(1 + \cos\varphi)}, \qquad c_3 = \frac{R}{2g}\left[\varsigma + 2(1 + \cos\varphi_3)\right]\dot\varphi_3^2. \tag{18}$$

The angular acceleration is

$$\ddot\varphi = \frac{\sin\varphi}{\varsigma + 2(1 + \cos\varphi)}\left(\frac{g}{R} + \dot\varphi^2\right). \tag{19}$$

The corresponding normal and friction force follow from (4). One must verify a posteriori that $|F| < \mu_s N$ and $N > 0$. If the hoop came momentarily to rest at $\varphi = \varphi_3$ so that $\dot\varphi_3 = 0$ and $\dot x_C(\varphi_3) = 0$ then $c_3 = 0$ in (18). If $\dot\varphi_3 = 0$ but $\dot x_C(\varphi_3) \neq 0$ then the hoop slips back rather than role forward. In this case, the equations from Section 2.2 hold with the negative values of $\dot\varphi$ in (16).

**2.4. The effects of the mass of the hoop.** If $\gamma_h$ is a uniform mass density of the hoop, its mass is $m_h = (r^2 - 1)\pi R_0^2\gamma_h$ and its centroidal moment of inertia $J_h = 0.5(1 + r^2)m_h R_0^2$. If $\gamma_m$ is the mass density of the disk, its mass is $m = k^2\pi R_0^2\gamma_m$ with its centroidal moment of inertia $J_m = 0.5k^2 m R_0^2$. Thus, the mass and inertia ratios are

$$\frac{m_h}{m} = \frac{r^2 - 1}{k^2}\frac{\gamma_h}{\gamma_m}, \qquad \frac{J_h}{J_m} = \frac{r^2 + 1}{k^2}\frac{m_h}{m}. \tag{20}$$

The ratio of the contributions from the hoop and the disk to the moments of inertia with respect to the mass center $G$ of the hoop/disk system are

$$\frac{J_h^G}{J_m^G} = \frac{(r^2+1)(1+m_h/m)^2 + 2(r-1)^2}{k^2(1+m_h/m)^2 + 2(m_h/m)^2(r-1)^2} \frac{m_h}{m}. \tag{21}$$

For a very thin hoop, the two inertia ratios are nearly the same, that is,

$$\frac{J_h}{J_m} \approx \frac{J_h^G}{J_m^G} \approx \frac{2}{k^2}\frac{m_h}{m}, \qquad \frac{m_h}{m} \approx \frac{2(r-1)}{k^2}\frac{\gamma_h}{\gamma_m}. \tag{22}$$

For a very low density of the hoop material and a high density of the disk material (such as a hoop of some foamed plastic or a porous cellular material and a disk made of tungsten), the ratio $\gamma_h/\gamma_m$ would be of the order of $10^{-2}$. Then, if $r = 1.02$ and $k = 0.1$, the mass ratio is $m_h/m \approx 0.04$ while the moment of inertia ratios are $J_h/J_m \approx J_h^G/J_m^G \approx 8.24$. This illustrates the importance of the rotational inertia of the hoop even for very light hoops whenever the attached disk is sufficiently small. In order for $J_h/J_m$ to be equal to $1/10$, which would imply that the rotational inertia of the hoop can be ignored, the thickness of the hoop would have to be exceedingly small: $r = 1.00025$ in the case where $k = 0.1$ and $\gamma_h/\gamma_m \approx 10^{-2}$. Consequently, in Section 3 we present the results of calculations for both vanishing and nonvanishing mass ratios $m_h/m$.

## 3. Numerical results

In Section 3.1 we present numerical results for infinitesimally thin massless hoops ($r = 1$, $m_h = 0$) and a small disk of mass $m$ and radius $\rho = 0.1R$. The static and kinetic friction coefficients used are $\mu_s = 0.35$ and $\mu = 0.3$. In Section 3.2 we discuss the results for of a massless hoop with larger disks attached. The effects of the nonvanishing mass of the hoop on the resulting motion of the system and the interaction pulses are considered in Section 3.3, and the effects of the coefficient of friction are examined in Section 3.4. In all cases, the initial configuration of the hoop/disk system was specified to be $\varphi_0 = 10°$. A similar analysis can be performed for other inclination angles.

**3.1. _Massless hoop and a disk with $k = 0.1$._** Figure 2 shows the time variation of the horizontal velocity component of the contact point of an infinitesimally thin massless hoop during its first three rotation cycles, when the radius of the attached disk is $\rho = 0.1R$. The initial horizontal plateau corresponds to rolling portion of the motion, from $\varphi_0$ to $\varphi_1 = 0.71402$ rad. This is followed by spinning from $\varphi_1$ to $\varphi_2 = 3.18085$ rad, rolling from $\varphi_2$ to $\varphi_3 = 3.20455$ rad, and skidding from $\varphi_3$ to $\varphi_4 = 4.54542$ rad, which is the end of the first clockwise rotation of the hoop. The high precision is needed in calculations to accurately identify the small intervals of slip or stick near $\varphi = \pi$. The variation of the contact point velocity during the first interaction pulse (at time $t \cong 5.74\sqrt{R/g}$) is shown in Figure 2, right. The short horizontal plateau corresponds to brief rolling of the hoop. The skidding continues by a counterclockwise rotation from $\varphi_4$ to $\varphi_5 = 2.49277$ rad, which is the end of the first cycle of rotation of the hoop (at $t \cong 8.84\sqrt{R/g}$). The velocity of the contact point is positive during the entire second pulse. The other cycles follow and are dominated by skidding with brief intermissions by spinning and rolling during the pulses under clockwise rotation of the hoop (odd-numbered pulses). The time variations of the normal and friction force during the first three rotation cycles are shown in the left halves of Figures 3 and 4.
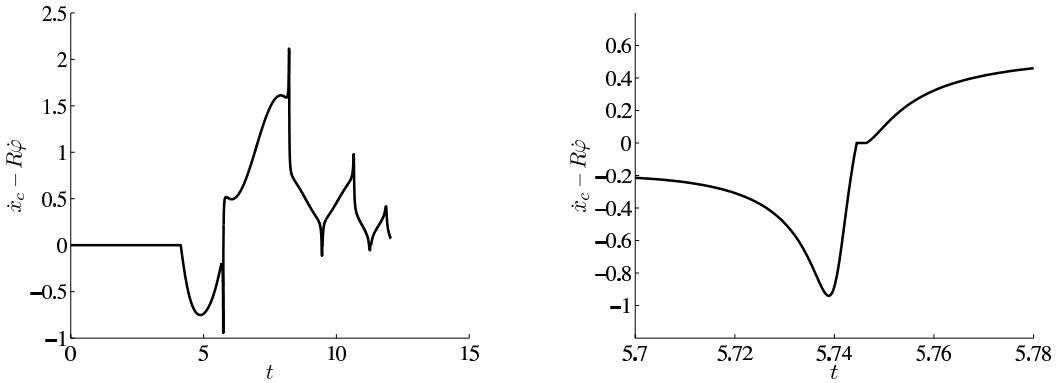
**Figure 2.** Left: Time variation of the velocity of the contact point of an infinitesimally thin massless hoop (scaled by $\sqrt{Rg}$) in the case $k = 0.1$. Right: The same velocity around the first interaction pulse indicating its rapid change, which includes a brief rolling period ($\dot{x}_c = R\dot{\varphi}$) in between spinning and skidding. The time scale is $\sqrt{R/g}$.



**Figure 3.** Left: Time variation of the normal force (scaled by $mg$) during the first three cycles of rotation of an infinitesimally thin massless hoop in the case $k = 0.1$. Right: The corresponding change during the first interaction pulse. The time scale is $\sqrt{R/g}$.
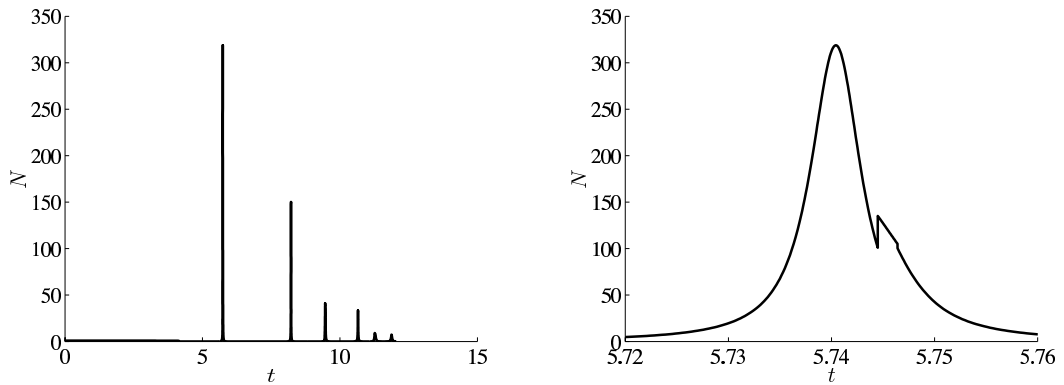


**Figure 4.** Left: Time variation of the friction force (scaled by $mg$) during the first three cycles of rotation of an infinitesimally thin massless hoop in the case $k = 0.1$. Right: The corresponding change during the first interaction pulse. The time scale is $\sqrt{R/g}$.
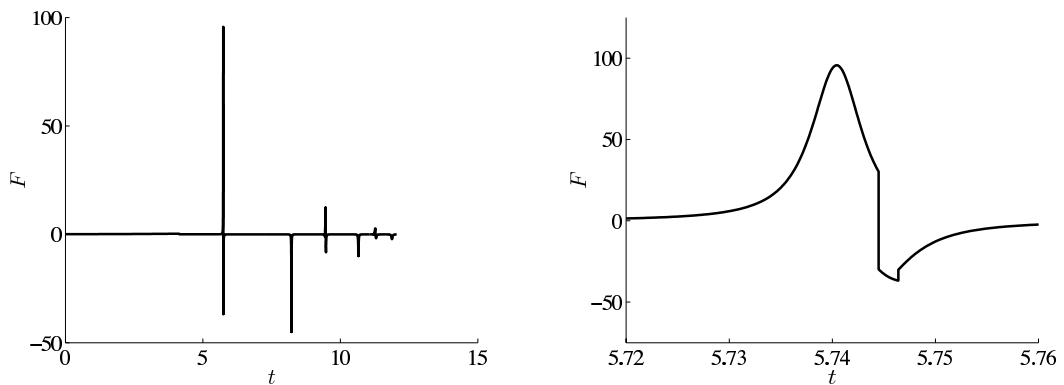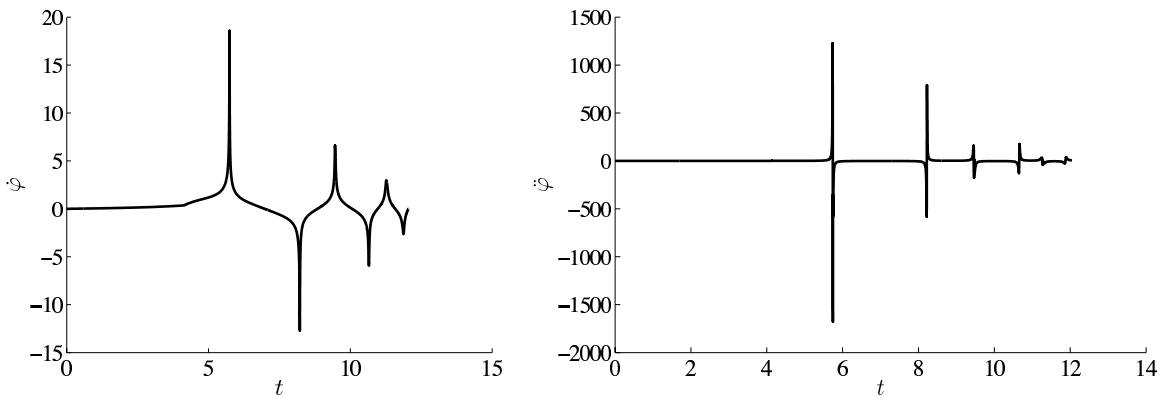
**Figure 5.** Left: Time variation of the angular velocity (scaled by $\sqrt{g/R}$) during the first three rotation cycles of an infinitesimally thin massless hoop in the case $k = 0.1$. Right: Time variation of the angular acceleration (scaled by $g/R$). The time scale is $\sqrt{R/g}$.

The jumps in the normal and friction force due to transitions from spinning to rolling and from rolling to skidding during the first pulse are shown in the right halves of Figures 3 and 4, consistent with the variation of the contact point velocity shown in Figure 2, right.

The normal force is finite during the initial rolling interval and is almost equal to zero afterwards except for its rapid buildup near $\varphi = \pi$ when the small disk passes just above the horizontal surface. The large values of $N$ are due to large values of the angular velocity $\dot{\varphi}$ near $\varphi = \pi$ and correspondingly large accelerations $\ddot{x}$ and $\ddot{y}$ of the center of the disk.[1] Note a discontinuous change of the normal force at the transition from rolling to spinning. The friction force around $\varphi = \pi$ shows a rapid change from positive values (spinning) to negative values (skidding) consistent with the variation of the contact point velocity, shown in Figure 2. It is due to this change in the direction of the friction force during a brief period of the sharp interaction pulse that the time integral of the friction force is not equal to $\mu$ times the time integral of the normal force.[2] The time variation of the angular velocity and the angular acceleration during the first three rotation cycles of the hoop are shown in Figure 5.

**3.2. *Massless hoop and larger disks.*** As the radius of the disk increases, and with it its rotational inertia, the intensity of the interaction pulse around $\varphi = \pi$ decreases. This is illustrated by considering an infinitesimally thin massless hoop with a disk of radius $\rho = 0.25R$. For brevity, only the first clockwise

---

[1]Under a large normal force, the hoop and the supporting surface would deform if their deformability was included in the analysis, and the elastic energy stored during this deformation would provide a propulsion for a possible hopping of the hoop at $\varphi = \pi$. The dynamics of an elastic hoop was studied by Theron [2002]. The inclusion of the mass of the hoop, which significantly decreases $N_{\max}$, is considered in Section 3.3.

[2]A similar situation arises in the mechanics of frictional impact of colliding bodies. Modeling of such impacts was greatly stimulated by Kane's [1984] double pendulum *dynamics puzzle* where the frictional component of an impulse is assumed to be equal to the normal component multiplied by the coefficient of kinetic friction. For some values of the coefficients of friction and normal restitution and for some kinematic parameters, this leads to an increase of kinetic energy when the pendulum impacts on a rough horizontal surface. Keller [1986] explained this by noting that there was a reversal of the slip direction during the impact process, and thus the coefficient of proportionality between the tangential and normal impulse was not equal to the coefficient of kinetic friction. Since then numerous papers has been published proposing different models of frictional impact as evidenced by comprehensive treatments of the subject in [Brach 1991; Brogliato 1999; Stronge 2000; Stewart 2000].
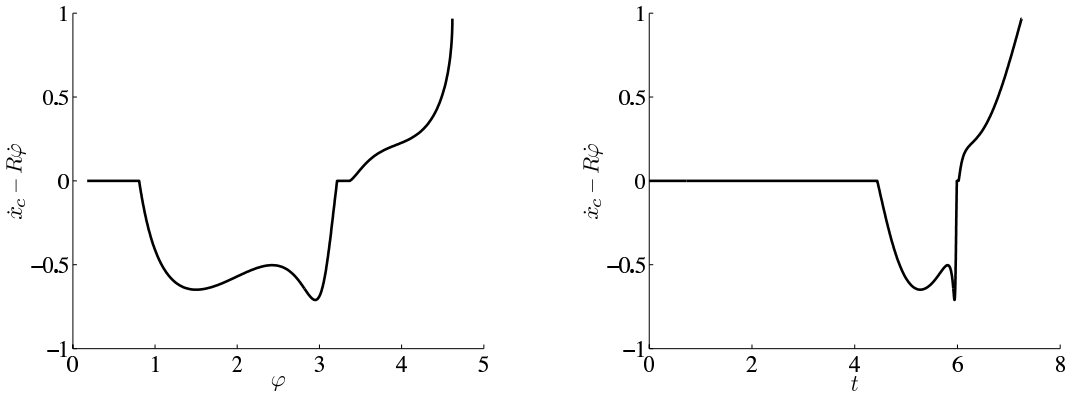
**Figure 6.** Left: Angle variation of the velocity of the contact point of the hoop (scaled by $\sqrt{Rg}$) during the first clockwise rotation of the hoop in the case $k = 0.25$. Right: The corresponding time variation of the same velocity. The time scale is $\sqrt{R/g}$.

rotation of the hoop is considered. Figure 6 shows the variation of the horizontal velocity component of the contact point. The initial horizontal plateau corresponds to rolling portion of the motion, from $\varphi_0$ to $\varphi_1 = 0.80625 \, \text{rad}$. This is followed by spinning from $\varphi_1$ to $\varphi_2 = 3.21545 \, \text{rad}$, rolling from $\varphi_2$ to $\varphi_3 = 3.37076 \, \text{rad}$, and skidding from $\varphi_3$ to $\varphi_4 = 4.61783 \, \text{rad}$, which is the end of the first clockwise rotation of the hoop. The normal and friction force are plotted versus the angle $\varphi$ in Figure 7. The peak values of both forces are greatly reduced from their values corresponding to small disks with $k = 0.1$.

If the hoop with an attached disk with radius $\rho = 0.75R$ is released from rest at $\varphi_0 = 10°$, the rolling mode prevails throughout the motion of the hoop ($\dot{x}_C = R\dot{\varphi}$ and $|F| < \mu_s N$), which is described by the closed form solution in Section 2.1. Here, the maximum normal force is $N_{\max} = 1.3 \, mg$, compared with $N_{\max} = 3.52 \, mg$ in the case where $\rho = 0.5R$, $N_{\max} = 32.4 \, mg$ in the case where $\rho = 0.25R$, and $N_{\max} = 318 \, mg$ in the case where $\rho = 0.1R$. Numerical evaluations also reveal that for $\varphi_0 = 10°$, the smallest radius of the disk for which the rolling prevails throughout the motion of the hoop is $\rho = 0.5385R$. The corresponding maximum normal force is $N_{\max} = 2.94 \, mg$.
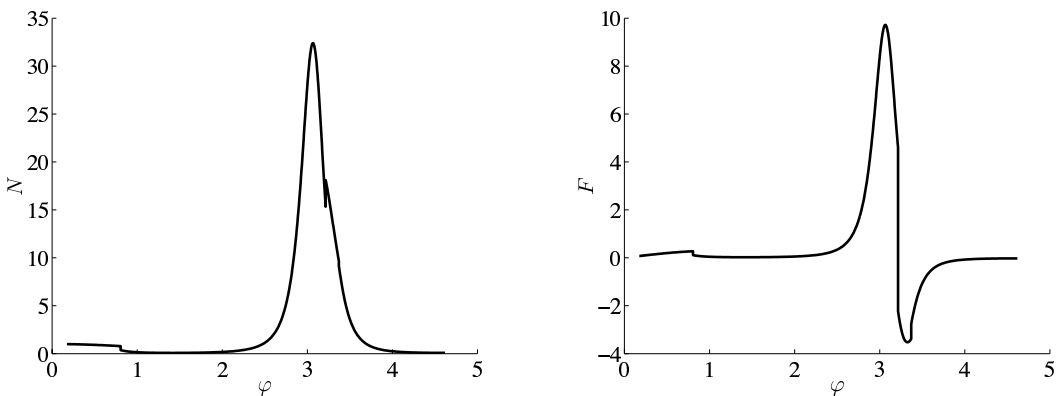


**Figure 7.** Left: Angle variation of the normal force (scaled by $mg$) during the first clockwise rotation of the hoop, in the case $k = 0.25$. Right: The corresponding friction force.

**3.3.** *The effects of the mass of the hoop.* In this subsection we present the results of calculations with the included mass of the hoop. The angle variation of the velocity of the contact point of the hoop and the horizontal surface (scaled by $\sqrt{Rg}$) during the first clockwise rotation of the hoop is shown in Figure 8, left (in the case $\varphi_0 = 10°$, $k = 0.1$, and $r = 1.02$). The dotted curve is for $m_h/m = 0$, the dashed curve is for $m_h/m = 0.01$, and the solid curve is for $m_h/m = 0.1$. Figure 8, right, shows a dramatic reduction of the magnitude of the corresponding normal force near $\varphi = \pi$ as the mass ratio $m_h/m$ increases from 0 to 1/10. Similar decrease is observed for the friction component of the force.

With the increase of the size of the disk, the ratio $J_h/J_m$ decreases. For example, if $r = 1.02$ and $\gamma_h/\gamma_m \approx 10^{-2}$, one finds from (20) that for $k = 0.25$ the mass and inertia ratios are $m_h/m = 0.0064$ and $J_h/J_m = 0.2048$ while for $k = 0.5$ these ratios are $m_h/m = 0.0016$ and $J_h/J_m = 0.0128$. In the latter case the rotational inertia of a light thin hoop can be reasonably ignored. The results for an infinitesimally thin massless hoop with a disk of radius $\rho = 0.75R$ were discussed in Section 3.2.

The variations of the normal and friction force in the case of equal mass densities of the hoop and the disk when $r = 1.02$ and $k = 0.1$ (giving rise to the mass ratio $m_h/m \approx 4.04$) are shown in Figure 9. In this case, the rolling prevails throughout the motion. The interaction pulse is mild with the greatly reduced magnitudes of the maximum normal and friction force ($N_{max} \approx 5.425mg$ versus the static normal force of $5.04mg$).

**3.4.** *The effects of the coefficient of friction.* The coefficient of friction affects the extent of rolling and rolling/sliding motion of the hoop as well as the magnitude of the reactions between the hoop and the horizontal surface. Figure 10, left, shows the angle variation of the velocity of the contact point of an infinitesimally thin massless hoop in the case $\varphi_0 = 10°$ and an exceedingly small disk ($k = 10^{-5}$) simulating a point mass. The dashed curve is for $\mu_s = 0.35$ and $\mu = 0.3$, while the solid curve is for $\mu_s = 0.7$ and $\mu = 0.6$. The extent of the initial rolling increases with the increase of the coefficient of friction. Figure 10, right, shows the behavior near $\varphi = \pi$. For $\mu = 0.3$ and $\mu_s = 0.35$ the interaction



**Figure 8.** Left: Angle variation of the velocity of the contact point of the hoop and the horizontal surface (scaled by $\sqrt{Rg}$) in the case $\varphi_0 = 10°$, $k = 0.1$, and $r = 1.02$, during the first clockwise rotation of the hoop. The dotted curve is for $m_h/m = 0$, the dashed curve is for $m_h/m = 0.01$, and the solid curve is for $m_h/m = 0.1$. Right: The corresponding variation of the normal force $N$ (scaled by $mg$) indicating a dramatic reduction of its magnitude near $\varphi = \pi$ with the increase of the mass ratio $m_h/m$.

**Figure 9.** Left: Angle variation of the normal force (scaled by $mg$) during the first clockwise rotation of the hoop in the case $r = 1.02$, $k = 0.1$ and the equal mass densities so that the mass ratio $m_h/m = 4.04$. Right: The corresponding friction force.

pulse is characterized by skidding to spinning to skidding transitions, while for $\mu = 0.6$ and $\mu_s = 0.7$ the pulse is characterized by skidding to slipping to rolling to skidding transitions. The horizontal distance traveled by the hoop before the sharp pulse and the final coordinates of the center of the disk at the end of the first clockwise rotation of the hoop are greater for the higher coefficient of friction. The mechanical energy at the end of the first clockwise rotation is also greater for the higher coefficient of friction ($E = 1.80266 \, mg$ for $\mu = 0.6$ versus $E = 1.38862 \, mg$ for $\mu = 0.3$) thus illustrating that in the two considered cases there is less dissipation due to friction in the case of a higher coefficient of friction. This is because the higher coefficient of friction in general promotes more rolling, which is the energy preserving motion in the absence of reactive rolling moment.

Figure 11 shows the variations of the normal and friction force during the first clockwise rotation of the hoop, in the case $r = 1.02$, $k = 0.1$, and $m_h/m = 0.1$, corresponding to four selected values of the friction coefficient. The maximum normal force is greatest in the case of the frictionless spinning
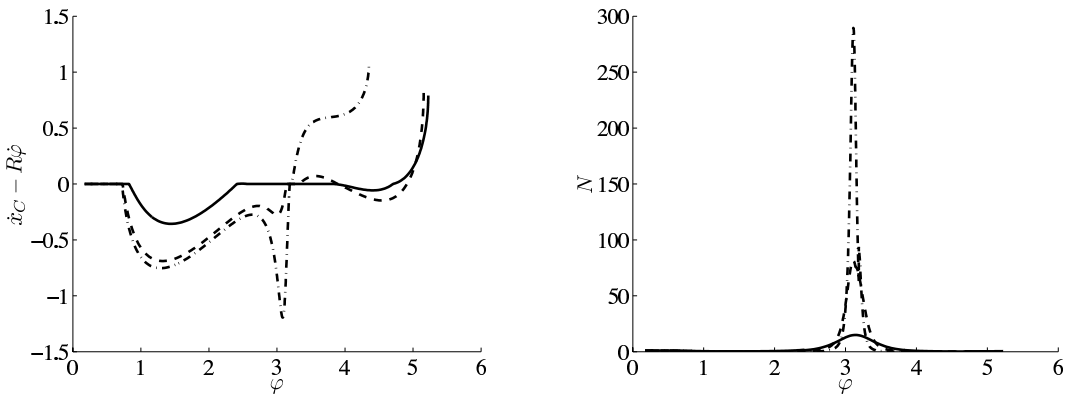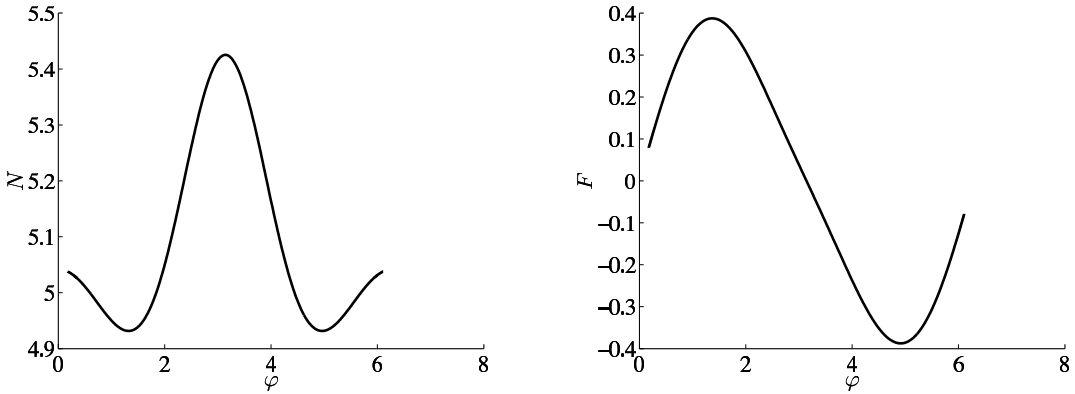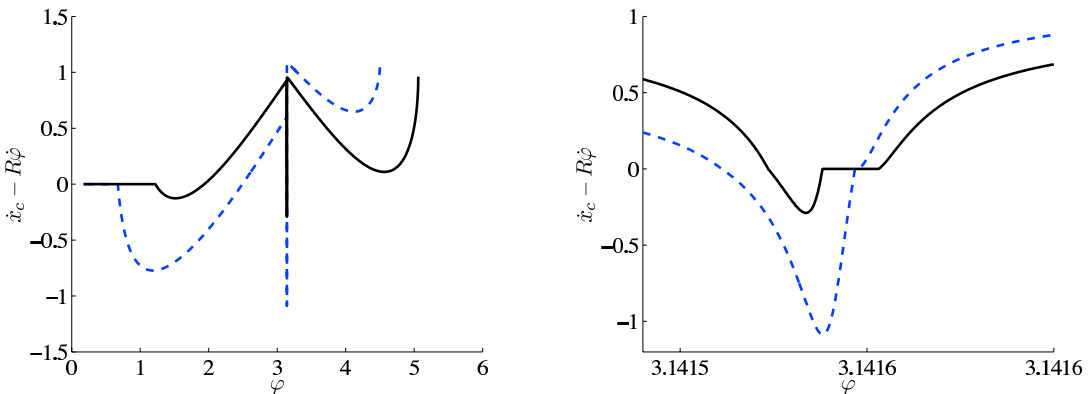


**Figure 10.** Left: Angle variation of the velocity of the contact point of the hoop and the horizontal surface (scaled by $\sqrt{Rg}$) in the case $k = 10^{-5}$. The dashed curve is for $\mu_s = 0.35$ and $\mu = 0.3$ while the solid curve corresponds to $\mu_s = 0.7$ and $\mu = 0.6$. Right: The same near $\varphi = \pi$.
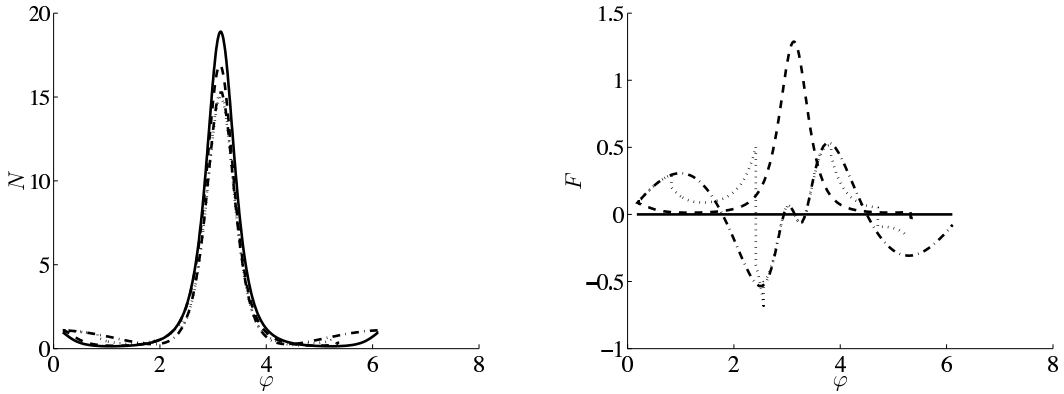
**Figure 11.** Angle variation of the normal force (left), and friction force (right), both scaled by $mg$, during the first clockwise rotation of the hoop with $k = 0.1$, $r = 1.02$, and $m_h/m = 0.1$. The solid curve is for $\mu = 0$, the dashed curve is for $\mu_s = 0.09$ and $\mu = 0.076$, the dotted curve is for $\mu_s = 0.35$ and $\mu = 0.3$, and the dotted/dashed curve is for $\mu_s = 1.2$ and $\mu = 1$.

($\mu = 0$, $F = 0$). The second selected value of the coefficient of static friction is twice greater than the minimum coefficient of static friction required for rolling at the inception of motion, calculated from (9). For the remaining two higher values of the coefficient of friction, it is found that the corresponding $N_{\max}$ is nearly the same, although for $\mu_s = 0.35$ and $\mu = 0.3$ the motion is characterized by the stages of rolling and combined rolling/sliding, while for $\mu_s = 1.2$ and $\mu = 1$ pure rolling prevails throughout the motion. The minimum coefficient of static friction required for the rolling to prevail throughout the motion of the hoop is about 0.78.

Figure 12 shows the corresponding variations of the square of the angular velocity $\dot{\varphi}^2$ and the angular acceleration $\ddot{\varphi}$ of the hoop, which explains the mild differences in the normal force for a sufficiently high coefficient of friction ($\mu = 0.3$ versus $\mu = 1$). The angular velocities and the angular accelerations are nearly the same in these two cases, and so are the corresponding normal forces. The friction forces are
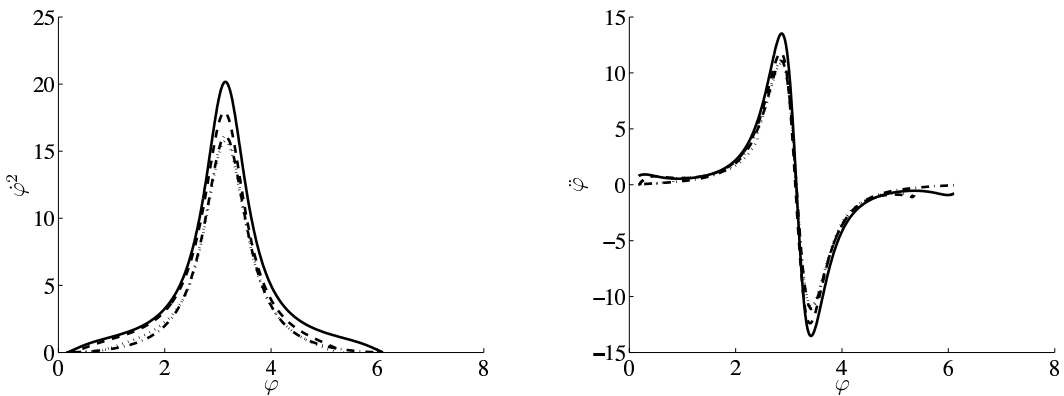


**Figure 12.** Angle variation of the square of the angular velocity (left), and the angular acceleration (right), both scaled by $g/R$, corresponding to Figure 11.

different, because they are proportional to the coefficient of friction during the combined rolling/sliding stages of motion.

There is an interval of rolling around $\varphi = \pi$ during which the friction force is almost the same for $\mu_s = 0.35$ and $\mu_s = 1.2$ being well below $0.35\,N$. This is because the angular velocities and the angular accelerations are almost the same in these two cases as are the reactive forces $N$ and $F$. Note that in Figure 12, left, the angular velocity $\dot{\varphi}$ does not depend on the coefficient of friction during the initial rolling stage of motion; only the extent of this rolling depends on $\mu_s$, so that the curves for $\dot{\varphi}^2$ depart from each other at different angles $\varphi = \varphi(\mu_s)$. Further analysis of the effect of friction on the motion of the loaded hoop can be found in [Theron and Maritz 2008].

## 4. Summary

In this paper we presented an analysis of motion of a light hoop with an attached heavy circular disk released to move on a rough horizontal surface. This motion involves a complex kinematics and kinetics, which reveal a variety of information of possible interest for the mechanics of frictional impact. When the radius of the disk is small relative to the radius of a light hoop, the motion is characterized by the sequence of sharp interaction pulses between the hoop and the horizontal surface during which several transitions between the stick, slip, and reversed slip can take place. This is accompanied by the corresponding changes in the friction force, which includes abrupt reversal of its direction, and rapid increase and discontinuous change of the normal component of the reactive force. The energy dissipation takes place predominantly during the short interaction pulses. The intensity of sharp interaction between the hoop and the horizontal surface, as well as the complexity of stick/slip transitions, diminish with the increasing size of the disk or the mass of the hoop. For sufficiently large disks, the rolling without transition to sliding prevails throughout the motion. The effects of the coefficient of friction on dynamic interactions, stick/slip transitions, and the energy dissipation are discussed. The analysis have demonstrated that the time integral of the tangential component of the interaction pulse is in general different from the product of the coefficient of kinetic friction and the time integral of the normal component of the interaction pulse, which is analogous to the nonproportionality of the normal and tangential impulses most commonly found in the mechanics of frictional impact. The obtained results may thus facilitate better understanding of the involved kinematics and kinetics of the latter problems in which the time variation of the normal and friction force during the impact process cannot be determined within the model of rigid body mechanics [Seifried et al. 2005; Lubarda 2009].

## Acknowledgment

## References

[Brach 1991] R. M. Brach, *Mechanical impact dynamics: rigid body collisions*, Wiley, New York, 1991.

[Brogliato 1999] B. Brogliato, *Nonsmooth mechanics*, Springer, London, 1999.

[Butler 1999] J. P. Butler, "Hopping hoops don't hop", *Amer. Math. Monthly* **106**:6 (1999), 565–568.

[Johnson 1985] K. L. Johnson, *Contact mechanics*, Cambridge University Press, Cambridge, 1985.

[Kane 1984]  T. R. Kane, "A dynamics puzzle", *Stanford Mechanics Alumni Club Newsletter* **6** (1984).

[Kane and Levinson 1985]  T. R. Kane and D. A. Levinson, *Dynamics: theory and applications*, McGraw-Hill, New York, 1985.

[Keller 1986]  J. B. Keller, "Impact with friction", *J. Appl. Mech.* (*ASME*) **53**:1 (1986), 1–4.

[Kilmister and Reeve 1966]  C. W. Kilmister and J. E. Reeve, *Rational mechanics*, Elsevier, New York, 1966.

[Littlewood 1986]  J. E. Littlewood, *Littlewood's miscellany*, edited by B. Bollobás, Cambridge University Press, Cambridge, 1986.

[Liu and Yun 2004]  Y. Liu and X. Yun, "Qualitative analysis of a rolling hoop with mass unbalance", *Acta Mech. Sinica* **20**:6 (2004), 672–675.

[Lubarda 2009]  V. A. Lubarda, "The bounds on the coefficients of restitution for the frictional impact of rigid pendulum against a fixed surface", *J. Appl. Mech.* (*ASME*) (2009). Accepted.

[Pritchett 1999]  T. Pritchett, "The hopping hoop revisited", *Amer. Math. Monthly* **106**:7 (1999), 609–617.

[Seifried et al. 2005]  R. Seifried, W. Schiehlen, and P. Eberhard, "Numerical and experimental evaluation of the coefficient of restitution for repeated impacts", *Int. J. Impact Eng.* **32**:1–4 (2005), 508–524.

[Stewart 2000]  D. E. Stewart, "Rigid-body dynamics with friction and impact", *SIAM Rev.* **42**:1 (2000), 3–39.

[Stronge 2000]  W. J. Stronge, *Impact mechanics*, Cambridge University Press, Cambridge, 2000.

[Theron 2000]  W. F. D. Theron, "The rolling motion of an eccentrically loaded wheel", *Amer. J. Phys.* **68**:9 (2000), 812–820.

[Theron 2002]  W. F. D. Theron, "The dynamics of an elastic hopping hoop", *Math. Comput. Model.* **35**:9-10 (2002), 1135–1147.

[Theron and du Plessis 2001]  W. F. D. Theron and N. M. du Plessis, "The dynamics of a massless hoop", *Amer. J. Phys.* **69**:3 (2001), 354–359.

[Theron and Maritz 2008]  W. F. D. Theron and M. F. Maritz, "The amazing variety of motions of a loaded hoop", *Math. Comput. Model.* **47**:9-10 (2008), 1077–1088.

[Tokieda 1997]  T. F. Tokieda, "The hopping hoop", *Amer. Math. Monthly* **104**:2 (1997), 152–154.

[Whittaker 1961]  E. T. Whittaker, *A treatise on the analytical dynamics of particles and rigid bodies: with an introduction to the problem of three bodies*, 4th ed., Cambridge University Press, Cambridge, 1961.

VLADO A. LUBARDA: vlubarda@ucsd.edu
*Department of Mechanical and Aerospace Engineering, University of California, San Diego, 9500 Gilman Drive,*
*La Jolla, CA 92093-0411, United States*

# DELAMINATION OF THIN COATINGS AT SCRATCHING: EXPERIMENTS AND NUMERICS

FREDRIK WREDENBERG AND PER-LENNART LARSSON

Scratching of thin coatings on hard substrates is studied experimentally and numerically, in the latter case by use of the finite element method. In particular the delamination behaviour at scratching, by increasing the normal load up to failure, is of interest. The adhesion of the coating to the substrate is modelled as a cohesive zone where relevant model parameters are determined experimentally using the double cantilever beam test with uneven bending moments (DCB-UBM). Good correlation between experimental and numerical results were achieved and the most important finding confirms the fact that the delamination behaviour was very much dependent on the critical energy release rate of the film/substrate interface. The results achieved are directly relevant for thin film polymer coatings but can also be applied in more general situations as a comprehensive parameter study is performed using the finite element method.

## 1. Introduction

Scratch testing is commonly used as a technique for studying mechanical properties of materials near their surface. In one of the earliest attempts to use scratching for characterisation, Mohs introduced his hardness scale [1824], in which materials were graded based on the capacity of a harder material to leave a visible scratch on a softer material if the two are rubbed against each other. The scratch test may also be used to test the adhesion of coatings, as is done throughout the coating industry. Typically then, a diamond stylus is drawn across a coated surface with increasing normal load until some well defined failure occurs and the critical load is achieved. This technique can be of substantial importance and is used for the ranking of coating adhesion. Furthermore the scratch test is used for tribological testing.

It is possible to distinguish between two main different types of scratching mechanism. The first one, which here is termed *mild* scratching, is when the behaviour does not involve or is not significantly influenced by any interface properties. If the material is sufficiently tough the scratch deformation will be governed by the bulk constitutive properties. The second type, termed *severe* scratching, occurs if the material toughness is sufficiently low and the formation of cracks takes place. Alternatively, when scratching of coatings is at issue, delamination occurs. Regarding the transition from mild to severe scratching, experimental results are presented in [Bertrand-Lambotte et al. 2002]. It appears likely, at least if no cracks develop, that the scratch process is very similar to conventional indentation testing and that thus can be well described by conventional material properties. In fact, scratch tests have been used to measure elastic and plastic properties [Xie and Hawthorne 2000].

Indentation testing and scratch testing, indeed, show many similar features. When it comes to indentation a great deal of knowledge has been gained over the years regarding the mechanical behaviour at

---

*Keywords:* scratching, finite element analysis, contact, delamination, cohesive zone, adhesion, thin film.

indentation. Sharp indenters are most often used, for practical reasons, at least when modern experimental devices such as the nanoindenter (or other types of instrumented indentation devices) are at issue. For such indenters semiempirical relations for material characterisation were derived and used already in the late 1940's and early 1950's, in particular for metals and alloys [Tabor 1951]. In short, from comprehensive experimental investigations Tabor derives a relation

$$H = C\sigma_{\text{repr}}, \tag{1}$$

between the indentation hardness $H$, here defined as the mean contact pressure at indentation and scratching, and the material yield stress $\sigma_{\text{repr}}$ at a representative value on the accumulated (effective) plastic strain, $\epsilon_{\text{p}} = \epsilon_{\text{repr}}$.

Based partly on these results, further progress was achieved by Johnson [1970; 1985], who showed from theoretical considerations that indentation testing (for example, indentation hardness $H$) on different materials can be well correlated by using a nondimensional parameter,

$$\Lambda = \frac{E \tan \beta}{(1 - \nu^2)\sigma_{\text{repr}}}, \tag{2}$$

where $E$ is Young's modulus, $\nu$ is Poisson's ratio and $\beta$ the attack angle as specified in Figure 1. Johnson's work also suggests that indentation properties for various materials will fall into one out of three levels as indicated in Figure 2. In short, these levels can be characterised as follows. In level I, $\Lambda \leq 3$, very little plastic deformation occurs during the indentation test and all global properties can be derived from an elastic analysis. In level II, $3 < \Lambda \leq 30$, an increasing amount of plastic deformation is present and both the elastic and the plastic properties of the material will influence the outcome of a hardness test according to [Johnson 1970; 1985].

Finally, in level III, $\Lambda > 30$, plastic deformation is present all over the contact area and elasticity no longer influences the hardness value of the material. This is also the region pertinent to most standard engineering metals, and it is also the region where the Tabor formula (1) applies. The indentation results presented in [Tabor 1951] and [Johnson 1970; 1985] have in previous years been verified (and also improved) by the use of finite element methods [Laursen and Simo 1992; Giannakopoulos et al. 1994; Laval 1995; Larsson et al. 1996; Mesarovic and Fleck 1999].
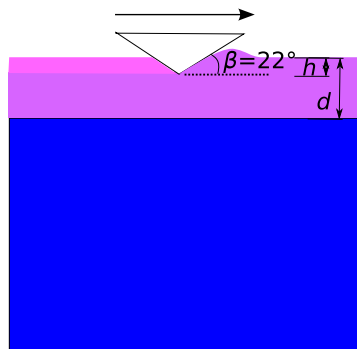


**Figure 1.** The stylus scratching the film at a depth of $h$. The film has thickness $d$ and the stylus has attack angle $\beta = 22°$.
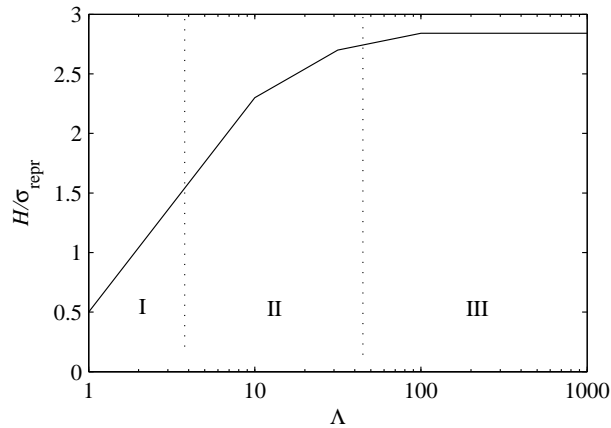
**Figure 2.** Sketch of the characteristic behaviour of indentation hardness [Johnson 1985]. The indentation hardness $H$ divided by the representative stress $\sigma_{\text{repr}}$ is plotted against the nondimensional strain parameter $\Lambda$.

In the same manner as for indentation testing, Bucaille et al. [2001] analyse cone scratching of perfectly plastic materials and their results also indicate that the Johnson parameter in (2) can, indeed, be used for the correlation of scratch parameters as well as indentation parameters. In the same reference the authors find, as could be expected, that the strain levels at scratching are much higher than at indentation, but this finding is not explored in connection with the concept of representative strains (as only perfectly plastic material behaviour is at issue).

Wredenberg and Larsson [2007] present a numerical approach for modelling the scratch test (from a mechanical point of view) using the finite element method. For one thing, these authors find that there exists a representative level of plastic strain of approximately 35% at frictionless scratching using a conical stylus with $\beta = 22°$. The corresponding stress level ($\sigma_{\text{repr}} = \sigma$ when $\epsilon_{\text{p}} = 35\%$) was used throughout our analysis when appropriate. Furthermore, as the scratch test is often used to determine characteristics of polymeric coatings, this is also under investigation [Briscoe et al. 1996; Gauthier et al. 2001]. It should be mentioned in this context that for polymers in particular, the Johnson parameter $\Lambda$ only gives a rough estimate of the deformation behaviour at scratching due to strain hardening effects in the material surrounding the stylus [Bucaille 2001; Bucaille et al. 2002; Hochstetter et al. 2003; Bucaille et al. 2004]. The representative strain value is of course also dependent on the conical angle and the material law. Due to the complexity of the boundary value problem at scratching, high accuracy of results can only be obtained if numerical methods, preferably the finite element method (FEM), are relied upon. Recently quite a few such analyses have been presented, and further progress based on FEM analyses of the scratch test has also been achieved in [Bucaille et al. 2004] for polymeric materials modelled by using standard elastoplasticity, corresponding to stage II rheology (see Figure 2).

When performing scratch experiments a number of phenomena may complicate the evaluations of the experiments. Estimating the scratch depth can prove arduous due to difficulties in detecting initial contact, at least when using a conical stylus. During scratching of polymeric materials, time dependence may come into effect [Briscoe et al. 1996], both during the actual scratching and afterwards when the

residual deformation is to be measured. Also at scratching of polymers, the deformation is to a great extent elastic, making the estimation of the actual contact area based on the residual groove complicated [Briscoe et al. 1996].

From a practical point of view, a very important aspect of scratching of thin film/substrate systems concerns delamination along the film-substrate interface. This matter has been rather extensively investigated for hard coatings but not so for soft films (perhaps the only exception being results in [Yueguang et al. 2002] pertinent to the "scraping" of a plastic lamella off a substrate). Possible reasons for this are the inherent difficulties associated with an analysis relating the delamination load to the elastic plastic deformation around the stylus. In this context, it was established as far back as [Benjamin and Weaver 1960] that the delamination load primarily depends on the properties of the interface between film and substrate, while Frey et al. [1994], for example, suggest that delamination can be determined by measuring the apparent coefficient of friction.

With all this in mind it seems desirable to perform an investigation of the delamination behaviour at scratching of soft thin films on hard substrates. This was also the aim of this study, where the delamination mechanism of thin polymeric films, undergoing large deformations and high levels of plasticity, was analysed numerically and experimentally. In doing so, when polymeric films are at issue, the deformation of the substrate was neglected for obvious reasons. A previously experimentally characterised vinyl ester plate [Wredenberg and Larsson 2009] was machined to a thin film and adhered to a steel substrate using an epoxy resin. This was done to minimise the residual stresses [Francis et al. 2002] and material property gradients intrinsic to the polymerisation of a film directly to the substrate. Additionally, this enabled testing of the mechanical properties of the film material in bulk, which can be difficult if the film material exists only in a "film state". Furthermore the scratch procedure was simulated numerically using the finite element method. In the simulations the adhesion of the film to the substrate was represented by a cohesive zone. The numerical simulation allowed for the variation of cohesive properties of the film substrate interface as well as for the mechanical properties of the film itself, resulting in a relatively extensive parametric study. The use of a cohesive zone model allows for the definition of a separation energy, $G_c$, necessary for the delamination of the film, as suggested by many authors for the case of elastic films [Bull 1991; Perry 1983; Malzbender and de With 2001].

We should note that a detailed description of the constitutive behaviour of the polymeric coating was not our highest priority, but rather the investigation of the fracture behaviour of the coating/substrate system.

## 2. Theoretical background

The present analysis is concerned with the scratching of thin film/substrate systems using a sharp conical stylus assumed to be rigid. It therefore seems appropriate to first of all introduce some basic quantities related to scratching. In the presentation below, $F$ and $A$ represent contact load and contact area, the indices $n$ and $t$ represent the normal and tangential components of these quantities, and $h$ is the scratch depth shown in Figure 1. It should also be mentioned that quasistatic conditions are assumed to prevail during the scratching process.

The hardness quantities of interest during scratching are the normal hardness,
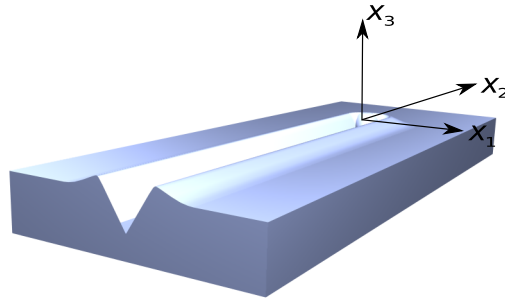
$$H_n = F_n/A_n, \tag{3}$$

**Figure 3.** Cartesian coordinates $x_i$ (following the tip of the stylus). Scratching is performed in the $x_2$ direction.

and the tangential hardness,

$$H_t = F_t/A_t. \tag{4}$$

During a scratch test on homogeneous materials, $H_n$, $H_t$, and the ratio $h/\sqrt{A}$ are constant, and stresses and strains are functions of the dimensionless variables $x_i/\sqrt{A}$ (the Cartesian coordinate system is shown in Figure 3) and material properties alone. This is of course not the case at scratching (or normal indentation) of thin film/substrate systems with increasing load, as the field variables then also depend on the ratio $h/d$, with $d$ being the film thickness as shown in Figure 1. However, when the indentation depth is held constant during the test, steady-state conditions prevail in the absence of cracking and the global quantities defined above are constant.

Another important parameter at scratching is the apparent coefficient of friction defined as

$$\mu_0 = \frac{F_t}{F_n}. \tag{5}$$

This parameter is also sometimes called the macroscopic coefficient of friction and will be discussed in relevant circumstances below.

In the present analysis, as indicated above, it was assumed that the material was adequately described by classical elastoplasticity. Despite this, the resulting boundary value problem became very much involved (particularly so when a film/substrate boundary was introduced into the problem), and it was necessary to use the finite element method in order to arrive at results of acceptable accuracy. The basic numerical scheme for an analysis of the corresponding homogeneous problem is developed in [Wredenberg and Larsson 2007], with characteristics for a thin films analysis being introduced in [Larsson and Wredenberg 2008]. This scheme was also closely adhered to in the present investigation, but obviously while also accounting for cracking using a cohesive zone model. The most important elements in the numerical approach are discussed in some detail below.

For the constitutive specification, the standard incremental rate-independent Prantl–Reuss equations for classical large deformation von Mises plasticity with isotropic hardening were used and formulated according to

$$\hat{\tau}_{ij} = \frac{E}{(1+\nu)}\left(\delta_{ik}\delta_{jl} + \frac{\nu}{(1-2\nu)}\delta_{ij}\delta kl - \frac{3\tau'_{ij}\tau'_{kl} - (E/(1+\nu))}{2\tau_e^2(\frac{2}{3}K + E/(1+\nu))}\right)D_{kl}. \tag{6}$$

In (6), $\delta_{ij}$ is the Kronecker identity tensor, $D_{ij}$ is the rate of deformation, and $\hat{\tau}_{ij}$ is the Jaumann rate of the Kirchhoff stress $\tau_{ij}$. The Kirchhoff stress is related to the Cauchy stress $\sigma_{ij}$ as $\tau_{ij} = J\sigma_{ij}$, where $J$ is the ratio of volume in the current state to volume in the previous state. Furthermore, $\tau_e$ and $\hat{\tau}_{ij}$ are the von Mises effective stress and deviatoric stress, respectively. Finally, $K$ is the instantaneous slope of the uniaxial compressive Kirchhoff stress. Note that (6) is only valid at plastic loading when $\tau_e = \tau(\epsilon_p)$, the initial yield stress being given by $\tau_Y = \tau(0)$. At elastic loading, or unloading, a hypoelastic formulation of Hooke's law, pertinent to the first part of (6), was relied on. Obviously, within this setting, kinematic hardening effects were not included in the analysis. Such effects can certainly influence the outcome of a scratch test but particularly so during the unloading sequence of the test. In this analysis, the loading part of the scratch test was of primary interest and for this reason, only isotropic hardening was considered.

The novelty of this investigation lies in the analysis of delamination between the film and the substrate. In its simplest form the criterion describing initial crack growth reads

$$G = G_c, \tag{7}$$

where $G$ is the total energy release rate and $G_c$ is the critical energy release rate at mode I crack propagation. However, it is well known that the delamination process can be severely influenced by mode mixity, and for this reason the more general criterion

$$G = G_c(\psi), \tag{8}$$

was used, as suggested in [Hutchinson and Suo 1991] for mixed mode crack propagation along a weak plane. This energy may then be allowed to vary depending on the mode of crack growth (mode I, mode II or a combination thereof). The mode mixity may be described by a parameter $\psi$ [Hutchinson and Suo 1991], defined as

$$\psi = \frac{2}{\pi} \arctan \frac{K_{II}}{K_I}. \tag{9}$$

Here $K_I$ and $K_{II}$ are mode I and II stress intensity factors, respectively. In the present study this dependence was investigated through the use of the double cantilever beam (DCB) loaded by uneven bending moments (UBM) as described in [Sørensen and Jacobsen 2003] and [Sørensen et al. 2006]. According to these investigations, the energy release rate may be calculated using the J-integral as

$$G = J = \frac{21(M_1^2 + M_2^2) - 6(M_1 M_2)}{4B^2 H^3 E}(1 - v^2), \tag{10}$$

assuming plane deformation and $|M_1| < M_2$ (see Figure 4). In (10), $B$ is the specimen width, $H$ the specimen height, $E$ the elastic modulus, and $M_1$ and $M_2$ the applied bending moments (see Figure 4). In this case (9) can also be expressed in terms of the bending moments [Sørensen et al. 2006] acting on the DCB as

$$\psi = \frac{2}{\pi} \arctan\left(\frac{\sqrt{3}}{2} \frac{M_1 + M_2}{M_1 - M_2}\right), \quad |M_1| < M_2. \tag{11}$$



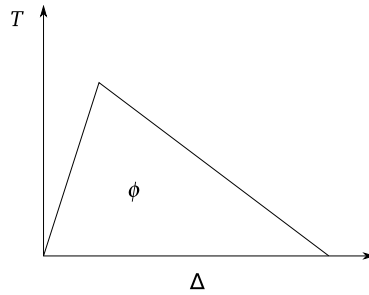**Figure 4.** Double cantilever beam with uneven bending moments.

**Figure 5.** Bilinear traction-separation cohesive law.

The DCB-UBM was chosen since it exhibits the attractive quality of the energy release rate being independent of the crack location, since the crack length is not present in (10); this makes it only necessary to measure the bending moments during the testing.

To be able to model the creation of a new surface with the accompanying separation energy at delamination of a film/substrate interface numerically, a cohesive zone model was used. Commonly the cohesive laws are defined through an interfacial potential $\phi$ with a traction vector $\boldsymbol{T} = (T_\text{n}, T_\text{t})$ acting on the cohesive surface [Xu and Needleman 1994; Needleman 1987; Ortiz and Pandolfi 1999] as

$$\boldsymbol{T} = \frac{\partial \phi(\boldsymbol{\Delta})}{\partial \boldsymbol{\Delta}}. \tag{12}$$

Here $\boldsymbol{\Delta} = (\Delta_\text{n}, \Delta_\text{t})$ indicates the separation of the surfaces. Generally, as the cohesive surfaces separate the traction will increase until a maximum is reached, after which it will decrease to zero, resulting in complete separation (see Figure 5). Consequently, the area under the curve is the energy needed for separation.

## 3. Experimental analysis

In conjunction with the scratch experiments, fracture mechanics experiments were conducted to determine the properties of the film/substrate interface. All experiments were performed at room temperature.

**3.1. *The scratch setup.*** Scratching experiments were performed by dragging a conical diamond (with the angle $\beta = 22°$) over the surface of a specimen, using a MTS 66202A-01 biaxial servohydraulic machine with an Instron 8500 control unit. The diamond stylus had a 20 $\mu$m tip defect. The normal forces were measured with a MTS load cell and the tangential forces were measured by a load cell built in-house. During the test the normal and tangential forces were recorded. The rotational motion of the actuator was transformed to a translational motion by a carriage sliding on a rail (see Figure 6). During scratching the normal load was linearly increased. After the scratching procedure the specimen was removed and the point of delamination (that is, the position on the specimen where the initial delamination occurred) was recorded and related to the corresponding load. The delamination load was found by measuring the point of initial delamination on the scratched specimen (see Figure 9 on page 1052). As the load was linearly increased during scratching, the delamination load could be found through linear interpolation of the applied scratch load.
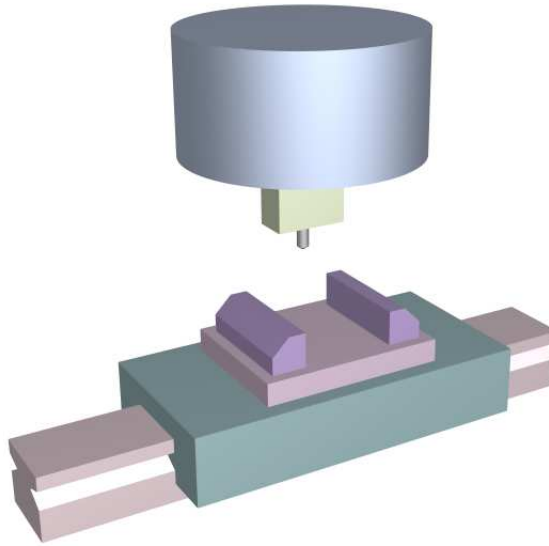
**Figure 6.** The experimental scratch setup with a carriage (green) sliding on a rail. Above are two force transducers (shear and normal). The specimen is placed in the vice (purple) in the center.

Scratch speeds of 1 mm/s and 0.1 mm/s over a total scratch length of 42 mm were used. The experimental results proved to be somewhat dependent on scratch speed (to be discussed in some detail below). Scratching was initialised at a normal load of 50 N and linearly increased to 150 N during the procedure.

**3.2. *Determination of cohesive parameters.*** In order to determine the mix-mode behaviour of the cohesive law, double cantilever beam specimens were prepared. The specimens were subsequently loaded with uneven bending moments to achieve an arbitrary mode-mixity, $\psi$ [Sørensen et al. 2006], as can be seen in Figure 4. The individual cantilever beams were machined to a length, width $B$ and thickness $H$ of 180 mm, 10 mm and 5 mm, respectively. The contribution of the film strip to the J-integral was assumed to be small as the stiffness of the steel part of the DCB was much larger, and the film strip was thin compared to the steel, thus allowing the energy release rate to be calculated according to (10). As an example, if the contribution of the film strips was taken into account for the case of $M_1 = 0$, this would result in a J approximately 2% larger. The maximum stresses ($\sigma_{\mathrm{max,n}}$ and $\sigma_{\mathrm{max,t}}$, to be discussed in some detail below; see Figure 8) in the cohesive law were determined by uniaxial tensile and pure shear tests, where the film was glued between two cylindrical steel bars. The bars were then either pulled apart (tensile) or twisted (shear) with increasing force until the film/steel interface failed. The shear test was set up in the same configuration as the DCB test, with pure bending moments so as to minimise the normal stresses introduced.

**3.3. *Preparation of specimens.*** The scratch specimens were composed of a steel substrate with a vinyl ester film adhered to it by means of an epoxy resin. Prior to adhesion to the substrate, the film was machined to a thickness of 0.9 mm from a thick slate of which bulk mechanical properties have already been investigated in [Wredenberg and Larsson 2009].

After the film was placed on top of the substrate, the specimens were vacuum bagged at 50 kPa and allowed to cure for 24 hours at 40° C. When completed, each specimen was approximately 25 mm wide by 55 mm long and 15 mm thick. The resulting adhesive layer was approximately 6 $\mu$m thick.

The DCB specimens were prepared in a similar fashion. Here two steel beams were adhered to a film strip by use of the same epoxy resin as used for the scratch specimen (see Figure 4). To allow for a well defined initial crack, the film strip and the steel beams were given a coat of wax covering the first two centimeters. These specimens were also vacuum bagged and allowed to cure in the same way as in the case of the scratch specimens. Here the resulting adhesive layer was approximately 8 $\mu$m thick.

The cylindrical specimens were pushed together by springs (as the shape of the specimen was not suitable for vacuum bagging), giving an adhesive thickness of approximately 5 $\mu$m after being cured for 24 hours at 40° C. In all specimens the film thickness was 0.9 mm.

## 4. Numerical analysis

A numerical analysis using the finite element method was performed with the aid of the commercial FEM package [ABAQUS 2008]. For details of the numerical analysis for homogeneous and film/substrate systems, see [Wredenberg and Larsson 2007; Larsson and Wredenberg 2008]; here we discuss only some basic features and details concerning the cohesive zone analysis. As already stated above, regarding the constitutive specification, the incremental rate-independent Prandtl–Reuss equations for classical large deformation von Mises plasticity with isotropic hardening was relied upon.

As the material experienced very large strains, adaptive meshing was used to maintain the element integrity. The mesh, shown in Figure 7, was composed of some 80000 eight-node linear reduced integration elements. These elements were chosen since they show a faster convergence with respect to mesh refinement than tetrahedral elements and do not have the inherent contact problems of quadratic elements [ABAQUS 2008]. The stylus was assumed to be perfectly rigid and Coulomb friction was assumed when appropriate. All of the results presented are pertinent to a perfectly sharp conical stylus. In order to ensure a relevant comparison between experimental and numerical results, experimental scratch depths were chosen in such a way that any influence from the stylus tip defect was negligible (as investigated carefully in each case through numerical simulations).

As regards boundary conditions, the surface outside the contact area was assumed traction free, and within the area of contact, unilateral kinematic constraints, given by the shape of the conical indenter/stylus depicted in Figure 1, were imposed.
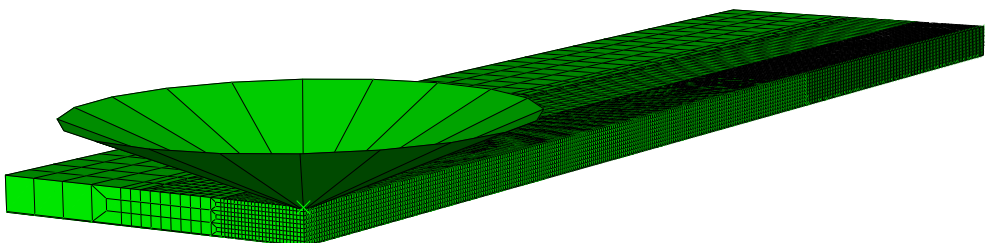


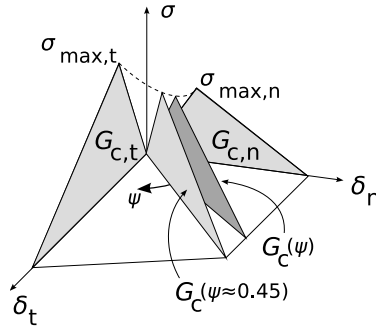**Figure 7.** Finite element mesh used in the simulations.

**Figure 8.** Sketch of the mixed mode cohesive law used in the numerical simulations. The critical energy release rate is labeled $G_c(\psi)$ and the maximum traction $\sigma_{max}$. $\delta$ indicate crack opening. The indices $n$ and $t$ indicate normal and shear respectively.

To account for the adhesive bond between the film and the substrate, 10000 cohesive elements with a traction-separation law were utilised (see Figure 8). The cohesive law used was defined by five parameters: the maximum cohesive stresses ($\sigma_{max,n}$ and $\sigma_{max,t}$) and the critical energy release rates for three levels of mode-mixity: $G_c(\psi = 0)$, $G_c(\psi \approx 0.45)$ and $G_c(\psi = 1)$. The damage initiation criterion (the dashed line in Figure 8) could be expressed as

$$\left(\frac{\sigma_n}{\sigma_{max,n}}\right)^2 + \left(\frac{\sigma_t}{\sigma_{max,t}}\right)^2 = 1, \tag{13}$$

where $\sigma_n$ and $\sigma_t$ are the tractions in the normal and shear direction respectively.

The cohesive elements were for numerical purposes given an initial stiffness (in tension/compression and shear) of 30 TPa/m, corresponding to the initial slope of the cohesive law. A study of the importance of this parameter on the delamination load can be seen in Table 1. From the table it can be concluded that any of the tested stiffness values would suffice. Ultimately the stiffness of 30 TPa/m was chosen as it allows reasonably large elements, and thus lower computational times, as a stiffer cohesive law requires a denser element mesh.

Delamination was said to occur when some cohesive element experienced more than 99% of accumulative damage, meaning that the cohesive deformation had passed the point of maximum traction and that the tractions were down to 99% of the maximum tractions of an undamaged element (see Figure 5). This choice was not of any real importance, but was made in order to avoid any numerical peculiarities involved in the case of a value being 100% accumulated damage. Indeed, changing this value to 100% would cause an indistinguishable change in the simulated delamination load.

| Stiffness (TPa/m) | 20 | 30 | 40 | 80 |
|---|---|---|---|---|
| Delamination load (N) | 87.8 | 88.6 | 88.5 | 87.8 |

**Table 1.** Influence of stiffness of the cohesive elements on the delamination load. (The last entry was computed with a higher mesh density.)

## 5.  Results and discussion

Below, the experimental and numerical results in this investigation are shown and analysed. Initially, the relevant experimental results (scratching and cohesive zone results) are presented and discussed. Then, the experimental results are compared with corresponding numerical ones. Such a comparison is certainly of substantial interest in itself but is presently also of interest in order to ensure the reliability of the numerical approach to, in particular, delamination at scratching of thin film/substrate systems. This feature is of direct importance in the present investigation as regards the accuracy of the results of the numerical parametric study included in this study (the presentation of the outcome of the parametric study constitutes the major part of this section of the paper).

**5.1.  *Experimental results.***  The normal load at which delamination of the vinyl ester film from the substrate occurred, $F_{\text{delam}}$, can be seen in Table 2, along with the normal scratch hardness $H_{\text{n}}$ of (3), at the two different scratch speeds. The hardness was evaluated at half of the scratch length, that is, the scratch width was measured right in the middle between the starting point and finishing point of the residual groove in order to avoid any influence from the specimen boundary. The projected contact area, $A_{\text{norm}}$, was calculated assuming a contact of semicircular shape, according to standard procedure at scratch testing [Williams 1996], as

$$A_{\text{norm}} = (w/2)^2 \, \frac{\pi}{2}, \tag{14}$$

where $w$ is the residual groove width. The delamination load data did not show a significant dependence on the scratch speed; see Table 2. When averaging all delamination loads regardless of scratch speed the delamination normal load reached the value 105 N (with a standard deviation of 12 N). The corresponding tangential load was found to be 28 N, which was in line with the measured apparent coefficient of friction ($\mu_0$) of 0.28, as will be discussed in some more detail below.

In Figure 9 two typical scratches can be seen along with the delamination of the film (the lighter area). All scratches experienced some cracking in the wake of the stylus as seen in Figure 10. The load at which these cracks formed varied from sample to sample. In around one third of the scratches, delamination occurred prior to the formation of the cracks shown in Figure 10. When investigating this phenomenon, no correlation between the formation of cracks and the delamination load could be found.

As regards the model parameters to be introduced in the numerical analysis, this mainly concerned the constitutive parameters pertinent to the vinyl ester film as well as the interfacial coefficient of friction $\mu_{\text{i}}$. The experimentally determined uniaxial stress-strain curve for the vinyl ester film-material is shown in Figure 11. The stress-strain curves in this figure were determined through compression tests of cylindrical specimens, with a length of approximately 5 mm. Some limited sensitivity to strain (deformation) rate effects were found, but as shown in Table 2 the delamination load is not influenced significantly. Again,

| Scratch speed (mm/s) | $F_{\text{delam}}$ (N) | $H_{\text{n}}$ (MPa) |
|:---:|:---:|:---:|
| 0.1 | 97.5 (8.3) | 367 (20) |
| 1.0 | 110 (11.1) | 365 (10) |

**Table 2.**  Experimental results for the delamination load $F_{\text{delam}}$ and the normal scratch hardness $H_{\text{n}}$ (standard deviation).
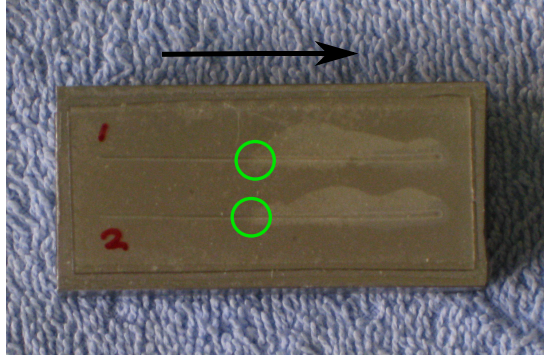
**Figure 9.** Delaminated scratch specimen with two scratches performed. The points of initial delamination are indicated by green circles. The scratch direction is indicated by the arrow.
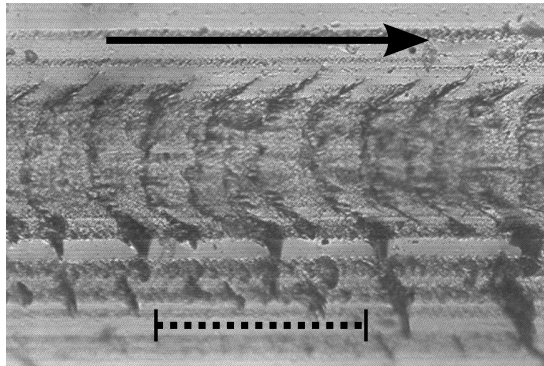


**Figure 10.** Cracks in the bottom of the scratch groove similar to the ones observed in [Browning et al. 2006; Holmberg et al. 2005]. The scratch direction is indicated by the arrow and the scale is given by the dashed line (0.25 mm). The scratch width was approximately 0.97 mm at this point.

we emphasise that the focus here was the fracture behaviour rather than a detailed description of the constitutive behaviour of the polymer.

Obviously this material exhibits softening after initial plastic deformation. Softening is then followed by extensive hardening, which could not be easily described constitutively as cracking then occurred during the tensile test (as well as barreling during a corresponding compressive test). This issue is discussed below. Furthermore, the uniaxial experiments indicate that the Johnson parameter $\Lambda$ of (2)) takes on the value 21 for vinyl ester. In [Wredenberg and Larsson 2007; 2009] master curves for the relation between $\Lambda$ and the ploughing part of the coefficient of friction, here denoted $\mu_p(\Lambda)$, are presented, and it can thus be concluded that $\mu_p(\Lambda) \approx 0.21$ here. The current measurements gave an apparent coefficient of friction of $\mu_0 \approx 0.28$, and remembering that the interfacial and ploughing friction may be separated as

$$\mu_0 = \mu_i + \mu_p(\Lambda), \tag{15}$$

**Figure 11.** Typical stress-strain curve of the presently analysed vinyl ester. Deformation rates: 0.0001 mm/s (continuous line) and 0.001 mm/s (dotted-dashed line).

for $\mu_i < 0.2$ [Wredenberg and Larsson 2007; Bowden and Tabor 1950; Goddard and Wilman 1962], it was concluded that the coefficient of interfacial friction $\mu_i$ was 0.07. Thi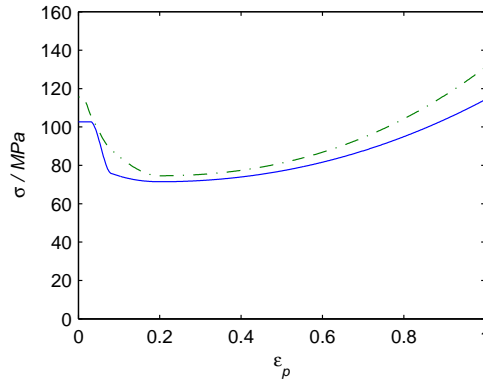s value was then used throughout the numerical simulations (in contrast to the situation at normal indentation [Carlsson et al. 2000], relevant local and global variables are quantitatively very much influenced by the presence of interfacial friction).

As regards the fracture mechanics results, double cantilever beam experiments were performed for three different bending moment ratios: $M_1/M_2 = -1$, $M_1/M_2 = 0$ and $M1/M2 = 1$, corresponding to mode mixities $\psi = 0$, $\psi \approx 0.45$ and $\psi = 1$; see (11). As seen in Figure 12, the critical energy release rate is substantially higher for pure mode II ($\psi = 1$) than for pure mode I ($\psi = 0$) loading. The maximum normal cohesive stress and maximum shear cohesive stress were found to be $\sigma_{\max,n} = 21$ MPa and $\sigma_{\max,t} = 27$ MPa respectively.

**5.2.** *Numerical results: comparison with experiments.* The numerical model described above was used in the present paper in order to perform a comprehensive parametric study regarding the influence from different parameters on the delamination load. In order to determine the reliability of the numerical approach a comparison between numerical and experimental results pertinent to vinyl ester was performed. Accordingly, corresponding values for delamination load and (normal) scratch hardness were compared. It was then assumed that quasistatic conditions prevailed, that is, that the uniaxial stress-strain relations were determined from experiments performed at such values of the strain rate that rate effects could be
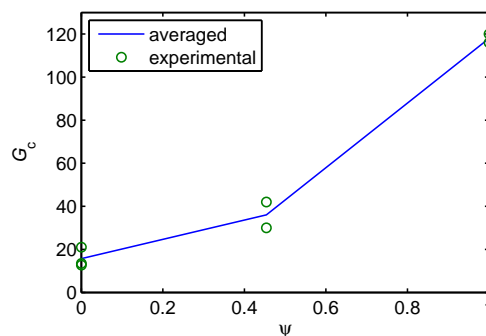


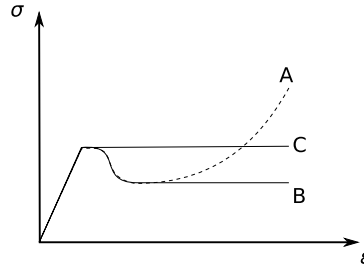**Figure 12.** Results from the critical energy release rate measurements.

**Figure 13.** Sketch of film stress-strain relations used in the numerical simulations.

neglected. In this context it should be mentioned that some small rate effects were noticed when the scratch experiments were performed at different speeds; see Table 2. As a comparison at quasistatic conditions were aimed at, the experimental results pertinent to a scratch speed being 0.1 mm/s were used for this purpose.

The shape of the stress-strain curve used in the numerical model deserves some further discussion. As mentioned, the material showed softening after initial deformation and then hardening, as seen in Figures 11 and 13 (material A). This indicates that the value of $\Lambda$ in (2) is approximately 21. However, as discussed above, the subsequent hardening could not be well described due to cracking (and barreling) during the uniaxial tensile test. For this reason the stress-strain behaviour was modelled, in the numerical simulations, using materials corresponding to curves B and C of Figure 13. Material B is described by no hardening after softening, while material C is an elastic-perfectly plastic material but with the elastic modulus adjusted in such a way that the value of $\Lambda$ was 21, as determined from the uniaxial experiments.

Remembering that both softening and hardening characterised the material it seems likely that these effects are represented "in average" by material C, and for this reason this material was singled out to be used in the numerical calculations when closeness to experimental conditions was to be investigated. A comparison between experimental and numerical results is shown in Table 3, where it should be emphasised that the hardness values reported correspond to the hardness for a homogeneous vinyl ester material. Obviously, the two sets of results are close and, remembering the difficulties involved in interpreting the outcome of the scratch/delamination experiments, this feature gives some definite confidence in the numerical procedure used in the present analysis, especially considering that qualitative effects are of primary importance to the parametric study (even though quantitative results also are of interest). It should be noted in passing that normal cone indentation of vinyl ester was also performed experimentally and numerically (material C), and that in this case the two sets of results were almost identical, which gives us further confidence in the numerical procedure.

|  | $F_{\text{delam}}$ (N) | $H_{\text{n}}$ (MPa) |
|---|---|---|
| Experimental | 97.5 (8.3) | 367 (20) |
| Simulated | 88 | 344 |

**Table 3.** Comparison of simulated and experimental results for the delamination load, $F_{\text{delam}}$, and the normal scratch hardness, $H_{\text{n}}$. (Standard deviation)

Finally in this context it should be emphasised that material C, in Figure 13, was used in the numerical simulations in the present comparison as this material was obviously more appropriate when reproducing the experiments. However, a polymer such as vinyl ester obviously exhibits softening after initial plastic deformation and in order to include this effect in the parametric study presented below it was thought advisable to use material B, in Figure 13, as a reference material in this study. It should be emphasised though that the exclusion of the strain hardening phenomenon renders the results less general.

### 5.3. *Numerical results: parametric study.*

In the present parametric study the numerical simulation of scratching of vinyl ester film (material B in Figure 13 in order to include features related to softening) was taken as a reference simulation. Interestingly, in this reference simulation (with the interfacial coefficient of friction being 0.07 as discussed above), the depth at which the delamination occurs is only $h/d \approx 0.16$, which means that the global scratch properties such as friction, hardness etc. are virtually unaffected by the presence of the substrate, according to [Larsson and Wredenberg 2008]. This is of course not the case for systems with tougher interfaces for which the stylus will penetrate further before delamination occurs, but definitely gives some further confidence regarding the assumption of a nondeformable substrate. Indeed a deformable substrate could easily be included in the calculations, but this requires a more comprehensive parametric study, which was not considered in this initial investigation. When appropriate in the presentation below, superscript "sim" and "meas" refer to the parameters used in the simulations and the parameters experimentally determined, respectively. A typical delamination shape is shown in Figure 14.

Initially an investigation of two extremes was made where the cohesive strength (the critical energy release rate $G_c$ and the maximum stress $\sigma_{max}$) in either normal or shear mode was set to infinity. As a result it was obvious that the delamination of the vinyl ester film was shear driven, as increasing the cohesive strength in the normal mode had no effect on the delamination load, whereas setting the cohesive strength in the shear mode to infinity led to an "undelaminable" interface.

The numerical study was started with an investigation of the influence from the critical energy release rate. A factor, $F_G$, defined as

$$G_c^{sim}(\psi) = F_G G_c^{meas}(\psi), \tag{16}$$

was used for this purpose. The results are shown in Figure 15 and it is very obvious that $F_G$ had a strong influence on the delamination load. In all figures concerning the delamination load, legends *normal* and
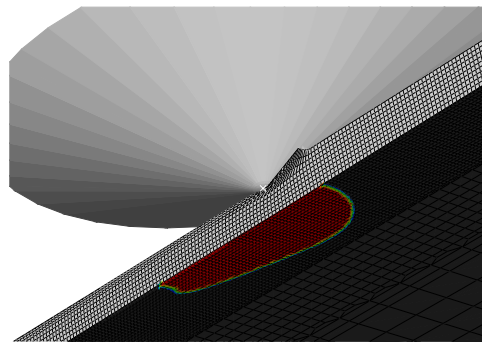


**Figure 14.** Simulated delamination of a vinyl ester coating (the red area is delaminated).
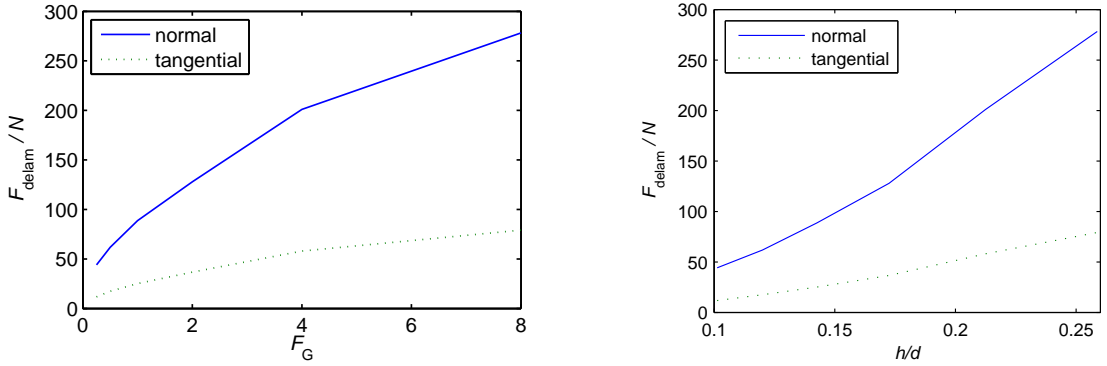
**Figure 15.** Left: delamination load as a function of the critical energy release rate factor $F_G$. The maximum cohesive stress is kept constant. Right; delamination load as a function of the scratch depth to coating thickness ratio, $h/d$.
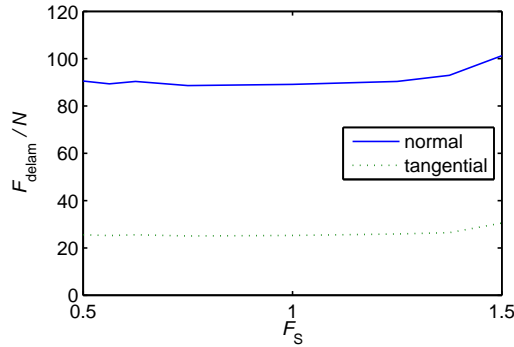


**Figure 16.** Delamination load as a function of maximum stress factor $F_S$. The critical energy release rate is kept constant.

*tangential* refer to the loads acting on the stylus normal to the scratched surface and along the scratched surface in the scratch direction, respectively. In the right half of the figure, the delamination load results from left half are plotted against the scratch depth at delamination to the coating thickness ratio, and the results give further confidence in the assumptions of a nondeformable substrate, as shown in [Larsson and Wredenberg 2008]. Even at the extreme value $h/d \approx 0.25$ substrate effects are very small.

Similarly, we introduced a maximum stress factor $F_S$, multiplying the maximum cohesive stress ($\sigma_{\max,n}$ and $\sigma_{\max,t}$) so that

$$\sigma_{\max,n}^{\mathrm{sim}} = F_S \sigma_{\max,n}^{\mathrm{meas}}, \tag{17}$$

$$\sigma_{\max,t}^{\mathrm{sim}} = F_S \sigma_{\max,t}^{\mathrm{meas}}, \tag{18}$$

while maintaining the same value on the critical energy release rate, in the cohesive law. From the left side of Figure 15 and from Figure 16 it may be concluded that the most influential cohesive parameter, as far as the delamination load is concerned, was the separation energy and to a much lesser extent the maximum cohesive stress.
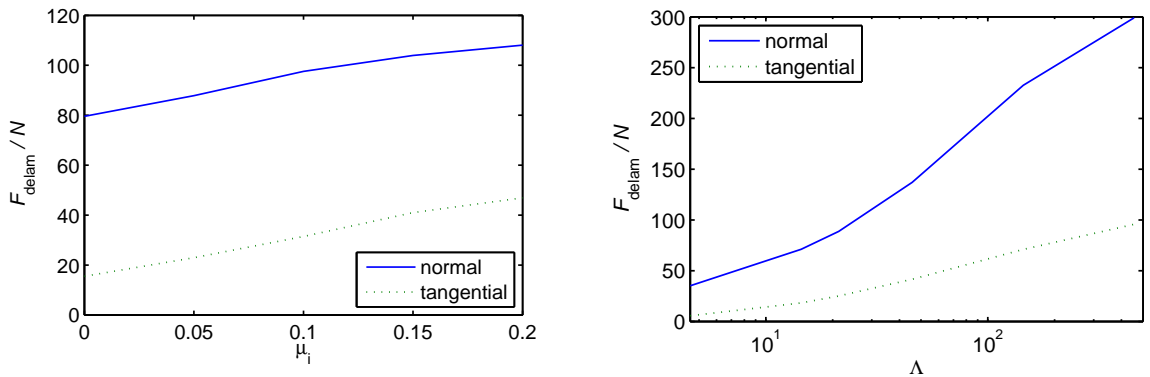
**Figure 17.** Delamination load as a function of the interfacial coefficient of friction $\mu_i$ (left) and of the parameter $\Lambda$ of (2) (right).

Since the interfacial coefficient of friction $\mu_i$ was expected to have a large impact on the delamination load, we performed simulations with varying $\mu_i$ (Figure 17, left). For moderate levels of the interfacial coefficient of friction ($\mu_i$), surprisingly little effect on the delamination load was seen, suggesting that frictionless simulations might suffice for most cases. This also indicates that no special regard need be taken to friction when performing scratch experiments in order to determine the adhesion of thin coatings. This certainly simplifies the evaluation of such experiments. As the interfacial friction coefficient $\mu_i$ was increased beyond $\approx 0.2$ — which was not the case for any of the scratched materials in [Wredenberg and Larsson 2007] — the material in front of the stylus would fold over on itself halting the simulation due to failing mesh integrity, in reality probably causing loss of material.

As in [Wredenberg and Larsson 2007; Larsson and Wredenberg 2008], it may be interesting to relate the delamination load to the Johnson parameter $\Lambda$ of Equation (2). In Figure 17, right, it can be seen how the delamination force monotonically increases with increasing $\Lambda$. This was most likely due to smaller penetration of the stress field into the film layer as the deformation is increasingly dominated by plasticity. Larsson and Wredenberg [2008] find that the global parameters at scratching are more affected by the substrate at low $\Lambda$.

Also the ploughing coefficient of friction at the occurrence of delamination showed very similar behaviour to that of homogeneous materials, as reported in [Larsson and Wredenberg 2008]; see Figure 18. In the figure, the ploughing coefficient of friction $\mu_p$ was calculated from the results in Figure 17, right, through the use of (15).

Furthermore a yield stress factor, $F_P$, was defined as

$$\sigma_Y^{\text{sim}} = F_P \sigma_Y^{\text{meas}}. \tag{19}$$

In (19), $\sigma_Y^{\text{sim}}$ is (with the notation adopted previously) the yield stress used in the simulations and $\sigma_Y^{\text{meas}}$ is the measured yield stress of the vinyl ester. As $F_P$ was varied, the elastic modulus of the film was adjusted in order to maintain the original $\Lambda$.

Lowering the yield stress will, as expected also lower the scratch hardness and subsequently increase the scratch depth. On the other hand, increasing the yield stress (as in Figure 19) will increase the hardness of the film and thus keep the region of high stresses away from the film/substrate interface,
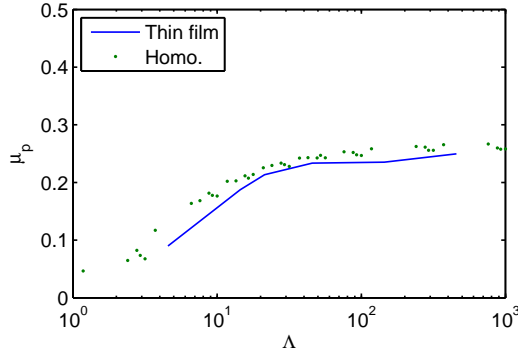
**Figure 18.** Ploughing coefficient of friction at delamination compared to results for homogeneous materials in [Larsson and Wredenberg 2008].
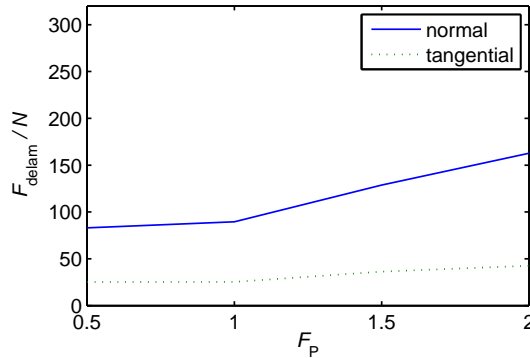


**Figure 19.** Delamination load as a function of yield stress factor $F_P$. The Johnson parameter $\Lambda = 21$. For values of $F_P < 0.5$ the film would not delaminate without the stylus actually scraping the substrate.

causing a higher delamination load. When simulating scratching with small values of $F_P$ ($< 0.5$) the film would not delaminate until the stylus actually scraped the substrate, at which state it may be expected that the stylus tip geometry greatly influenced the outcome of the test.

Since polymeric materials often display pressure sensitivity [Bubeck et al. 1984; Quinson et al. 1997; Rottler and Robbins 2001], this was investigated by means of a Drucker–Prager elastic-plastic material. The pressure sensitivity of a Drucker–Prager material is characterised by (together with the standard assumptions in von Mises plasticity) a parameter known as the *friction angle*, $\alpha$, allowing the yield stress to vary with the mean stress $\sigma_m$. The yield surface (see Figure 20) may then be described as

$$\sigma_e + \tan(\alpha)\sigma_m = \sigma_0, \tag{20}$$

where $\sigma_0$ is the yield stress at zero mean stress (pure shear) and $\sigma_e$ is the effective stress. A series of simulations was performed with different friction angles $\alpha$.

Figure 21 shows the delamination load as a function of this parameter. Experimentally, for the vinyl ester in question, the friction angle $\alpha$ was found to be very small (about 2°), well within the values tested in Figure 21. This indicates that this phenomenon did not significantly influence the results.
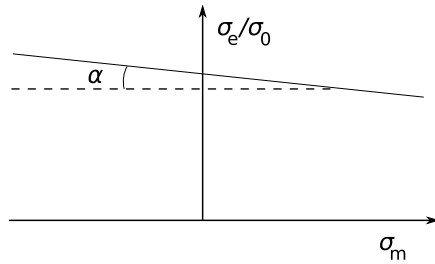
**Figure 20.** Sketch of the Drucker–Prager yield surface.
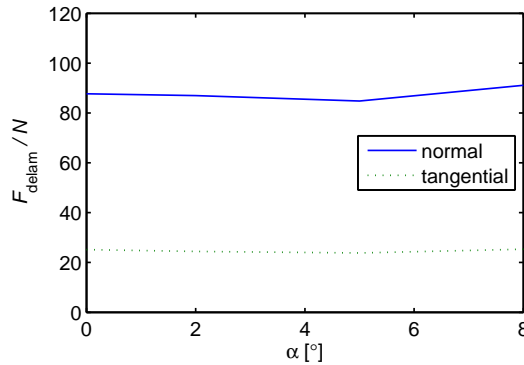


**Figure 21.** Investigation of the influence of pressure sensitivity (friction angle $\alpha$) on the delamination load.

As a final comment we stress that the present choice of attack on the delamination problem, using cohesive zone modelling, was based on the fact that such an analysis does not require a preexisting crack. An alternative direct attack on the delamination problem based on linear fracture mechanics, in the spirit of [Nilsson et al. 1993; Larsson 1991], for example, is of course also possible, but less accurate.

## 6. Conclusions

The present investigation is concerned with experimental and numerical analysis of scratching of thin polymeric films, and particularly with delamination behaviour. The most important results can be summarised as follows:

- The delamination resistance was in large part dependent on the critical energy release rate of the film/substrate interface and less on the maximum tractions of the interface.

- The influence of the coefficient of interfacial friction had only a limited effect on the delamination load.

- Increasing hardness and the Johnson parameter of Equation (2), both important scratch parameters, led to increasing delamination load.

- For moderate levels of pressure sensitivity (such as displayed by the vinyl ester tested in this paper) there was virtually no effect on the delamination load.

## Acknowledgements

## References

[ABAQUS 2008] *ABAQUS manual*, Version 6.7, Hibbit and Karlsson and Sorensen Inc., Pawtucket, RI, 2008.

[Benjamin and Weaver 1960] P. Benjamin and C. Weaver, "Measurement of adhesion of thin films", *Proc. R. Soc. Lond. A* **254**:1277 (1960), 163–176.

[Bertrand-Lambotte et al. 2002] P. Bertrand-Lambotte, J. L. Loubet, C. Verpy, and S. Pavan, "Understanding of automotive clearcoats scratch resistance", *Thin Solid Films* **420–421** (2002), 281–286.

[Bowden and Tabor 1950] F. P. Bowden and D. Tabor, *The friction and lubrication of solids*, Clarendon, Oxford, 1950.

[Briscoe et al. 1996] B. J. Briscoe, P. D. Evans, S. K. Biswas, and S. K. Sinha, "The hardness of poly(methylmethacrylate)", *Tribol. Int.* **29**:2 (1996), 93–104.

[Browning et al. 2006] R. L. Browning, G.-T. Lim, A. Moyse, H.-J. Sue, H. Chen, and J. D. Earls, "Quantitative evaluation of scratch resistance of polymeric coatings based on a standardized progressive load scratch test", *Surf. Coat. Technol.* **201**:6 (2006), 2970–2976.

[Bubeck et al. 1984] R. A. Bubeck, S. E. Bales, and H.-D. Lee, "Changes in yield and deformation of polycarbonates caused by physical aging", *Polym. Eng. Sci.* **24**:14 (1984), 1142–1148.

[Bucaille 2001] J. L. Bucaille, *Simulation numérique de l'indentation et de la rayure des verres organiques*, Ph.D. thesis, Écoles des Mines de Paris, 2001.

[Bucaille et al. 2001] J. L. Bucaille, E. Felder, and G. Hochstetter, "Mechanical analysis of the scratch test on elastic and perfectly plastic materials with the three-dimensional finite element modeling", *Wear* **249**:5–6 (2001), 422–432.

[Bucaille et al. 2002] J. L. Bucaille, E. Felder, and G. Hochstetter, "Identification of the viscoplastic behavior of a polycarbonate based on experiments and numerical modeling of the nano-indentation test", *J. Mater. Sci.* **37**:18 (2002), 3999–4011.

[Bucaille et al. 2004] J. L. Bucaille, E. Felder, and G. Hochstetter, "Experimental and three-dimensional finite element study of scratch test of polymers at large deformations", *J. Tribol.* (*ASME*) **126**:2 (2004), 372–379.

[Bull 1991] S. J. Bull, "Failure modes in scratch adhesion testing", *Surf. Coat. Technol.* **50**:1 (1991), 25–32.

[Carlsson et al. 2000] S. Carlsson, S. Biwa, and P.-L. Larsson, "On frictional effects at inelastic contact between spherical bodies", *Int. J. Mech. Sci.* **42**:1 (2000), 107–128.

[Francis et al. 2002] L. F. Francis, A. V. McCormick, D. M. Vaessen, and J. A. Payne, "Development and measurement of stress in polymer coatings", *J. Mater. Sci.* **37**:22 (2002), 4717–4731.

[Frey et al. 1994] N. Frey, P. Mettraux, G. Zambelli, and D. Landolt, "Modified scratch test for study of the adhesion of ductile coatings", *Surf. Coat. Technol.* **63**:3 (1994), 167–172.

[Gauthier et al. 2001] C. Gauthier, S. Lafaye, and R. Schirrer, "Elastic recovery of a scratch in a polymeric surface: experiments and analysis", *Tribol. Int.* **34**:7 (2001), 469–479.

[Giannakopoulos et al. 1994] A. E. Giannakopoulos, P.-L. Larsson, and R. Vestergaard, "Analysis of Vickers indentation", *Int. J. Solids Struct.* **31**:19 (1994), 2679–2708.

[Goddard and Wilman 1962] J. Goddard and H. Wilman, "A theory of friction and wear during the abrasion of metals", *Wear* **5**:2 (1962), 114–135.

[Hochstetter et al. 2003] G. Hochstetter, A. Jimenez, J. P. Cano, and E. Felder, "An attempt to determine the true stress-strain curves of amorphous polymers by nanoindentation", *Tribol. Int.* **36**:12 (2003), 973–985.

[Holmberg et al. 2005] K. Holmberg, A. Laukkanen, H. Ronkainen, and K. Wallin, "Tribological analysis of fracture conditions in thin surface coatings by 3D FEM modelling and stress simulations", *Tribol. Int.* **38**:11–12 (2005), 1035–1049.

[Hutchinson and Suo 1991] J. W. Hutchinson and Z. Suo, "Mixed mode cracking in layered materials", *Adv. Appl. Mech.* **29** (1991), 63–191.

[Johnson 1970] K. L. Johnson, "The correlation of indentation experiments", *J. Mech. Phys. Solids* **18**:2 (1970), 115–126.

[Johnson 1985] K. L. Johnson, *Contact mechanics*, Cambridge University Press, Cambridge, 1985.

[Larsson 1991] P.-L. Larsson, "On delamination buckling and growth in circular and annular othotropic plates", *Int. J. Solids Struct.* **27**:1 (1991), 15–28.

[Larsson and Wredenberg 2008] P.-L. Larsson and F. Wredenberg, "On indentation and scratching of thin films on hard substrates", *J. Phys. D Appl. Phys.* **41**:7 (2008), 074022.

[Larsson et al. 1996] P.-L. Larsson, A. E. Giannakopoulos, E. Söderlund, D. J. Rowcliffe, and R. Vestergaard, "Analysis of Berkovich indentation", *Int. J. Solids Struct.* **33**:2 (1996), 221–248.

[Laursen and Simo 1992] T. A. Laursen and J. C. Simo, "A study of the mechanics of microindentation using finite elements", *J. Mater. Res.* **7**:3 (1992), 618–626.

[Laval 1995] P. Laval, *Étude théorique et expérimentale de l'indentation des matériaux élastoplastiques homogènes ou revêtus*, Ph.D. thesis, Écoles des Mines de Paris, 1995.

[Malzbender and de With 2001] J. Malzbender and G. de With, "Analysis of scratch testing of organic-inorganic coatings on glass", *Thin Solid Films* **386**:1 (2001), 68–78.

[Mesarovic and Fleck 1999] S. D. Mesarovic and N. A. Fleck, "Spherical indentation of elastic-plastic solids", *Proc. R. Soc. Lond. A* **455**:1987 (1999), 2707–2728.

[Mohs 1824] F. Mohs, *Grundriss der Mineralogie*, Dresden, 1824.

[Needleman 1987] A. Needleman, "A continuum model for void nucleation by inclusion debonding", *J. Appl. Mech.* (*ASME*) **54**:3 (1987), 523–531.

[Nilsson et al. 1993] K.-F. Nilsson, J. C. Thesken, P. Sindelar, A. E. Giannakopoulos, and B. Storåkers, "A theoretical and experimental investigation of buckling induced delamination growth", *J. Mech. Phys. Solids* **41**:4 (1993), 749–782.

[Ortiz and Pandolfi 1999] M. Ortiz and A. Pandolfi, "Finite-deformation irreversible cohesive elements for three-dimensional crack-propagation analysis", *Int. J. Numer. Methods Eng.* **44**:9 (1999), 1267–1282.

[Perry 1983] A. J. Perry, "Scratch adhesion testing of hard coatings", *Thin Solid Films* **107**:2 (1983), 167–180.

[Quinson et al. 1997] R. Quinson, J. Perez, M. Rink, and A. Pavan, "Yield criteria for amorphous glassy polymers", *J. Mater. Sci.* **32**:5 (1997), 1371–1379.

[Rottler and Robbins 2001] J. Rottler and M. O. Robbins, "Yield conditions for deformation of amorphous polymer glasses", *Phys. Rev. E* **64**:5 (2001), 051801.

[Sørensen and Jacobsen 2003] B. F. Sørensen and T. K. Jacobsen, "Determination of cohesive laws by the *J* integral approach", *Eng. Fract. Mech.* **70**:14 (2003), 1841–1858.

[Sørensen et al. 2006] B. F. Sørensen, K. Jørgensen, T. K. Jacobsen, and R. C. Østergaard, "DCB-specimen loaded with uneven bending moments", *Int. J. Fract.* **141**:1–2 (2006), 163–176.

[Tabor 1951] D. Tabor, *Hardness of metals*, Clarendon, Oxford, 1951.

[Williams 1996] J. A. Williams, "Analytical models of scratch hardness", *Tribol. Int.* **29**:8 (1996), 675–694.

[Wredenberg and Larsson 2007] F. Wredenberg and P.-L. Larsson, "On the numerics and correlation of scratch testing", *J. Mech. Mater. Struct.* **2**:3 (2007), 573–594.

[Wredenberg and Larsson 2009] F. Wredenberg and P.-L. Larsson, "Scratch testing of metals and polymers: experiments and numerics", *Wear* **266**:1–2 (2009), 76–83.

[Xie and Hawthorne 2000] Y. Xie and H. M. Hawthorne, "A controlled scratch test for measuring the elastic property, yield stress and contact stress-strain relationship of a surface", *Surf. Coat. Technol.* **127**:2–3 (2000), 130–137.

[Xu and Needleman 1994] X.-P. Xu and A. Needleman, "Numerical simulations of fast crack growth in brittle solids", *J. Mech. Phys. Solids* **42**:9 (1994), 1397–1434.

[Yueguang et al. 2002] W. Yueguang, Z. Manhong, and T. Shan, "Characterization of the fracture work for ductile film undergoing the micro-scratch", *Acta Mech. Sinica* **18**:5 (2002), 494–505.

FREDRIK WREDENBERG: fredrik@hallf.kth.se
*KTH Solid Mechanics, Royal Institute of Technology, 10044 Stockholm, Sweden*

PER-LENNART LARSSON: pelle@hallf.kth.se
*KTH Solid Mechanics, Royal Institute of Technology, 10044 Stockholm, Sweden*

# MORPHOLOGICAL PROCESSING OF PROPER ORTHOGONAL MODES FOR CRACK DETECTION IN BEAM STRUCTURES

Konstantinos C. Gryllias, Ioannis N. Koukoulis, Christos T. Yiakopoulos, Ioannis A. Antoniadis and Christopher G. Provatidis

A two-step approach for crack detection in beam structures is presented. As a first step, a number of proper orthogonal modes (POMs) of a beam are extracted, using proper orthogonal decomposition, a powerful and elegant method (closely related to principal component analysis) aimed at obtaining low-dimensional approximations of high-dimensional processes, taking into account nonlinearities and minimizing noise effects.

Then, alternatively to other approaches, morphological processing is proposed for the further processing of the POMs. The basic concept of morphological processing is to modify the shape of an object by transforming it through its interaction with another object, called the structuring element. Using an appropriate morphological processing procedure, the position and the depth of the cracks can be estimated by isolating the sudden local change effect of the cracks on the spatial variation of the shape of each POM. For this purpose, the four basic morphological operators (dilation, erosion, opening, closing) are compared, using two different types of structuring elements. The erosion operator with a spline structuring element is shown to present the best results.

Finally, the performance of the method is assessed on different beam structures affected by breathing cracks, with respect to the influence of several factors, such as boundary conditions, crack location, crack depth, crack distance, measurement noise level and space resolution of measurement points. In all cases, the method presents a robust behavior.

## 1. Introduction

The presence of cracks in engineering structures, especially in aerospace, civil and mechanical engineering infrastructures, may lead to catastrophic failures with serious results (loss of lives, extensive downtimes, delays, etc). As a consequence, a plethora of analytical, numerical and experimental methodologies, approaches and techniques have been proposed for crack detection, focused on different types of structures including aircraft, civil infrastructures such as bridges and buildings, as well as laboratory specimens, such as beams and plates. Such work is reviewed, for example, in [Sohn et al. 2004; Doebling et al. 1998; Dimarogonas 1996; Randall 2002].

Damage can be defined by comparing different responses of a system, as they result from changes into its state, introduced as a result of the damage [Sohn et al. 2004]. A five-step damage state classification system was proposed in [Rytter 1993], examining the existence, location, type and extent of the damage, and lastly the possibility of a prognosis for the remaining useful life of the system. The presence of a crack in a structure introduces local flexibility and as a result, provokes changes at the dynamic behavior

of the structure. Therefore, a large number of methodologies for crack detection have been developed, based on detecting changes in various dynamic properties of the structure, such as natural frequencies, modal damping, mode shapes, transfer functions etc., as those changes result as a consequence of the damage.

The easiest, simplest and most popular method for damage detection is by identifying changes in natural frequencies. In a relevant pioneer paper [Lifshitz and Rotem 1969], the use of vibration measurements for damage detection is proposed. A methodology for damage detection, localization and quantification based on natural frequency shifts is proposed in [Cawley and Adams 1979]. In order to overcome difficulties related to natural-frequency-shifts-based crack detection, methodologies utilizing changes in mode shapes have been also proposed. A very interesting comparison between a frequency-based and a mode shape-based method for damage detection in beam like structures is presented in [Kim et al. 2003]. Changes in mode shapes are much more sensitive, compared to changes in natural frequencies. However, a crack may not influence the lower mode shapes, which are usually measured. Operational and environmental conditions, such as temperature, humidity, loads and boundary conditions may cause changes that hide those resulting from damage [Farrar et al. 1994; Cawley 1997].

In case of multiple cracks, additional issues are involved, such as orientation of cracks with respect to each other, change in mode shapes and complexity. In [Ostachowicz and Krawczuk 1991] the effect of positions and depths of two cracks on the natural frequency of cantilever beams is analyzed. The effect of crack depth and location on the eigenfrequencies of a double-cracked beam is studied in [Ruotolo and Surace 1997]. Among others, some very good reviews on analysis of structures under multiple cracks are presented in [Ruotolo and Surace 1997; Sekhar 2008].

Most of these works concerning cracks include a combination of analytical or computational models with experimental results [Alvandi and Cremona 2006; Wang and Deng 1999; Bamnios et al. 2002; Chang and Chen 2005; Douka et al. 2003; Loutridis et al. 2004; Hadjileontiadis et al. 2005a; Sahin and Shenoi 2003]. Among them [Alvandi and Cremona 2006] and [Sahin and Shenoi 2003] involve finite element models. As a result of the advanced capabilities of modelling methods such as FEM, substitution of the experimental procedure by appropriate FEM based computations and random noise addition has been proposed to simulate the experimental procedure [Luzzato 2003; Andreaus et al. 2007; Zhong and Oyadiji 2007; Galvanetto and Violaris 2007]. Additionally, in order to lead to a more reliable analysis, the practice of adding artificial noise to the analytical or numerical results has been also used [Alvandi and Cremona 2006; Hadjileontiadis et al. 2005b].

Concerning analytical models, as those are used particularly in beams with open cracks, the region of the crack was initially modelled as an area characterized by a reduced flexural rigidity [Rytter 1993], while later, the beam was simulated considering the area of the crack as a rotational spring [Wang and Deng 1999], [Bamnios et al. 2002; Chang and Chen 2005; Douka et al. 2003; Loutridis et al. 2004; Hadjileontiadis et al. 2005a; Hadjileontiadis et al. 2005b]. Additionally, an analytical model has been proposed [Douka et al. 2004] to model a plate with a transverse crack. However, considering the most appropriate modelling approach for a crack in a structure such as a beam, the presence of a crack causes the structure to exhibit a strongly nonlinear behavior, if the crack successively opens and closes ("breathes")@during the vibration. In order to take into account a breathing crack, beam models with bilinear spring-mass system have been developed [Luzzato 2003; Cheng et al. 1999; Loutridis et al. 2005; Douka and Hadjileontiadis 2005; Guo and Billings 2007]. These models mostly assume that the crack

is either open or closed; however there is at least one implementation of a continuous breathing crack model [Cheng et al. 1999]. Concerning the spectral effect of a breathing crack, it is generally considered [Luzzato 2003; Cheng et al. 1999] that the use of the breathing crack model is necessary, because in this case the natural frequency reduction is much smaller than that for an open crack case.

In this paper, an alternative approach for crack detection in structures is presented. As a first step, the proper orthogonal decomposition (POD) method is used, in order to obtain a number of the proper orthogonal modes (POMs) of a cracked cantilever beam. POD, closely related to principal component analysis, is a powerful and elegant method of data analysis aimed at obtaining low-dimensional approximate descriptions of high-dimensional nonlinear processes and eliminating noise effects [Lumley 1967; Azeez and Vakakis 1997; Lenaerts et al. 2001].

Then, alternatively to other approaches, morphological processing is proposed in this paper for analyzing the shape of the resulting POMs. The basic concept of morphological processing [Serra 1982; Maragos and Schafer 1987] is to modify the shape of an object, equivalently considered as a set, by transforming it through its interaction with another object, called the "structuring element". Using appropriate morphological processing, the position of the crack can be estimated by isolating the local sudden change effect of the crack on the spatial variation of each POM.

The rest of the paper is organized as follows. The method of proper orthogonal decomposition of structures is reviewed in Section 2 and the basic concepts of morphological processing of one-dimensional functions are reviewed in Section 3. A sensitivity analysis is performed is Section 4 between a 3D, a plain stress 2D and a plain strain 2D finite element modeling approach for a cantilever beam and as a result, the 2D plane stress model is shown to present the optimal behavior, providing the same actual level of accuracy with far less needed computational time. The four basic morphological operators (dilation, erosion, opening, closing) using two different types of structuring elements are compared in Section 5 and the erosion operator with a spline structuring element is shown to present the best results. Finally, the performance of the method is assessed on a cantilever beam in Section 6 and on a simple beam in Section 7, with respect to the influence of several factors, such as crack location, crack depth, crack distance, measurement noise level and space resolution of measurement points. In all cases, the method presents a robust behavior with respect to the determination of both the location and the depth of the crack.

## 2. Proper orthogonal decomposition (POD)

Proper orthogonal decomposition (POD) was first applied to turbulence problems by [Lumley 1967]. It identifies a useful set of basis functions and the dimension of the subspace necessary to achieve a satisfactory approximation of the system. It has been shown [Feeny 1997] that the application of POD to measured displacements of a discrete structure with a known mass matrix can lead to an estimation of the normal modes. The POD also facilitates the resolution of the partial differential equations through their projection into a reduced-order model [Azeez and Vakakis 1997] and for this reason it has been applied for vibro-impact systems.

**2.1.** *Mathematical formulation of the POD.* The POMs are shown here to be the eigenfunctions of the space correlation tensor. The definitions and formulation presented here follow closely the ones used in [Lenaerts et al. 2001]. Let $u(x, t)$ be a random field on some domain $\Omega$. Since the POD requires dealing

with zero-mean signals, it is necessary to define $v(x, t)$ by subtracting the mean $U(x) = \langle u \rangle$ from $v(x, t)$:

$$u(x, t) = U(x) + v(x, t). \tag{1}$$

These fields are sampled at finite number of points in time. Then, at a fixed time $t_n$ the system displays a snapshot $v_n(x)$, which is a continuous function on $\Omega$. The aim of the POD is to find the most representative structure $\phi(x)$ of the ensemble of $N$ snapshots. This is accomplished by minimizing the objective function (OF) $\lambda$:

$$\text{Minimize} \left\{ \lambda = \sum_{n=1}^{N} (\phi(x) - v_n(x))^2 \right\}, \quad \forall x \in \Omega. \tag{2}$$

Equation (2) means that the sum of the differences squared between $v_n(x)$ and $\phi(x)$ should be minimized and can also be written in terms of a maximization problem:

$$\text{Maximize} \left\{ \lambda = \frac{(1/N) \sum_{n=1}^{N} \left( \int_{\Omega} \phi(x) v_n(x) d\Omega \right)^2}{\int_{\Omega} \phi(x) \phi(x) d\Omega} \right\}, \quad \forall x \in \Omega. \tag{3}$$

In order to make the computation unique, we impose the orthonormality condition

$$\int_{\Omega} \varphi(x)^2 dx = 1. \tag{4}$$

Using the notation

$$(f, g) \equiv \int_{\Omega} f(x) g(x) d\Omega$$

for the inner product of $f$ and $g$, and

$$\langle v_n \rangle \equiv \frac{1}{N} \sum_{n=1}^{N} v_n(x)$$

for an average of snapshots, it turns out that the ensemble average of the inner products between $v_n(x)$ and $\phi(x)$ must be maximized:

$$\text{Maximize} \left\{ \lambda = \frac{\langle (\phi, v_n)^2 \rangle}{(\phi, \phi)} \right\}, \quad \forall x \in \Omega. \tag{5}$$

The numerator can be expanded to

$$\langle (\varphi, v_n)^2 \rangle = \frac{1}{N} \sum_{n=1}^{N} \left\{ \int_{\Omega} \varphi(x) v_n(x) dx \int_{\Omega} \varphi(x') v_n(x') dx' \right\}$$

$$= \int_{\Omega} \left\{ \int_{\Omega} \left( \frac{1}{N} \sum_{n=1}^{N} v_n(x) v_n(x') \right) \varphi(x) dx \right\} \varphi(x') dx'. \tag{6}$$

The two-point correlation function $K$ is defined as

$$K(x, x') = \frac{1}{N} \sum_{n=1}^{N} v_n(x) v_n(x'). \tag{7}$$

Hence, (6) becomes

$$\langle (\varphi, v_n)^2 \rangle = \int_\Omega \left\{ \int_\Omega (K(x, x')) \varphi(x) \, dx \right\} \varphi(x') \, dx'. \tag{8}$$

In view of (8) and (3), the optimization problem can be reduced to the integral eigenvalue problem

$$\int_\Omega (K(x, x')) \phi(x') \, dx' = \lambda \phi(x). \tag{9}$$

Equation (9) has a finite number of orthogonal solutions $\phi_i(x)$, called the POMs with corresponding real and positive eigenvalues $\lambda_i$. The eigenvalue with the largest magnitude is the maximum which is achieved in the maximization problem (5). The second largest eigenvalue is the maximum of the same problem restricted to the space orthogonal to the first eigenfunction, and so forth. In order to make the computation unique, the eigenfunctions are normalized. Therefore, the POMs can be used as a basis for the decomposition of the field $v(x, t)$:

$$v(x, t) = \sum_{i=1}^{N} \alpha_i(t) \phi_i(x). \tag{10}$$

Moreover, by construction, the POMs capture more energy than any other modes. It should also be noted that the time-dependent coefficients $\alpha_i(t)$ in Equation (10) are uncorrelated [Azeez and Vakakis 1997].

Thus, the POD can be viewed as a biorthogonal decomposition because of the space/time symmetry of the decomposition. For an accurate approximation of the tensor (7) it is necessary to perform a long and expensive simulation.

**2.2. *Discrete formulation.*** Suppose $N$ linear snapshots $v_i$ of size $M$ obtained for instance by measurements of the acceleration at $M$ locations. The $M \times M$ covariance matrix $C$ is defined as

$$C = \frac{1}{N} \sum_{i=0}^{N-1} v_i v_i^T. \tag{11}$$

Its eigensolutions $(\phi_k, \lambda_k)$, which satisfy

$$C \phi_k = \lambda_k \phi_k, \quad k = 0, \dots, N-1, \tag{12}$$

with

$$\lambda_0 \geq \lambda_1 \geq \cdots \geq \lambda_{N-1} > 0, \tag{13}$$

characterize the proper orthogonal decomposition. Each eigenvector $\phi_k$ is associated with an eigenvalue $\lambda_k$. If the eigenvalues are normalized, they represent the relative energy captured by the corresponding POM. This decomposition is the best basis in terms of decorrelation. The brute computation of the eigensolutions of $C$ is called the *direct method*. However, due to the space-time symmetry property, an alternative method, called the *method of snapshots*, can be employed.

**2.3. *Computation of the POD using SVD.*** The complete biorthogonal decomposition of the data may be obtained by the use of the SVD. Let $x_i(t)$ denote a response time history, where $x$ is a vector containing

the displacement, velocity or acceleration at $M$ discrete locations. We form the discrete matrix

$$X = \begin{bmatrix} x_1(t_1) & \cdots & x_1(t_N) \\ \vdots & \ddots & \vdots \\ x_M(t_1) & \cdots & x_M(t_N) \end{bmatrix}. \tag{14}$$

Thus, each row corresponds to a time history at one location and each column corresponds to a snapshot of the system at a specific time. Now, the singular-value decomposition of matrix $X$ can be written as

$$X = U \Sigma V^T \tag{15}$$

with $U$ denoting an orthonormal matrix (size $M \times M$) of eigenvectors of $XX^T$ and $V$ an orthonormal matrix (size $N \times N$) of eigenvectors of $X^T X$. The size of the matrix $\Sigma$ is $M \times N$ but only the main diagonal has non-zero elements which are the singular values of $X$, sorted in descending order. If the matrix $X$ is rank deficient, i.e. some rows (or columns) can be generated by a linear superposition of the others, a few singular values will be zero. The SVD has a lot of applications, e.g. the estimation of the rank of a matrix, the filtering of measurement noise and so forth. In this paper, the aim of the SVD is to compute the POMs and the normalized basic shapes including the response time histories.

## 3. Basic concepts of morphological processing of one-dimensional functions

Mathematical morphology (MM) was at first introduced as an image-processing method, based on set theory [Serra 1982; Maragos and Schafer 1987]. Since the key element in MM is the set, MM uses nonlinear set processing transformations, starting with two basic operations, Minkowski addition and Minkowski subtraction, based on which a number of morphological operators can be constructed. The basic concept of morphological processing is to use these operators in order to modify the shape of an object, which is considered as a set, by transforming it through its interaction with a second object, called the *structuring element*. The structuring element practically is compact and has a simpler shape compared to the original object.

Limiting for simplicity purposes the application of MM in one-dimensional functions (signals), two different and equivalent approaches in representing functions by sets can be used, in order to apply the set based MM operations.

The first uses the concept of the cross-section of a function, defined as

$$X_t(f) = \{x \in D : f(x) \geq t\}, t \in V, \tag{16}$$

where $f(x)$ is the function under consideration, $D$ is the domain of definition of $f(x)$ over the set $Z$ of integers or the set $R$ of real numbers, $V$ is the range space of $f(x)$, and $t$ is a specified threshold. A graphical presentation of the cross section of a function is shown in Figure 1, left.

Provided practically that the function $f(x)$ is continuous with some possible positive jumps (upper semicontinuous function), then its cross-sections form a sequence of sets which allow the reconstruction of the function as follows [Serra 1982]:

$$f(x) = \sup\{t \in R : x \in X_t\}. \tag{17}$$
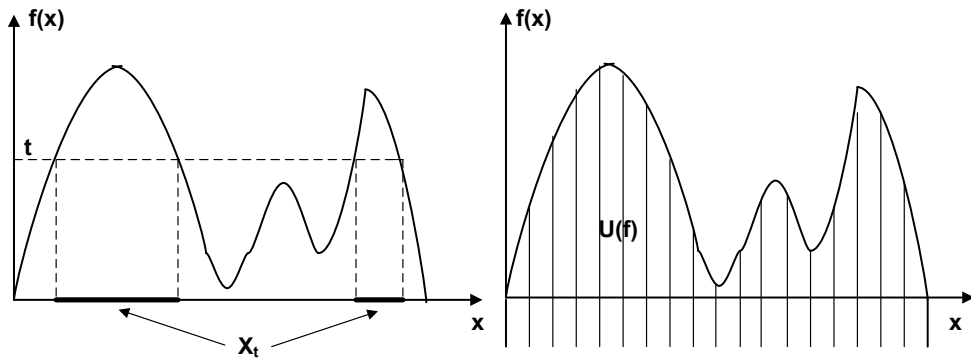
**Figure 1.** Graphical representation of the cross section $X_t(f)$ and of the umbra $U(f)$ of a function $f(x)$.

The second approach uses the umbra $U(f)$ of the function, represented in Figure 1, right. This is a set $U$ defined in the Cartesian plane by

$$U = \big\{(x,t) : t \le f(x)\big\} = \big\{(x,t) : x \in X_t(f)\big\}$$
$$= \big\{(x,t) : w(x,\alpha) \in U, \ \forall \alpha < t\big\}. \tag{18}$$

The function $f(x)$ can be reconstructed from its umbra:

$$f(x) = \sup\{t \in R : (x,t) \in U(f)\}. \tag{19}$$

Since, according to these definitions, signals can be linked to sets, morphological filtering [Maragos and Schafer 1987] proceeds to the modification of their geometrical characteristics by morphologically processing the signal with another signal or function, called the *structuring element*, which in practice is compact and of a simple shape. Thus a morphological filter is a set mapping operation, which must satisfy four basic requirements: translation invariance, scale invariance, dependence only on the local features of the signal, and upper semicontinuity (meaning that values for arguments near $x$ cannot be far above the value at $x$, though they can jump down).

Using the equivalent cross-section or umbra representation of a function by sets, Minkowski addition and subtraction between two functions can be defined as

$$(f \oplus g)(x) = \sup_{y \in D}\{f(y) + g(x-y)\}, \qquad (f \ominus g)(x) = \sup_{y \in D}\{f(y) - g(x-y)\}. \tag{20}$$

Here $D$ can be arbitrary, but for practical applications we may assume that $D$ is a compact subset of the real line $\mathbb{R}$ or of the integers $\mathbb{Z}$, containing the support of the function $f(x)$. Using the operations in (20), the four basic morphological operations are defined as

$$\text{Dilation, dil}(f,g): \quad (f \oplus g^r)(x) = f(x) \oplus g(-x) = \sup_{y \in D}\{f(y) + g(y-x)\}, \tag{21}$$

$$\text{Erosion, er}(f,g): \quad (f \ominus g^r)(x) = f(x) \ominus g(-x) = \inf_{y \in D}\{f(y) - g(y-x)\}, \tag{22}$$

$$\text{Closing, cl}(f,g): \quad (f \bullet g)(x) = [(f \oplus g^r) \ominus g](x), \tag{23}$$

$$\text{Opening, op}(f,g): \quad (f \circ g)(x) = [(f \ominus g^r) \oplus g](x), \tag{24}$$

where $g^r(x)$ denotes the reflected (symmetric) function of $g(x)$ with respect to the origin of the $x$-axis. These four operations are translation invariant. Opening and dilation are extensive, while erosion and closing are nonextensive operations. Opening and closing are also idempotent operations. For further properties of morphological operations, like distributivity, serial and parallel composition, separability, existence of fixed points, and invertibility, see [Maragos and Schafer 1987].

Compared to the classical linear convolution $f * g$ operation between the two functions $f(x)$ and $g(x)$, the Minkowski addition and subtraction operations of functions can be alternatively defined as nonlinear morphological convolutions, in which the multiplication between the two functions is replaced by summation or subtraction and the summation or integration of the result is replaced by the max or min operations. A similar remark holds for linear correlation, if the reflected function $g^r(x)$ is used, instead of $g(x)$.

However, the nonlinearity of the dilation and the erosion operators results in important differences between these signal operations and the traditional linear convolutions; for instance, serial interconnections of dilations and erosions lead to entirely different nonlinear systems. Thus, there is an infinite variety of nonlinear operators created by cascading dilations and erosions via max, min, addition or subtraction. A thorough treatment of the relations between linear and morphological filtering operations is developed in [Maragos and Schafer 1987], leading to an equivalent representation of the morphological filters above in terms of linear filters. Equations (21)–(24) can be significantly simplified if $g(x)$ is an even function and if sampled functions are used. For a signal $f(k)$, defined over a domain $D_f$, and for a function $g(u)$ of length $L$ over a domain $D_g$, called the structuring element, the dilation and the erosion of the signal $f(k)$ by the element $g(u)$ are defined as

$$\text{dil}(k) = (f \oplus g)(k) = \max_{y \in Dg}\{f(k+u) + g(u)\}, \tag{25}$$

$$\text{er}(k) = (f \ominus g)(k) = \min_{u \in Dg}\{f(k+u) - g(u)\}. \tag{26}$$

Similarly, based on erosion and dilation, the closing and the opening operations of the signal $f(k)$ by the element $g(u)$ are further defined as

$$\text{cl}(k) = (f \bullet g)(k) = \text{er}(\text{dil}(k)), \tag{27}$$

$$\text{op}(k) = (f \circ g)(k) = \text{dil}(\text{er}(k)). \tag{28}$$

The geometrical interpretation of these four basic morphological operations for functions can be directly derived by the one used for sets, if the umbra or the cross-section analysis of functions is used. For example, the umbra of the opening is the union of all the translates of the umbra of the structuring element, which can "fit inside" the umbra of the original function.

An example of the application of the four morphological operators to a signal is presented in Figure 2. The erosion of the signal presents a tendency to smooth the abrupt variations of the signal by eliminating the abrupt positive peaks of the signal and enlarging the area around the abrupt negative peaks. The dilation operation leads again to a smoother form of the signal, however this time by "filling" or "dilating" the signal in the areas around the positive peaks. The opening operator eliminates only the positive peaks, while the closing operator eliminates only the negative peaks.
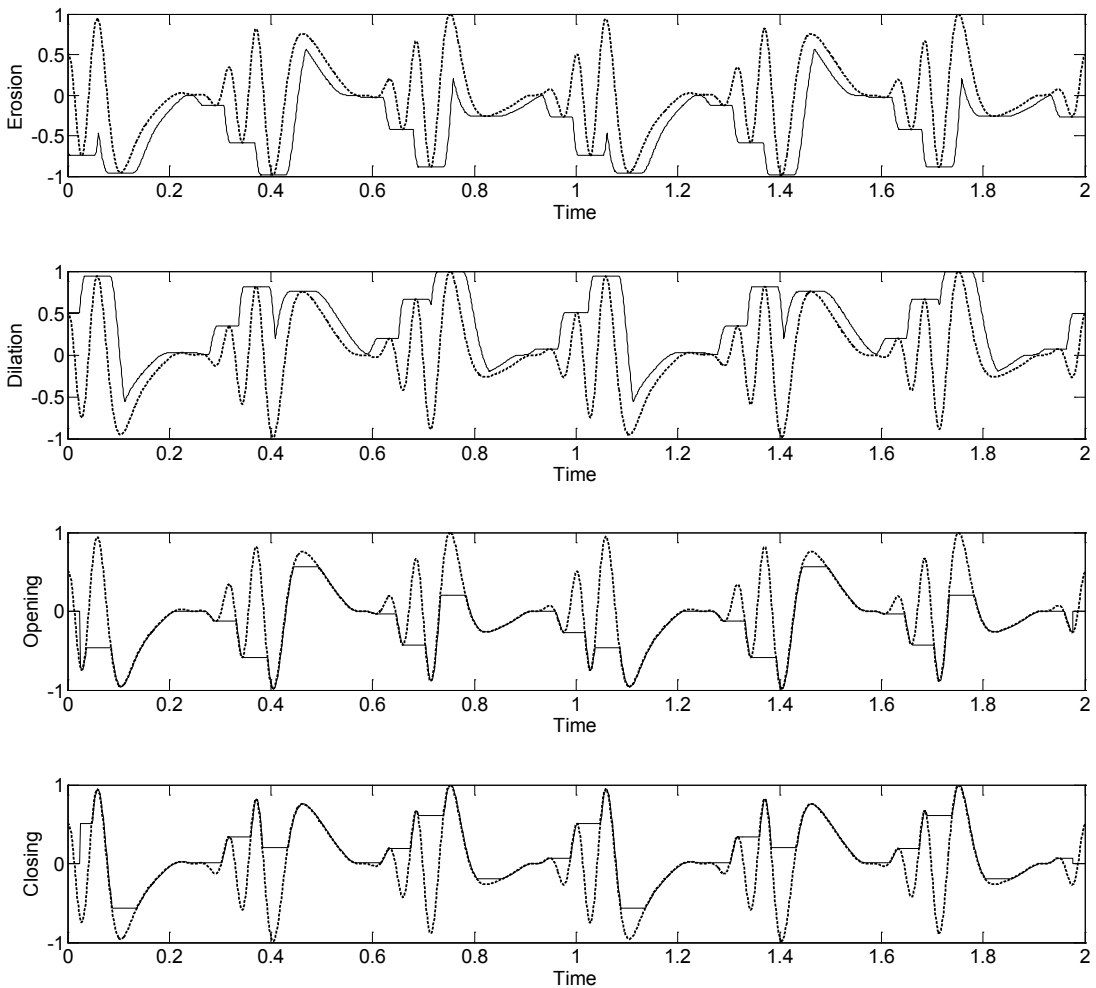
**Figure 2.** Results of applying the four basic morphological operations to a function (thick dotted line), using a flat structuring element. The thin continuous line is the signal after the operation.

## 4. Finite element modelling procedure

In order to select an appropriate FEM model to be subsequently used, a comparison is performed between a plane strain 2D model, a plane stress 2D model and a 3D model. The purpose of the analysis is to estimate if the results obtained by an appropriate 2D model can reach the accuracy of a significantly more CPU time consuming 3D model. The analysis includes (I) the healthy structures, (II) an open crack case, (III) a breathing crack case. In the particular case of a breathing crack, contact analysis is performed. All models have been developed in ANSYS 10.0 finite element code.

A clamped cantilever beam of length $l = 300$ mm, of uniform square cross-section $w \times w = 20 \times 20$ mm$^2$, with a breathing crack located at $l_c = 150$ mm measured from the clamped end, is considered. The crack has a uniform depth $d = 4$ mm (Relative crack depth $\alpha = d/w = 0.2$ i.e. 20%). The material
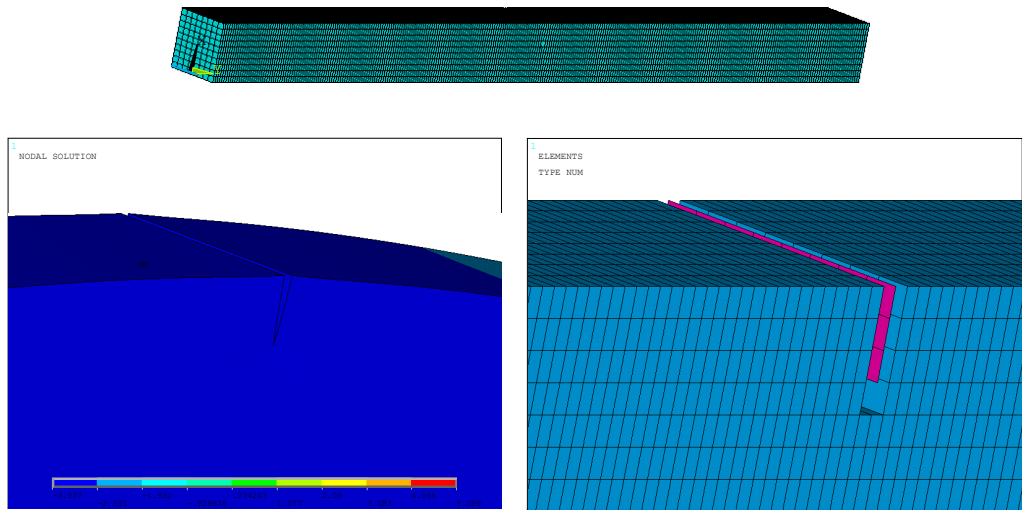
**Figure 3.** Top: full view of the 3D finite element model. Bottom: zoom of the model in the area of the crack.

properties of a typical Plexiglas material have been considered. The beam is excited by a lateral impact load of 2 MPa uniformly imposed along the vertical free edge, thus causing the crack to open and close.

The finite element mesh consists of 300 subdivisions along the length $l$ and 10 along the other two edges ($w$) of the cross-section, as shown in Figure 3. The 3D model is built of 8-node solid elements (SOLID45), while on the area of crack surface contact elements were used. The 2D models are built of 4-node elements (PLANE42) in plane stress and plane strain mode. In the case of a breathing crack, line contact elements are used.

First, the natural frequencies for the healthy structure and for the structure with the open crack are calculated. The results are presented in Table 1. As can be noticed, the plane stress model presents an excellent agreement with the 3D model, resulting in less than 0.5% underestimation. On the other hand, the plane strain model results in a natural frequency overestimation of more than 8% with respect to the 3D model. These results do not change essentially when the mesh density is doubled.

In the case of a breathing crack, transient response analysis is performed. The sampling frequency (inverse of the time step) is chosen as 10 KHz and the total time of the analysis as 0.1 s. No damping is

| | Beam without crack | | | Beam with an open crack | | |
|------|------|------|------|------|------|------|
| mode | 3D | 2D plane stress | 2D plane strain | 3D | 2D plane stress | 2D plane strain |
| 1st | 51.92 | 51.69 | 56.49 | 51.29 | 51.02 | 55.75 |
| 2nd | 318.59 | 317.22 | 345.70 | 303.40 | 300.89 | 327.87 |
| 3rd | 864.20 | 860.65 | 934.26 | 863.94 | 860.38 | 933.96 |

**Table 1.** Natural frequencies (Hz) of a beam without a crack and for an open crack, as calculated using a three-dimensional, a two-dimensional plane stress and a two-dimensional plane strain finite element model.
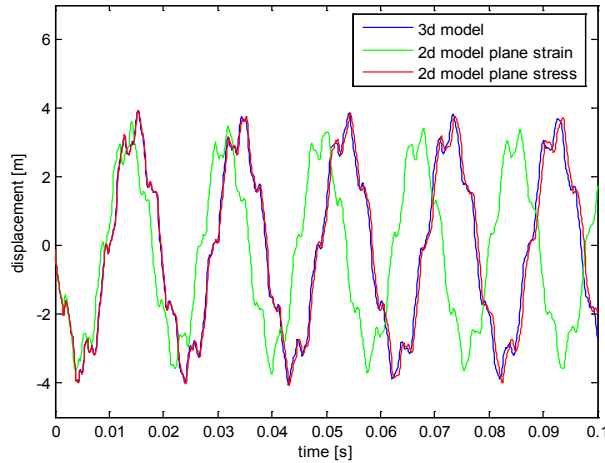
**Figure 4.** Transverse displacements at the free end of a cantilever beam presenting a breathing crack, using three-dimensional, two-dimensional plane stress and two-dimensional plane strain breathing crack finite element models.

used. The displacement responses over time, as obtained by the three models, are presented in Figure 4. As shown, although the plane stress model has a hardly noticeable difference on the first eigenfrequency than the 3D model, it represents an excellent agreement with the 3D model in terms of displacement amplitude, verifying the corresponding results of Table 1. On the other hand, the plane strain model results in a higher first eigenfrequency and in smaller amplitude compared to the 3D model.

These results show that the 2D plane stress model can be used to reliably describe the case of a beam with a crack, regardless of the type of the crack (open, closed or breathing).

## 5. Selection of morphological operators and structuring elements

Cracks result in changes of mode shapes, which are much more sensitive to the presence and features of the crack, compared to changes in natural frequencies. However, the presence of damage may not be quite apparent in mode shapes of the lower modes usually measured. For example, the first three POMs are presented in Figure 5 for the cracked beam, described in Section 4.
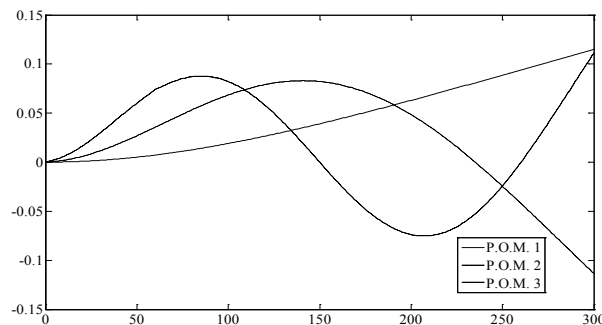


**Figure 5.** Proper orthogonal modes for the cantilever beam with crack location at 60 mm and relative crack depth 20%.
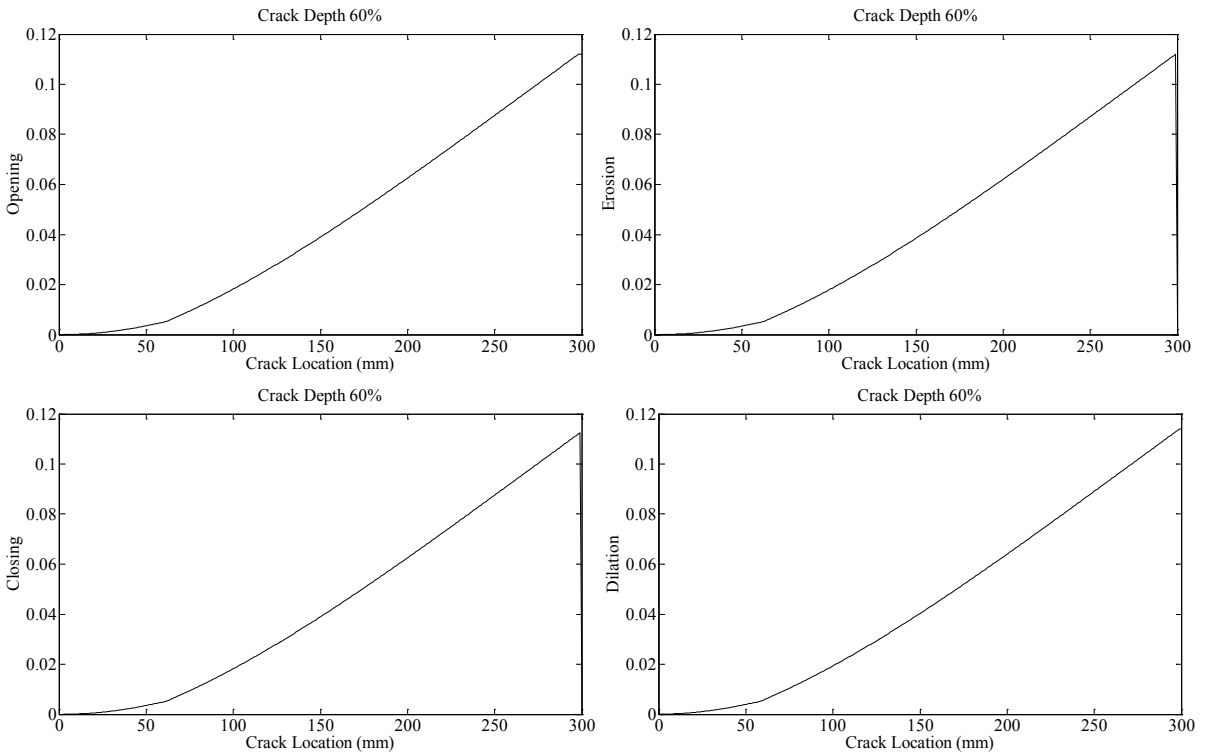
**Figure 6.** Morphological operators (opening, closing, dilation, erosion) using POM 1 and a flat structuring element.

For this reason, mathematical morphology is further used for processing the shape of the POMs. The effect of each one of the four basic morphological operators of Section 3 (erosion, dilation, opening and closing) are applied on the 3 first POMs in order to examine their ability for better determination of the features of the crack. Furthermore, the choice of a proper structuring element is equally essential for the success of morphological processing.

First a flat structuring element is used. Flat structuring elements are the simplest ones with a straight-forward application, since the only parameter to be selected is their corresponding length $L$. The results can be seen in Figure 6. Although a small change of the slope at the morphological operators can be observed at the location of the crack, this change is not easily identifiable, in order to clearly reveal the existence of the crack.

Then, a spline is used as the structuring element. This spline is created using the corresponding POM of an uncracked beam. The length of the structuring element is selected equal to 1/60 times the length of the beam. The resulting morphological operators are shown in Figure 7. A peak corresponding to the location of the crack is clearly observed at the results of the erosion and of the opening operation, even when the crack is at the first stages (relative crack depth 5%). As a result, both these two morphological operators can be used in principle as crack indicators.
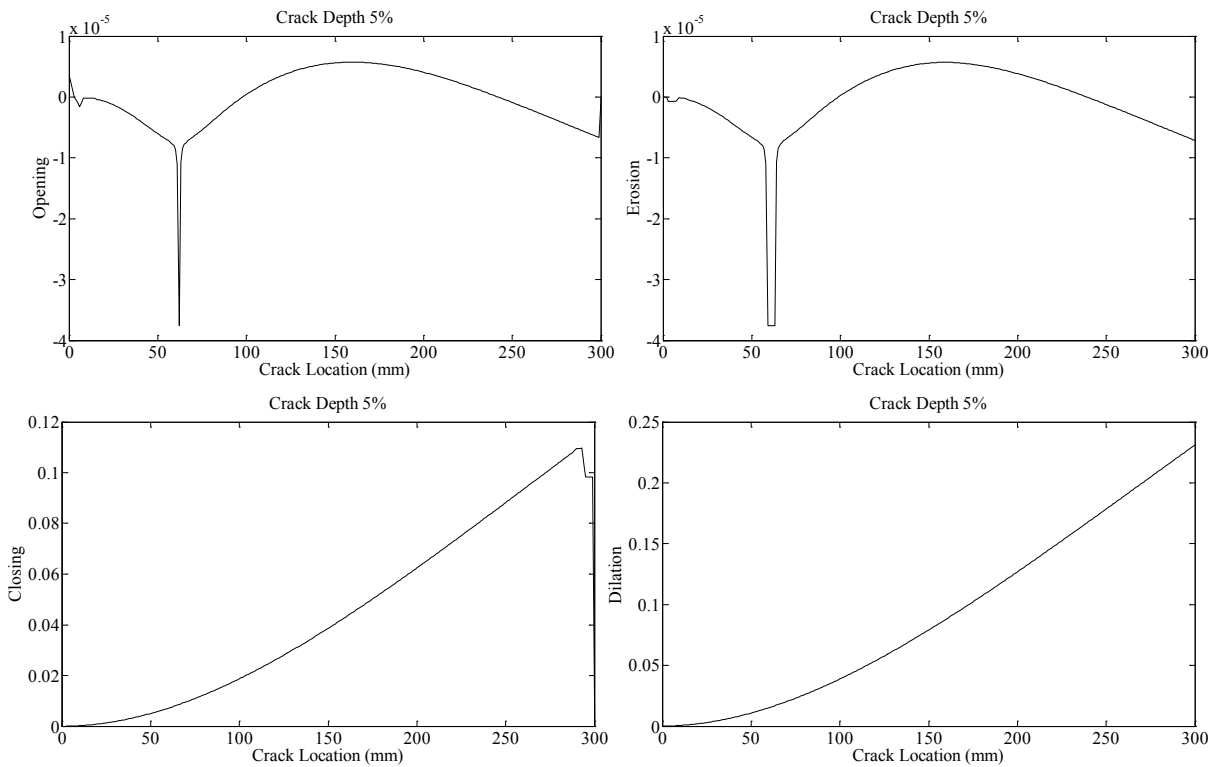
**Figure 7.** Morphological operators (opening, closing, dilation, erosion) using POM 1 and a spline structuring element, for cantilever beam, crack location at 60 mm, 60% relative crack depth and ANL = 0%.

In the remaining part of the paper, the erosion operator will be used, as it presents a wider peak than opening, a feature which indicates increased robustness. In view of (26) and (28), the opening operator requires more computation time, as its computation involves two steps.

## 6. Performance assessment in a cantilever beam

In order to assess the efficiency of the proposed approach, its performance with respect to a number of features is been evaluated, such as ability to accurately identify the location and depth of the crack, the identification and the distance of multiple cracks under different depths, the robustness to external noise and the spatial resolution of measurement points.

In the subsequent analysis, the cantilever beam of Section 4 is further processed, using a 2D plane stress model, according to the analysis of Section 4. Single or multiple cracks are introduced each time at distances $l_c = 60$ mm, $l_c = 150$ mm, $l_c = 240$ mm from the clamped end. The relative crack depths $\alpha$ are typically chosen as 10%, 20%, 30%, 40% and 60%. The transverse displacement measurements are obtained at spatial distances of 1 mm along the beam, resulting in a number of $M = 301$ points (spatial locations) available. The erosion operator with a spline structuring element of a length equal to 1/60 of the total beam length is used according to the results in Section 5.

**Figure 8.** Morphological index using POM 1 with relative crack depth of 10%, ANL = 0%, cantilever beam and crack location at 60 mm (left) or 240 mm (right).

**6.1.** *Determination of crack location and depth.* As already shown in Section 5, the location of the crack can be identified by the sudden change of the erosion morphological operation. The efficiency of this observation is further evaluated under the different crack locations and sizes mentioned above. As seen in Figure 8, the method gives very good results even in the worst case, when the crack is located away from the clamped end at $l_c = 240$ mm and the relative crack depth is only 10%.

In view of this good agreement concerning the crack location, we examine further in Figure 9 the correlation of the evolution of the crack depth with the value of the erosion operator at the crack location. We observe a monotonic increase of the morphological operator with the crack depth. This result can be further exploited in order to use also the value of the morphological operator at the location of the crack as an index (morphological index) to identify the depth of the crack.

However, as seen in Figure 9, left, the results become more clear when the crack is near the middle of the beam. Crack location becomes more difficult when the crack is located near the free ends of the beam.

Contrarily, comparison of just the singular values cannot lead to diagnostic information of the same quality and reliability, as can be observed from Figure 9, right.
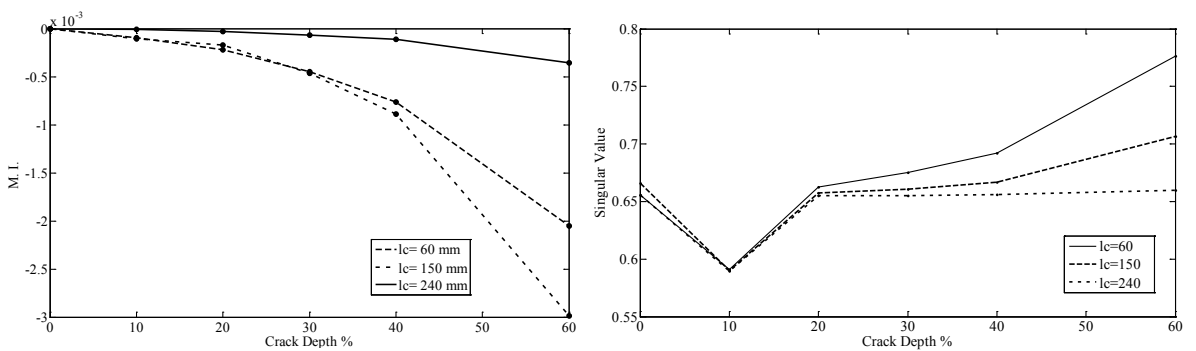


**Figure 9.** Evolution with crack depth of the morphological index (left) and the first singular value (right) at three locations (ANL = 0%, cantilever beam).
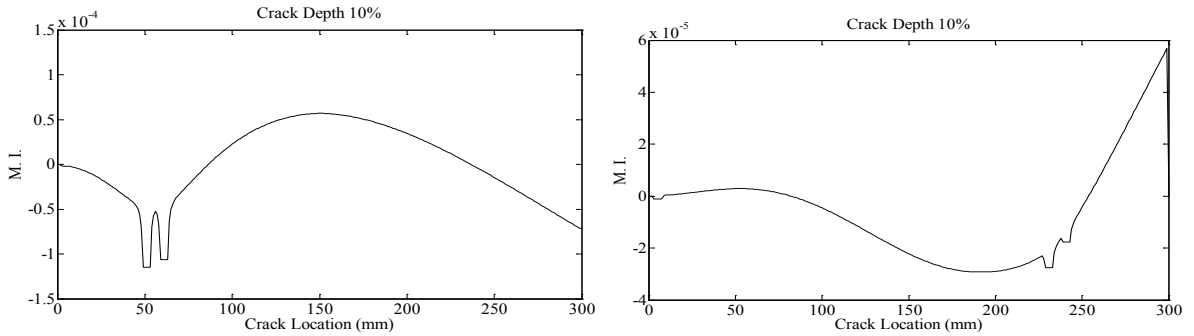
**Figure 10.** Morphological index using POM 1 with equal relative crack depth of 10%, ANL = 0%, cantilever beam and crack locations at 50 mm and 60 mm (left) or 230 mm and 240 mm (right).

**6.2. *Effects of multiple cracks.*** Two breathing cracks are then simultaneously introduced at different locations of the beam. In view of Figure 10, a peak corresponding to the location of the cracks is again clearly observed, even when the cracks are at the first stage (relative crack depth $\alpha = 10\%$). The method is still able to provide reliable results, even at the worst case when the cracks are located away from the clamped end and closely spaced at $l_{c1} = 230$ mm and $l_{c2} = 240$ mm.

**6.3. *Effects of noise.*** In order to examine the effect of noise or measurement errors on the sensitivity of the method, artificial noise was added to the waveforms of the displacements, with an added noise level ANL increased up to a significant amount of 30%. In the case of a single crack, satisfactory results are obtained even for the smallest crack depth of 10% when the crack is located at $l_c = 60$ mm and $l_c = 150$ mm (Figure 11).

In the case of a crack located at $l_c = 240$ mm, the detection of the location is easier for big cracks (greater than 40%) and somewhat obscured for smaller ones (less than 30%), as shown in Figure 12. The results become more clear when the third POD is used instead of the first (Figure 13).

However, Figure 14 shows that the worst case, which corresponds to a crack location at $l_c = 240$ mm, a relative crack depth of 10% and an ANL of 30%, represents the limits of the detection capability of the method.
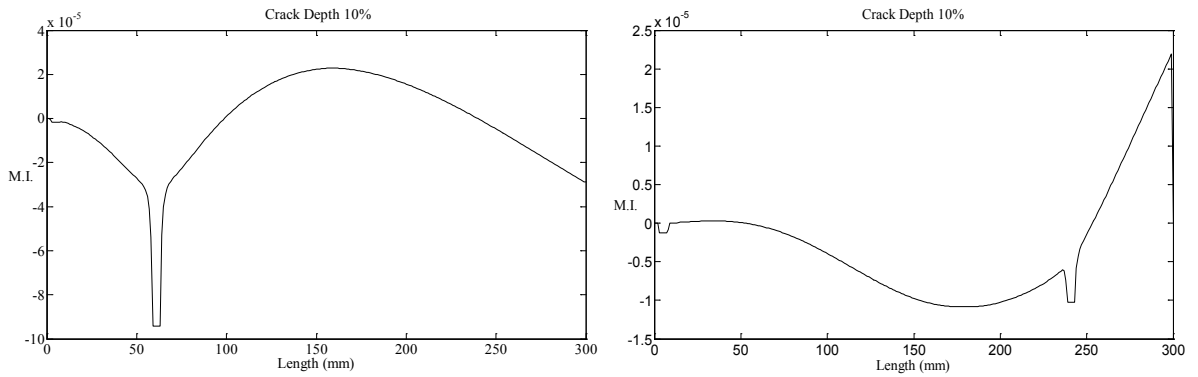


**Figure 11.** Morphological index using POM 1 with relative crack depth 10%, ANL = 30%, cantilever beam and crack location at 60 mm (left) or 150 mm (right).
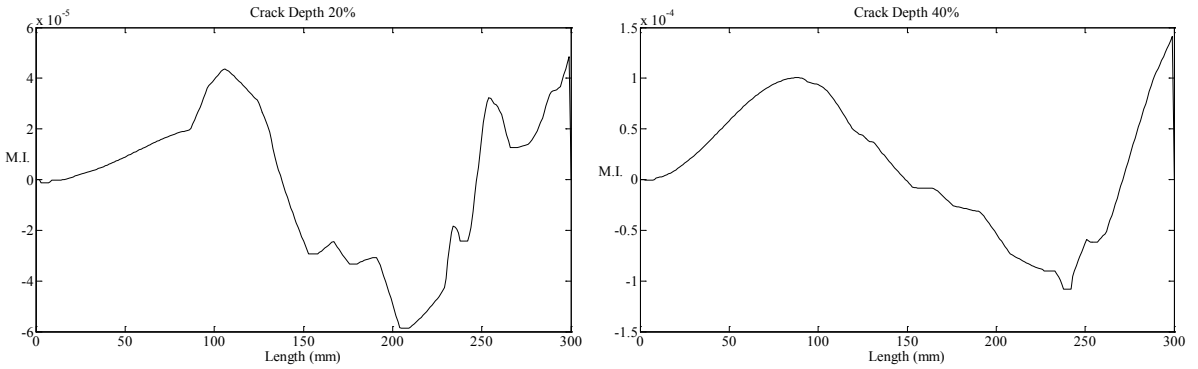
**Figure 12.** Morphological index using POM 1 with relative crack depth 20% (left) or 40% (right) ANL = 30%, cantilever beam and crack location at 240 mm,
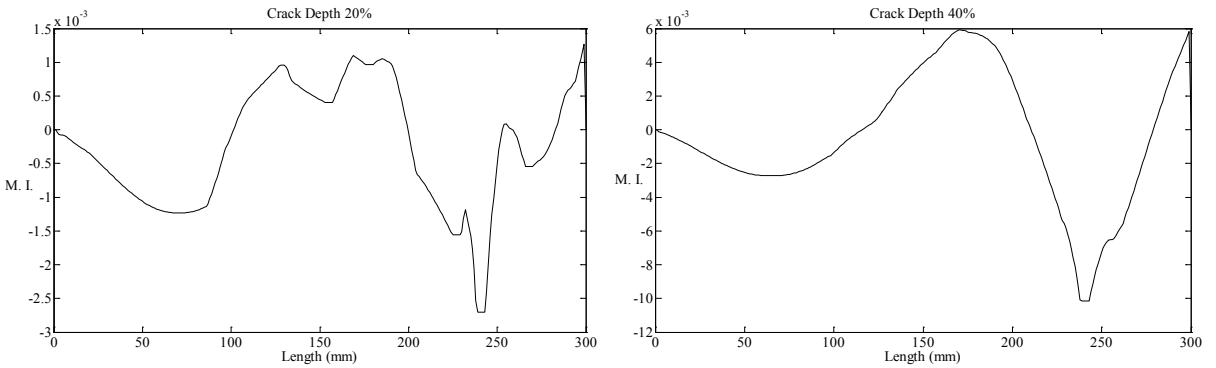


**Figure 13.** Morphological index using POM 3 for same configuration as in Figure 12.
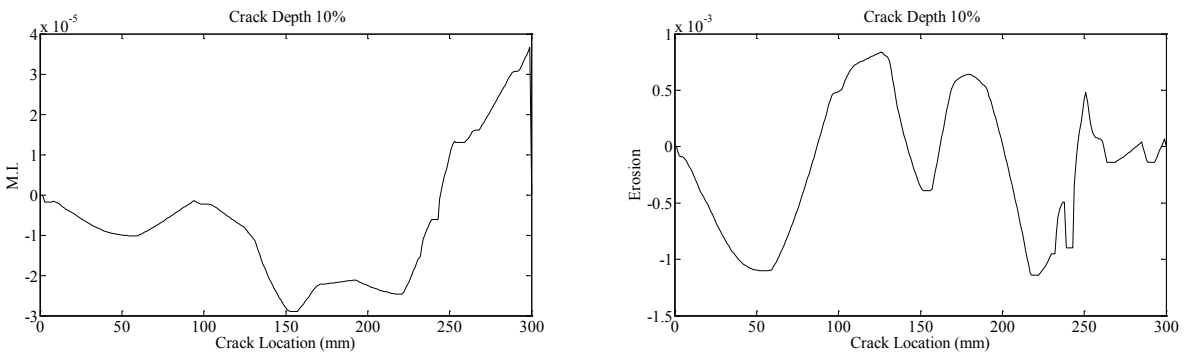


**Figure 14.** Morphological index using POM 1 (left) or POM 3 (right) with relative crack depth 10%, and ANL = 30%, cantilever beam and crack location at 240 mm.

The evolution of the morphological index with crack depth is presented in Figure 15. Although the method has reached its detection capability limits, the morphological index is still able to follow the increase in crack depth.
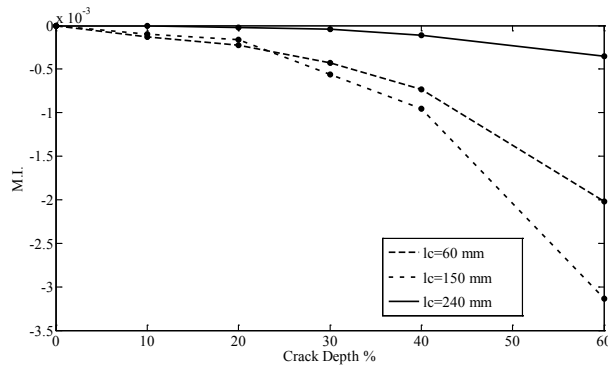
**Figure 15.** Evolution of the morphological index with crack depth at three locations (ANL=30%, cantilever beam).
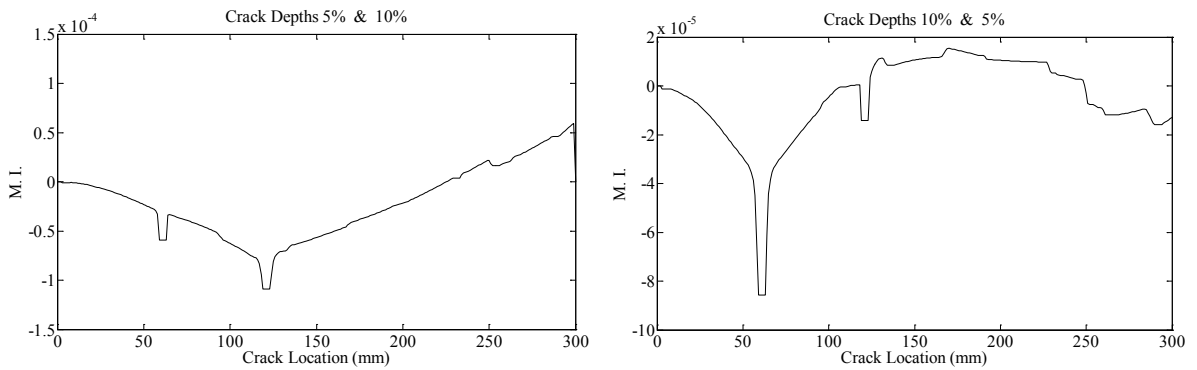


**Figure 16.** Morphological index using POM 1 with relative crack depths of 5% and 10% (left) or 10% and 5% (right), ANL = 30%, cantilever beam, and crack locations at 60 mm and 120 mm.

In the case of multiple cracks, the crack localization is clear for cracks located at $l_{c1} = 60$ mm, and $l_{c2} = 120$ even at the initial stages of the crack (relative crack depths equal or less than 10%) and for an ANL up to 30% (Figure 16).

The worst case corresponds to crack locations at $l_{c1} = 60$ mm and $l_{c2} = 240$ mm. In the case of an ANL equal to 20%, crack determination is still possible, even when the relative depth of one crack is 10% and of the other is only 5% (Figure 17).

When the ANL increases to 30%, the method reaches again its detection capability limits (Figure 18).

**6.4.** *Effect of spatial resolution of measurement points.* Finally, the effect of decreasing the number of measurement points to the detection capabilities of the method has been evaluated. As a result, in the cases where the two cracks are located far one from each other, the number of the required measurement points can be reduced from $M = 301$ to less than $M = 51$ points, as can be observed in Figure 19. However, as expected, in the cases where the two cracks are close to each other, the method might identify them as a single. This problem can be overcome by increasing the special resolution of the measurement points only locally in the areas of cracks.

**Figure 17.** Morphological index using POM 1 with relative crack depths of 10% and 5% (left) or 5% and 10% (right), ANL = 20%, cantilever beam, and crack locations at 60 mm and 240 mm.
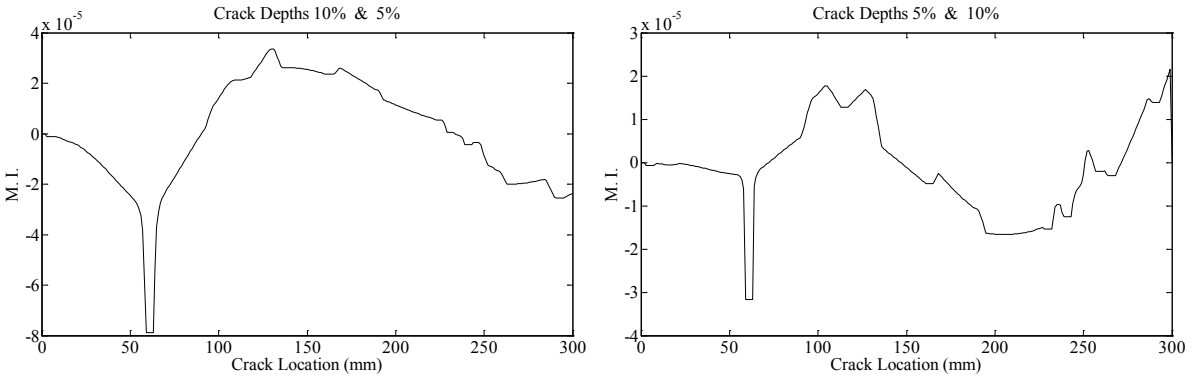


**Figure 18.** Morphological index using POM 1 with relative crack depths of 10% and 5% (left) or 5% and 10% (right), ANL = 30%, cantilever beam, and crack locations at 60 mm and 240 mm.
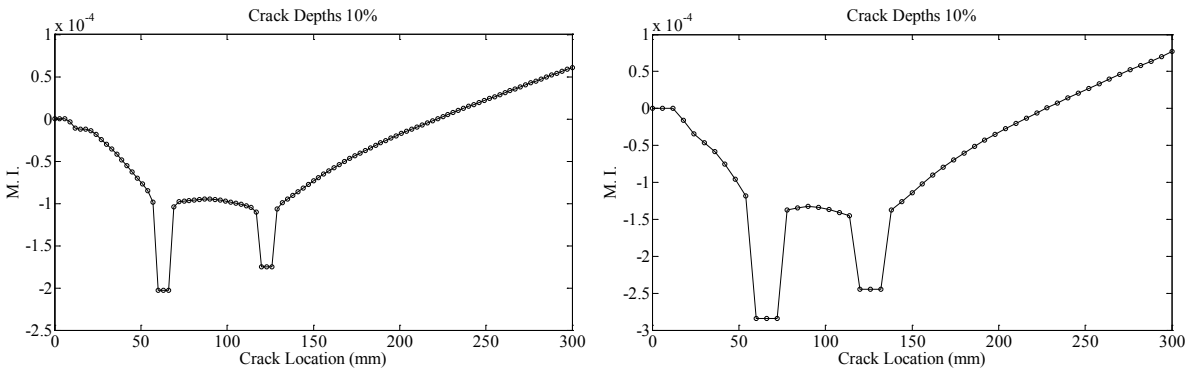


**Figure 19.** Morphological index using POM 1 with crack locations at 60 mm and 120 mm, equal relative crack depths of 10%, ANL = 0%, cantilever beam, length of the structuring element equal to $L/100$ and number of spatial points $M$ equal to 101 (left) or 51 (right).
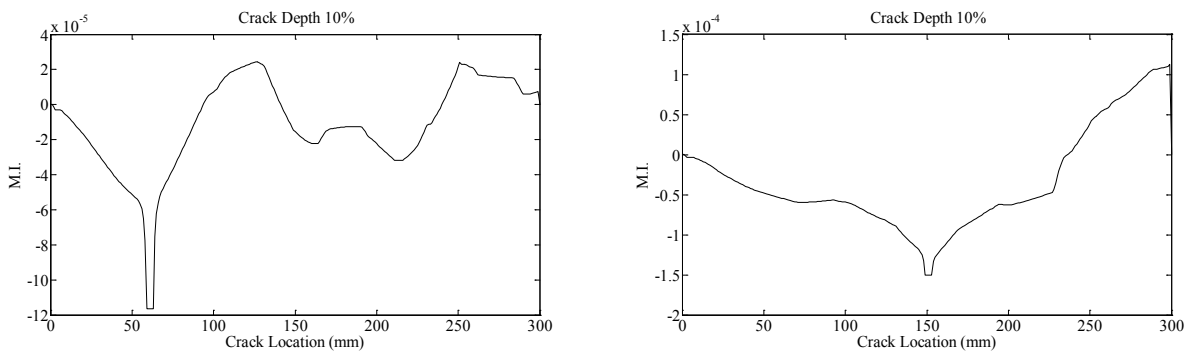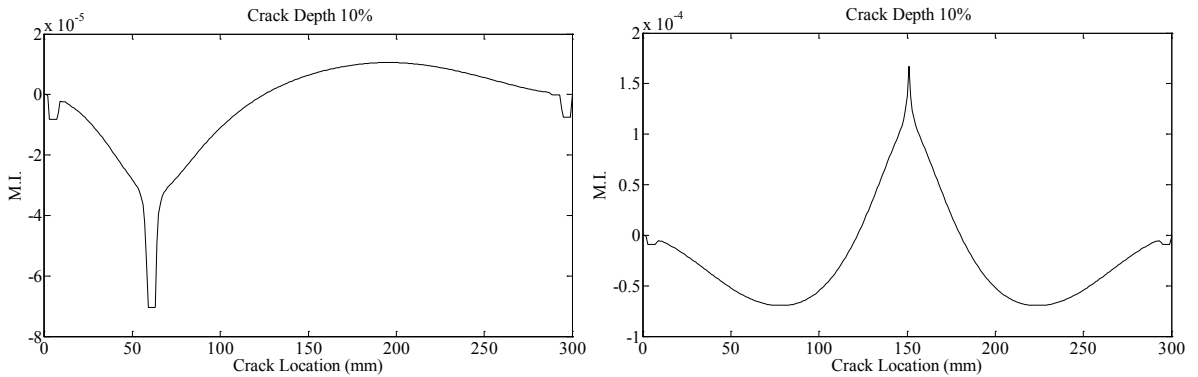
**Figure 20.** Morphological index using POM 1 with relative crack depth of 10%, ANL $=$ 0%, simply supported beam and crack location at 60 mm (left) or 150 mm (right).

## 7. Performance assessment in a simply supported beam

The beam of Section 4 is again considered, using a 2D plane stress model, according to the analysis of Section 4. However, this time, the beam is simply supported at both its ends. Single or multiple cracks are introduced each time at distances $l_c = 60$ mm and $l_c = 150$ mm from the beam end. The relative crack depths $\alpha$ are typically chosen as 10%, 20%, 30%, 40%, 50% and 60%. The transverse displacement measurements are obtained at spatial distances of 1 mm along the beam, resulting in a number of $M = 301$ points (spatial locations) available. The erosion operator with a spline structuring element of a length equal to 1/60 of the total beam length is used according to the results in Section 5.

**7.1.** *Determination of crack location and depth.* As seen in Figure 20, the method gives again very good results even when the relative crack depth is only 10%. Consequently, the evolution of the crack depth with the value of the erosion operator at the crack location is again further examined. As shown in Figure 21, a monotonic increase of the morphological operator is observed with the increase of the crack depth.
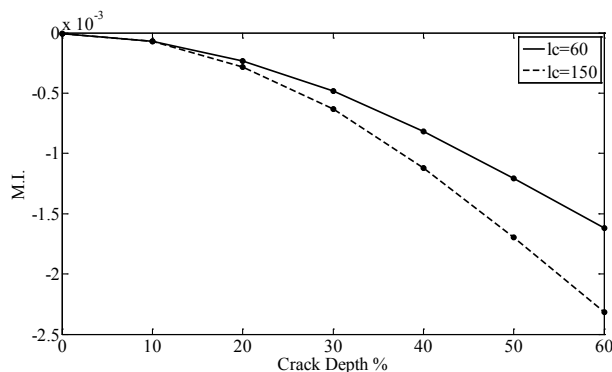


**Figure 21.** Evolution of morphological index with crack depth at two locations (ANL $=$ 0%, simple beam).

**7.2.** *Effects of multiple cracks.* Two breathing cracks are then simultaneously introduced at different locations of the beam. In Figure 24 on the next page we again observe peaks corresponding to the location of the cracks. These peaks are clearly visible in the case of equal crack depths with relative crack depths as small as 10%. However, in the case of unequal crack depths, the method reaches its limits, with the smaller crack depth being just visible.

**7.3.** *Effects of noise.* In order to examine the effect of noise or measurement errors on the sensitivity of the method, artificial noise was added to the waveforms of the displacements, with an added noise level ANL increased up to a significant amount of 30%. In the case of a single crack, satisfactory results are obtained even for the smallest crack depth of 10%, when the crack is located at the middle of the beam at $l_c = 150$ mm (Figure 22).

In the case of a crack located at $l_c = 60$ mm, the detection of the crack location is easier in case of big cracks (greater than 20%), as shown in Figure 23. However, in view of Figure 22, it is evident that the worst case, which corresponds to a crack location at $l_c = 60$ mm, a relative crack depth of 10% and an ANL of 30%, represents the limits of the detection capability of the method.
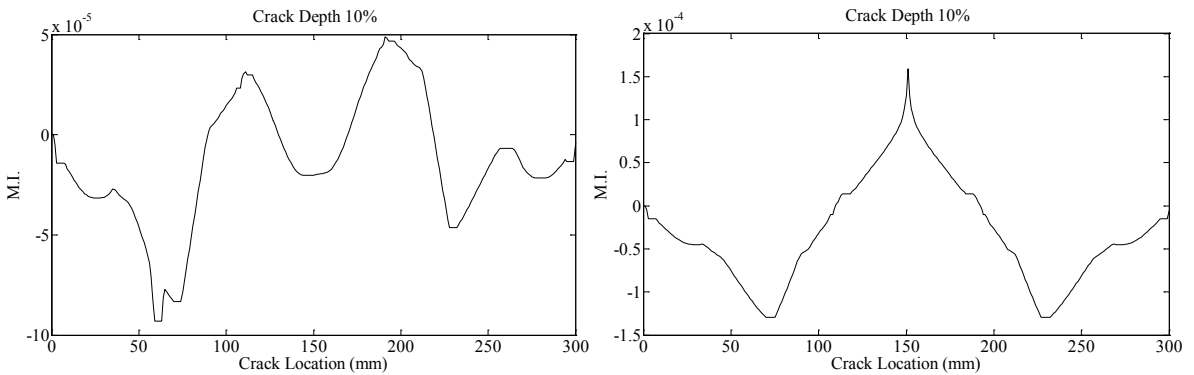


**Figure 22.** Morphological index using POM 1 with relative crack depth 10%, ANL=30%, simply supported beam and crack location at 60 mm (left) or 150 mm (right).
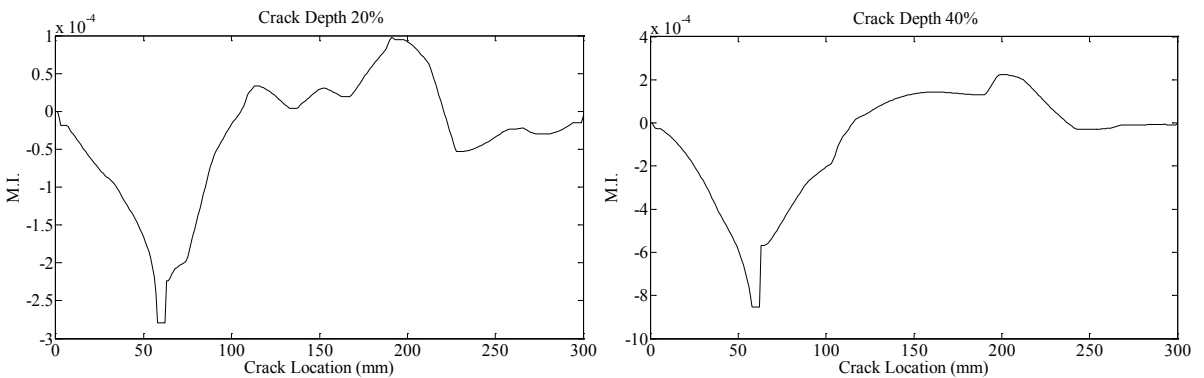


**Figure 23.** Morphological index using POM 1 with relative crack depth 20% (left) or 40% (right), ANL=30%, simply supported beam and crack location at 60 mm.
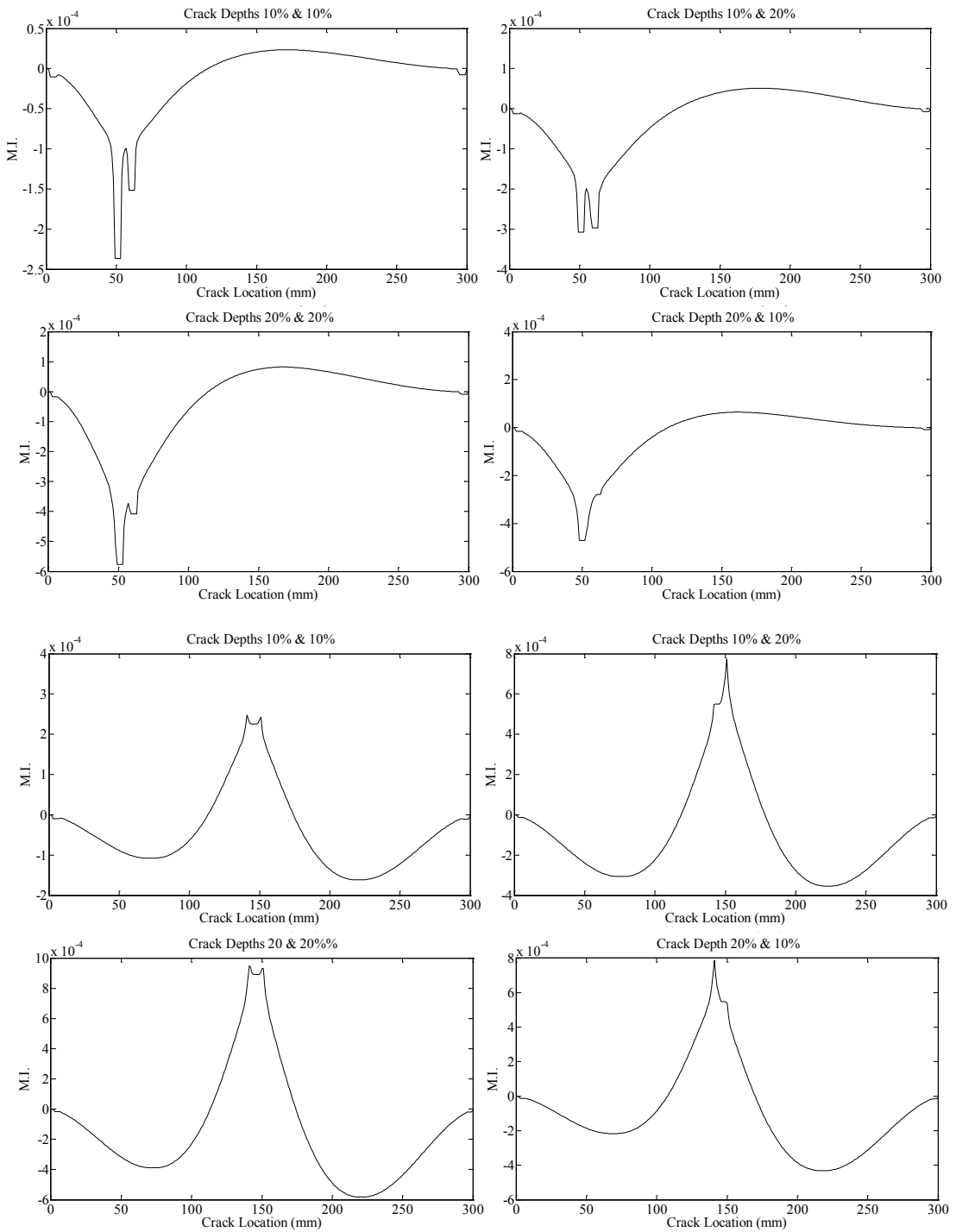
**Figure 24.** Morphological index using POM 1 for two cracks located at 50 mm and 60 mm (top two rows) or 140 mm and 150 mm (bottom rows), ANL = 0%, simply supported beam, with various relative crack depths.
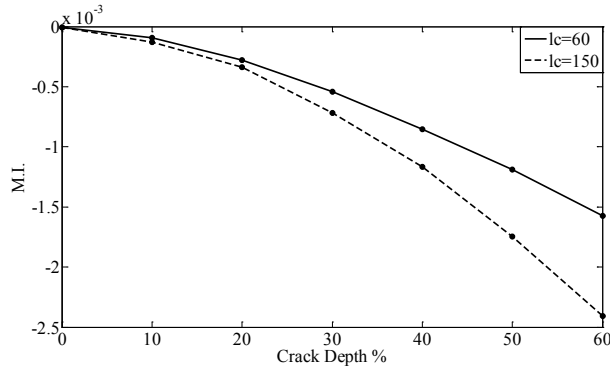
**Figure 25.** Evolution of the morphological index with crack depth at two locations for (ANL=30%, simply supported beam).

The evolution of the morphological index with crack depth is shown in Figure 25. Although the method has reached its detection capability limits, the morphological index is still able to follow the increase of the depth of the crack.

In the case of multiple cracks, Figure 27 on the next page suggests that the effect of noise is marginal, compared to the effect of unequal cracks (Section 7.2).

**7.4. *Effect of spatial resolution of measurement points.*** Finally, the effect of decreasing the number of measurement points to the detection capabilities of the method is again evaluated, for a crack located at $l_c = 60$ mm. In view of Figure 26, the number of the required measurement points can be reduced from $M = 301$ to less than $M = 51$ points. However, as again expected, in the cases where the two cracks are close to each other, the method might identify them as a single. This problem can be overcome by increasing the spatial resolution of the measurement points only locally in the areas of cracks.
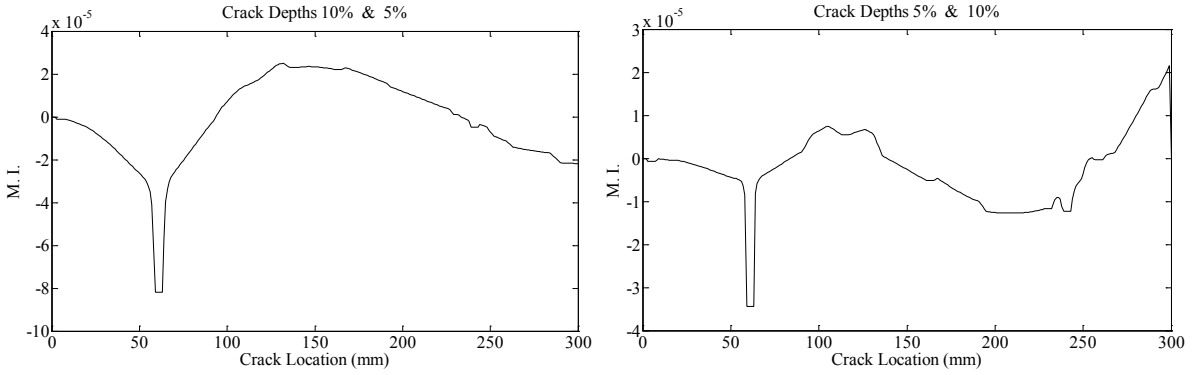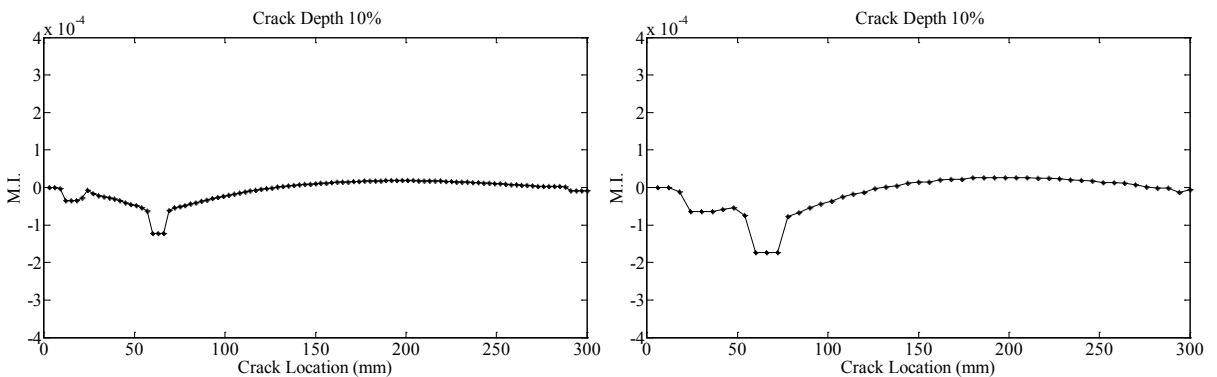


**Figure 26.** Morphological index using P.O.M. 1 with crack location at 60 mm for relative crack depth of 10%, ANL $= 0\%$, simply supported beam, length of the structuring element equal to $L/100$ and number of spatial points used as A) $M = 101$ points (Left), B) $M = 51$ points (Right)
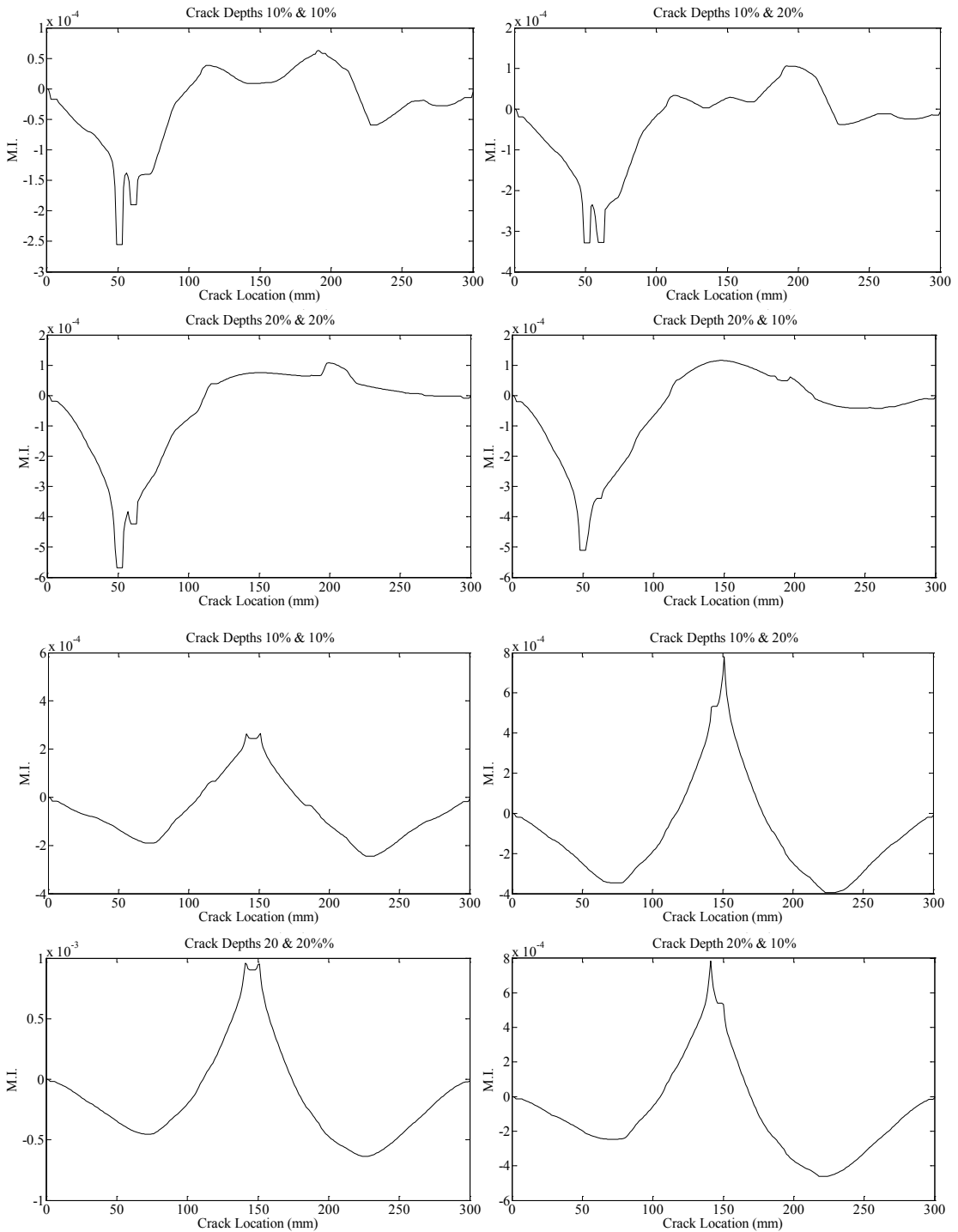
**Figure 27.** Morphological index using POM 1 for two cracks located at 50 mm and 60 mm (top two rows) or 140 mm and 150 mm (bottom rows), ANL = 30%, simply supported beam, with various relative crack depths.

## 8. Conclusion

A comparison of different FEM models (2D plane stress, 2D plane strain, 3D) used to model a cantilever beam with a crack indicates that the 2D plane stress model can accurately and reliably model the crack effect, whether if the crack is of open, closed or breathing type. From the four basic morphological operators (erosion, dilation, opening, and closing) used to process the proper orthogonal modes of the cracked beam, the erosion operator using a spline structuring element presents the best behavior.

The proposed method, as assessed both in a cantilever and in a simply supported beam, can lead to the efficient detection both of the crack location, as well as of the crack size. Due to the fact that POMs are used instead of modes, nonlinear effects can be taken into account and noise effects can be eliminated. The morphological index can follow the evolution of the crack depth, even when the signal to noise ratio reaches 30%. The results become clearer when more than one POM is used. In the case of double-cracked beam structures, the analysis of the effect of different crack depths, noise level and spatial resolution of the measured points indicate that the proposed method can present also robust results.

## Acknowledgements

## References

[Alvandi and Cremona 2006]  A. Alvandi and C. Cremona, "Assessment of vibration-based damage identification techniques", *J. Sound Vib.* **292**:1–2 (2006), 179–202.

[Andreaus et al. 2007]  U. Andreaus, P. Casini, and F. Vestroni, "Non-linear dynamics of a cracked cantilever beam under harmonic excitation", *Int. J. Non-Linear Mech.* **42**:3 (2007), 566–575.

[Azeez and Vakakis 1997]  M. F. Azeez and A. F. Vakakis, "Numerical and experimental analysis of the nonlinear dynamics due to impacts of a continuous overhung rotor", in *Proceedings of the 1997 ASME Design Engineering Technical Conferences* (*DETC97*) (Sacramento, CA, 1997), edited by B. Ravani, ASME, New York, 1997.

[Bamnios et al. 2002]  Y. Bamnios, E. Douka, and A. Trochidis, "Crack identification in beam structures using mechanical impedance", *J. Sound Vib.* **256**:2 (2002), 287–297.

[Cawley 1997]  P. Cawley, "Long range inspection of structures using low frequency ultrasound", pp. 1–17 in *Structural damage assessment using advanced signal processing procedures: proceedings of DAMAS '97* (Sheffield, 1997), edited by J. M. Dulieu-Smith et al., Sheffield Academic Press, Sheffield, 1997.

[Cawley and Adams 1979]  P. Cawley and R. D. Adams, "The location of defects in structures from measurements of natural frequencies", *J. Strain Anal. Eng. Des.* **14**:2 (1979), 49–57.

[Chang and Chen 2005]  C.-C. Chang and L.-W. Chen, "Detection of the location and size of cracks in the multiple cracked beam by spatial wavelet based approach", *Mech. Syst. Signal Process.* **19**:1 (2005), 139–155.

[Cheng et al. 1999]  S. M. Cheng, X. J. Wu, W. Wallace, and A. S. J. Swamidas, "Vibrational response of a beam with a breathing crack", *J. Sound Vib.* **225**:1 (1999), 201–208.

[Dimarogonas 1996]  A. D. Dimarogonas, "Vibration of cracked structures: a state of the art review", *Eng. Fract. Mech.* **55**:5 (1996), 831–857.

[Doebling et al. 1998]  S. W. Doebling, C. R. Farrar, and M. B. Prime, "A summary review of vibration-based damage identification methods", *Shock Vib. Digest* **30**:2 (1998), 91–105.

[Douka and Hadjileontiadis 2005]  E. Douka and L. J. Hadjileontiadis, "Time-frequency analysis of the free vibration response of a beam with a breathing crack", *NDT&E Int.* **38**:1 (2005), 3–10.

[Douka et al. 2003]  E. Douka, S. Loutridis, and A. Trochidis, "Crack identification in beams using wavelet analysis", *Int. J. Solids Struct.* **40**:13–14 (2003), 3557–3569.

[Douka et al. 2004]  E. Douka, S. Loutridis, and A. Trochidis, "Crack identification in plates using wavelet analysis", *J. Sound Vib.* **270**:1–2 (2004), 279–295.

[Farrar et al. 1994]  C. R. Farrar, W. E. Baker, T. M. Bell, K. M. Cone, T. W. Darling, T. A. Duffey, A. Eklund, and A. Migliori, "Dynamic characterization and damage detection in the I-40 bridge over the Rio Grande", Technical Report LA-12767-MS, Los Alamos National Laboratory, Los Alamos, NM, 1994.

[Feeny 1997]  B. F. Feeny, "Interpreting proper orthogonal modes in vibrations", in *Proceedings of the 1997 ASME Design Engineering Technical Conferences* (*DETC97*) (Sacramento, CA, 1997), edited by B. Ravani, ASME, New York, 1997.

[Galvanetto and Violaris 2007]  U. Galvanetto and G. Violaris, "Numerical investigation of a new damage detection method based on proper orthogonal decomposition", *Mech. Syst. Signal Process.* **21**:3 (2007), 1346–1361.

[Guo and Billings 2007]  L. Z. Guo and S. A. Billings, "Detection of fatigue cracks in a beam using a spatio-temporal dynamical system identification method", *J. Sound Vib.* **299**:1–2 (2007), 22–35.

[Hadjileontiadis et al. 2005a]  L. J. Hadjileontiadis, E. Douka, and A. Trochidis, "Crack detection in beams using kurtosis", *Comput. Struct.* **83**:12–13 (2005), 909–919.

[Hadjileontiadis et al. 2005b]  L. J. Hadjileontiadis, E. Douka, and A. Trochidis, "Fractal dimension analysis for crack identification in beam structures", *Mech. Syst. Signal Process.* **19**:3 (2005), 659–674.

[Kim et al. 2003]  J.-T. Kim, Y.-S. Ryu, H.-M. Cho, and N. Stubbs, "Damage identification in beam-type structures: frequency-based method vs mode-shape-based method", *Eng. Struct.* **25**:1 (2003), 57–67.

[Lenaerts et al. 2001]  V. Lenaerts, G. Kerschen, and J. C. Golinval, "Proper orthogonal decomposition for model updating of non-linear mechanical systems", *Mech. Syst. Signal Process.* **15**:1 (2001), 31–43.

[Lifshitz and Rotem 1969]  J. M. Lifshitz and A. Rotem, "Determination of reinforcement unbonding of composites by a vibration technique", *J. Compos. Mater.* **3**:3 (1969), 412–423.

[Loutridis et al. 2004]  S. Loutridis, E. Douka, and A. Trochidis, "Crack identification in double-cracked beams using wavelet analysis", *J. Sound Vib.* **277**:4–5 (2004), 1025–1039.

[Loutridis et al. 2005]  S. Loutridis, E. Douka, L. J. Hadjileontiadis, and A. Trochidis, "A two-dimensional wavelet transform for detection of cracks in plates", *Eng. Struct.* **27**:9 (2005), 1327–1338.

[Lumley 1967]  J. L. Lumley, "The structure of inhomogeneous turbulent flows", pp. 166–178 in *Atmospheric Turbulence and Radio Wave Propagation*, edited by A. M. Yaglom and V. I. Tatarski, Nauka, Moscow, 1967.

[Luzzato 2003]  E. Luzzato, "Approximate computation of non-linear effects in a vibrating cracked beam", *J. Sound Vib.* **265**:4 (2003), 745–763.

[Maragos and Schafer 1987]  P. Maragos and R. Schafer, "Morphological filters, I: Their set-theoretic analysis and relations to linear shift-invariant filters", *IEEE Trans. Acoust. Speech Signal Process.* **35**:8 (1987), 1153–1169.

[Ostachowicz and Krawczuk 1991]  W. M. Ostachowicz and M. Krawczuk, "Analysis of the effect of cracks on the natural frequencies of a cantilever beam", *J. Sound Vib.* **150**:2 (1991), 191–201.

[Randall 2002]  R. B. Randall, "State of the art in monitoring rotating machinery", pp. 1457–1477 in *Noise and vibration engineering: proceedings of ISMA 2002* (Leuven, 2002), vol. 4, edited by P. Sas and B. van Hal, Katholieke Universiteit Leuven, Department of Mechanical Engineering, Leuven, 2002.

[Ruotolo and Surace 1997]  R. Ruotolo and C. Surace, "Damage assessment of multiple cracked beams: numerical results and experimental validation", *J. Sound Vib.* **206**:4 (1997), 567–588.

[Rytter 1993]  A. Rytter, *Vibration based inspection of civil engineering structures*, Ph.D. thesis, Aalborg University, Aalborg, 1993.

[Sahin and Shenoi 2003]  M. Sahin and R. A. Shenoi, "Quantification and localisation of damage in beam-like structures by using artificial neural networks with experimental validation", *Eng. Struct.* **25**:14 (2003), 1785–1802.

[Sekhar 2008]  A. S. Sekhar, "Multiple cracks effects and identification", *Mech. Syst. Signal Process.* **22**:4 (2008), 845–878.

[Serra 1982]  J. Serra, *Image analysis and mathematical morphology*, Academic Press, New York, 1982.

[Sohn et al. 2004]  H. Sohn, C. R. Farrar, F. M. Hemez, D. D. Shunk, D. W. Stinemates, B. R. Nadler, and J. J. Czarnecki, "A review of structural health monitoring literature: 1996–2001", Technical Report LA-13976-MS, Los Alamos National Laboratory, Los Alamos, NM, 2004, Available at http://institute.lanl.gov/ei/shm/pubs/LA_13976_MSa.pdf.

[Wang and Deng 1999]  Q. Wang and X. Deng, "Damage detection with spatial wavelets", *Int. J. Solids Struct.* **36**:23 (1999), 3443–3468.

[Zhong and Oyadiji 2007]  S. Zhong and S. O. Oyadiji, "Crack detection in simply supported beams without baseline modal parameters by stationary wavelet transform", *Mech. Syst. Signal Process.* **21**:4 (2007), 1853–1884.

KONSTANTINOS C. GRYLLIAS: kosgryl@central.ntua.gr
*National Technical University of Athens, School of Mechanical Engineering, Heroon Polytechniou 9, 15780 Athens, Greece*

IOANNIS N. KOUKOULIS: jkouk@central.ntua.gr
*National Technical University of Athens, School of Mechanical Engineering, Heroon Polytechniou 9, 15780 Athens, Greece*

CHRISTOS T. YIAKOPOULOS: chryiako@central.ntua.gr
*National Technical University of Athens, School of Mechanical Engineering, Heroon Polytechniou 9, 15780 Athens, Greece*

IOANNIS A. ANTONIADIS: antogian@central.ntua.gr
*National Technical University of Athens, School of Mechanical Engineering, Heroon Polytechniou 9, 15780 Athens, Greece*

CHRISTOPHER G. PROVATIDIS: cprovat@central.ntua.gr
*National Technical University of Athens, School of Mechanical Engineering, Heroon Polytechniou 9, 15780 Athens, Greece*
http://users.ntua.gr/cprovat/

# STATISTICS OF MICROSTRUCTURE, PEAK STRESS AND INTERFACE DAMAGE IN FIBER REINFORCED COMPOSITES

VOLODYMYR I. KUSHCH, SERGII V. SHMEGERA AND LEON MISHNAEVSKY JR.

This paper addresses an effect of the fiber arrangement and interactions on the peak interface stress statistics in a fiber reinforced composite material (FRC). The method we apply combines the multipole expansion technique with the representative unit cell model of composite bulk, which is able to simulate both the uniform and clustered random fiber arrangements. By averaging over a number of numerical tests, the empirical probability functions have been obtained for the nearest neighbor distance and the peak interface stress. It is shown that the considered statistical parameters are rather sensitive to the fiber arrangement, particularly cluster formation. An explicit correspondence between them has been established and an analytical formula linking the microstructure and peak stress statistics in FRCs has been suggested. Application of the statistical theory of extreme values to the local stress concentration study has been discussed. It is shown that the peak interface stress distribution in the fibrous composite with uniform random microstructure follows a Fréchet-type asymptotic distribution rule. Based on the established statistical distributions, a simple microdamage model of FRC is suggested.

## 1. Introduction

A quantitative analysis of an effect caused by the distribution of inhomogeneities in a heterogeneous material on its local and overall mechanical behavior is one of the most challenging problems of the micromechanics of composites. This problem stems from the actual needs of materials science since random microstructure is inherent for most heterogeneous materials including fiber reinforced composites (FRCs). The complexity in formulating the FRC strength theory arises from the fact that the strength limit/fracture onset is governed by the maximum local stress rather than by its mean value. Except in the very dilute case, interaction between the fibers results in stress concentration on them which deviates from that observed for a single fiber embedded in an unbounded matrix and, due to the randomness of the structure of the composite, is a random function of spatial coordinates. The peak stress location and level are rather sensitive to the arrangement type of the fibers and, therefore, their reliable prediction requires an adequate account of microstructure statistics of actual FRCs and interactions between the fibers. This problem becomes even tougher when the local stress concentration in composites with statistically nonuniform fiber distribution is considered. The difficulty associated with a quantitative description of this effect comes from the fact that the ergodic hypothesis does not hold for the materials with nonuniform microstructure and, therefore, ensemble averaging cannot be replaced by volume averaging and substantial statistical analysis is required (see, for example, [Beran 1968; Torquato 2002]).

A promising way to account for fiber arrangement statistics and interactions between fibers is known in the mechanics of composites as *regularization*, or *representative unit cell* approach (see, for example, [Golovchan et al. 1993; Byström 2003; Drago and Pindera 2007]). It is based on modeling the structure

of an actual heterogeneous solid by a periodic medium whose representative unit cell contains a number of inhomogeneities. This approach appears to be advantageous in that the quasirandom microstructure of such a material, with prescribed statistical structure parameters, can be specified explicitly. Moreover, due to the deterministic nature of this model, it is possible to formulate and solve the periodic model problem accurately and thereby to account for the interactions among the inclusions in a rigorous manner. Below, we refer to a few publications, most relevant to the problem under study, where the above mentioned approach was applied.

The papers [Pyrz 1994a; 1994b; Pyrz and Bochenek 1998] address the problems encountered in the quantitative description of arrangements and correlations in unidirectional fiber reinforced composite materials. It has been indicated there that both topological and second-order statistics are related to the local stress variability under transverse loading conditions. Particular attention was paid to the variability of interfacial maximal radial stresses, and the conclusion was made that peak radial stresses increase with a decrease in the space between fibers. However, the stress analysis performed there must be considered as rather qualitative because the iterative model method they applied is based on superposition of Eshelby's solutions and thus assumes constancy of stress inside the fiber. This assumption may be acceptable for the mean stress evaluation in a weakly heterogeneous material; however, a peak local stress even in the two-fiber problem (see [Buryachenko and Kushch 2006], for example) cannot be captured this way. As shown in [Ganguly and Poole 2004] by comparison with numerical solutions, the iterative model can only be applied to dilute composites with widely separated fibers; more exactly, it is limited to distributions where the minimum interfiber distance exceeds the fiber radius three or more times. To account for interactions between the closely-placed fibers typical of FRC microstructure, an accurate analytical or numerical method should be applied.

In [Babuška et al. 1999], an analysis is focused on the stochastic constitutive properties and statistics of the peak local fiber-matrix interface stresses. For this purpose, a file of the fibers' location and diameter was generated by processing the digitized micrograph of the composite plate cut and, these data were used to formulate the structure model and boundary-value problem. The traction boundary conditions at the cell sides were taken into account by means of a superframe. The numerical method used to solve for stress is the $p$-version of the finite element method combined with the homogenization procedure. The authors have obtained descriptive statistics of peak interface stresses in FRCs and have shown that actual distribution of fibers produces only a minor effect on the overall elastic properties of the composite.

Chen and Papathanasiou [2004] have used a parallel many-processor implementation of the boundary element method to study the peak stresses in an FRC using a model containing 144 fibers randomly placed inside the square matrix domain. The cell geometry was generated using a Monte Carlo algorithm, controlling the minimum allowable interfiber and fiber-cell side spacing. The resulting interface stresses were found to follow a Weibull-like distribution and the conclusion was reached that the key structure parameter affecting the interface stresses is the distance between the fibers.

In [Kushch et al. 2008] we developed an efficient, multipole expansion technique-based method and numerical code for evaluating the microstress field in a fibrous composite. The method combines the superposition principle, the theory of complex potentials, and Fourier series expansion, in order to reduce the meso cell model problem to an ordinary, well-posed set of linear algebraic equations. By averaging over a number of random structure realizations, statistically meaningful results have been obtained for both the local stress and effective elastic moduli of disordered fibrous composites. It was found, in

particular, that the peak interface stress distribution is fitted well by Gumbel-type statistics of extreme values.

In the present paper, the method of [Kushch et al. 2008] is applied to study the relationship between the fiber arrangement type and the local peak interface stress statistics in FRCs. To this end, the representative unit cell model of fibrous composites capable of simulating both the uniform and clustered random fiber arrangements is used. A series of computational experiments has been carried out and the empirical probability functions have been obtained for the nearest neighbor distance and the peak interface stress. It is shown that the statistical parameters considered are rather sensitive to the fiber arrangement, particularly cluster formation. An explicit correspondence between them is established and the relevant analytical formulas are written. Application of the statistics of extremes to the local stress concentration study is discussed and the conclusion is reached that, with a high degree of probability, the peak interface stress distribution in FRCs with uniform random arrangement of fibers follows the Fréchet rule. Based on the established statistical distributions of local peak stress, a simple microdamage model of FRCs has been suggested.

## 2. Representative cell model of random structure FRCs

**2.1.** *Model geometry.* It was already pointed out in the Introduction that reliable prediction of FRC damage onset and accumulation requires the use of a geometric model statistically close to the microstructure of an actual FRC and an adequate account for interactions between the fibers. This, in turn, necessitates a statistical description of both the geometry and local stress field because random microstructure is inherent for the most FRCs (and hence the stress field appears to be a random function of spatial coordinates as well). On the other hand, the local damage level and strength limit of an FRC is governed by the peak local stress level (rather than its mean value) and location, which is quite sensitive to the fiber arrangement. Therefore, using the probability theory formalism seems to be an adequate, and probably the only consistent, way of linking the statistical parameters of microstructure and peak local stress distribution.

To meet these requirements, we use the many-fiber two-dimensional unit cell model of the FRC bulk, shown in Figure 1. Specifically, we consider a quasirandom, or generalized periodic, model structure (as in [Golovchan et al. 1993; Byström 2003], among others) with the periods $a$ and $b$ along the axes $Ox_1$ and $Ox_2$, respectively, a unit cell of which contains a certain number of fibers of radius $R$, aligned in the $x_3$ direction and circular in cross-section. Within a cell, the fibers can be placed arbitrarily but without overlapping. A geometry of the unit cell is given by its length $a$ and height $b$ and the coordinates $(X_{1q}, X_{2q})$ of the centers of inclusions $O_q$, $q = 1, 2, \ldots, N$. The whole composite bulk can be obtained by translating the cell in two orthogonal directions. Besides the global Cartesian coordinate system $Ox_1x_2$, we introduce the local, inclusion-related coordinate systems $Ox_{1q}x_{2q}$ with origins in $O_q$. Also, we will use the complex-valued variables

$$z = x_1 + ix_2, \quad z_q = x_{1q} + ix_{2q}, \tag{1}$$

representing the point $x = (x_1, x_2)^T$ in the complex planes $Ox_1x_2$ and $Ox_{1q}x_{2q}$, respectively. Clearly, $z = z_q + Z_q$, where $Z_q = X_{1q} + iX_{2q}$. The number $N$ of fibers with centers inside the cell can be taken to be sufficiently large to approach the microstructure of an actual disordered composite.
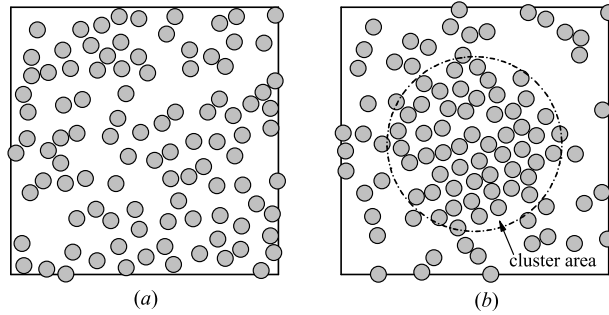
**Figure 1.** Unit cell model of the FRC bulk with (a) uniform and (b) clustered microstructure.

To generate the quasirandom structure shown in Figure 1, the molecular dynamics algorithm of growing particles is used. An idea of the algorithm is as follows: we start with a certain prescribed number of tiny fibers whose initial positions within a cell and initial velocities are given by the random number generator. Then, the fibers move toward each other, collide elastically, and grow steadily during a period of $1000N$ collisions. In the case any fiber (more exactly, its center) traversed the cell boundary, it enters the cell from the opposite side. It preserves both the fiber volume content and periodicity of structure. After the volume content of fibers reached the prescribed value, the system is further equilibrated for a period of $5000N$ collisions, sufficient to guarantee reproducible thermodynamic properties of the model [Torquato 2002].

The geometry considered can be characterized by several parameters, including the fiber volume content $c = N\pi R^2/ab$, coordination number, second-order intensity function, radial distribution function, etc. (see, for example, [Pyrz 1994b; Buryachenko et al. 2003]). The structure parameters we focus on are the normalized nearest-neighbor distance,

$$d_m = \min_{p \neq q} \left| Z_{pq} \right| / D,$$

and interfiber spacing $\delta = d_m - 1$, where $Z_{pq} = Z_p - Z_q$ defines the relative position of the fibers and $D = 2R$ is the diameter of a fiber. In the many-fiber models of FRC, the "minimum allowable interfiber spacing" parameter $\delta^*$ [Chen and Papathanasiou 2004] is often introduced so that any two fibers are effectively separated: $\delta \geq \delta^* > 0$. It is also known as the impenetrability parameter, in terms of the cherry-pit model [Torquato 2002]. Obviously, the smaller $\delta^*$ is, the stiffer the model boundary value problem is (no matter what analytical or numerical method we apply to solve it), and the higher the expected local stress concentration is. By prescribing a fixed allowable spacing $\delta^*$, we, in fact, predetermine the maximum allowable stress; and, to be consistent with practice, this parameter should be taken to be as small as possible. Some idea of how the stress concentration is affected by $\delta$ can be gotten from the stress asymptotes for nearly touching fibers. Note that the stress remains finite when the fibers are drawn together ($\delta \to 0$; see Figure 2): the stress singularity is expected only in the case of rigid (nondeformable) fibers. A small positive value is usually assigned to this parameter in order to separate fibers and thus alleviate either analytical or numerical analysis of the boundary value problem. In the present study, $\delta^* = 0.01$ is taken. Variation of this parameter slightly influences the absolute value of the local stress concentrations, but does not change the qualitative behavior of the local and averaged fields.
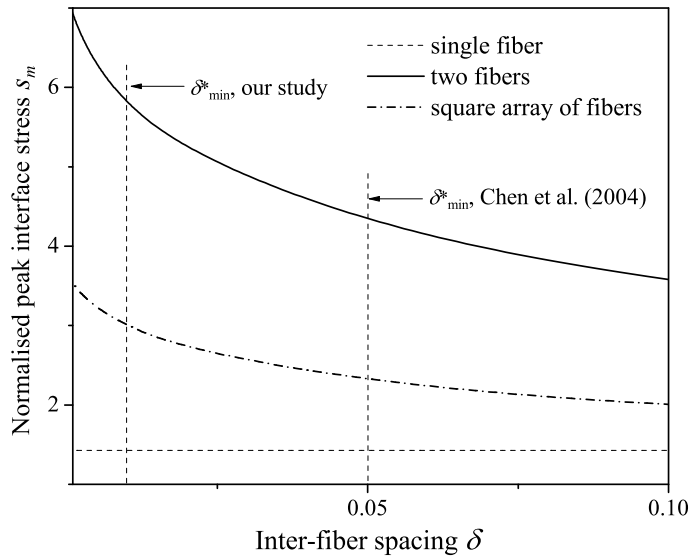
**Figure 2.** Interface stress concentration as a function of interfiber spacing.

The model we consider is sufficiently flexible to also simulate a composite with nonuniform distribution of fibers. Specifically, we consider the cluster of fibers of circular shape shown in Figure 1(b): its size is defined by the radius $R_{\text{cl}}$ or, alternatively, by the volume content of clusters $c_{\text{cl}} = \pi R_{\text{cl}}^2 / ab$. Due to presence in this model of an additional structure parameter, the cluster radius $R_{\text{cl}} \gg R$, it can be thought of as a meso level model; for more discussion on the subject, see [Mishnaevsky 2007]. It can be obtained in the following way: first, the uniform microstructure is generated as described above, with the fiber volume content $c_{\text{in}}$ equal to that inside the cluster. The fibers outside the cluster are then removed randomly, one by one, until the prescribed overall volume content $c$ is reached. A drawback of this simple method is that the random elimination procedure may lead to the percolation type structure. In principle, it is possible to fix this problem by applying the previously described "equilibration" procedure to the area outside the cluster. In our numerical study, the fiber volume content outside the cluster $c_{\text{out}}$ is sufficiently low and we expect the mentioned nonuniformity of the microstructure to produce a minor effect on the statistics of elastic fields.

**2.2. Model problem.** By adopting a two-dimensional model, we assume $\partial \sigma_{ij} / \partial x_3 = 0$: within this framework, the plane strain, plane stress and antiplane shear (in the $x_3$-direction) problems can be studied. Specifically, we consider the plane strain problem ($u_3 = 0$) as a consequence, and $\varepsilon_{33} = \varepsilon_{13} = \varepsilon_{23} = 0$ as well. Both the matrix and fiber materials are isotropic and linearly elastic.

We denote by $u_m = u_{m1} + i u_{m2}$ the displacement in a matrix material with a shear modulus $G_0$ and Poisson ratio $\nu_0$; $u_i^{(q)}$, $G_q$, and $\nu_q$ refer to displacement and elastic moduli, respectively, of the $q$th fiber, $q = 1, 2, \ldots, N$. Here, $u_i$ are the Cartesian components of the displacement vector $u = (u_1, u_2)^T$. At the matrix-fiber interfaces, perfect bonding conditions are prescribed:

$$\left( u_m - u_i^{(q)} \right) \big|_{|z_q|=R} = 0, \quad \left( \tau_n(u_m) - \tau_n(u_i^{(q)}) \right) \big|_{|z_q|=R} = 0, \qquad q = 1, 2, \ldots, N, \tag{2}$$

where $\tau_n = \sigma_{rr} + i \sigma_{r\varphi}$.

The stress field in the composite bulk is assumed to be macroscopically homogeneous, which means constancy of the volume-averaged, or macroscopic, strain $\varepsilon^* = \{\varepsilon_{ij}^*\} = \{\langle \varepsilon_{ij} \rangle\}$ and stress $\sigma^* = \{\sigma_{ij}^*\} = \{\langle \sigma_{ij} \rangle\}$ tensors, where $\langle f \rangle = \int_V f \, dV$ and $V$ is the cell volume; in our case, $V = ab$.

In the problem we consider, the far field load can be defined either by the macroscopic strain tensor $\varepsilon^*$, or by the macroscopic stress tensor $\sigma^*$. The first case is typical in the homogenization problem where the macroscopic, or effective, moduli are of the primary interest. On the other hand, using the macrostress tensor $\sigma^*$ as a load governing parameter is preferable in the local stress concentration study. Next, it is common knowledge that under macroscopic stress homogeneity conditions, periodicity of structure results in periodicity of relevant physical fields. In our case, the periodicity condition

$$\sigma_{ij}(z+a) = \sigma_{ij}(z+ib) = \sigma_{ij}(z) \tag{3}$$

can be alternatively regarded as the cell boundary condition providing continuity of the displacement and stress fields between the adjacent cells.

### 2.3. *Numerical method and implementation.*

It should be clearly understood that a one-time solution of the model problem for a specific realization of quasirandom geometry shown in Figure 1 is not sufficient for our purpose, even if it is highly accurate. A convergent and statistically valid solution requires a sufficiently large number of numerical tests $N_{\text{test}}$ to be conducted, with subsequent averaging the numerical data obtained. In this situation, the efficiency of the method we apply to solve for stress is of critical importance. It appears that a total computational cost of the direct numerical (finite element and boundary element) methods is exceedingly large. A preferable choice is the multipole expansion-based technique (see [Greengard and Helsing 1998; Wang et al. 2005], for example), which provides fast and accurate solutions for the problems of this kind. The theory and numerical algorithm of the method we apply in this work is exposed in [Kushch et al. 2008]. Here, we note only that this method combines the superposition principle, the theory of complex potentials, and the Fourier series technique to give an asymptotically exact solution. This means that, in order to get the exact values, one must solve an infinite set of linear equations. In practice, it is solved by applying the truncation method where only a finite number $N_{\text{eqn}}$ of equations and unknowns is retained in the infinite system. An approximate solution obtained in this way converges to the exact one with $N_{\text{eqn}} \to \infty$ and, thus, any desirable accuracy can be achieved by the proper choice of $N_{\text{eqn}}$.

Numerical efficiency of the method stems from the fact that the main part of the solution, namely, reduction of the cell model boundary-value problem to a system of linear algebraic equations, is done analytically. The matrix coefficients of this system are given by simple rational expressions and, unlike in the direct numerical schemes, involve no integration. Instead, they contain the absolutely convergent ordinary sums which can be calculated in advance. In fact, the most computation time is spent by the linear solver and, to provide high performance, the generalized minimum residuals (GMRES) algorithm of [Saad and Schultz 1986] with a block-Jacobi preconditioner is applied. In our numerical study we used open source GMRES code in Fortran [Fraysse et al. 1998], with minor modifications. All the below reported numerical data correspond to the uniaxial tension $\sigma_{22}^* = P$ of a model FRC (Figure 1). The following elastic properties of the components of the composite are taken: $E_0 = 3.2$ GPa and $\nu_0 = 0.36$ for the matrix; $E_p = 70.6$ GPa and $\nu_p = 0.25$ for fibers [Meraghni et al. 2002].

Three main parameters governing convergence and accuracy of the below performed statistical study are the number $N_{\text{fib}}$ of fibers with the centers inside the unit cell, the number $N_{\text{harm}}$ of harmonics retained in the series expansion of local field, and the number $N_{\text{test}}$ of the random structure realizations taken for averaging. Obviously, all these numbers should be taken to be sufficiently large to provide reliable numerical results. On the other hand, a total computational effort of this study scales as $(N_{\text{eqn}})^2 N_{\text{test}}$, where the number of equations retained in the linear system is $N_{\text{eqn}} = 2 N_{\text{fib}} N_{\text{harm}}$. To minimize computational time, the appropriate numbers $N_{\text{harm}}$, $N_{\text{fib}}$ and $N_{\text{test}}$ should be taken. Their choice is based on the convergence study of [Kushch et al. 2008]; in the subsequent numerical study, we take $N_{\text{harm}} = 20$, $N_{\text{fib}} = 100$ and $N_{\text{test}} = 50$. In our numerical experiments, we put $a = b = R\sqrt{\pi N_{\text{fib}}/c}$.

## 3. Peak interface stress in FRCs

**3.1.** *Deterministic models.* Now, we proceed with analysis of the local stress field in a FRC. Specifically, we study an effect caused by the fiber arrangement type on the interface stress concentration, or normalized peak stress,

$$s_m = \max_{0 \leq \varphi < 2\pi} \sigma_{rr}/P.$$

Assuming this stress is responsible for the damage (say, interface crack) onset, one can think of the "interface strength" affected by microstructure. Sometimes [Degrieck and van Paepegem 2001; Foster et al. 2006], the debonding criterion is taken in more general form

$$(\sigma_{rr})^2 + \beta(\sigma_{r\varphi})^2 = \text{const},$$

which, however, does not alter the way of the structure-strength relationship study. And, although we restrict ourselves to considering the uniaxial tension $\sigma_{22}^* = P$, the extension to the complex macrostress state is rather straightforward since the theory we use is valid for an arbitrary loading type.

In the case of periodic arrangement of fibers, one-to-one functional relationship between the structure parameters and stress concentration can be established. In Figure 2, the $s_m$ value is shown as a function of normalized nearest neighbor distance in the composite with a square packing of fibers, where $d_m = 2\sqrt{\pi/c}$. An accurate analysis shows that peak interface stress grows as the volume content $c$ of fibers increases. In the dilute case $c \to 0$ ($d_m \to \infty$), we have $s_m = 1.426$ (dashed line); the stress concentration between two fibers embedded in an unbounded solid ($Z_{12} = 0 + id_m$) is shown in Figure 2 by the dash-dotted line. As seen from the plot, the two-fiber solution can serve as the upper bound of the peak interface stress $s_m(d)$ in the composite, and the $s_m \approx 7$ observed for two nearly touching fibers is, probably, the maximum interface stress attainable in the composite of arbitrary microstructure for these phase properties and loading type. Note that for $\delta^* = 0.05$, adopted in [Chen and Papathanasiou 2004], the probable $s_m$ underestimation is almost twofold. As for the previously mentioned iterative model used in [Pyrz and Bochenek 1998], its applicability condition is $\delta^* > 0.5$ [Ganguly and Poole 2004], which, as seen from Figure 2, leaves no chance to get the correct numbers for local stress. In the subsequent numerical study, we put $\delta^* = 0.01$, which seems to be a reasonable compromise between accuracy and computational effort.

In the random structure FRCs, one cannot expect a deterministic correlation between the nearest neighbor distance and stress concentration $s_m$, as they both appear to be random numbers. Their statistical distributions will be analyzed below.

**3.2. *Peak stress statistics in the random structure FRC.*** For the ordered sample $s_m^{(q_1)} \le s_m^{(q_2)} \le \ldots \le s_m^{(q_N)}$ obtained from the computational experiment, we define the empirical cumulative probability function

$$\widehat{F}(\sigma) = \Pr\left[s_m^{(q_i)} < \sigma\right] = (i - 0.5)/N_{\text{fib}}. \tag{4}$$

Here, $s_m^{(q_i)}$ means a normalized peak stress at the interface between matrix and $q_i$th fiber. To obtain the test-independent data, $s_m^{(q_i)}$ were averaged over 50 runs at a given fiber volume content $c$. The empirical probability function (4) obtained by computer simulations for $c$ from 0.1 to 0.5 is shown in Figure 3.

Numerical study shows that there always exists (regardless of $c$) a relatively low fraction of fibers with rather high interface stress. As would be expected, the maximum stress is localized between the closely placed fiber pairs and greatly exceeds the mean stress value. In terms of interface strength, this means that debonding will occur in these "hot spots" much earlier than in the other sites. This observation correlates well with — and can be quite a plausible explanation of — the experimentally observed ([Brøndsted et al. 1997; van Paepegem and Degrieck 2002], among others), rapid FRC stiffness degradation due to matrix-fiber debonding at the initial stage of cyclic loading. Similar data were reported in [Kushch et al. 2008], where an analytical approximation of the peak stress distribution by the generalized "chain-of-bundles" rule $F(\sigma) = \exp(-\exp(-k(\sigma^\alpha - \sigma_c)))$, known also as the generalized Gnedenko–Gumbel distribution [Bolotin 1988] has been suggested. It was shown there that the Weibull's statistics of peak interface stress claimed in [Chen and Papathanasiou 2004] apply only to the model FRC with well-separated fibers ($\delta_{\min} \ge 0.05$), which considerably underestimates the true interface stress.

**3.3. *Peak interface stress and statistics of extremes.*** Thus, an intriguing question arises: is such a close correlation between the peak stress statistics obtained from numerical tests and the known statistical distributions, used by us as the fitting functions, simply a matter of luck? Or is it possibly the manifestation of a certain intrinsic rule? In attempt to answer this question, we refer to the statistical theory
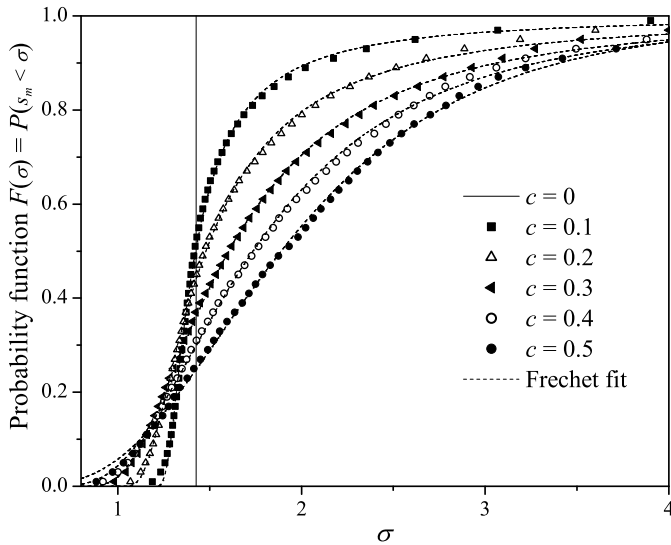


**Figure 3.** Empirical probability function of the peak interface stress $s_m$: an effect of fiber volume content.

of extreme values called *statistics of extremes*. This is a modern and rather promising branch of the probability theory [Beirlant et al. 2004]; for a reader unacquainted with the statistics of extremes, a brief introductory note is provided below.

Extreme values theory is concerned with probabilistic and statistical questions related to very high or very low values in sequences of random variables and in stochastic processes. The subject has a rich mathematical theory and applications in a variety of areas. Historically, work on extreme values problems may be traced back to as early as 1709, when N. Bernouilli discussed the mean largest distance $M(\xi)$ from the origin, given $N$ points $X_n$ lying at random on a straight line of a fixed length $L$: $\xi = \max_n X_n$. The first systematic account of the statistical theory of extremes was done by Gumbel [1958], who studied, in particular, statistics of meteorological phenomena such as snowfalls, wind gusts and river floodings. The typical problem of this class consists in finding the probability $\Pr[\max X_n \geq h]$ where, say, $X_n$ is the river level and $h$ is the dam height. Needless to say, this number is of vital importance because it speaks of the likelihood of catastrophic event. Analogous, practically important problems arise in a variety of areas including natural sciences, military and civil engineering, weather, climate, finances, stock marketing, etc.

The first writer to realize the close connection between specimen strength and distribution of extreme values seems to be F. T. Peirce of the British Cotton Industry Association. The application of essentially the same ideas to the study of the strength of materials was carried out by von Mises and W. Weibull, among others; for more details, see [Freudenthal 1968; Beirlant et al. 2004]. However, Gumbel was the first to call the attention of engineers and statisticians to the possible applications of the formal extreme-value theory to certain distributions which had previously been treated empirically. One of the principal results of this theory is the so-called *Three Types Theorem*, originally stated without mathematical proof in [Fisher and Tippett 1928] and later derived rigorously in [Gnedenko 1943]. It asserts that if a distribution function does not put all its mass at a single point, it must be one of three types:

Gumbel type: $\qquad G(x) = \Pr[\xi < x] = \exp\left(-\exp\left((x - p_1)/p_3\right)\right), \text{ all } x;$ $\qquad$ (5)

Fréchet type: $\qquad F(x) = \Pr[\xi < x] = \begin{cases} 0 & \text{for } x < p_1, \\ \exp\left(-(x - p_1)/p_3\right)^{-p_2} & \text{for } x \geq p_1; \end{cases}$ $\qquad$ (6)

Weibull type: $\qquad W(x) = \Pr[\xi < x] = \begin{cases} \exp\left(-(p_1 - x)/p_3\right)^{p_2} & \text{for } x \leq p_1; \\ 1 & \text{for } x > p_1; \end{cases}$ $\qquad$ (7)

where $p_1$, $p_2$, $p_3$ are parameters, the last two of which are positive. In fact, this theorem gives a rigorous theoretical substantiation to the already known, empirically found statistical distributions. Importantly, it also says what kind of distribution is expected in that or another case. They differ by shape and, due to their behavior at large $x$, are sometimes called long-tailed (Fréchet), medium-tailed (Gumbel) and short-tailed (Weibull). The corresponding distributions of $(-\xi)$ are also called extreme value distributions; in this case we come to the Weibull function in its commonly known form:

$$W(x) = 1 - \exp\left(-((x - p_1)/p_3)^{p_2}\right) \quad (x > p_1). \qquad (8)$$

Now, we come back to our problem and reveal that it also can be thought of in the context of statistics of extremes. We do not claim to have a rigorous proof of the applicability of the Three Types Theorem to the random variable $s_m = \max \sigma_{rr}/P$; rather, we try to check it numerically. For the uniaxial tension

|       | $c = 0.1$ | $c = 0.2$ | $c = 0.3$ | $c = 0.4$ | $c = 0.5$ | $b_{i0}$ | $b_{i1}$  | $b_{i2}$ |
|-------|-----------|-----------|-----------|-----------|-----------|----------|-----------|----------|
| $p_1$ | 1.19      | 0.939     | 0.473     | $-0.265$  | $-2.78$   | 1.246    | $-0.0441$ | 0.111    |
| $p_2$ | 1.45      | 1.65      | 2.27      | 3.29      | 6.70      | 1.393    | 0.0389    | 0.102    |
| $p_3$ | 0.181     | 0.433     | 0.962     | 1.79      | 4.42      | 0.128    | 0.0492    | 0.112    |

**Table 1.** Parameters of the fitting function (8).

$\sigma_{22}^* = P$, the conservative bound for $s_m$ is $s_m > 0$. Thus we consider, at least formally, the Fréchet distribution (6) as a plausible analytical form of the cumulative probability function $F(\sigma) = \Pr\{s_m < \sigma\}$. The values of parameters $p_i$ in (6), found by the least-square fit of the numerical data in Figure 3, are given in Table 1. The negative $p_1$ (for example, equal to $-2.78$ for $c = 0.5$) does not cause problems: while compressive $s_m$ is formally allowed in (6), the estimated probability of $(s_m < 0.5)$ is $6.3 \cdot 10^{-4}$ and that of $(s_m < 0)$ about $2 \cdot 10^{-10}$ — that is, an impossible event.

The corresponding best fit curves are shown in Figure 3 by the dashed lines. As seen from the plot, the results of (6) practically coincide with those of the computer simulation, if we take appropriate values for the $p_i$. An attempt to use the Gumbel distribution (5) as a fitting function (dash-dotted curves in Figure 4) cannot be considered as successful; the discrepancy is significant and peaks in the high stress area, which is the area responsible for strength and therefore the most interesting to us. Finally, the Weibull-type distribution (7) fails completely to approximate the data obtained from numerical experiments; but the fit by the Weibull function (8) is almost as good as that of (6). For $c = 0.1$ the goodness of the fit in terms of reduced $\chi^2$ parameter is equal to $1.5 \cdot 10^{-4}$ for (6), $1.5 \cdot 10^{-3}$ for (8) and $2.7 \cdot 10^{-3}$ for (5); the same tendency exists for higher values of $c$.

Thus, the conclusion can be drawn that, with a high degree of probability, the peak interface stress distribution in FRCs with uniform random arrangement of fibers follows the Fréchet rule. Using the data from Table 1, one also can find the dependencies $p_i = p_i(c)$. It turns out that all $p_i$ are fitted satisfactorily
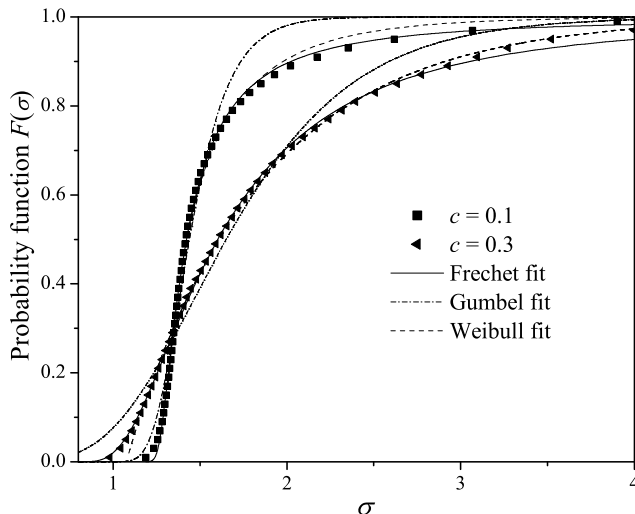


**Figure 4.** Fréchet, Weibull and Gumbel distributions as fitting functions.

by the function $p_i(c) = b_{i0} + b_{i1} \exp(c/b_{i2})$; the coefficients $b_{ij}$ are given in the last three columns of Table 1. Below, we take $F(\sigma) = \exp\big(-(p_3(c)/(\sigma - p_1(c)))^{p_2(c)}\big)$ as the analytical form of the probability function $\Pr[s_m < \sigma]$.

## 4. Correlation between microstructure and peak stress

**4.1.** *Microstructure statistics: nearest neighbor distance.* Since stress concentration on a given fiber is greatly amplified by the surrounding fibers, peak stress location and magnitude appear to be rather sensitive to the fiber arrangement type. Therefore, reliable prediction of $s_m$ distribution requires an adequate account for the microstructure statistics of actual FRCs. The most important factors characterizing microstructures of composites are shape, volume fraction, and arrangement of the constituents. The latter, in turn, can be characterized by several parameters, including coordination number, particle cage, interparticle spacing, second-order intensity (Ripley's) function, radial distribution function, nearest neighbor distribution function, two-point cluster function, etc. (see, for example, [Pyrz 1994b; Babuška et al. 1999; Torquato 2002; Buryachenko et al. 2003]).

At the same time, a very few publications are known to the authors where the relationships between the statistics of structure and local fields were established. The attempts to use the marked correlation function as a link between the geometrical features of a microstructure and stress concentration [Pyrz 1994a; 1994b; Pyrz and Bochenek 1998; Chen and Papathanasiou 2004] cannot be considered convincing. Probably, the most definite (mainly qualitative, however) conclusion drawn there is that $s_m$ amplification and its variability is strongly affected by the nearest neighbor distance and nearest neighbor orientations of adjacent fibers, and therefore the stress amplification is more pronounced for the clustered structure as compared with the statistically uniform one. An important and challenging question arises regarding the $s_m - d_m$ correlation in a FRC with random microstructure.

To answer this question, we use results of Torquato [1995] on nearest neighbor statistics for the packing of hard disks. He introduced the exclusion probability function $E(r)$, equal to the probability that a circular region of radius $r$ encompassing the reference fiber is free of other fiber centers. In our notation, $E(r) = \Pr[d_m > r/D]$. The following analytical representation was found by Torquato:

$$E(r) = \exp\big(-c(4a_0(r^2/D^2 - 1) + 8a_1(r/D - 1))\big), \tag{9}$$

where $a_0 = (1 + 0.128c)/(1 - c)^2$ and $a_1 = -0.564c/(1 - c)^2$. To apply these results to our case, we account for the parameter $\delta^*$ (minimum interfiber spacing) introduced in Section 2. Specifically, in (9) we use $\widetilde{r} = r/(1 + \delta^*)$ and $\widetilde{c} = c(1 + \delta^*)^2$ instead of $r$ and $c$.

Figure 5 compares the results calculated according to (9) with our numerical results on the nearest neighbor statistics. There, the symbols represent the empirical exclusion probability function obtained in the following way. First, for each fiber we find

$$d_m^{(q)} = \min_{p \neq q} |Z_{pq}|/D;$$

next, for the ordered sample $d_m^{(q_1)} \leq d_m^{(q_2)} \leq \ldots \leq d_m^{(q_N)}$ we define the empirical cumulative probability function

$$\widehat{E}(r) = \Pr\big[d_m^{(q_i)} > r/D\big] = 1 - (i - 0.5)/N_{\text{fib}}. \tag{10}$$
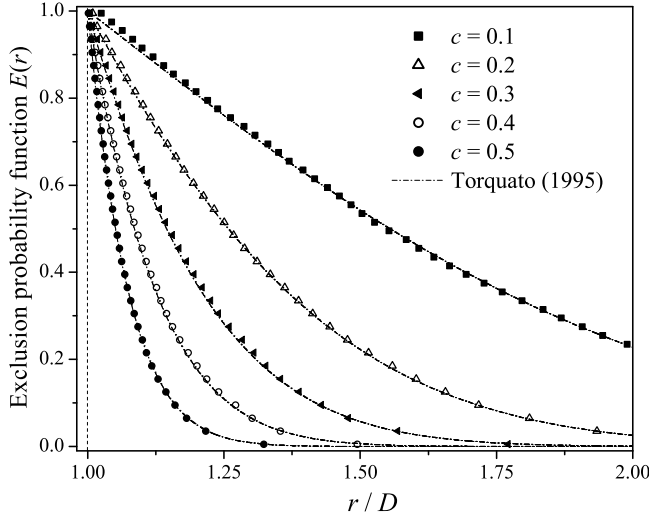
**Figure 5.** Exclusion probability function: numerical simulation and approximation.

To obtain the test-independent data, $d_m^{(q_i)}$ were averaged over 50 realizations of random structure for a given fiber volume content $c$. As seen from the plot, the results of the computer simulation are in very close agreement with the theory, which validates the algorithm and computer code used for generation of the cell geometry. Hence, one can use (9) as an analytical characteristic of the statistically uniform random microstructure of FRCs.

**4.2. *Stress concentration versus nearest neighbor distance.*** Both $s_m$ and $d_m$ are the random numbers: no direct functional dependence is expected between them. At the same time, such a relationship can be easily found between the arguments of the relevant probability functions, $F(\sigma)$ and $E(r)$. Namely, we equate the probability of finding the neighbor fiber at the distance larger than $d_m$ to the probability that the peak interface stress $s_m$ does not exceed a certain value $\sigma$. By combining (9) and (6) we get the explicit formula

$$\sigma(r) = p_1(c) + p_3(c)\big(c(4a_0(r^2/D^2 - 1) + 8a_1(r/D - 1))\big)^{-1/p_2(c)}. \tag{11}$$

The empirical dependencies $\sigma(r)$ obtained by matching the numerical data in Figures 3 and 5 are shown in Figure 6 by discrete symbols; the dash-dotted lines represent (11). As seen from the plot, agreement between the numerical data and their analytical representation is quite close. The tendency observed in Figure 6 of the peak stress decreasing with the increase of $c$ is to be anticipated: the higher the fiber volume content is, the less room is left for the isolated clusters of a few fibers where the high interface stress concentration is most probable.

Equation (11) deserves a certain criticism because $d_m$ is the leading, but in no way the only, factor affecting $s_m$. Another important structure parameter is the nearest neighbor orientation [Pyrz and Bochenek 1998] characterized by the angle $\varphi_m$ between the line connecting the centers of nearest fibers and loading direction. Some idea of correlation between $s_m$ and $\varphi_m$ can be gotten from Figure 7, where the raw data of computer simulation for $c = 0.4$ are shown. An angular dependence on peak stress is clearly seen: as expected, the highest $s_m$ is observed in the fiber pairs with $\varphi_m$ close to $\pm\pi/2$. For the sake of
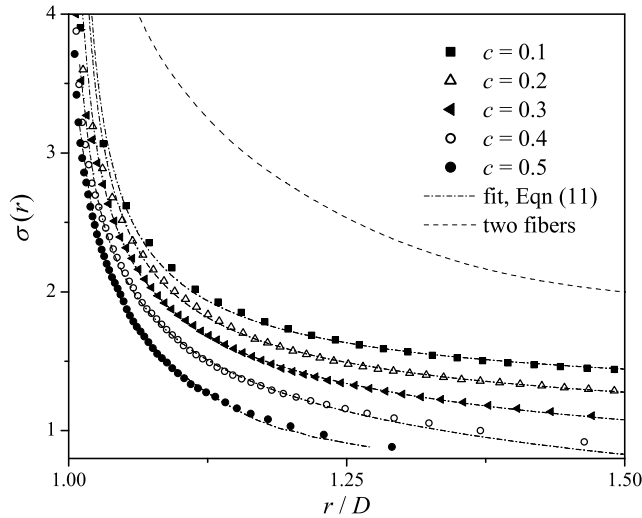
**Figure 6.** Peak interface stress versus interfiber distance: an effect of fiber volume content.
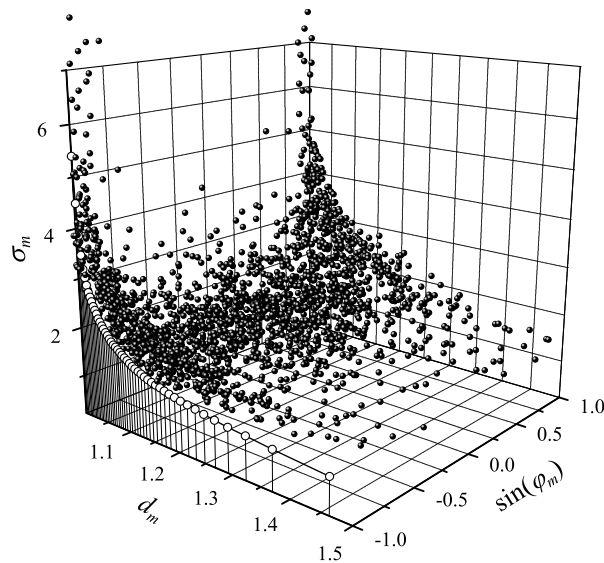


**Figure 7.** Peak interface stress versus nearest neighbor distance and orientation.

comparison, the corresponding curve $\sigma(r)$ taken from Figure 6 is shown in Figure 7 by the open circles. The conclusion can be made from this comparison that (11) gives a reasonable $s_m$ approximation for $\varphi_m$ close to $\pm\pi/2$ where the highest stress, and hence local damage, is expected.

Equation (11) is not perfect also in the sense that it does not work for $r = D$. The problem is that (6) allows for arbitrarily large stress and it results in singularity of (11) for touching fibers, which is not correct. This problem can be readily fixed by adding a small constant or $c$-dependent term to the expression in figure brackets. However, as seen from Figure 6, even in its present form it provides a rather good fit of the numerical data for, at least, $r/D \geq 1.02$.
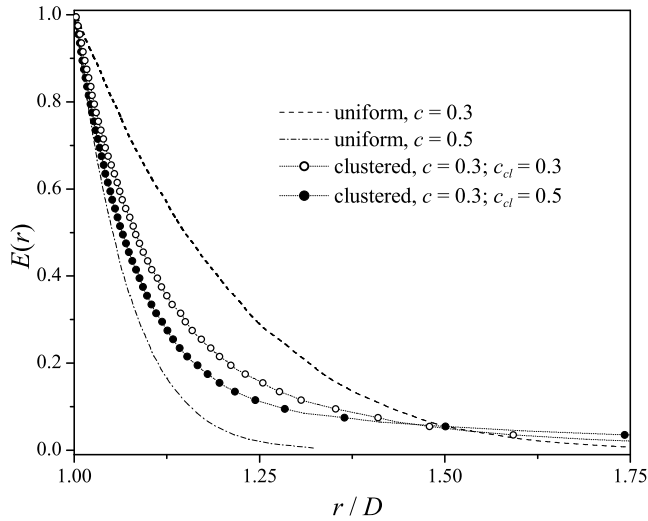
**Figure 8.** Exclusion probability function versus interfiber distance: an effect of cluster volume content.

**4.3.** *Effect of clustering.* Now, we consider local stress fields in FRCs containing fiber clusters of circular shape and estimate an effect of the cluster volume fraction $c_{cl}$. Specifically, we put the volume content of fibers in the cell and cluster $c = 0.3$ and $c_{in} = 0.5$, respectively. Obviously, $c = c_{in}c_{cl} + c_{out}(1 - c_{cl})$, where $c_{out}$ is the fiber volume content outside the cluster: for the clusters with $c_{cl} = 0.3$ and $c_{cl} = 0.5$, we get $c_{out} = 0.21$ and $c_{out} = 0.10$, respectively.

An effect of clusters on the exclusion probability function is seen in Figure 8, where the empirical function $\widehat{E}(r)$ obtained by computer simulation is shown by the solid and open circles. Here, for comparison's sake, we also plot $E(r)$ for FRC with uniform microstructure and $c = 0.3$ (dashed line) and $c = 0.5$ (dash-dotted line). As the comparison shows, it is rather sensitive to the nonuniformity in spatial distribution of fibers. Expectedly, a clustered structure contains a larger number of closely placed fibers. As a result, the initial slope of $\widehat{E}(r)$ is close to that of a uniform structure with $c = 0.5$ rather than $c = 0.3$ (recall that the overall fiber volume content in a clustered FRC is 0.3).

In Figure 9, the empirical probability function (4) $\widehat{F}(\sigma)$ is shown, calculated for the uniform and two clustered arrangements of fibers. The dash-dotted ($c_{cl} = 0.3$) and solid ($c_{cl} = 0.5$) curves deviate significantly from the dashed line representing the statistically uniform random structure. The data shown in Figure 9 confirm the observation made of [Pyrz 1994a] that the mean value of maximal radial stress shifts markedly towards higher values for clustered patterns. It is noteworthy, however, that the empirical function $F_s(\sigma)$ built over the cluster area and shown by the solid and open triangles in Figure 9 is statistically indistinguishable from that built over the whole cell area and shown in Figure 9 by dash-dotted and solid lines. This means that clusterization increases the peak interface stress on the fibers inside and outside the cluster simultaneously.

By analogy with Figure 6, one can match the numerical data in Figures 8 and 9 to get $\sigma(r)$ for a clustered structure (see Figure 10). Here, the difference between the uniform and clustered structure is also quite observable. The "universal" $\sigma(r)$ curve, valid for any fiber arrangement type, is improbable: instead, one can rather expect it to be dependent on the parameters determining the nonuniform structure.
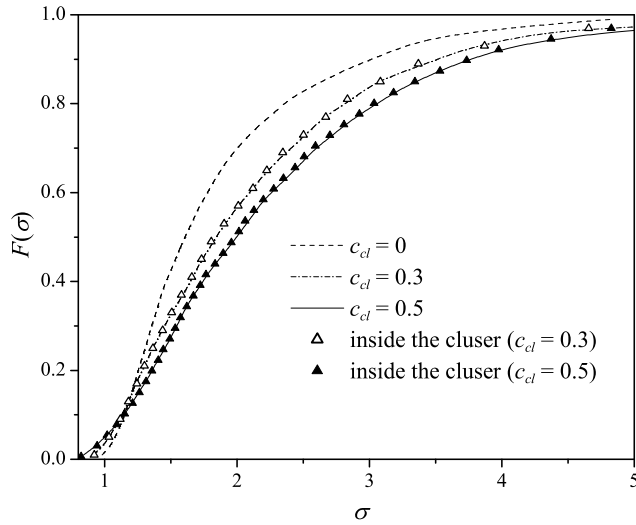
**Figure 9.** Peak interface stress distribution: an effect of the cluster volume content.
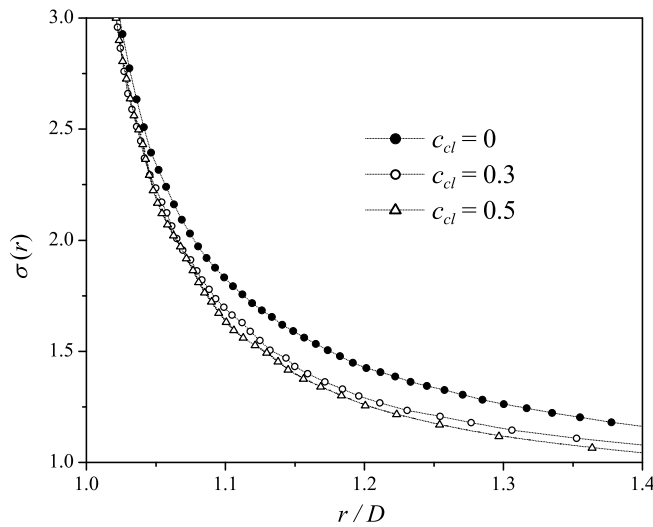


**Figure 10.** Peak interface stress versus interfiber distance: an effect of clusterization.

## 5. Microdamage model of FRC

The practical significance of the developed approach to studying the peak stress statistics is that it provides the theoretical background on which the micromechanics-based theories of FRC strength can be formulated. Below, we consider the simplest theory of this kind which, nevertheless, gives an idea of how available statistical information can be incorporated into the continuum damage model. Specifically, we assume that (a) the matrix-fiber interface is the "weakest link" in an FRC and that (b) debonding is

the only microdamage type. The damage criterion is taken in the form

$$\max_{0 \leq \varphi < 2\pi} \sigma_{rr} = \sigma_*,$$

where $\sigma_*$ is the interface strength: $\sigma_* = \text{const}$ for brittle fracture and $\sigma_* = \sigma_*(N_c)$ for fatigue, $N_c$ being a number of loading cycles. Alternatively, one can consider $\sigma_*$ to be varying randomly from fiber to fiber, with a known statistical rule. An elementary damage event is the interface crack appearance, so it seems natural to consider the interface crack density as a damage parameter. Namely, $D = N_{db}/N_{\text{tot}}$, where $N_{db}$ is a number of debonded fibers from a total number $N_{\text{tot}}$ of fibers in the representative volume element of FRC.

Now, we recognize that $N_{db}$ is a number of fibers with $s_m = \max \sigma_{rr}/P \geq \sigma_*/P$. Provided $N_{\text{tot}}$ is taken to be sufficiently large,

$$D = N_{db}/N_{\text{tot}} = \Pr\{s_m \geq \sigma_*/P\} = 1 - F(\sigma_*/P), \tag{12}$$

where $F$ is defined by (8). This formula gives an expression of damage level in terms of applied load $\sigma_{22}^* = P$ and interface strength $\sigma_*$. For example, assuming interface degradation due to cyclic loading, one can write the damage accumulation rule in an FRC as

$$D\left(N_c, \sigma_{22}^*, c\right) = 1 - \exp\left(-\left(\frac{p_3(c)}{\sigma_*(N_c)/P - p_1(c)}\right)^{p_2(c)}\right). \tag{13}$$

Note that (12) and (13) imply that $D$ is sufficiently low and interactions between the cracks can be neglected. That is, this model can describe an early stage of interface damage development, characterized by rapid stiffness reduction (see, for example, [Brøndsted et al. 1997; van Paepegem and Degrieck 2002]). At low $D$, the effect of interface cracks on the effective elastic modulus $E^*$ of FRC can be approximated by

$$E^*(D) = (1 - \beta D)E^*(0), \tag{14}$$

where $\beta$ is a factor to be found experimentally or from simulation (see [Meraghni et al. 1996; Zhao and Weng 1997], among others). Together with (13), Equation (14) gives an estimate of stiffness reduction degree versus number of loading cycles. Predicted by our theory normalized effective Young modulus $E^*(D(N_c))/E^*(0)$ for the fiber volume content $c = 0.2, 0.3, 0.4$ and $0.5$ is shown in Figure 11. Here, $\sigma_*(N_c) \backsim N_c^{-1/m}$ is assumed for interface fatigue; also, we put $\beta = 1.85$ and $m = 3$. As seen from the plot, theory reproduces, at least, qualitatively, the experimental observations in [Brøndsted et al. 1997; van Paepegem and Degrieck 2002].

It would be naive to expect close quantitative correlation between this simple model and the fatigue behavior of real-life FRCs. For each specific composite material, there is a number of factors affecting substantially its strength but not taken into account in our theory. However, the considered model can readily be generalized in many ways, including loading type, interface debonding criterion, fatigue law, residual (setting) stress, etc. Incorporation of these (as well as other analogous) features makes the model more realistic: at the same time, it necessitates conducting a new series of numerical experiments by analogy with those described above. This work would be the subject of a separate paper: here, we emphasize only that the developed approach does not require introducing any simplifying assumptions regarding the stress fields. In contrast to most existing continuum theories of FRC microdamage (for
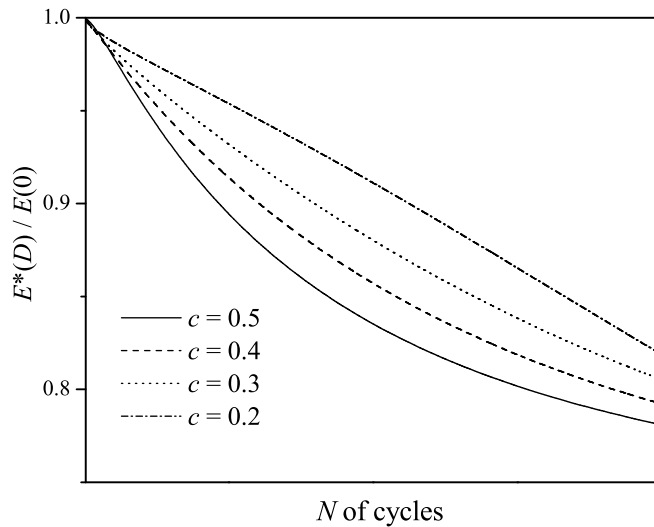
**Figure 11.** Stiffness reduction of an FRC due to cyclic loading.

their comprehensive review see, for example, [Degrieck and van Paepegem 2001]), we deal with the local, rather than phase-averaged, stress, which justifies application of the well-established strength criteria of phase materials and interfaces. Also, the proposed model provides a comprehensive account of microstructure and interactions between the fibers which cannot be expected in the theories based on the mean field or Eshelby-type models. Thus, the proposed approach captures the essential physical nature of the fatigue process and thus provides a reliable theoretical framework for a deeper insight into the fatigue damage initiation and accumulation phenomena in a fiber reinforced composite.

## 6. Conclusions

This paper addresses the effect of fiber arrangement and interactions on the peak interface stress statistics in a fiber reinforced material (FRC). The method we apply combines the multipole expansion technique with the representative unit cell model of random structure FRCs, capable of simulating both the uniform and clustered random fiber arrangements. By averaging over a number of numerical tests, the empirical probability functions have been obtained for the nearest neighbor distance and the peak interface stress. It is shown that the considered statistical parameters are rather sensitive to the fiber arrangement, particularly cluster formation. An explicit correspondence between them has been established and an analytical formula linking the microstructure and peak stress statistics in FRCs has been suggested. Application of the statistics of extremes to the local stress concentration study has been discussed. It is shown that the peak interface stress distribution in FRCs with uniform microstructure follows a Fréchet-type asymptotic distribution rule.

The presented numerical data demonstrate the potential of the developed approach: practical importance of the established relationships (as well as other analogous dependencies which can be obtained in this way) consists in the following. The ultimate goal of our simulations consists in development of the continuum theory of FRC strength. To accomplish this task, we need to link the microstructure parameters to the peak local stress statistics and microdamage initiation and accumulation rate. The

statistical parameters of an actual FRC microstructure and the constants entering the local stress distribution functions we found from the numerical experiments would be the input variables of this theory. As an example, a simple continuum model of interface damage accumulation in FRCs has been suggested based on the established in the work statistical distribution of peak interface stress.

## Acknowledgements

## References

[Babuška et al. 1999] I. Babuška, B. Andersson, P. J. Smith, and K. Levin, "Damage analysis of fiber composites, I: Statistical analysis on fiber scale", *Comput. Methods Appl. Mech. Eng.* **172**:1–4 (1999), 27–77.

[Beirlant et al. 2004] J. Beirlant, Y. Goegebeur, J. Segers, and J. Teugels, *Statistics of extremes: theory and applications*, Wiley, Chichester, 2004.

[Beran 1968] M. J. Beran, *Statistical continuum theories*, Monographs in Statistical Physics and Thermodynamics **9**, Interscience, New York, 1968.

[Bolotin 1988] V. V. Bolotin, *Prediction of service life for machines and structures*, ASME, New York, 1988.

[Brøndsted et al. 1997] P. Brøndsted, H. Lilholt, and S. I. Andersen, "Fatigue damage prediction by measurements of the stiffness degradation in the polymer matrix composites", pp. 370–377 in *International Conference on Fatigue of Composites: 8th International Spring Meeting* (Paris, 1997), edited by S. Degallaix et al., Soc. Française de Métallurgie et de Matériaux, Paris, 1997.

[Buryachenko and Kushch 2006] V. A. Buryachenko and V. I. Kushch, "Effective transverse elastic moduli of composites at non-dilute concentration of a random field of aligned fibers", *Z. Angew. Math. Phys.* **57**:3 (2006), 491–505.

[Buryachenko et al. 2003] V. A. Buryachenko, N. J. Pagano, R. Y. Kim, and J. E. Spowart, "Quantitative description and numerical simulation of random microstructures of composites and their effective elastic moduli", *Int. J. Solids Struct.* **40**:1 (2003), 47–72.

[Byström 2003] J. Byström, "Influence of the inclusions distribution on the effective properties of heterogeneous media", *Compos. B Eng.* **34**:7 (2003), 587–592.

[Chen and Papathanasiou 2004] X. Chen and T. D. Papathanasiou, "Interface stress distributions in transversely loaded continuous fiber composites: parallel computation in multi-fiber RVEs using the boundary element method", *Compos. Sci. Technol.* **64**:9 (2004), 1101–1114.

[Degrieck and van Paepegem 2001] J. Degrieck and W. van Paepegem, "Fatigue damage modeling of fibre-reinforced composite materials: review", *Appl. Mech. Rev.* (*ASME*) **54**:4 (2001), 279–300.

[Drago and Pindera 2007] A. Drago and M.-J. Pindera, "Micro-macromechanical analysis of heterogeneous materials: macroscopically homogeneous vs periodic microstructures", *Compos. Sci. Technol.* **67**:6 (2007), 1243–1263.

[Fisher and Tippett 1928] R. A. Fisher and L. H. C. Tippett, "Limiting forms of the frequency distribution of the largest or smallest member of a sample", *Math. Proc. Cambridge Philos. Soc.* **24**:2 (1928), 180–190.

[Foster et al. 2006] D. C. Foster, G. P. Tandon, and M. Zoghi, "Evaluation of failure behavior of transversely loaded unidirectional model composites", *Exp. Mech.* **46**:2 (2006), 217–243.

[Fraysse et al. 1998] V. Fraysse, L. Giraud, and G. S., "A set of flexible-GMRES routines for real and complex arithmetics", Technical Report TR/PA/98/20, CERFACS, 1998.

[Freudenthal 1968] A. M. Freudenthal, "Statistical approach to brittle fracture", Chapter 6, pp. 591–619 in *Fracture, an advanced treatise, 2: Mathematical fundamentals*, edited by H. Liebowitz, Academic Press, New York, 1968.

[Ganguly and Poole 2004] P. Ganguly and W. J. Poole, "Influence of reinforcement arrangement on the local reinforcement stresses in composite materials", *J. Mech. Phys. Solids* **52**:6 (2004), 1355–1377.

[Gnedenko 1943] B. V. Gnedenko, "Sur la distribution limite du terme maximum d'une série aléatoire", *Ann. Math.* **44**:3 (1943), 423–453.

[Golovchan et al. 1993] V. T. Golovchan, A. N. Guz, Y. Kohanenko, and V. I. Kushch, *Statics of materials*, Mechanics of Composites **1**, Naukova Dumka, Kiev, 1993.

[Greengard and Helsing 1998] L. Greengard and J. Helsing, "On the numerical evaluation of elastostatic fields in locally isotropic two-dimensional composites", *J. Mech. Phys. Solids* **46**:8 (1998), 1441–1462.

[Gumbel 1958] E. J. Gumbel, *Statistics of extremes*, Columbia University Press, New York, 1958.

[Kushch et al. 2008] V. I. Kushch, S. V. Shmegera, and L. Mishnaevsky, Jr., "Meso cell model of fiber reinforced composite: interface stress statistics and debonding paths", *Int. J. Solids Struct.* **45**:9 (2008), 2758–2784.

[Meraghni et al. 1996] F. Meraghni, C. J. Blakeman, and M. L. Benzeggagh, "Effect of interfacial decohesion on stiffness reduction in a random discontinuous-fibre composite containing matrix microcracks", *Compos. Sci. Technol.* **56**:5 (1996), 541–555.

[Meraghni et al. 2002] F. Meraghni, F. Desrumaux, and M. L. Benzeggagh, "Implementation of a constitutive micromechanical model for damage analysis in glass mat reinforced composite structures", *Compos. Sci. Technol.* **62**:16 (2002), 2087–2097.

[Mishnaevsky 2007] L. Mishnaevsky, Jr., *Computational mesomechanics of composites: numerical analysis of the effect of microstructures of composites on their strength and damage resistance*, Wiley, Chichester, 2007.

[van Paepegem and Degrieck 2002] W. van Paepegem and J. Degrieck, "A new coupled approach of residual stiffness and strength for fatigue of fibre-reinforced composites", *Int. J. Fatigue* **24**:7 (2002), 747–762.

[Pyrz 1994a] R. Pyrz, "Correlation of microstructure variability and local stress field in two-phase materials", *Mater. Sci. Eng. A* **177**:1–2 (1994), 253–259.

[Pyrz 1994b] R. Pyrz, "Quantitative description of the microstructure of composites, 1: Morphology of undirectional composite systems", *Compos. Sci. Technol.* **50**:2 (1994), 197–208.

[Pyrz and Bochenek 1998] R. Pyrz and B. Bochenek, "Topological disorder of microstructure and its relation to the stress field", *Int. J. Solids Struct.* **35**:19 (1998), 2413–2427.

[Saad and Schultz 1986] Y. Saad and M. H. Schultz, "GMRES: a generalized minimal residual algorithm for solving nonsymmetric linear systems", *SIAM J. Sci. Stat. Comput.* **7**:3 (1986), 856–869.

[Torquato 1995] S. Torquato, "Nearest-neighbor statistics for packings of hard spheres and disks", *Phys. Rev. E* **51**:4 (1995), 3170–3182.

[Torquato 2002] S. Torquato, *Random heterogeneous materials: microstructure and macroscopic properties*, Springer, New York, 2002.

[Wang et al. 2005] J. Wang, S. L. Crouch, and S. G. Mogilevskaya, "A fast and accurate algorithm for a Galerkin boundary integral method", *Comput. Mech.* **37**:1 (2005), 96–109.

[Zhao and Weng 1997] Y. H. Zhao and G. J. Weng, "Transversely isotropic moduli of two partially debonded composites", *Int. J. Solids Struct.* **34**:4 (1997), 493–507.

VOLODYMYR I. KUSHCH: vkushch@bigmir.net
*National Academy of Sciences of Ukraine, Institute for Superhard Materials, 2 Avtozavodskaya St., Kiev 04074, Ukraine*

SERGII V. SHMEGERA: ssmegera@bigmir.net
*National Academy of Sciences of Ukraine, Institute for Superhard Materials, 2 Avtozavodskaya St., Kiev 04074, Ukraine*

LEON MISHNAEVSKY JR.: leon.mishnaevsky@risoe.dk
*Technical University of Denmark, Risø National Laboratory for Sustainable Energy, Frederiksborgvej 399, 4000 Roskilde, Denmark*

# STEEL SHIM STRESSES IN MULTILAYER BEARINGS UNDER COMPRESSION AND BENDING

JAMES M. KELLY AND DIMITRIOS KONSTANTINIDIS

Solutions are given for the tensile stresses in the steel reinforcing shims of elastomeric isolators. The method makes use of generalized plane stress and uses a stress function approach, treating the shim as a thin plate with body forces generated by surface shears on the top and bottom of the plate. It is shown that the pressure in the rubber acts as a potential for these body forces. The solutions are applicable to low and moderate shape factor bearings where it is acceptable to assume that the elastomer is incompressible, and also to the more common current situation when the shape factor is so large that the compressibility of the rubber must be included. The stress state in the steel reinforcing plates is calculated for both pure compression of the bearing and for when the bearing is loaded by a bending moment. These two cases, separately and in combination, are the typical situation in current practice. While a solution for the stress state in the shims of a circular isolator, assuming incompressibility and under pure compression, has been available using an analogy with the stresses in a rotating circular plate, the use of the stress function method is new and suggests a method to extend the solutions to other shapes of isolator other than circular. The solutions for pure compression, including compressibility of the rubber, and the solutions for bending, both incompressible and compressible, are entirely new.

## 1. Introduction

The essential characteristic of the elastomeric isolator is the very large ratio of the vertical stiffness relative to the horizontal stiffness. This is produced by the reinforcing plates, which in current industry standard are thin steel plates. These plates prevent lateral bulging of the rubber but allow the rubber to shear freely. The vertical stiffness can be several hundred times the horizontal stiffness. The steel reinforcement has the effect of generating shear stresses in the rubber in the isolator, and these stresses act on the steel plates to cause tension stresses which, if they were to become large enough, could result in failure of the steel shims through yielding or fracture. The external pressure on the isolator at which this might happen is an important design quantity for an isolator, and it is therefore necessary to be able to estimate these tensile stresses under the applied external load. An analysis is given for the stresses in a circular isolator under the assumption that the rubber is incompressible, generally in the low to moderate shape factor case. The analysis is also extended to the large shape factor case where the assumption of incompressibility cannot be made, and the effect of the bulk modulus of the rubber must be included. In current practise, most seismic isolation bearings use very large shape factors, where bulk compressibility must be included. These analyses make use of a stress function based on the observation that the pressure in the rubber acts as a potential for the internal stresses in the steel plates. Solutions are given for pure compression loading on the bearing and for bending in the bearing. Both compression and bending are

*Keywords:* rubber, elastomeric bearings, steel shim stresses, compression, bending, seismic isolation.

important in this analysis since, in use, the lateral displacement of a bearing superposes on the bearing a bending moment that can add to or reduce the stresses due to compression, and could in principle generate increased tension stresses or, if large enough, cause compression stresses in the thin plates and lead to their failure due to buckling.

The basis for the requirements for the steel shim stresses in all the codes governing the design of elastomeric bearings for bridges or for vibration isolation is a very simplistic formula [Spitz 1978; Stanton and Roeder 1982] in which the rubber is assumed to be a liquid under pressure and only equilibrium is used. The geometry of the bearing is a thin strip, and the shim is inextensible. This result is almost certainly wrong and clearly cannot be applied to circular shims with holes or external loading other than pure compression. Finite element analysis has been used to verify the accuracy of the approximate solution for the pressure distribution in the rubber, for example by Billings [1992] and Imbimbo and De Luca [1998], and in principle could be used to compute the stresses in the shims for a specific design under a variety of loading conditions, but this does not appear to have been done; and, in any case, finite element analysis is unlikely to be a useful design tool for these fairly low-cost items. The method given in this paper, based on the use of a stress function approach, can be extended to different cross-sectional shapes and other types of external loading.

## 2. Compression and bending of a rubber pad within incompressibility theory

**2.1. *Pure compression.*** A linear elastic theory is the most common method used to predict the compression stiffness of a thin elastomeric pad. The first analysis of the compression stiffness was done using an energy approach by Rocard [1937]; further developments were made by Gent and Lindley [1959] and Gent and Meinecke [1970]. An approximate strength-of-materials-type theory, applicable to bearings with low to moderate shape factors, was developed in [Kelly 1996], based on the assumption that the material is incompressible. The solutions that are the starting point for the present analysis are developed in detail there and will only be given here in their final form.

The analysis is based on the kinematic assumptions that points on a vertical line before deformation lie on a parabola after loading, and that horizontal planes remain horizontal. We consider an arbitrarily shaped pad of thickness $t$ and locate a rectangular Cartesian coordinate system, $(x, y, z)$, in the middle surface of the pad, as shown in Figure 1, left. The right half of the same figure shows the displacement pattern under the kinematic assumptions above. This displacement field satisfies the constraint that the top and bottom surfaces of the pad are bonded to rigid substrates, and takes the form
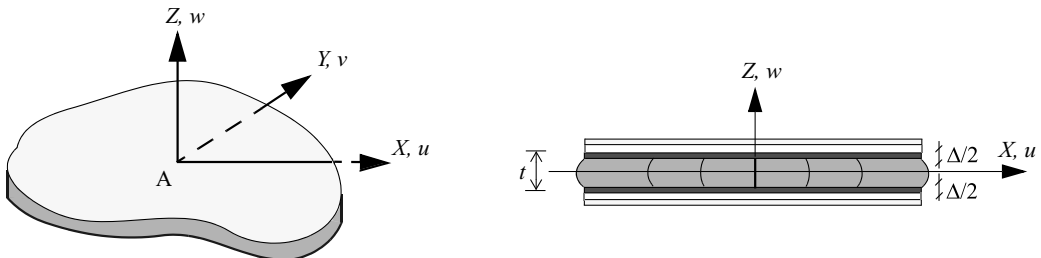


**Figure 1.** Constrained rubber pad and coordinate system.

$$u(x, y, z) = u_0(x, y)\left(1 - \frac{4z^2}{t^2}\right), \quad v(x, y, z) = v_0(x, y)\left(1 - \frac{4z^2}{t^2}\right), \quad w(x, y, z) = w(z). \quad (1)$$

The assumption of incompressibility produces a further constraint on the three components of strain, $\epsilon_{xx}$, $\epsilon_{yy}$, $\epsilon_{zz}$, in the form

$$\epsilon_{xx} + \epsilon_{yy} + \epsilon_{zz} = 0, \quad (2)$$

which leads to

$$(u_{0,x} + v_{0,y})\left(1 - \frac{4z^2}{t^2}\right) + w_{,z} = 0,$$

where the commas imply partial differentiation with respect to the indicated coordinate. Integration through the thickness provides the two-dimensional form of the incompressibility constraint as

$$u_{0,x} + v_{0,y} = \frac{3\epsilon_c}{2}, \quad (3)$$

where the compression strain $\epsilon_c$ is defined by

$$\epsilon_c = -\frac{w(t/2) - w(-t/2)}{t} = \frac{\Delta}{t} \quad (\epsilon_c > 0 \text{ in compression}).$$

The stress state is assumed to be dominated by the internal pressure, $p$, such that the normal stress components, $\sigma_{xx}$, $\sigma_{yy}$, $\sigma_{zz}$, can be equated to $-p$. The shear stress components, $\tau_{xz}$ and $\tau_{yz}$, generated by the constraints at the top and bottom of the pad, are included, but the in-plane shear stress, $\tau_{xy}$, is neglected. The equations of equilibrium for the stresses reduce under these assumptions to

$$\tau_{xz,z} = p_{,x}, \quad \tau_{yz,z} = p_{,y}. \quad (4)$$

We assume that the material is linearly elastic and that the shear stresses $\tau_{xz}$ and $\tau_{yz}$ are related to the shear strains by $G$, the shear modulus of the material. The equation for the pressure from which it and all other quantities can be derived is

$$p_{,xx} + p_{,yy} = \nabla^2 p = -\frac{12G\Delta}{t^3} = -\frac{12G}{t^2}\epsilon_c, \quad (5)$$

where $\epsilon_c = \Delta/t$ is the compression strain. The boundary condition, $p = 0$, on the edge of the pad completes the system for $p(x, y)$.

The vertical stiffness of a rubber bearing is given by the formula

$$K_V = \frac{E_c A}{t_r}, \quad (6)$$

where $A$ is the area of the bearing, $t_r$ is the total thickness of rubber in the bearing, and $E_c$ is the instantaneous compression modulus of the rubber-steel composite under the specified level of vertical load. The value of $E_c$ for a single rubber layer is controlled by the shape factor, $S$, defined as

$$S = \frac{\text{loaded area}}{\text{free area}},$$
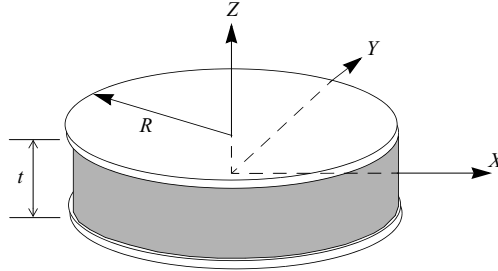
**Figure 2.** Coordinate system for a circular pad of radius $R$.

which is a dimensionless measure of the aspect ratio of the single layer of the elastomer. For example, for a circular pad of radius $R$ and thickness $t$,

$$S = \frac{R}{2t}. \tag{7}$$

To determine the compression modulus, $E_c$, we solve for $p$ from (5), and integrate over the area to determine the resultant normal load, $P$, from which $E_c$ is given by

$$E_c = \frac{P}{A\epsilon_c}. \tag{8}$$

For example for a circular pad of radius $R$, as shown in Figure 2, Equation (5) reduces to

$$\nabla^2 p = \frac{d^2 p}{dr^2} + \frac{1}{r}\frac{dp}{dr} = -\frac{12G}{t^2}\epsilon_c; \quad r = \sqrt{x^2 + y^2}. \tag{9}$$

The solution is

$$p = A \ln r + B - \frac{3G}{t^2} r^2 \epsilon_c,$$

where $A$ and $B$ are constants of integration; because $p$ must be bounded at $r = 0$ and $p = 0$ at $r = R$, the solution becomes

$$p = \frac{3G}{t^2}(R^2 - r^2)\epsilon_c. \tag{10}$$

It follows that

$$P = 2\pi \int_0^R p(r) r \, dr = \frac{3G\pi R^4}{2t^2}\epsilon_c,$$

and with $S = R/(2t)$ and $A = \pi R^2$, we have $E_c = 6GS^2$.

**2.2.** *Pure bending.* The bending stiffness of a single pad is computed using a similar approach. The displaced configuration is obtained in two stages. First visualize the deformation that would occur if the bending conformed to elementary beam theory (shown dotted in Figure 3). Because this cannot satisfy the incompressibility constraint, a further pure shear deformation is superimposed. The displacement field is given by

$$u(x, y, z) = u_0(x, y)\left(1 - \frac{4z^2}{t^2}\right) - \alpha\frac{z^2}{2t}, \quad v(x, y, z) = v_0(x, y)\left(1 - \frac{4z^2}{t^2}\right), \quad w(x, y, z) = \frac{\alpha z x}{t}. \tag{11}$$

Here, $\alpha$ is the angle between the rigid plates in the deformed configuration, and the bending is about the $y$-axis. The radius of the curvature, $\rho$, generated by the deformation, is related to $\alpha$ by $1/\rho = \alpha/t$ which, with the incompressibility condition, leads to

$$p_{,xx} + p_{,yy} = \frac{12G\alpha}{t^3}x, \tag{12}$$

with $p = 0$ on the edges.

The solution technique is to solve (12) for $p$ and to compute the bending moment, $M$, from

$$M = -\int_A p(x, y)x \, dA,$$

and use an analogy with beam theory, where $M = EI(1/\rho)$, to compute the effective bending stiffness $EI_{\text{eff}} = M/(\alpha/t)$.

For a circular pad of radius $R$ (Figure 2), the equation to be solved, using polar coordinates $r$ and $\theta$, is

$$p_{,rr} + \frac{1}{r}p_{,r} + \frac{1}{r^2}p_{,\theta\theta} = \frac{\alpha}{t}\frac{12G}{t^2}r\cos\theta. \tag{13}$$

The solution is

$$p(r, \theta) = \left(Ar + B\frac{1}{r} + Cr^3\right)\cos\theta,$$

where $C = (\alpha/t)(3G)/(2t^2)$. For the complete circle, $0 \le r \le R$, for $p$ to be bounded at $r = 0$ means $B = 0$, and using the boundary condition $p = 0$ at $r = R$, gives

$$p = \frac{3G}{2t^2}\frac{\alpha}{t}(r^2 - R^2)r\cos\theta \tag{14}$$

and

$$M = \frac{G\alpha}{8t^3}\pi R^6. \tag{15}$$

The effective moment of inertia in this case, taking $E = E_c = 6GS^2$, is $\pi R^4/12$, or one third of the conventional moment of inertia for the bending of a circular cross section.
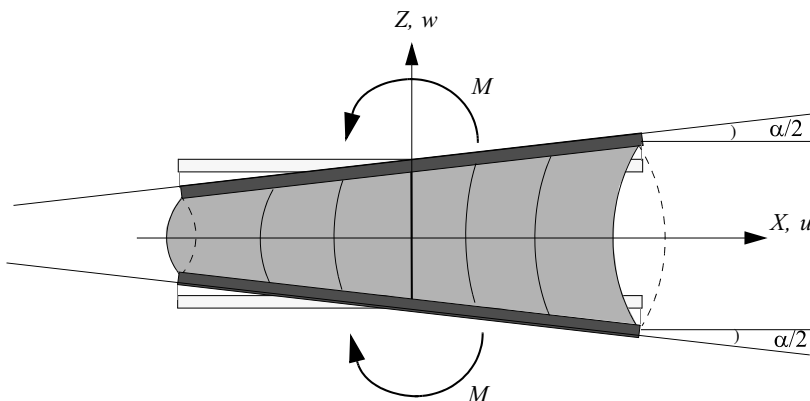


**Figure 3.** Pad between rigid constraint layers in pure bending.

It is useful to define a bending strain $\varepsilon_b$ analogous to the compression strain $\varepsilon_c$ through

$$\varepsilon_b = \frac{\alpha}{t}R = \frac{M}{EI_{\text{eff}}}R, \tag{16}$$

in terms of which we have

$$\nabla^2 p = p_{,rr} + \frac{1}{r}p_{,r} + \frac{1}{r^2}p_{,\theta\theta} = \frac{12G}{t^2 R}\varepsilon_b r \cos\theta \tag{17}$$

and

$$p = \frac{3G\varepsilon_b}{2Rt^2}(r^2 - R^2)r\cos\theta. \tag{18}$$

## 3. Steel stresses in circular bearings with incompressible rubber

The state of stress in a rubber layer, within a multilayer bearing under compression or bending, or a combination of the two, is assumed to be a state of pressure that would induce a bulging of the rubber were it not restrained by the thin steel reinforcing plates (often referred to as shims) that are bonded to the rubber. The restraint of the rubber by the steel causes shear stresses in the rubber which act on each side of the steel plate to induce tensile or compression stresses in the plane of the plate. It is possible to solve for these in-plane stresses using two-dimensional elasticity theory, assuming that the plate is in a state of generalized plane stress and that the surface shear stresses are equivalent to in-plane body forces. While it is possible to formulate the plane stress problem for an arbitrarily shaped plate, we consider only the circular bearing, and we will also use the notations for stresses and stress functions from [Timoshenko and Goodier 1970].

In polar coordinates $(r, \theta)$, the equations of equilibrium for the stresses in the rubber are, using the Timoshenko notation,

$$\begin{aligned}
\frac{\partial \sigma_r}{\partial r} + \frac{1}{r}\frac{\partial \tau_{r\theta}}{\partial \theta} + \frac{\partial \tau_{rz}}{\partial z} + \frac{\sigma_r - \sigma_\theta}{r} &= 0, \\
\frac{\partial \tau_{r\theta}}{\partial r} + \frac{1}{r}\frac{\partial \sigma_\theta}{\partial \theta} + \frac{\partial \tau_{\theta z}}{\partial z} + \frac{2\tau_{r\theta}}{r} &= 0, \\
\frac{\partial \tau_{rz}}{\partial r} + \frac{1}{r}\frac{\partial \tau_{\theta z}}{\partial \theta} + \frac{\partial \sigma_z}{\partial z} + \frac{\tau_{rz}}{r} &= 0.
\end{aligned} \tag{19}$$

It is assumed that $\sigma_r = \sigma_\theta = -p$, and are independent of $z$; and also that the in-plane shear stress $\tau_{r\theta}$ is negligible. Hence the first of these equations yields

$$\frac{\partial \tau_{rz}}{\partial z} = \frac{\partial p}{\partial r}, \tag{20}$$

and the second

$$\frac{\partial \tau_{\theta z}}{\partial z} = \frac{1}{r}\frac{\partial p}{\partial \theta}. \tag{21}$$

Inserting these equilibrium equations into the third equation in (19), differentiating with respect to $z$ and interchanging the order of differentiation changes it to

$$p_{,rr} + \frac{1}{r}p_{,r} + \frac{1}{r^2}p_{,\theta\theta} + \frac{\partial^2 \sigma_z}{\partial z^2} = 0.$$
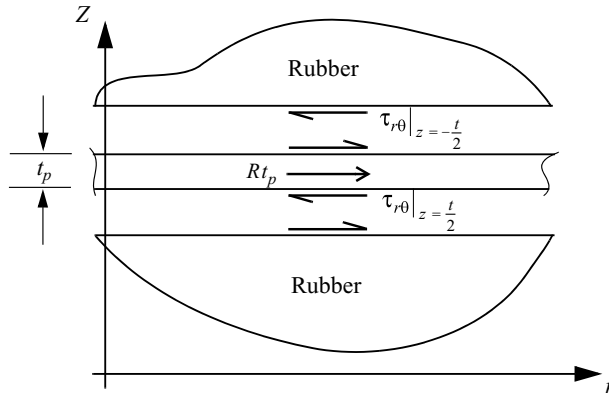
**Figure 4.** Shear stresses producing equivalent body forces in the plate.

This equation, with substitution from either (20) or (21), allow us, if necessary, to calculate the distribution of $\sigma_z$ through the thickness of the pad. Within the stress assumptions above we have $p = p(r, \theta)$ which means that we can write

$$\tau_{rz} = \frac{\partial p}{\partial r} z, \quad \tau_{\theta z} = \frac{1}{r} \frac{\partial p}{\partial \theta} z. \tag{22}$$

The shear stresses at the bottom of the rubber layer $\tau_{rz}|_{z=-t/2}$ and $\tau_{\theta z}|_{z=-t/2}$ become the shear stresses on the top surface of the plate, and the shear stresses at the top of the rubber layer $\tau_{rz}|_{z=t/2}$ and $\tau_{\theta z}|_{z=t/2}$ are the shear stresses on the lower surface of the plate (Figure 4).

The internal stresses in the steel shims satisfy the equilibrium equations

$$\frac{\partial \sigma_r}{\partial r} + \frac{1}{r} \frac{\partial \tau_{r\theta}}{\partial \theta} + \frac{\sigma_r - \sigma_\theta}{r} + R = 0, \quad \frac{\partial \tau_{r\theta}}{\partial r} + \frac{1}{r} \frac{\partial \sigma_\theta}{\partial \theta} + \frac{2\tau_{r\theta}}{r} + S = 0, \tag{23}$$

where $R$, $S$ are the equivalent body forces per unit volume created by the surface shear stresses and are given by

$$t_p R = \tau_{rz}\big|_{z=-t/2} - \tau_{rz}\big|_{z=t/2}, \quad t_p S = \tau_{\theta z}\big|_{z=-t/2} - \tau_{\theta z}\big|_{z=t/2},$$

where $t_p$ is the thickness of the steel shim, leading to

$$R = -\frac{\partial p}{\partial r} \frac{t}{t_p}, \quad S = -\frac{1}{r} \frac{\partial p}{\partial \theta} \frac{t}{t_p}. \tag{24}$$

It follows that the pressure plays the role of a potential, $V(r, \theta)$, for the body forces in the form $V = (t/t_p)p(r, \theta)$ with $R = -\partial V/\partial r$ and $S = -(1/r)\partial V/\partial \theta$. The equations of equilibrium for the plate then become

$$\frac{\partial(\sigma_r - V)}{\partial r} + \frac{1}{r} \frac{\partial \tau_{r\theta}}{\partial \theta} + \frac{(\sigma_r - V) - (\sigma_\theta - V)}{r} = 0, \quad \frac{\partial \tau_{r\theta}}{\partial r} + \frac{1}{r} \frac{\partial(\sigma_\theta - V)}{\partial \theta} + \frac{2\tau_{r\theta}}{r} = 0. \tag{25}$$

These equations are satisfied by a stress function $\Phi(r, \theta)$ for the stresses, such that

$$\sigma_r - V = \frac{1}{r} \frac{\partial \Phi}{\partial r} + \frac{1}{r^2} \frac{\partial^2 \Phi}{\partial \theta^2}, \quad \sigma_\theta - V = \frac{\partial^2 \Phi}{\partial r^2}, \quad \tau_{r\theta} = -\frac{\partial}{\partial r}\left(\frac{1}{r} \frac{\partial \Phi}{\partial \theta}\right); \tag{26}$$

and under the assumption of plane stress the equation for $\Phi$ is

$$\nabla^2\nabla^2\Phi + (1-\nu)\nabla^2 V = 0, \tag{27}$$

where $\nu$ is the Poisson ratio of the steel. In the case of pure compression the pressure satisfies (4):

$$\nabla^2 p = -\frac{12G}{t^2}\varepsilon_c, \tag{28}$$

and, for bending, (12):

$$\nabla^2 p = \frac{12Gr\cos\theta}{t^2 R}\varepsilon_b. \tag{29}$$

**3.1.** *Stress function solution for pure compression.* The stress function $\Phi$ for pure compression is given by the solution of

$$\nabla^2\nabla^2\Phi + \overline{C} = 0, \tag{30}$$

where $\overline{C}$ is a constant having the value

$$\overline{C} = -(1-\nu)\frac{t}{t_p}\frac{12G}{t^2}\varepsilon_c. \tag{31}$$

In this case the stress function depends only on $r$, and we look for a solution of that form. The result is [Timoshenko and Goodier 1970]

$$\Phi = A\ln r + Br^2\ln r + Cr^2 + D - \frac{\overline{C}r^4}{64}.$$

The resulting stresses are given by

$$\sigma_r - \frac{t}{t_p}p(r) = \frac{A}{r^2} + B(1+2\ln r) + 2C - \frac{\overline{C}r^2}{16}, \quad \sigma_\theta - \frac{t}{t_p}p(r) = -\frac{A}{r^2} + B(3+2\ln r) + 2C - \frac{3}{16}\overline{C}r^2.$$

It is clear that both $A$ and $B$ must vanish for the completely circular plate, and using $\sigma_r(R) = 0$ and the fact that the pressure is also zero at $r = R$, we have $2C = \overline{C}R^2/16$. Using the pressure from (10) and $\overline{C}$ from (31), the solution for the tensile stresses becomes

$$\sigma_r = \frac{3G}{tt_p}\frac{3+\nu}{4}(R^2 - r^2)\varepsilon_c = 3GS^2\varepsilon_c\frac{t}{t_p}(3+\nu)\left(1 - \frac{r^2}{R^2}\right),$$

$$\sigma_\theta = \frac{3}{4}\frac{G\varepsilon_c}{tt_p}\left((3+\nu)R^2 - (1+3\nu)r^2\right) = 3GS^2\varepsilon_c\frac{t}{t_p}\left(3+\nu - (1+3\nu)\frac{r^2}{R^2}\right). \tag{32}$$

The distribution of the stresses in the plate under pure compression is shown in Figure 5.

At the center of the plate we have

$$\sigma_{\max} = \sigma_r = \sigma_\theta = \frac{6GS^2}{2}\frac{t}{t_p}\varepsilon_c(3+\nu). \tag{33}$$

By expressing the maximum value of the stresses in terms of the average pressure over the plate, $p_{\text{ave}}$, given by

$$p_{\text{ave}} = E_c\varepsilon_c = 6GS^2\varepsilon_c, \tag{34}$$
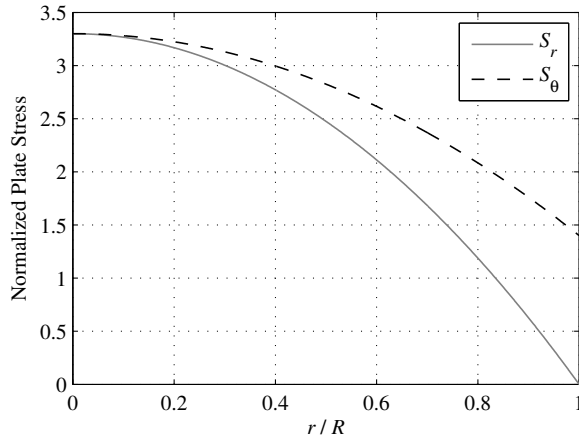
**Figure 5.** Plate stresses in compression, assuming incompressibility.

then

$$\frac{\sigma_{\max}}{p_{\text{ave}}} = \frac{3+\nu}{2}\frac{t}{t_p}, \tag{35}$$

which can be used to determine the maximum pressure needed to cause yield in the shim at the center. This shows why, under normal circumstances, the stresses in the shims due to the pressure is not considered important. For example, if we have steel shims 3.0 mm thick and rubber layers 15.0 mm thick, the stresses in the steel due to a pressure of 7.0 MPa (which is standard) are only 58 MPa, well below the yield level of the plate material. If the tension stress at the center is in fact at the level of the yield stress of the material, $\sigma_o$, then the average pressure to initiate yield is $p_{\text{ave}} = 2\sigma_o(t_p/t)/(3+\nu)$. This is only the start of yield, but the plate will experience further yielding as the pressure increases. The zone of yielding will spread from the center to the outer radius so that the pressure can increase further until the entire plate has yielded, that is, until the region $0 \le r \le R$ is fully plastic.

Note that the problem in this case is the same as that for the stresses in a thin disk due to centrifugal forces. That solution is given in Timoshenko and Goodier [1970] using an entirely different approach based on displacements, and, except for constants, is identical to this. The same reference also provides the solution for a circular plate of radius $b$ with a central hole of radius $a$, which for $a \le r \le b$ is

$$\sigma_r = \frac{3}{4}\frac{G\varepsilon_c}{tt_p}(3+\nu)\left(b^2+a^2-\frac{a^2b^2}{r^2}-r^2\right), \quad \sigma_\theta = \frac{3}{4}\frac{G\varepsilon_c}{tt_p}(3+\nu)\left(b^2+a^2+\frac{a^2b^2}{r^2}-\frac{1+3\nu}{3+\nu}r^2\right). \tag{36}$$

The maximum radial stress is at $R = \sqrt{ab}$, where

$$\sigma_r = \frac{3}{4}\frac{G\varepsilon_c}{tt_p}(3+\nu)(b-a)^2, \tag{37}$$

and the maximum tangential stress is at the inner boundary, where

$$\sigma_\theta = \frac{3}{4}\frac{G\varepsilon_c}{tt_p}(3+\nu)\left(b^2+\frac{1-\nu}{3+\nu}a^2\right). \tag{38}$$

This is always larger than the maximum radial stress. When the radius $a$ of the hole becomes very small, the maximum tangential stress approaches a value twice as large as that for the complete circular plate. This another example of a stress concentration at a small hole.

**3.2.** *Stress function solution for pure bending.* For the case of pure bending on the pad, the equation for the stress function takes the form

$$\nabla^2 \nabla^2 \Phi + \bar{C} r \cos \theta = 0, \tag{39}$$

where now

$$\bar{C} = (1 - \nu) \frac{12G}{t t_p R} \varepsilon_b. \tag{40}$$

We look for a solution of the form

$$\Phi(r, \theta) = f(r) \cos \theta.$$

From [Timoshenko and Goodier 1970], the ordinary differential equation for $f$ is

$$\frac{d^4 f}{dr^4} + \frac{2}{r} \frac{d^3 f}{dr^3} - \frac{3}{r^2} \frac{d^2 f}{dr^2} + \frac{3}{r^3} \frac{df}{dr} - \frac{3}{r^4} f + \bar{C} r = 0. \tag{41}$$

The solution is

$$f(r) = A r^3 + \frac{B}{r} + C r + D r \ln r - \frac{\bar{C} r^5}{192}. \tag{42}$$

The resulting stresses are

$$\sigma_r - \frac{t}{t_p} p = \left( 2A r - \frac{2B}{r^3} + \frac{D}{r} \right) \cos \theta + \bar{R},$$

$$\sigma_\theta - \frac{t}{t_p} p = \left( 6A r + \frac{2B}{r^3} + \frac{D}{r} \right) \cos \theta + \bar{S},$$

$$\tau_{r\theta} = \left( 2A r - \frac{2B}{r^3} + \frac{D}{r} \right) \sin \theta + \bar{T},$$

where

$$\bar{R} = \left( \frac{1}{r} \frac{\partial}{\partial r} + \frac{1}{r^2} \frac{\partial^2}{\partial \theta^2} \right) \left( -\frac{\bar{C} r^5}{192} \cos \theta \right) = -\frac{\bar{C} r^3}{48} \cos \theta,$$

$$\bar{S} = \frac{\partial^2}{\partial r^2} \left( -\frac{\bar{C} r^5}{192} \cos \theta \right) = -\frac{5 \bar{C} r^3}{48} \cos \theta,$$

$$\bar{T} = -\frac{\partial}{\partial r} \left( \frac{1}{r} \frac{\partial}{\partial \theta} \left( -\frac{\bar{C} r^5}{192} \cos \theta \right) \right) = -\frac{\bar{C} r^3}{48} \sin \theta.$$

For the complete plate $0 \leq r \leq R$, both $B$ and $D$ must vanish, giving

$$\sigma_r = \frac{t}{t_p} p(r, \theta) + 2A r \cos \theta - \frac{\bar{C} r^3}{48} \cos \theta;$$

and since $p(r, \theta)$ is zero on the boundary, the requirement that $\sigma_r(R, \theta) = 0$ gives $2A = \bar{C} R^2 / 48$, leading to the final results
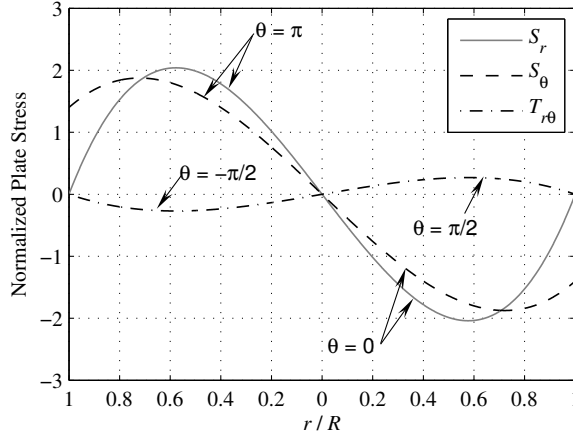
**Figure 6.** Plate stresses under bending moment for the incompressible case.

$$\sigma_r(r,\theta) = -\frac{G\varepsilon_b}{4tt_pR}(5+\nu)(R^2-r^2)r\cos\theta,$$

$$\sigma_\theta(r,\theta) = \frac{G\varepsilon_b}{4tt_pR}\big((1+5\nu)r^2-3(1+\nu)R^2\big)r\cos\theta, \tag{43}$$

$$\tau_{r\theta}(r,\theta) = -\frac{G\varepsilon_b}{4tt_pR}(1-\nu)(R^2-r^2)r\sin\theta.$$

These results are plotted as nondimensional stresses in Figure 6.

$$S_r = \frac{\sigma_r(r,\theta)}{GS^2\varepsilon_b(t/t_p)} = -(5+\nu)\left(1-\left(\frac{r}{R}\right)^2\right)\frac{r}{R}\cos\theta,$$

$$S_\theta = \frac{\sigma_\theta(r,\theta)}{GS^2\varepsilon_b(t/t_p)} = \left((1+5\nu)\left(\frac{r}{R}\right)^2-3(1+\nu)\right)\frac{r}{R}\cos\theta, \tag{44}$$

$$T_{r\theta} = \frac{\tau_{r\theta}(r,\theta)}{GS^2\varepsilon_b(t/t_p)} = (1-\nu)\left(1-\left(\frac{r}{R}\right)^2\right)\frac{r}{R}\sin\theta.$$

## 4. Steel stresses due to compression in circular pads with large shape factors

The theory for the compression of a rubber pad given in the preceding section is based on two assumptions: first, that the displacement pattern is defined by (1); second, that the normal stress components in all three directions are equal to the pressure, $p$, in the material. The equation that is solved for $p$ results from the integration of the incompressibility constraint, that is, Equation (2), through the thickness of the pad, leading to an equation for $p(x, y)$ of the form given in (5). To include the influence of bulk compressibility, we need only replace the incompressibility constraint by

$$\varepsilon_{xx} + \varepsilon_{yy} + \varepsilon_{zz} = -\frac{p}{K}, \tag{45}$$

where $K$ is the bulk modulus. Integration through the thickness leads to an equation for $p(x, y)$ of the form

$$\nabla^2 p - \frac{12p}{t^2}\frac{G}{K} = -\frac{12G}{t^2}\varepsilon_c, \tag{46}$$

that is solved as before, with $p = 0$ on the edge of the pad.

We now consider a circular pad with a large shape factor, an external radius $R$, and a thickness $t$. The pressure in the pad is axisymmetrical, that is, $p = p(r)$ where $0 \leq r \leq R$; therefore, (46) becomes

$$\frac{d^2 p}{dr^2} + \frac{1}{r}\frac{dp}{dr} - \lambda^2(p - K\varepsilon_c) = 0, \tag{47}$$

where $\lambda^2 = 12G/(Kt^2)$. The boundary conditions to be satisfied are $p = 0$ at $r = R$, and $p$ is finite at $r = 0$.

The solution involves the modified Bessel functions of the first and second kinds, $I_0$ and $K_0$. Because the solution is bounded at $r = 0$, the term in $K_0$ is excluded, and the general solution for $p(r)$ is

$$p(r) = K\left(1 - \frac{I_0(\lambda r)}{I_0(\lambda R)}\right)\varepsilon_c. \tag{48}$$

Integrating $p$ over the area of the pad gives

$$P = K\pi R^2\left(1 - \frac{2}{\lambda R}\frac{I_1(\lambda R)}{I_0(\lambda R)}\right)\varepsilon_c, \tag{49}$$

where $I_1$ is the modified Bessel function of the first kind of order 1.

The resulting expression for the compression modulus is

$$E_c = K\left(1 - \frac{2}{\lambda R}\frac{I_1(\lambda R)}{I_0(\lambda R)}\right), \tag{50}$$

where

$$\lambda R = \left(\frac{12GR^2}{Kt^2}\right)^{1/2} = \left(\frac{48G}{K}\right)^{1/2}S,$$

and the shape factor, $S$, is $R/(2t)$.

The tension stresses in the steel reinforcing plates can be calculated in the same way as before by using the stress function method. The equation for the stress function remains the same,

$$\nabla^2\nabla^2\Phi + (1 - \nu)\nabla^2 V = 0;$$

and the definition of the potential $V(r, \theta)$ is the same, $V = \frac{t}{t_p}p(r, \theta)$; but the pressure now satisfies the equation

$$\nabla^2 p - \frac{12p}{t^2}\frac{G}{K} = -\frac{12G}{t^2}\varepsilon_c. \tag{51}$$

Thus the stress function now must satisfy the equation

$$\nabla^2\nabla^2\Phi + (1 - \nu)\frac{t}{t_p}\left(\frac{12G}{t^2}\left(\frac{p}{K} - \varepsilon_c\right)\right) = 0. \tag{52}$$

With $p$ given by (48), we have

$$\nabla^2\nabla^2\Phi - (1-v)\frac{t}{t_p}\frac{12G}{t^2}\frac{I_0(\lambda r)}{I_0(\lambda R)}\varepsilon_c = 0. \tag{53}$$

The solution for pure compression is rotationally symmetric, and the complementary part of the solution remains the same, but it is necessary to determine the particular integral that corresponds to the term $I_0(\lambda r)$. To develop this, we recall that in radial symmetry,

$$\nabla^2\nabla^2(f) = \frac{1}{r}\frac{d}{dr}\left(r\frac{d}{dr}\left(\frac{1}{r}\frac{d}{dr}\left(r\frac{df}{dr}\right)\right)\right). \tag{54}$$

By taking $f = I_0(\lambda r)$, changing the variable to $x = \lambda r$, and recalling that $x$ so defined is dimensionless and that $\lambda$ is a reciprocal length, we have $\nabla^2\nabla^2\Phi|_r = (1/\lambda^4)\nabla^2\nabla^2\Phi|_x$. Thus we have successively

$$\frac{1}{x}\frac{d}{dx}\left(x\frac{d}{dx}\left(\frac{1}{x}\frac{d}{dx}\left(x\frac{df}{dx}\right)\right)\right) = I_0(x),$$

$$x\frac{d}{dx}\left(\frac{1}{x}\frac{d}{dx}\left(x\frac{df}{dx}\right)\right) = \int xI_0(x)dx = xI_1(x),$$

$$\frac{1}{x}\frac{d}{dx}\left(x\frac{df}{dx}\right) = \int I_1(x)dx = I_0(x),$$

$$x\frac{df}{dx} = \int xI_0(x)dx = xI_1(x),$$

$$f = I_0(x).$$

The result for the stress function is $\Phi = A\ln r + Br^2\ln r + Cr^2 + D + \frac{1}{\lambda^4}\bar{C}I_0(\lambda r)$, where now the constant $\bar{C}$ is given by

$$\bar{C} = (1-v)\frac{t}{t_p}\frac{12G}{t^2}\frac{1}{I_0(\lambda R)}\varepsilon_c. \tag{55}$$

The stresses in the plate are now given by

$$\sigma_r - \frac{t}{t_p}p(r) = \frac{A}{r^2} + B(1+2\ln r) + 2C + \frac{\bar{C}}{\lambda^2}\frac{I_1(\lambda r)}{\lambda r},$$

$$\sigma_\theta - \frac{t}{t_p}p(r) = -\frac{A}{r^2} + B(3+2\ln r) + 2C + \frac{\bar{C}}{\lambda^2}\left(I_0(\lambda r) - \frac{I_1(\lambda r)}{\lambda r}\right).$$

Since in the case of a complete plate $A$ and $B$ must vanish, and the pressure is zero at the outside radius, the condition that $\sigma_r(R) = 0$ means that

$$C = -\frac{\bar{C}}{2\lambda^2}\frac{I_1(\lambda R)}{\lambda R},$$

and, with $p(r)$ given by (48), we have

$$\sigma_r = \frac{t}{t_p}K\varepsilon_c\left(1 - \frac{I_0(\lambda r)}{I_0(\lambda R)} - \frac{1-v}{I_0(\lambda R)}\left(\frac{I_1(\lambda R)}{\lambda R} - \frac{I_1(\lambda r)}{\lambda r}\right)\right),$$

$$\sigma_\theta = \frac{t}{t_p}K\varepsilon_c\left(1 - \frac{I_0(\lambda r)}{I_0(\lambda R)} - \frac{1-v}{I_0(\lambda R)}\left(\frac{I_1(\lambda R)}{\lambda R} + \frac{I_1(\lambda r)}{\lambda r} - I_0(\lambda r)\right)\right). \tag{56}$$

At the center of the plate, the stresses become
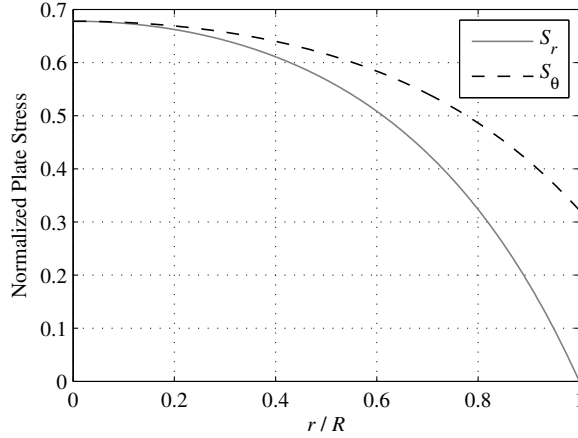
**Figure 7.** Plate stresses in compression for the large shape factor case.

$$\sigma_r = \sigma_\theta = \frac{t}{t_p} K \varepsilon_c \left( 1 - \frac{1}{I_0(\lambda R)} - \frac{1-\nu}{I_0(\lambda R)} \left( \frac{I_1(\lambda R)}{\lambda R} - \frac{1}{2} \right) \right). \tag{57}$$

To illustrate these results, we look at the case when the shape factor is 30, the rubber shear modulus is 0.42 MPa, and the bulk modulus is 2000 MPa, giving $\lambda R = 3$. The normalized plate stresses denoted by $S_r = \sigma_r / ((t/t_p)K\varepsilon_c)$ and $S_\theta = \sigma_\theta / ((t/t_p)K\varepsilon_c)$ are shown as functions of $r/R$ in Figure 7.

If we compare the maximum value of the stress at the center of the plate of this solution with the same result for the incompressible case, we can use (50) to determine the average pressure, and (57) to get

$$\frac{\sigma_{\max}}{p_{\text{ave}}} = \frac{t}{t_p} \frac{I_0(\lambda R) - 1 - (1-\nu)\left(I_1(\lambda R)/(\lambda R) - \frac{1}{2}\right)}{I_0(\lambda R) - 2I_1(\lambda R)/(\lambda R)}. \tag{58}$$

Figure 8 is a graph of (58) for a range of values of $\lambda R$ from 0 to 5 (0 being the incompressible case). It shows that for the same value of $\varepsilon_c$ and $t/t_p$, the peak stresses are smaller. This implies that the result for the incompressible computation is a conservative estimate of the stresses in the large shape factor case,
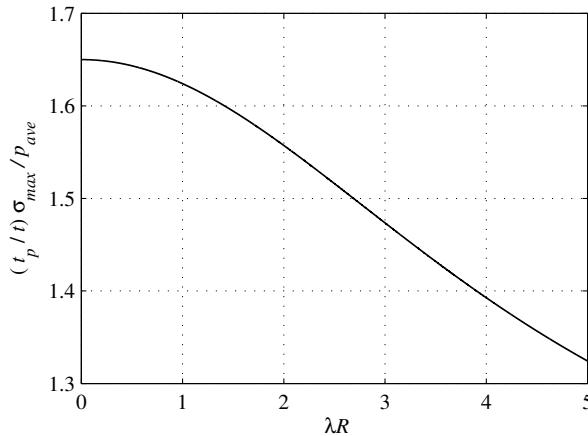


**Figure 8.** Ratio of maximum plate stresses for compressible and incompressible cases.

which, if it can be used, greatly simplifies the prediction of the maximum value of the tension stress in this case.

## 5. Steel stresses due to bending in circular pads with large shape factors

For a circular pad, the equation to be solved is

$$p_{,rr} + \frac{1}{r}p_{,r} + \frac{1}{r^2}p_{,\theta\theta} - \lambda^2 p = \frac{\alpha}{t}\lambda^2 K r \cos\theta, \tag{59}$$

with $p = 0$ at $r = R$.

The result for $p(r,\theta)$ is

$$p = \frac{\alpha K}{t}\left(R\frac{I_1(\lambda r)}{I_1(\lambda R)} - r\right)\cos\theta = K\varepsilon_b\left(\frac{I_1(\lambda r)}{I_1(\lambda R)} - \frac{r}{R}\right)\cos\theta. \tag{60}$$

It follows that the $\nabla^2 p$ reduces to

$$\nabla^2 p = \frac{12G}{t^2}\frac{I_1(\lambda r)}{I_1(\lambda R)}\cos\theta\,\varepsilon_b, \tag{61}$$

and that the equation to be solved for the stress function becomes

$$\nabla^2\nabla^2\Phi + (1-\nu)\frac{t}{t_p}\frac{12G}{t^2}\frac{I_1(\lambda r)}{I_1(\lambda R)}\cos\theta\,\varepsilon_b = 0. \tag{62}$$

We look for a solution of the form

$$\Phi(r,\theta) = f(r)\cos\theta.$$

From [Timoshenko and Goodier 1970], the ordinary differential equation for $f$ is

$$\frac{d^4 f}{dr^4} + \frac{2}{r}\frac{d^3 f}{dr^3} - \frac{3}{r^2}\frac{d^2 f}{dr^2} + \frac{3}{r^3}\frac{df}{dr} - \frac{3}{r^4}f + \bar{C}I_1(\lambda r) = 0, \tag{63}$$

where for this case we have

$$\bar{C} = (1-\nu)\frac{t}{t_p}\frac{12G}{t^2}\frac{\varepsilon_b}{I_1(\lambda R)}. \tag{64}$$

The complementary part of the solution is

$$f(r) = Ar^3 + \frac{B}{r} + Cr + Dr\ln r,$$

and the particular integral can be shown (after considerable algebraic manipulation) to be $-(\bar{C}/\lambda^4)I_1(\lambda r)$.

The resulting stresses are

$$\sigma_r - \frac{t}{t_p}p = \left(2Ar - \frac{2B}{r^3} + \frac{D}{r}\right)\cos\theta + \bar{R},$$

$$\sigma_\theta - \frac{t}{t_p}p = \left(6Ar + \frac{2B}{r^3} + \frac{D}{r}\right)\cos\theta + \bar{S},$$

$$\tau_{r\theta} = \left(2Ar - \frac{2B}{r^3} + \frac{D}{r}\right)\sin\theta + \bar{T},$$

where

$$\bar{R} = \Big(\frac{1}{r}\frac{\partial}{\partial r} + \frac{1}{r^2}\frac{\partial^2}{\partial \theta^2}\Big)\Big(-\frac{\bar{C}I_1(\lambda r)\cos\theta}{\lambda^4}\Big) = \frac{2I_1(\lambda r) - I_0(\lambda r)\lambda r}{\lambda^2 r^2}\frac{\bar{C}}{\lambda^2}\cos\theta,$$

$$\bar{S} = \frac{\partial^2}{\partial r^2}\Big(-\frac{\bar{C}I_1(\lambda r)\cos\theta}{\lambda^4}\Big) = \frac{I_0(\lambda r)\lambda r - I_1(\lambda r)(2 + \lambda^2 r^2)}{\lambda^2 r^2}\frac{\bar{C}}{\lambda^2}\cos\theta,$$

$$\bar{T} = -\frac{\partial}{\partial r}\Big(\frac{1}{r}\frac{\partial}{\partial \theta}\Big(-\frac{\bar{C}I_1(\lambda r)\cos\theta}{\lambda^4}\Big)\Big) = \frac{2I_1(\lambda r) - I_0(\lambda r)\lambda r}{\lambda^2 r^2}\frac{\bar{C}}{\lambda^2}\sin\theta.$$

For the complete plate $0 \le r \le R$, both $B$ and $D$ must vanish and $\sigma(R, \theta) = 0$, giving

$$A = \frac{1}{2R}\frac{I_0(\lambda R)\lambda R - 2I_1(\lambda R)}{\lambda^2 R^2}\frac{\bar{C}}{\lambda^2}.$$

Substituting for $p(r, \theta)$ from (60) and $\bar{C}$ from (64), and making use of $\lambda^2$ from (47), leads to

$$\sigma_r = K\varepsilon_b\frac{t}{t_p}\Big(\frac{I_1(\lambda r)}{I_1(\lambda R)} - \frac{r}{R} + \frac{1-\nu}{I_1(\lambda R)}\Big(\frac{I_0(\lambda R)\lambda R - 2I_1(\lambda R)}{\lambda^2 R^2}\frac{r}{R} - \frac{I_0(\lambda r)\lambda r - 2I_1(\lambda r)}{\lambda^2 r^2}\Big)\Big)\cos\theta,$$

$$\sigma_\theta = K\varepsilon_b\frac{t}{t_p}\Big(\frac{I_1(\lambda r)}{I_1(\lambda R)} - \frac{r}{R} + \frac{1-\nu}{I_1(\lambda R)}\Big(3\frac{I_0(\lambda R)\lambda R - 2I_1(\lambda R)}{\lambda^2 R^2}\frac{r}{R} + \frac{I_0(\lambda r)\lambda r - I_1(\lambda r)(\lambda^2 r^2 + 2)}{\lambda^2 r^2}\Big)\Big)\cos\theta,$$

$$\tau_{r\theta} = K\varepsilon_b\frac{t}{t_p}\frac{1-\nu}{I_1(\lambda R)}\Big(\frac{I_0(\lambda R)\lambda R - 2I_1(\lambda R)}{\lambda^2 R^2}\frac{r}{R} - \frac{I_0(\lambda r)\lambda r - 2I_1(\lambda r)}{\lambda^2 r^2}\Big)\sin\theta. \tag{65}$$

These results are plotted in Figure 9 again for the case where $\lambda R = 3$.
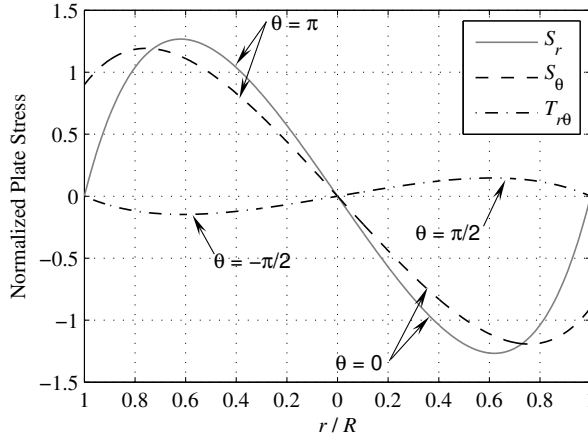


**Figure 9.** Plate stresses for bending in the large shape factor case.

# 6. Conclusion

The essential characteristic of the elastomeric isolator is the very large ratio of the vertical stiffness relative to the horizontal stiffness. This is produced by the reinforcing plates, which in current industry standard are thin steel plates. These plates prevent lateral bulging of the rubber, but allow the rubber

to shear freely. The vertical stiffness can be several hundred times the horizontal stiffness. The steel reinforcement has the effect of generating shear stresses in the rubber in the isolator and these stresses act on the steel plates to cause tension stresses which, if they were to become large enough, could result in failure of the steel shims through yielding or fracture. The external pressure on the isolator at which this might happen is an important design quantity for an isolator and it is therefore necessary to be able to estimate these tensile stresses under the applied external load. When the isolator is subject to shear deformation, a bending moment is generated by the unbalanced shear forces at the top and bottom of the bearing. These bending moments also affect the stresses in the steel shims and, in contrast to the case of pure compression, the stresses in the steel plates can be compressive and could produce buckling of the shims. No previous solution for the stresses due to bending moments in a bearing has been available. Here we provide analyses for the circular isolator for the two cases: namely, when the rubber can be assumed to be incompressible, generally in the low to moderate shape factor case, and also for the more typical situation, when the shape factor is sufficiently large that compressibility of the rubber needs to be taken into account in the theory. The solution for the compressible case both in pure compression and bending is new.

## References

[Billings 1992]  L. J. Billings, *Finite element modelling of elastomeric seismic isolation bearings*, Ph.D. thesis, University of California, Irvine, CA, 1992.

[Gent and Lindley 1959]  A. N. Gent and P. B. Lindley, "The compression of bonded rubber blocks", *Proc. Inst. Mech. Eng.* **173**:3 (1959), 111–122.

[Gent and Meinecke 1970]  A. N. Gent and E. A. Meinecke, "Compression, bending, and shear of bonded rubber blocks", *Polym. Eng. Sci.* **10**:1 (1970), 48–53.

[Imbimbo and De Luca 1998]  M. Imbimbo and A. De Luca, "F.E. stress analysis of rubber bearings under axial loads", *Comput. Struct.* **68**:1–3 (1998), 31–39.

[Kelly 1996]  J. M. Kelly, *Earthquake-resistant design with rubber*, 2nd ed., Springer, London, 1996.

[Rocard 1937]  Y. Rocard, "Note sur le calcul des propriétès élastiques des supports en caoutchouc adhérent", *J. Phys. Radium* **8**:5 (1937), 197–203.

[Spitz 1978]  I. Spitz, "The design and behavior of elastomeric bearing pads", *Die Siviele Ingenieur in Suid-Afrika* **20** (September 1978), 219–229.

[Stanton and Roeder 1982]  J. F. Stanton and C. W. Roeder, "Elastomeric bearings design, construction, and materials", NCHRP Report 248, Transportation Research Board, Washington, DC, August 1982.

[Timoshenko and Goodier 1970]  S. P. Timoshenko and J. N. Goodier, *Theory of elasticity*, 3rd ed., McGraw-Hill, New York, 1970.

JAMES M. KELLY: jmkelly@berkeley.edu
*University of California at Berkeley, Pacific Earthquake Engineering Research Center, 1301 South 46th Street, Richmond, CA 94804-4698, United States*

DIMITRIOS KONSTANTINIDIS: dakon@berkeley.edu
*University of California at Berkeley, Pacific Earthquake Engineering Research Center, 1301 South 46th Street, Richmond, CA 94804-4698, United States*

# A REFINED SINE-BASED FINITE ELEMENT WITH TRANSVERSE NORMAL DEFORMATION FOR THE ANALYSIS OF LAMINATED BEAMS UNDER THERMOMECHANICAL LOADS

PHILIPPE VIDAL AND OLIVIER POLIT

In the framework of a sine model family, two new three-node beam finite elements including the transverse normal effect are designed for the analysis of laminated beams. They are based on a sine distribution with layer refinement and a second-order expansion for the deflection. The transverse shear strain is obtained using a cosine function, avoiding the use of shear correction factors. This kinematics accounts for the interlaminar continuity conditions on the interfaces between layers, and the boundary conditions on the upper and lower surfaces of the beam. A conforming FE approach is carried out using Lagrange and Hermite interpolations. It is important to notice that the number of unknowns is independent of the number of layers.

Both mechanical and thermomechanical tests for thin and thick beams are presented in order to evaluate the capability of these new finite elements to give accurate results with respect to elasticity or finite element reference solutions. Both convergence velocity and accuracy are discussed and this new finite element yields very satisfactory results at a low computational cost. In particular, the transverse stress computed from the constitutive relation is well estimated with regards to classical equivalent single layer models. This work focuses on the necessity to take into account the transverse normal stress, especially for thick beam and coupled analysis.

## 1. Introduction

Composite and sandwich structures are widely used in industry due to their excellent mechanical properties, especially their high specific stiffness and strength. In this context, they can be subjected to severe mechanical and thermal conditions (through heating or cooling). For composite design, an accurate knowledge of displacements and stresses is required. Hence it is important to take into account the effects of transverse shear deformation due to a low ratio of transverse shear modulus to axial modulus, or failure due to delamination. In fact, such effects can play an important role in the behavior of structures, and it is desirable to evaluate precisely their influence on local stress fields in each layer, particularly on the interface between layers.

The aim of this paper is to develop two finite elements including the transverse normal deformation, so as to obtain accurate predictions for the behavior of laminated composite beams subjected to mechanical and thermal loading. This analysis is limited to the elasticity area in relation to small displacements. In this context, we put the emphasis on the need to take into account the transverse normal effect, in particular for thermal conditions and for thick structures.

Several theories exist in the mechanics literature for composite or sandwich structures (beams and

plates for the present scope). They have been extended to thermomechanical problems as well. The following classification is associated with the dependence on the number of degrees of freedom (DOFs) with respect to the number of layers:

- The equivalent single layer approach (ESL): the number of unknowns is independent of the number of layers, but continuity of transverse shear and normal stresses is often violated at layer interfaces. The first work for one-layer isotropic plates was proposed in [Basset 1890]. Then, we can distinguish classical laminate theory [Tanigawa et al. 1989] (based on the Euler–Bernoulli hypothesis and leading to inaccurate results for composites and moderately thick beams, because both transverse shear and normal strains are neglected), first-order shear deformation theory [Mindlin 1951] (for composite laminates see [Yang et al. 1966]), and higher-order theories [Librescu 1967; Whitney and Sun 1973; Lo et al. 1977; Reddy 1984].

  In this family, some studies take into account transverse normal deformation. A nonconstant polynomial expression for the out-of-plane displacement is considered in [Kant et al. 1997; Cook and Tessler 1998; Barut et al. 2001; Kant and Swaminathan 2002; Matsunaga 2002; Rao and Desai 2004; Subramanian 2006; Swaminathan and Patil 2007] with a higher-order theory. Specific functions such as the exponential are also used [Soldatos and Watson 1997; Liu and Soldatos 2002]. All these studies are based on a displacement approach, although other approaches are formulated on the basis of mixed formulations [Carrera 2000b; Kim and Cho 2007]. The finite element method is also applied [Kant and Gupta 1988; Vinayak et al. 1996; Subramanian 2001; Zhang and Kim 2005]. In the framework of thermomechanical problems, different approaches have been developed, including mixed formulations [Tessler et al. 2001] and displacement-based ones [Rolfes et al. 1998; Ali et al. 1999; Rohwer et al. 2001; Robaldo 2006].

- The layerwise approach (LW): the number of DOFs depends on the number of layers. This theory aims at overcoming the ESL shortcoming of allowing discontinuity of out-of-plane stresses on the interface layers. It was introduced in [Heller and Swift 1971; Swift and Heller 1974], and also used in [Pagano 1969; Whitney 1969; Srinivas 1973]. For recent contributions, see [Reddy 1989; Shimpi and Ainapure 2001; Kärger et al. 2006]. A mixed formulation also exists [Mau 1973; Murakami 1986].

  Again, some models taking into account the transverse normal effect have been developed: [Icardi 2001; Pai and Palazotto 2001] within a displacement based approach and [Carrera 1999; 2000b; 2004; Rao and Desai 2004] within a mixed formulation. For the thermomechanical analysis, readers can refer to [Robaldo 2006] (displacement) and [Carrera 2000a; Gherlone and di Sciuva 2007] (mixed).

In this framework, refined models have been developed in order to improve the accuracy of ESL models while avoiding the computational burden of the LW approach. Based on physical considerations and after some algebraic transformations, the number of unknowns becomes independent of the number of layers. Whitney [1969] has extended the work of Ambartsumyan [1969] for symmetric laminated composites with arbitrary orientation and a quadratic variation of the transverse stresses in each layer. A family of models, called zig-zag models, was first employed in [di Sciuva 1986], then in [Bhaskar and Varadan 1989; Lee et al. 1992; Cho and Parmerter 1993]. More recently, it was modified and improved in [Gaudenzi et al. 1995; Averill and Yip 1996; Aitharaju and Averill 1999; di Sciuva and Icardi 2001; Kapuria et al. 2003; Gherlone and di Sciuva 2007] with different-order kinematics assumptions, taking into account transverse normal strain.

Another way to improve the accuracy of results consists in the sublaminates strategy, which is proposed in [Flanagan 1994; Averill and Yip 1996]. The number of subdivisions of the laminate thickness determines the accuracy of the approach. It allows localization of the layer refinement without increasing the order of approximation. Nevertheless, the computational cost increases with the number of numerical layers. For recent studies, the reader can also refer to [Icardi 2001; Rao and Desai 2004; Gherlone and di Sciuva 2007].

The literature just cited deals with only some aspects of the broad research activity about models for layered structures and corresponding finite element formulations. An extensive assessment of different approaches has been made in [Noor and Burton 1990; Reddy 1997; Carrera 2002; 2003; Zhang and Yang 2009]. About the particular point of the evaluation of transverse normal stresses, see [Kant and Swaminathan 2000; Mittelstedt and Becker 2007].

In this work, two new finite elements for rectangular laminated beam analysis are built, in order to have a low cost tool that is efficient and simple to use. Our approach is associated with ESL theory. The elements are totally free of shear locking and are based on a refined shear deformation theory [Touratier 1992a] avoiding the use of shear correction factors for laminates. They are based on the sine model of [Ganapathi et al. 1999]. The important new feature is the capability of the model to include the transverse normal effect. So, the transverse displacement is written under a second-order expansion which avoids the Poisson locking mechanism [Carrera and Brischetto 2008]. For the in-plane displacement, the double superposition hypothesis from [Li and Liu 1997] is used: three local functions are added to the sine model. Finally, this process yields to only six or seven independent generalized displacements. All interface and boundary conditions are exactly satisfied for displacements and transverse shear stress. Therefore, this approach takes into account physical meaning.

As far as the interpolation of these finite elements is concerned, our elements are $C^0$-continuous except for the transverse displacement associated with bending, which is $C^1$.

We now outline the remainder of this article. First the mechanical formulation for the different models is described. For each of these approaches, the associated finite element is given. They are illustrated by numerical tests performed upon various laminated and sandwich beams. A parametric study is given to show the effects of different parameters such as the length-to-thickness ratio and the number of DOFs. The accuracy of computations is also evaluated by comparison with an exact 3D theory for laminates in bending [Pagano 1969; Ali et al. 1999] and also 2D finite element computations using commercial software. We put the emphasis on the direct calculation of the transverse shear stress from the constitutive relations. The results of our model are then compared with the approach consisting in calculating transverse shear stresses from the equilibrium equations, as in [Chaudhri 1986; Barbero et al. 1990; Vinayak et al. 1996; Liu and Soldatos 2002; Kapuria et al. 2004; Tahani 2007]. In this framework, other approaches are proposed to evaluate transverse shear or normal stresses accurately. Some authors use a hybrid mixed finite element formulation [Han and Hoa 1993] or an iterative predictor-corrector computational procedure [Noor and Malik 1999]. The transverse normal stress is calculated from the integration of the equilibrium equation, avoiding the discontinuity that arises from the use of the constitutive law.

Finally, other numerical examples are presented to demonstrate the effectiveness of the proposed finite elements in coupled analysis. Computations for thick and thin beams of laminated composites are compared to exact 2D elasticity solutions under thermomechanical loading.
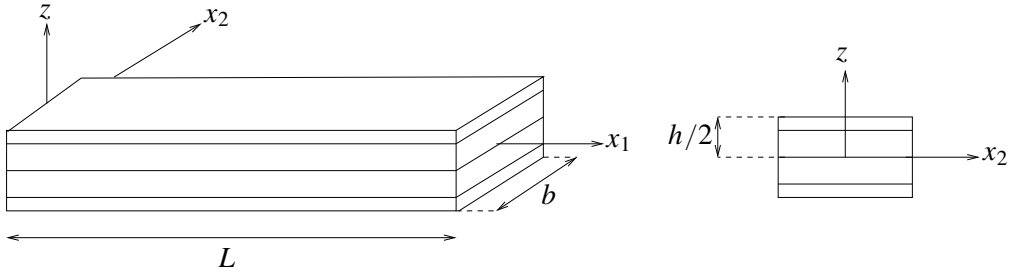
**Figure 1.** The laminated beam and coordinate system.

## 2. Resolution of the thermomechanical problem

***The governing equations for thermomechanics.***  Let us consider a beam occupying the domain

$$\mathcal{B} = [0, L] \times \left[-\frac{h}{2} \le z \le \frac{h}{2}\right] \times \left[-\frac{b}{2} \le x_2 \le \frac{b}{2}\right]$$

in a Cartesian coordinate $(x_1, x_2, z)$. The beam has a rectangular uniform cross section of height $h$ and width $b$ and is assumed to be straight. The beam is made of *NC* layers of different linearly elastic materials. Each layer may be assumed to be orthotropic in the beam axes. The $x_1$ axis is taken along the central line of the beam whereas $x_2$ and $z$ are the two axes of symmetry of the cross section intersecting at the centroid, see Figure 1. As shown in this figure, the $x_2$ axis is along the width of the beam. This work is based upon a displacement approach for geometrically linear elastic beams.

*Constitutive relation.*  Each layer of the laminate is assumed to be orthotropic. Using matrix notation, the thermoelastic stress-strain law of the $k$-th layer is given by

$$\begin{bmatrix} \sigma_{11}^{(k)} \\ \sigma_{33}^{(k)} \\ \sigma_{13}^{(k)} \end{bmatrix} = \begin{bmatrix} C_{11}^{(k)} & C_{13}^{(k)} & 0 \\ & C_{33}^{(k)} & 0 \\ \text{symmetric} & & C_{55}^{(k)} \end{bmatrix} \begin{bmatrix} \varepsilon_{11}^{(k)} - \alpha_{11}^{(k)} \Delta T \\ \varepsilon_{33}^{(k)} - \alpha_{33}^{(k)} \Delta T \\ \varepsilon_{13}^{(k)} \end{bmatrix}, \quad \text{that is, } [\sigma^{(k)}] = [C^{(k)}][\varepsilon^{(k)}], \quad (1)$$

where $\Delta T$ is the temperature rise, $[\sigma]$ is the stress tensor, $[\varepsilon]$ is the strain tensor, the $C_{ij}$ are the 3D stiffness coefficients, and $\alpha_{ij}$ are the thermal expansion coefficients obtained after a transformation from the material axes to the Cartesian coordinate system.

*The weak form of the boundary value problem.*  Using the above matrix notation and for admissible virtual displacement $\vec{u}^* \in U^*$, the variational principle is this:

   *Find $\vec{u}$ in the space $U$ of admissible displacements such that*

$$-\int_{\mathcal{B}} [\varepsilon(\vec{u}^*)]^T [\sigma(\vec{u})] d\mathcal{B} + \int_{\mathcal{B}} [u^*]^T [f] d\mathcal{B} + \int_{\partial\mathcal{B}_F} [u^*]^T [F] d\partial\mathcal{B} = \int_{\mathcal{B}} \rho [u^*]^T [\ddot{u}] d\mathcal{B}, \quad \forall \vec{u}^* \in U^*, \quad (2)$$

*where $[f]$ and $[F]$ are the prescribed body and surface forces applied on $\partial\mathcal{B}_F$, $\varepsilon(\vec{u}^*)$ is the virtual strain, and $\rho$ is the mass density.*

   Equation (2) is a classical starting point for finite element approximations.

***The displacement field for laminated beams.*** Based on the sine function [Touratier 1991; Dau et al. 2006], we now present two models that take into account transverse normal deformation:

- SinRef-6p, a refined sine model with second-order expansion for the transverse displacement and the refinement added in each layer; and

- SinRef-7p, a refined sine model with one more unknown than SinRef-6p for in-plane displacement.

These models are based on

- works on beams, plates and shells such as [Ganapathi et al. 1999; Touratier 1991; 1992a; 1992b; Polit and Touratier 2002; Vidal and Polit 2006; 2009], covering the refined theory, and

- the so-called 1,2-3 double-superposition theory of [Li and Liu 1997].

It also follows the local-global approach studied in [Sze et al. 1998; Wu et al. 2005; Zhen and Wanji 2007].

These refined models (see [Vidal and Polit 2008]) take into account the continuity conditions between layers of the laminate for both displacements and transverse shear stress, and the free conditions on the upper and lower surfaces owing to the Heaviside function.

The kinematics of the two models is assumed to be of the following particular form, where the prime stands for differentiation with respect to $x_1$ and $H$ is the Heaviside step function ($H(z) = 1$ if $z \geq 0$ and $H(z) = 0$ otherwise):

1. The 6-parameter SinRef-6p model:

$$
\begin{cases}
u_1(x_1, x_2, z) = u(x_1) - zw_0(x_1)' + f(z)(\omega_3(x_1) + w_0(x_1)') \\
\qquad\qquad\qquad + \sum_{k=1}^{NC} (\bar{u}_{\text{loc}}^{(k)}(x_1, z) + \hat{u}_{\text{loc}}^{(k)}(x_1, z))(H(z - z_k) - H(z - z_{k+1})), \quad (3) \\
u_3(x_1, x_2, z) = w_0(x_1) + zw_1(x_1) + z^2 w_2(x_1).
\end{cases}
$$

2. The 7-parameter SinRef-7p model:

$$
\begin{cases}
u_1(x_1, x_2, z) = u(x_1) + zv(x_1) + f(z)(\omega_3(x_1) + w_0(x_1)') \\
\qquad\qquad\qquad + \sum_{k=1}^{NC} (\bar{u}_{\text{loc}}^{(k)}(x_1, z) + \hat{u}_{\text{loc}}^{(k)}(x_1, z))(H(z - z_k) - H(z - z_{k+1})), \quad (4) \\
u_3(x_1, x_2, z) = w_0(x_1) + zw_1(x_1) + z^2 w_2(x_1).
\end{cases}
$$

In the classic approach, $w_0$ is the bending deflection following the $z$ direction, while $u$ is associated with the uniform extension of the cross section of the beam along the central line, and $\omega_3$ is the shear bending rotation around the $z$ axis.

Note that the kinematic constraint concerning the relation with the derivative of the deflection ($v(x_1) = -w_0(x_1)_{,1}$) is relaxed in the SinRef-7p model.

The local functions $\bar{u}_{\text{loc}}^{(k)}$ and $\hat{u}_{\text{loc}}^{(k)}$ are based on the first few Legendre polynomials, which are $A_1(\zeta) = \zeta$, $A_2(\zeta) = -\frac{1}{2} + \frac{3}{2}\zeta^2$, and $A_3(\zeta) = -\frac{3}{2}\zeta + \frac{5}{2}\zeta^3$. They can be written as

$$
\bar{u}_{\text{loc}}^{(k)}(x_1, z) = A_1(\zeta_k)u_{31}^k(x_1) + A_2(\zeta_k)u_{32}^k(x_1), \qquad \hat{u}_{\text{loc}}^{(k)}(x_1, z) = A_3(\zeta_k^3)u_{33}^k(x_1), \quad (5)
$$
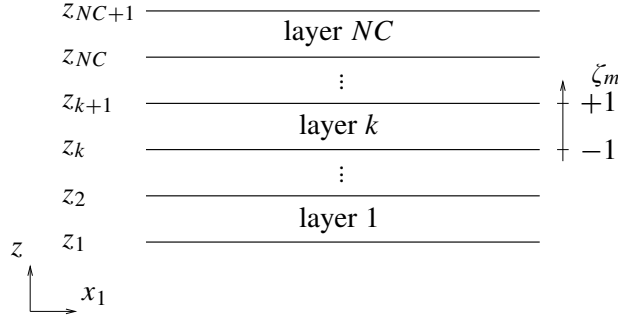
**Figure 2.** Transverse coordinate of the laminated beam.

where we have introduced the nondimensional coordinate

$$\zeta_k = a_k z - b_k, \qquad \text{with } a_k = \frac{2}{z_{k+1} - z_k} \text{ and } b_k = \frac{z_{k+1} + z_k}{z_{k+1} - z_k} \tag{6}$$

(see Figure 2). Legendre polynomials are orthogonal over the interval $[-1, 1]$ to constants and to each other — that is, $\int_{-1}^{1} A_i(\zeta_k)\, d\zeta_k = 0$ for $i = 1, 2, 3$ and $\int_{-1}^{1} A_i(\zeta_k) A_j(\zeta_k) d\zeta_k = 0$ for $i \neq j$.

From (3), classical beam models can be deduced without the local functions and the two higher-order terms of the transverse displacement:

- Euler–Bernoulli: $\qquad\qquad\qquad\qquad\qquad f(z) = 0,$

- Timoshenko: $\qquad\qquad\qquad\qquad\qquad f(z) = z,$

- sine model: $\qquad\qquad\qquad\qquad\qquad f(z) = \dfrac{h}{\pi} \sin \dfrac{\pi z}{h}.$

The derivative of this last function will represent the transverse shear strain distribution due to bending. Note that it is not necessary to introduce transverse shear correction factors because the two models in this work predict the shear energy sufficiently accurately, thanks to the higher-order kinematic assumptions.

At this stage, $3 \times NC + 5$ generalized displacements are included in the SinRef-6p model and $3 \times NC + 6$ in the SinRef-7p model; see (3)+(5) and (4)+(5), respectively.

We next turn to the task of deriving relations between the kinematic unknowns from

- lateral boundary conditions, and

- interlaminar continuity conditions (displacement, transverse shear stress).

In the following, we only focus on the SinRef-7p model. The same procedure can be carried out for the SinRef-6p model by setting $v(x_1) = -w_0(x_1)_{,1}$.

*Continuity conditions and free conditions.* From the displacement field (4), continuity conditions on displacements and the interlaminar stress must be imposed. For an interface layer $k \in \{2, \dots, NC\}$, we have:

- Displacement continuity conditions as in [Sze et al. 1998]:

$$\bar{u}_{\text{loc}}^{(k)}(x_1, z_k) = \bar{u}_{\text{loc}}^{(k-1)}(x_1, z_k), \qquad k = 2, \dots, NC,$$
$$\hat{u}_{\text{loc}}^{(k)}(x_1, z_k) = \hat{u}_{\text{loc}}^{(k-1)}(x_1, z_k), \qquad k = 2, \dots, NC. \tag{7}$$

- Transverse shear stress continuity between two adjacent layers:

$$\sigma_{13}^{(k)}(x_1, z_k^+) = \sigma_{13}^{(k-1)}(x_1, z_k^-), \qquad k = 2, \dots, NC. \tag{8}$$

So, $3 \times (NC - 1)$ conditions are imposed, which allows us to reduce the number of unknowns to 9 generalized displacements.

Free conditions of the transverse shear stress on the upper and lower surfaces must also be verified. So, we have

$$\sigma_{13}^{(1)}\left(x_1, z = -\frac{h}{2}\right) = 0, \qquad \sigma_{13}^{(NC)}\left(x_1, z = \frac{h}{2}\right) = 0. \tag{9}$$

Finally, the number of generalized displacements is reduced to 7, which is independent from the number of layers.

*Relation between the generalized displacements.* Using the notations introduced in (5), the conditions (7)–(9) can be written in the following form:

$$[A]\{v\} = \{b\}u_{31}^1(x_1) + \{c\}(\omega_3(x_1) + w_0(x_1)') + \{d\}(v(x_1) + w_0(x_1)') + \{e\}w_1(x_1)' + \{f\}w_2(x_1)', \tag{10}$$

where $[A]$ is a $(3\,NC - 1) \times (3\,NC - 1)$ matrix, and $\{b\}$, $\{c\}$, $\{d\}$, $\{e\}$, $\{f\}$, and

$$\{v\}^T = \left\{ u_{32}^1 \ u_{33}^1 \ \vdots \ u_{31}^j \ u_{32}^j \ u_{33}^j \ \vdots \ u_{31}^{NC} \ u_{32}^{NC} \ u_{33}^{NC} \right\}^T$$

are vectors with $3\,NC - 1$ components.

From the resolution of this linear system, relations between $u_{31}^j$ $(j \neq 1)$, $u_{32}^j$, $u_{33}^j$, $j = 1, \dots, NC$, and $u_{31}^1$ can be deduced. This relation can be written in the following form:

$$u_{3i}^j(x_1) = \beta_i^j\left(\omega_3(x_1) + w_0(x_1)'\right) + \eta_i^j\left(v(x_1) + w_0(x_1)'\right)$$
$$+ \delta_i^j u_{31}^1(x_1) + \lambda_i^j w_1(x_1)' + \mu_i^j w_2(x_1)', \quad j = 1, \dots, NC, \quad i = 1, 2, 3, \tag{11}$$

with $\delta_1^1 = 1$ and $\beta_1^1 = \eta_1^1 = \lambda_1^1 = \mu_1^1 = 0$, and where $\beta_i^j$, $\delta_i^j$, $\lambda_i^j$, $\mu_i^j$, and $\eta_i^j$ $(i = 1, 2, 3)$ are the coefficients deduced from (10).

Finally, the 7 unknowns become $u$, $w_0$, $\omega_3$, $v$, $w_1$, $w_2$, and $u_{31}^1$. It is noted that the SinRef-6p model involves 6 unknowns ($u$, $w_0$, $\omega_3$, $w_1$, $w_2$, and $u_{31}^1$).

*Expression of strains.* Matrix notation can be easily defined using a generalized displacement vector as

$$[u]^T = [F_u(z)][\mathscr{E}_u], \quad [\mathscr{E}_u]^T = \left[ u \ \cdots \ w_0 \ w_{0,1} \ \cdots \ \omega_3 \ \cdots \ u_{31}^1 \ \cdots \ v \ \cdots \ w_1 \ w_{1,1} \ \cdots \ w_2 \ w_{2,1} \right], \tag{12}$$

and $[F_u(z)]$ depends on the normal coordinate $z$ according to

$$[F_u(z)] = \begin{bmatrix} 1 & 0 & F_{u\,13}(z) & F_{u\,14}(z) & F_{u\,15}(z) & F_{u\,16}(z) & 0 & F_{u\,18}(z) & 0 & F_{u\,110}(z) \\ 0 & 1 & 0 & 0 & 0 & 0 & z & 0 & z^2 & 0 \end{bmatrix}, \tag{13}$$

where

$$F_{u\,13}(z) = f(z) + S_\beta(z) + S_\eta(z), \qquad F_{u\,15}(z) = S_\delta(z), \qquad F_{u\,18}(z) = S_\lambda(z),$$
$$F_{u\,14}(z) = f(z) + S_\beta(z), \qquad F_{u\,16}(z) = z + S_\eta(z), \qquad F_{u\,110}(z) = S_\mu(z),$$

and

$$S_\beta(z) = \sum_{k=1}^{NC} \left(\zeta_k \beta_1^k + \left(-\tfrac{1}{2} + \tfrac{3}{2}\zeta_k^2\right)\beta_2^k + \left(-\tfrac{3}{2}\zeta_k + \tfrac{5}{2}\zeta_k^3\right)\beta_3^k\right)\Delta H(k, k+1),$$

$$S_\delta(z) = \sum_{k=1}^{NC} \left(\zeta_k \delta_1^k + \left(-\tfrac{1}{2} + \tfrac{3}{2}\zeta_k^2\right)\delta_2^k + \left(-\tfrac{3}{2}\zeta_k + \tfrac{5}{2}\zeta_k^3\right)\delta_3^k\right)\Delta H(k, k+1),$$

$$S_\eta(z) = \sum_{k=1}^{NC} \left(\zeta_k \eta_1^k + \left(-\tfrac{1}{2} + \tfrac{3}{2}\zeta_k^2\right)\eta_2^k + \left(-\tfrac{3}{2}\zeta_k + \tfrac{5}{2}\zeta_k^3\right)\eta_3^k\right)\Delta H(k, k+1),$$

$$S_\lambda(z) = \sum_{k=1}^{NC} \left(\zeta_k \lambda_1^k + \left(-\tfrac{1}{2} + \tfrac{3}{2}\zeta_k^2\right)\lambda_2^k + \left(-\tfrac{3}{2}\zeta_k + \tfrac{5}{2}\zeta_k^3\right)\lambda_3^k\right)\Delta H(k, k+1),$$

$$S_\mu(z) = \sum_{k=1}^{NC} \left(\zeta_k \mu_1^k + \left(-\tfrac{1}{2} + \tfrac{3}{2}\zeta_k^2\right)\mu_2^k + \left(-\tfrac{3}{2}\zeta_k + \tfrac{5}{2}\zeta_k^3\right)\mu_3^k\right)\Delta H(k, k+1),$$

with $\Delta H(k, k+1) = H(z - z_k) - H(z - z_{k+1})$.

The strains for the laminated beam are

$$\varepsilon_{11} = u_{,1} + z v_{,1} + (f(z) + S_\beta(z))(w_{0,11} + \omega_{3,1}) + S_\delta(z)u^1_{31,1}$$
$$+ S_\lambda(z)w_{1,11} + S_\mu(z)w_{2,11} + S_\eta(z)(w_{0,11} + v_{,1}),$$

$$\varepsilon_{33} = w_1 + 2z w_2, \tag{14}$$

$$\gamma_{13} = (f(z)_{,3} + S_\beta(z)_{,3})(w_{0,1} + \omega_3) + S_\delta(z)_{,3}u^1_{31}$$
$$+ (0 + S_\eta(z)_{,3})(w_{0,1} + v) + (z + S_\lambda(z)_{,3})w_{1,1} + (z^2 + S_\mu(z)_{,3})w_{2,1}.$$

These expressions can be described in matrix notation by

$$[\varepsilon] = [F_s(z)][\mathcal{E}_s],$$

$$[\mathcal{E}_s]^T = \left[u_{,1} \;\vdots\; w_{0,1}\; w_{0,11} \;\vdots\; \omega_3\; \omega_{3,1} \;\vdots\; u^1_{31}\; u^1_{31,1} \;\vdots\; v\; v_{,1} \;\vdots\; w_1\; w_{1,1}\; w_{1,11} \;\vdots\; w_2\; w_{2,1}\; w_{2,11}\right], \tag{15}$$

and $[F_s(z)]$ depends on the normal coordinate $z$ as

$$[F_s(z)] = \begin{bmatrix} 1 & 0 & f(z) + S_\beta(z) + S_\eta(z) & 0 & \cdots \\ 0 & 0 & 0 & 0 & \cdots \\ 0 & 1 + \left(f(z)_{,3} + S_\beta(z)_{,3} + S_\eta(z)_{,3}\right) & 0 & \left(f(z)_{,3} + S_\beta(z)_{,3}\right) & \cdots \end{bmatrix}$$

$$\begin{bmatrix} \left(f(z) + S_\beta(z)\right) & 0 & S_\delta(z) & 0 & z + S_\eta(z) & 0 & 0 & S_\lambda(z) & 0 & 0 & S_\mu(z) \\ 0 & 0 & 0 & 0 & 0 & 1 & 0 & 0 & 2z & 0 & 0 \\ 0 & S_\delta(z)_{,3} & 0 & 1 + S_\eta(z)_{,3} & 0 & 0 & z + S_\lambda(z)_{,3} & 0 & 0 & z^2 + S_\mu(z)_{,3} & 0 \end{bmatrix}. \tag{16}$$

*Matrix expression for the weak form.* From the weak form of the boundary value problem (2), and using (15) and (16), an integration throughout the cross-section is performed analytically in order to obtain an unidimensional formulation. Therefore, the first left term of (2) can be written in the following form:

$$\int_{\mathcal{B}} [\varepsilon(\vec{u}^*)]^T [\sigma(\vec{u})]\, d\mathcal{B} = \int_0^L [\mathcal{E}_s^*]^T [k][\mathcal{E}_s]\, dx_1, \qquad [k] = \int_\Omega [F_s(z)]^T [C][F_s(z)]\, d\Omega, \tag{17}$$

where $[C]$ is the constitutive law given on page 1130 and $\Omega$ represents the cross-section

$$\left[-\frac{h}{2} \le z \le \frac{h}{2}\right] \times \left[-\frac{b}{2} \le x_2 \le \frac{b}{2}\right].$$

$$
\begin{array}{|l} u \\ w_0 \quad w_1 \\ w_{0,1}\, w_{1,1} \\ \omega_3 \quad w_2 \\ u_{31}^1 \quad w_{2,1} \end{array}
\qquad
\begin{array}{|l} u \\ \omega_3 \\ u_{31}^1 \end{array}
\qquad
\begin{array}{|l} u \\ w_0 \quad w_1 \\ w_{0,1}\, w_{1,1} \\ \omega_3 \quad w_2 \\ u_{31}^1 \quad w_{2,1} \end{array}
$$

$$
\begin{array}{|l} u \quad v \\ w_0 \quad w_1 \\ w_{0,1}\, w_{1,1} \\ \omega_3 \quad w_2 \\ u_{31}^1 \quad w_{2,1} \end{array}
\qquad
\begin{array}{|l} u \\ \omega_3 \\ u_{31}^1 \\ v \end{array}
\qquad
\begin{array}{|l} u \quad v \\ w_0 \quad w_1 \\ w_{0,1}\, w_{1,1} \\ \omega_3 \quad w_2 \\ u_{31}^1 \quad w_{2,1} \end{array}
$$

**Figure 3.** Description of the laminated beam finite element DOF. SinRef-6p (left) and SinRef-7p (right).

In (17), the matrix $[k]$ is the integral of the beam's material characteristics throughout the cross-section. An advantage of the Legendre polynomials is the easy calculation of the matrices $[k]$, arising from orthogonality (page 1132).

**The finite element approximation.** This section is devoted to the finite element approximation of the generalized displacement, see the matrices $[\mathscr{E}_s]$, $[\mathscr{E}_s^*]$, $[\mathscr{E}_u]$, and $[\mathscr{E}_u^*]$ from (15) and (12). We describe it briefly; for details see [Ganapathi et al. 1999; Vidal and Polit 2008].

*The geometric approximation.* Given the displacement field constructed above for sandwich and laminated beams, a corresponding finite element is developed in order to analyze the behavior of laminated beam structures under combined loads. Let us consider the $e$-th element $L_e{}^h$ of the mesh $\bigcup L_e{}^h$. This element has three nodes, denoted by $(g_j)_{j=1,2,3}$, see Figure 3. The coordinate $x_1$ of a point on the central line of the beam is approximated by

$$
x_1(\xi) = \sum_{j=1}^{2} Nl_j(\xi) x_1{}^e(g_j), \tag{18}
$$

where the $Nl_j(\xi)$ are Lagrange linear interpolation functions and the $x_1{}^e(g_j)$ are Cartesian coordinates (measured along the $x_1$ axis) of node $g_j$ of element $L_e{}^h$. The isoparametric or reduced coordinate $\xi$ ranges in the interval $[-1, 1]$.

*Interpolation for the bending-traction beam element.* The finite element approximations of the assumed displacement field components are hereafter symbolically written as $u_i{}^h(x_1, x_2, z)$ where the superscript $h$ refers to the mesh $\bigcup L_e{}^h$.

The kinematic equation (4) states that the transverse displacement $w_0^h$ must be $C^1$-continuous; the rotation angle $\omega_3{}^h$, the extension displacement $u^h$, and the variables $v^h$ and $u_{31}^1$ might be only $C^0$-continuous. Therefore, the generalized displacements $w_0^h$, $w_1^h$, and $w_2^h$ are interpolated by the Hermite cubic functions $Nh_j(\xi)$.

According to the transverse shear locking condition, the other shear bending generalized displacements and the rotation angle $\omega_3{}^h$ are interpolated by Lagrange quadratic functions, denoted by $Nq_j(\xi)$. This choice allows the same order of interpolation for both $w_{0,1}^h$ and $\omega_3{}^h$ in the corresponding transverse shear strain components due to bending, thus avoiding transverse shear locking according to the field compatibility approach [Polit et al. 1994].

Finally, the generalized displacements $u^h$, $v^h$, $u_{31}^1$ are interpolated by Lagrange quadratic functions.

*Elementary matrices.* Having defined all the finite element mechanical approximations, we can now deduce the elementary stiffness matrix $[K_{uu}^e]$ from (17). It has the expression

$$[K_{uu}^e] = \int_{L_e} [B]^T [k][B] \, dL_e, \tag{19}$$

where $[B]$ is deduced from the relation between the generalized displacement vectors (15) and the elementary vector of DOFs, denoted by $[q_e]$:

$$[\mathscr{E}_s] = [B][q_e]. \tag{20}$$

The matrix $[B]$ contains only the derivatives of the interpolation functions and the Jacobian components. The same technique can be used to define the elementary mechanical load vector, denoted $[B_u^e]$, but it is not detailed here.

## 3. Results and discussion

In this section, several static tests are presented validating our finite element and evaluating its efficiency. The influence of transverse normal stress is also discussed and evaluated through the integration of the equilibrium equation. Then, a thermomechanical problem is carried out.

*Mechanical analysis.* The aim of our investigation is to study the efficiency of these new elements to analyze the flexural behavior of highly inhomogeneous laminated beams for static mechanical problems under global and localized pressure. The results are compared with those obtained with SinRef-c, the sine model with Heaviside function [Vidal and Polit 2008], which does not take into account the transverse normal effect; and also with reference solutions (the exact solution [Pagano 1969] or a 2D solution calculated with ANSYS). To evaluate the performance of the element in bending, we considered various cases in the next three sections.

*Properties of the finite element.* Before proceeding to the detailed analysis, numerical computations are carried out for the rank of the element (spurious mode), convergence properties and the effect of aspect ratio (shear locking).

The test concerns simply supported thick symmetric composite beams and is taken from [Pagano 1969]. It is detailed below.

Geometry: Composite cross-ply beam $(0°/90°/0°)$ and length to thickness ratio $S = 4$ ($S = \frac{L}{h}$); half of the beam is meshed. All layers have the same thickness.

Boundary conditions: Simply supported beam subjected to a sinusoidal load $q(x_1) = q_0 \sin \frac{\pi x_1}{L}$.

Material properties:

$$E_L = 172.4 \, \text{GPa}, \quad E_T = 6.895 \, \text{GPa}, \quad G_{LT} = 3.448 \, \text{GPa}, \quad G_{TT} = 1.379 \, \text{GPa}, \quad \nu_{LT} = \nu_{TT} = 0.25,$$

where $L$ refers to the fiber direction, and $T$ refers to the transverse direction.

This element has a proper rank without any spurious energy modes when exact integration is applied to obtain the stiffness matrix [Ganapathi et al. 1999]. For this purpose, a scheme with three integration points is used. There is also no need to use shear correction factors here, as the transverse strain is represented by a cosine function.

| N | number of DOFs | $\bar{w}(L/2,0)$ | error | $\bar{\sigma}_{13}(0,0)$ | | | |
|---|---|---|---|---|---|---|---|
| | | | | direct | error | equil. eq. | error |
| 1 | 12 | 2.8984 | 0.4% | 1.4395 | 0.6% | 0.9404 | 34% |
| 2 | 24 | 2.8897 | 0.1% | 1.4184 | 0.9% | 1.2974 | 9% |
| 4 | 48 | 2.8887 | 0.1% | 1.4168 | 1% | 1.3960 | 2% |
| 8 | 96 | 2.8886 | 0.0% | 1.4167 | 1% | 1.4212 | 0.7% |
| 16 | 192 | 2.8886 | 0.0% | 1.4328 | 0.1% | 1.4421 | 0.7% |

**Table 1.** $\bar{\sigma}_{13}(0,0)$ and $\bar{w}(L/2,0)$ for different number of DOFs: mesh convergence study, with three layers $(0°/90°/0°)$, $S = 4$, SinRef-6p. The word "direct" labels results derived from the constitutive equation, rather than the equilibrium equation.

Table 1 gives the convergence of the SinRef-6p model for the transverse displacement and the transverse shear stress for $S = 4$. For this last component, results can be obtained using the constitutive relation (column labeled "direct" with its corresponding percent error), or alternatively using the equilibrium equation at the postprocessing level, that is

$$\sigma_{13}(z) = -\int_{-h/2}^{z} \sigma_{11,1} \, dx_3,$$

(column labeled "equil. eq" and its error). It must be noticed that the deflection is less sensitive to the mesh than the shear stress. The convergence velocity is very high. Based on progressive mesh refinement, a $N = 8$ mesh is adequate to model the thick laminated beam for a bending analysis. Moreover, the results obtained with coarse meshes are in good agreement with the reference values. Note that this model gives very good results for the transverse shear stress calculated with the constitutive relation.

Considering various values for the aspect ratio, the normalized displacement obtained at the middle of the simply supported composite beam is shown in Figure 4 along with the exact solution [Pagano 1970], and they are found to be in excellent agreement. It is also inferred from Figure 4 that the present
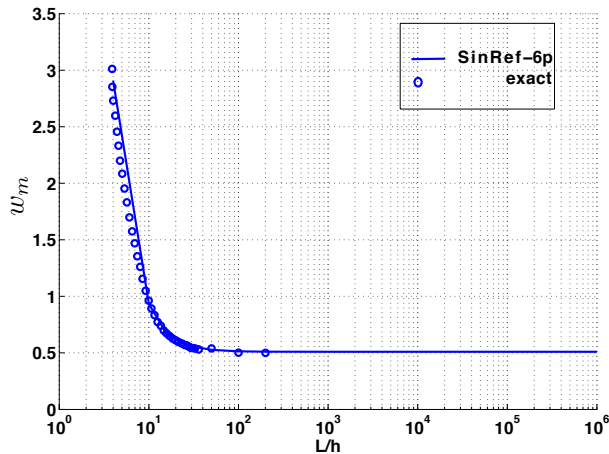


**Figure 4.** Nondimensional maximum displacement $w_m = 100u_3(L/2,0)E_T h^3/(q_0 L^4)$ versus aspect ratio $S$, with three layers $(0°/90°/0°)$, mesh $N = 8$, SinRef-6p model.

element is free from the shear locking phenomenon as the element is developed using a field compatibility approach.

*Bending analysis of laminated composite beam.* This test is about simply supported symmetric and antisymmetric composite beams from Reference [Pagano 1970]. It is detailed below.

Geometry: Composite cross-ply beam $(0°/90°/0°)$ and $(0°/90°)$ and length to thickness ratio from $S = 2$ to $S = 40$; half of the beam is meshed. All layers have the same thickness.

Boundary conditions: Simply supported beam subjected to a sinusoidal load $q(x_1) = q_0 \sin \dfrac{\pi x_1}{L}$.

Material properties: Same properties as on page 1136.

Mesh: $N = 8$.

Results: The results $(\bar{u}, \bar{w}, \bar{\sigma}_{11}, \bar{\sigma}_{13})$ are made nondimensional using

$$\bar{u} = \frac{E_T u_1(0, h/2)}{h q_0}, \quad \bar{w} = \frac{100 E_T u_3(L/2, 0)}{S^4 h q_0}, \quad \bar{\sigma}_{11} = \frac{\sigma_{11}(L/2, \pm h/2)}{q_0}, \quad \bar{\sigma}_{13} = \frac{\sigma_{13}(0, 0 \text{ or } -h/4)}{q_0}. \quad (21)$$

The two layer case $(0°/90°)$ is presented first. The numerical results for deflection, in-plane displacement, shear stress, and in-plane stress are given in Tables 2–4 with respect to the span-to-thickness ratio:

| | | | $\bar{u}(0, h/2)$ | | | | |
|---|---|---|---|---|---|---|---|
| $S$ | SinRef-7p | error | SinRef-6p | error | SinRef-c | error | exact |
| 2 | 0.760 | 0.3% | 0.801 | 5% | 0.848 | 11% | 0.762 |
| 4 | 4.55 | 0.1% | 4.60 | 1% | 4.78 | 5% | 4.55 |
| 20 | 485.22 | < 0.1% | 485.32 | < 0.1% | 486.20 | 0.2% | 485.15 |
| 40 | 3856.1 | < 0.01% | 3856.3 | < 0.01% | 3858.7 | < 0.1% | 3856.3 |
| | | | $\bar{w}(L/2, 0)$ | | | | |
| $S$ | SinRef-7p | error | SinRef-6p | error | SinRef-c | error | exact |
| 2 | 10.691 | 1% | 10.438 | 3% | 10.5608 | 2% | 10.849 |
| 4 | 4.682 | 0.2% | 4.614 | 1% | 4.696 | < 0.1% | 4.695 |
| 20 | 2.702 | < 0.1% | 2.699 | 0.1% | 2.703 | < 0.1% | 2.703 |
| 40 | 2.639 | 0.01% | 2.638 | < 0.1% | 2.640 | < 0.1% | 2.639 |

**Table 2.** $\bar{u}(0, h/2)$ and $\bar{w}(L/2, 0)$ for different values of $S$, with two layers $(0°/90°)$.

| | | | | maximum of $\bar{\sigma}_{13}$ | | | | | | | |
|---|---|---|---|---|---|---|---|---|---|---|---|
| | | SinRef-7p | | | | SinRef-6p | | | | SinRef-c | |
| $S$ | direct | error | equil.eq | error | direct | error | equil.eq | error | direct | error | equil.eq | error | exact |
| 2 | 1.213 | 5% | 1.112 | 3% | 1.121 | 3% | 1.163 | 0.6% | 1.202 | 4% | 1.248 | 8% | 1.155 |
| 4 | 2.761 | 2% | 2.679 | 1% | 2.546 | 5% | 2.717 | 0.4% | 2.588 | 4% | 2.768 | 2% | 2.706 |
| 20 | 14.709 | 0.6% | 14.540 | 0.5% | 13.463 | 7% | 14.549 | 0.5% | 13.450 | 8% | 14.555 | 0.5% | 14.620 |
| 40 | 29.488 | 0.5% | 29.167 | 0.5% | 26.981 | 7% | 29.172 | 0.5% | 26.940 | 8% | 29.165 | 0.5% | 29.324 |

**Table 3.** Maximum value of $\bar{\sigma}_{13}$ for different values of $S$, with two layers $(0°/90°)$. The maximum occurs at $(0, -h/4)$ for $S = 4, 20, 40$.

| | | | | | | | |
|---|---|---|---|---|---|---|---|
| | | | $\bar{\sigma}_{11}(L/2, -h/2)$ | | | | |
| $S$ | SinRef-7p | error | SinRef-6p | error | SinRef-c | error | exact |
| 2 | 9.9 | 12% | 10.0 | 13% | 11.1 | 26% | 8.8 |
| 4 | 30.8 | 2% | 31.0 | 3% | 31.9 | 6% | 30.0 |
| 20 | 702.7 | 0.4% | 703.1 | 0.5% | 703.5 | 0.5% | 699.7 |
| 40 | 2803.3 | 0.3% | 2803.7 | 0.4% | 2803.1 | 0.3% | 2792.6 |

**Table 4.** $\bar{\sigma}_{11}(L/2, -h/2)$ for different values of $S$, with two layers ($0°/90°$).

$S = 2$ (very thick), $S = 4$ (thick), $S = 20$ (moderately thick), or $S = 40$ (thin). The percent error with respect to $S$ are also compared in these tables. The variation of the normalized in-plane, transverse shear, and normal stresses, and the transverse displacement through the thickness ($S = 2$, $S = 4$) are presented in Figures 5–7 for further comparison (only the most critical tests).
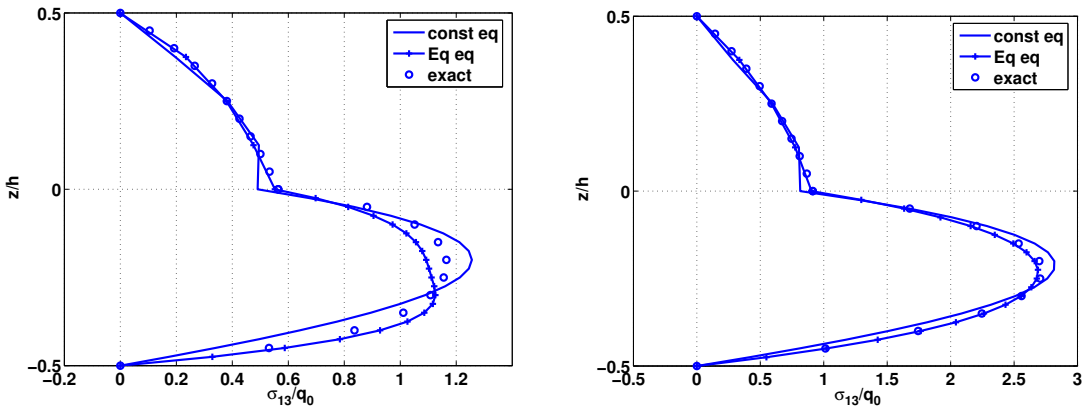


**Figure 5.** Distribution of $\bar{\sigma}_{13}$ along the thickness, $S = 2$ (left) and $S = 4$ (right), with two layers ($0°/90°$), SinRef-7p.
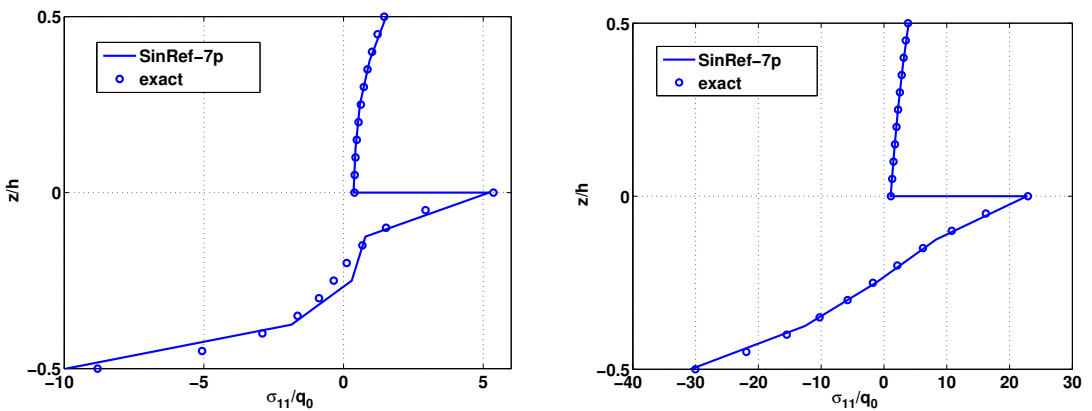


**Figure 6.** Distribution of $\bar{\sigma}_{11}$ $S = 2$ (left) and $\bar{\sigma}_{11}$ $S = 4$ (right) along the thickness, with two layers ($0°/90°$), SinRef-7p.
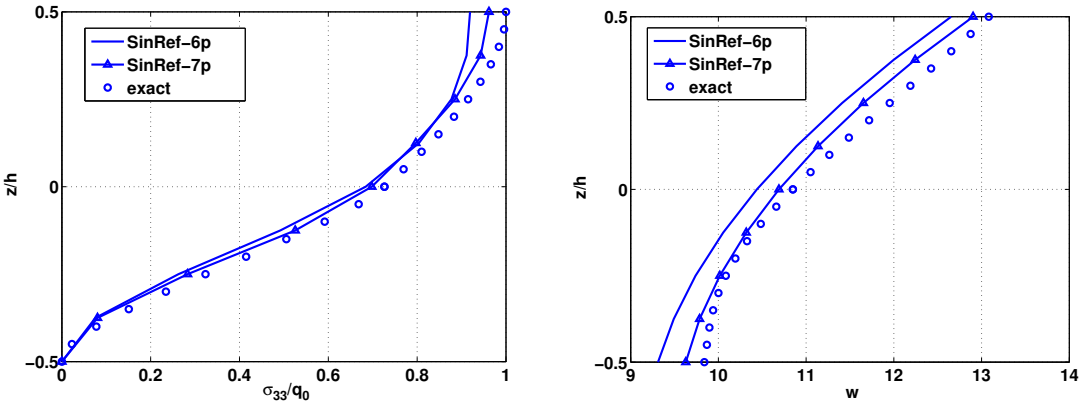
**Figure 7.** Distribution of $\bar{\sigma}_{33}$ (left) and $\bar{w}$ (right) along the thickness, $S = 2$, with two layers $(0°/90°)$.

For the displacements, the SinRef-7p model gives more precise results than the two other models, especially for the very thick case. For $S \geq 4$, the error is less than 1% for the deflection, and less than 5% for the in-plane displacement regardless of the model. For $S = 2$, the two present models take into account the nonconstant variation through the thickness (see Figure 7, right).

Concerning the stresses, the evolution of the transverse shear stress is improved using one more unknown in the model (see Table 3) but no influence is denoted for the in-plane stress (see Table 4). The effect of the transverse normal stress in the model allows us to improve the accuracy of $\bar{\sigma}_{13}$ and $\bar{\sigma}_{11}$, especially for the very thick beam. For the SinRef-7p model, errors on $\bar{\sigma}_{13}$ calculated from the constitutive law are less than 5%. For the in-plane stress, all the errors are less than 6% for $S \geq 4$.

It is seen from Figures 5–7 that the SinRef-7p element performs very well for thick as well as thin beams (all results are not presented here for brevity). The distribution of the in-plane displacement (not presented here) and stress is similar to the exact Pagano solution regardless of the length-to-thickness ratio. The transverse shear stress obtained using the equilibrium equation gives excellent results, especially for

| | $\bar{u}(0, h/2)$ | | | | | | |
|---|---|---|---|---|---|---|---|
| $S$ | SinRef-7p | error | SinRef-6p | error | SinRef-c | error | exact |
| 2 | 0.237 | 8% | 0.238 | 9% | 0.204 | 6% | 0.218 |
| 4 | 0.944 | 0.5% | 0.945 | 0.6% | 0.942 | 0.3% | 0.939 |
| 20 | 66.776 | 0.1% | 66.758 | 0.1% | 66.864 | < 0.01% | 66.869 |
| 40 | 517.88 | < 0.1% | 517.84 | 0.04% | 518.08 | < 0.01% | 518.08 |
| | $\bar{w}(L/2, 0)$ | | | | | | |
| $S$ | SinRef-7p | error | SinRef-6p | error | SinRef-c | error | exact |
| 2 | 8.505 | 0.2% | 8.488 | 0.4% | 8.746 | 2% | 8.524 |
| 4 | 2.888 | < 0.1% | 2.888 | 0.04% | 2.908 | < 1% | 2.887 |
| 20 | 0.617 | < 0.01% | 0.617 | 0.01% | 0.617 | < 0.1% | 0.617 |
| 40 | 0.537 | < 0.01% | 0.537 | < 0.01% | 0.537 | < 0.01% | 0.537 |

**Table 5.** $\bar{w}(L/2, 0)$ and $\bar{u}(0, h/2)$ for different values of $S$, with three layers $(0°/90°/0°)$.

| | | | | | | | | | | | | |
|---|---|---|---|---|---|---|---|---|---|---|---|---|
| | | | | | $\bar{\sigma}_{13}(0,0)$ | | | | | | | |
| | SinRef-7p | | | | SinRef-6p | | | | SinRef-c | | | |
| $S$ | direct | error | equil.eq | error | direct | error | equil.eq | error | direct | error | equil.eq | error | exact |
| 2 | 0.5328 | 0.2% | 0.5312 | 0.5% | 0.4841 | 9% | 0.5300 | 0.8% | 0.4989 | 6% | 0.5379 | 0.6% | 0.5343 |
| 4 | 1.4303 | <0.1% | 1.4216 | 0.7% | 1.4167 | 1% | 1.4212 | 0.7% | 1.4213 | <1% | 1.4236 | <1% | 1.4318 |
| 20 | 8.7480 | <0.01% | 8.6965 | 0.5% | 9.006 | 2.9% | 8.697 | 0.5% | 9.0052 | 2.9% | 8.6973 | <1% | 8.7490 |
| 40 | 17.642 | <0.01% | 17.539 | 0.5% | 18.186 | 3% | 17.539 | 0.5% | 18.184 | 3% | 17.539 | <1% | 17.634 |

**Table 6.** $\bar{\sigma}_{13}(0,0)$ for different values of $S$, with three layers ($0°/90°/0°$).

| | | | | | | | |
|---|---|---|---|---|---|---|---|
| | | | $\bar{\sigma}_{11}(L/2, h/2)$ | | | | |
| $S$ | SinRef-7p | error | SinRef-6p | error | SinRef-c | error | exact |
| 2 | 9.70 | 9% | 9.74 | 9% | 8.07 | 9% | 8.90 |
| 2 $(-h/2)$ | 6.96 | 1.2% | 7.01 | 1.9% | 8.07 | 17% | 6.87 |
| 4 | 18.4 | 2% | 19.0 | 1% | 18.6 | 1% | 18.8 |
| 20 | 264.2 | 0.3% | 264.0 | < 0.5% | 264.0 | < 0.5% | 263.2 |
| 40 | 1023.2 | 0.3% | 1023.0 | < 0.5% | 1023.0 | < 0.5% | 1019.8 |

**Table 7.** $\bar{\sigma}_{11}(L/2, h/2)$ for different values of $S$, with three layers ($0°/90°/0°$).

the very thick beam with $S = 2$ (see Figure 5). For design applications, the variation of the transverse shear stress deduced from the constitutive relation yields satisfactory distributions even for the very thick beam, without computational cost at the postprocessing level. The accuracy of the transverse normal stress is also very good (see Figure 7, left).

Next we consider the three-layer case ($0°/90°/0°$). The results are summarized in Tables 5–7. Figures 8–11 (SinRef-7p model) show the transverse normal and shear stresses and out-of-plane displacement. All models give excellent results for $S = 4, 20, 40$. Again, note that the SinRef-7p model improves the accuracy of the results for both displacements and transverse shear stresses especially for thick laminates.
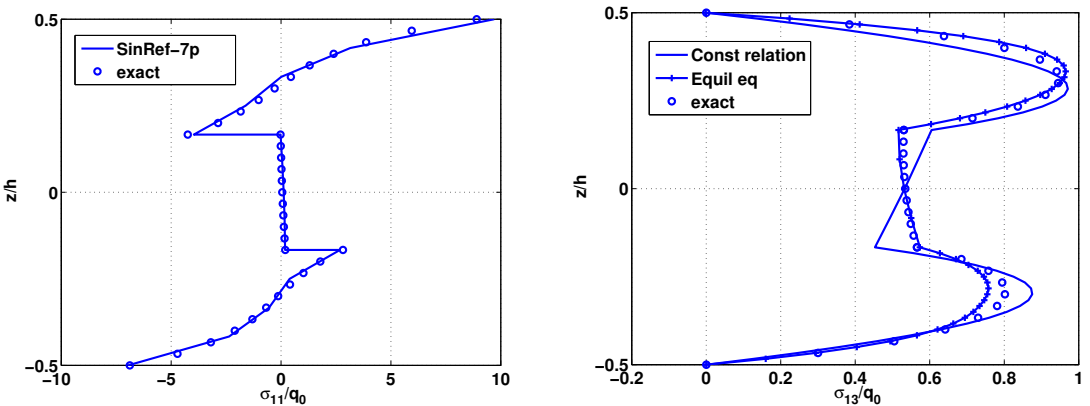


**Figure 8.** Distribution of $\bar{\sigma}_{13}$ along the thickness, $S = 2$, with three layers ($0°/90°/0°$), SinRef-7p.
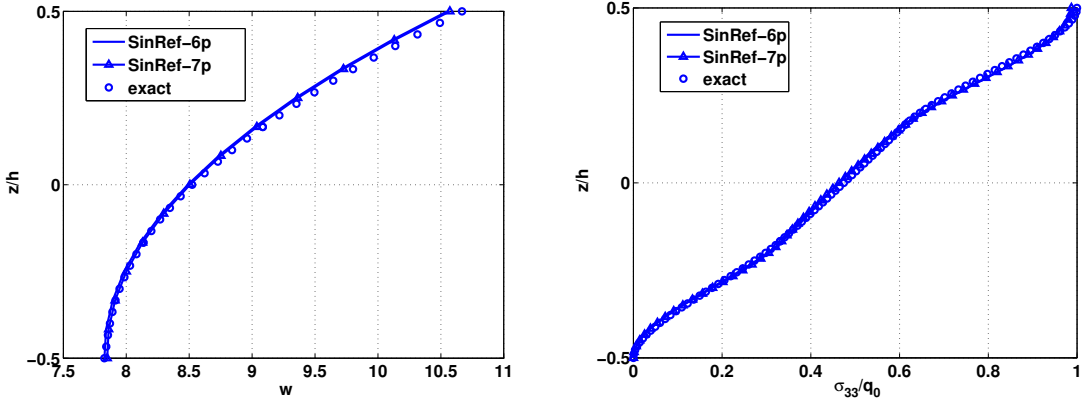
**Figure 9.** Distribution of $\bar{w}$ and $\bar{\sigma}_{33}$ along the thickness, $S = 2$, with three layers $(0°/90°/0°)$.
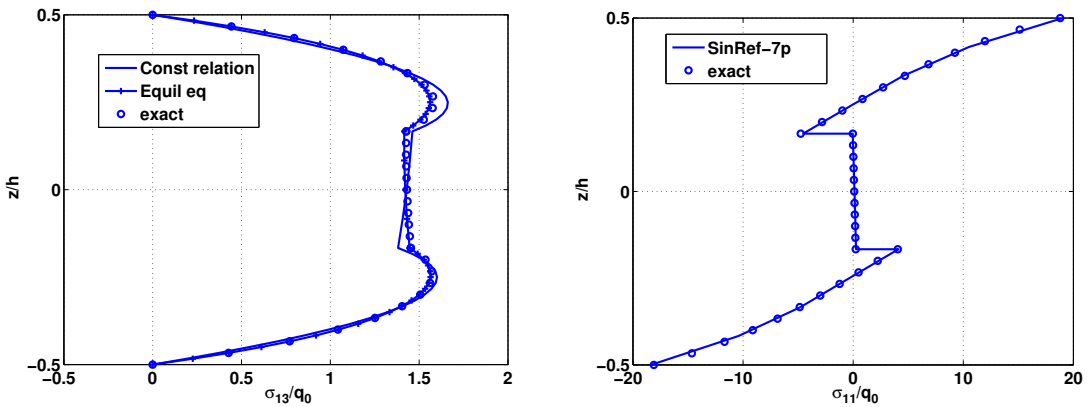


**Figure 10.** Distribution of $\bar{\sigma}_{13}$ and $\bar{\sigma}_{11}$ along the thickness, $S = 4$, $0°/90°/0°$, SinRef-7p.
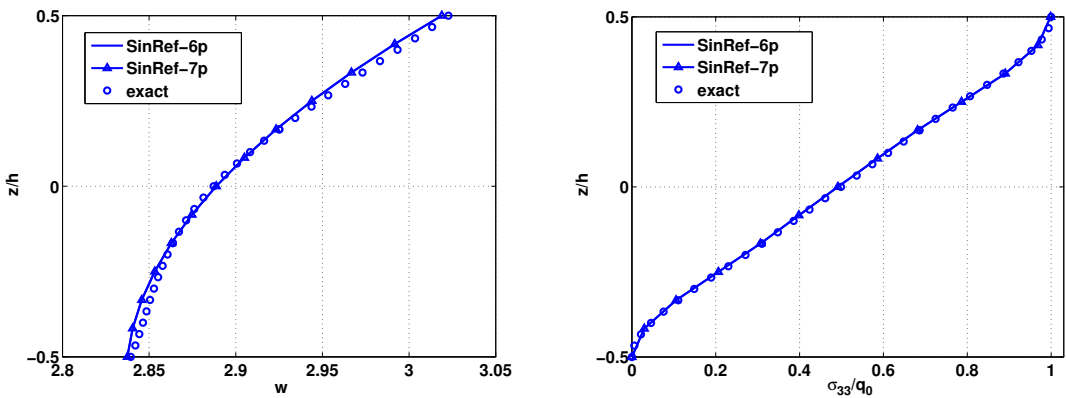


**Figure 11.** Distribution of $\bar{w}$ (left) and $\bar{\sigma}_{33}$ (right) along the thickness, $S = 4$, $0°/90°/0°$.

The error is less than 0.7% for in-plane and transverse displacements, and transverse shear stress with $S \geq 4$. The variation of the transverse shear stress calculated from the constitutive relation also gives good results. Moreover, for $S = 2$, Figure 11, left, shows that $\bar{w}$ is nonconstant. Note that the two
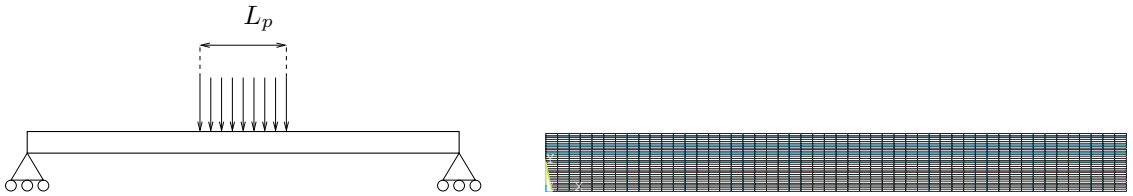
**Figure 12.** Left: beam under localized pressure. Right: the ANSYS mesh.

models with stretching effects take into account the nonsymmetrical variation of the transverse shear and the in-plane stress through the thickness (see Figure 8).

*Bending analysis of laminated composite beam under localized pressure.* This test is about simply supported symmetric and antisymmetric composite beams submitted to a localized pressure. It focuses on the capability of these elements to capture local behavior. It is detailed below.

Geometry: Composite cross-ply beam $(0°/90°/0°)$ and $(0°/90°)$ and $S = 4$; half of the beam is meshed. All layers have the same thickness.

Boundary conditions: Simply supported beam subjected to a transverse pressure $q(x_1) = q_0$ applied on a line located at the beam center and whose dimension is $L_p = L/8$ (see Figure 12).

Material properties: Same properties as on page 1136.

Mesh: $N = 16$.

Results: The reference solution is issued from a 2D elasticity analysis with a very refined mesh including 3800 DOFs in ANSYS. The element PLANE82 is used.

The results are shown in Table 8. We observe that the three models perform quite well with respect to the 2D solution except for the in-plane stress in the SinRef-c model. This is due to the nonsymmetrical results across the thickness which can not be taken into account in this model. From Figures 13 and 14, it can be noticed that the transverse displacement is nonconstant across the thickness. In all cases, the models including the transverse deformation are in excellent agreement with the reference solution.
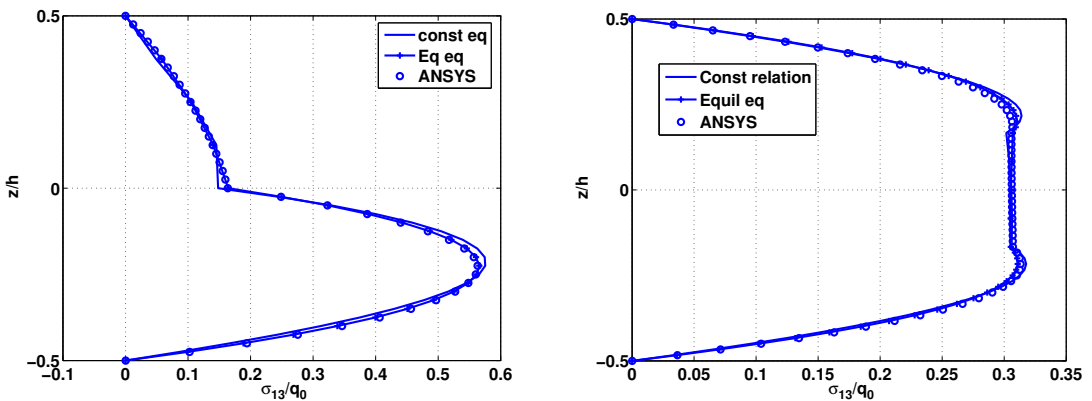


**Figure 13.** Distribution of $\bar{\sigma}_{13}$ along the thickness, $S = 4$, with two layers (left) and three layers (right), SinRef-7p, localized pressure.

|  |  | $(0°/90°/0°)$ | | | | $(0°/90°)$ | | | |
|  |  | $(x_1, z)$ |  | error | ANSYS | $(x_1, z)$ |  | error | ANSYS |
| SinRef-7p | $\bar{\sigma}_{13}$ direct | $(0, 0)$ | 0.3059 | 0.1% | 0.3061 | $(0, -h/4)$ | 0.5656 | 1% | 0.5602 |
|  | $\bar{\sigma}_{13}$ equiv.eq | $(0, 0)$ | 0.3055 | 0.2% |  | $(0, -h/4)$ | 0.5616 | 0.2% |  |
|  | $\bar{\sigma}_{11}$ | $(L/2, -h/2)$ | 6.4510 | 14% | 5.6406 | $(L/2, -h/2)$ | 9.8455 | 9% | 8.9715 |
|  | $\bar{w}$ | $(L/2, 0)$ | 0.7809 | 0.4% | 0.7847 | $(L/2, 0)$ | 1.2510 | 0.8% | 1.2617 |
|  | $\bar{u}$ | $(0, h/2)$ | 0.2131 | 1% | 0.2165 | $(0, h/2)$ | 1.0774 | 0.1% | 1.0788 |
| SinRef-6p | $\bar{\sigma}_{13}$ direct | $(0, 0)$ | 0.3084 | 0.7% | 0.3061 | $(0, -h/4)$ | 0.5117 | 8% | 0.5602 |
|  | $\bar{\sigma}_{13}$ equiv.eq | $(0, 0)$ | 0.3048 | 0.4% |  | $(0, -h/4)$ | 0.5290 | 5% |  |
|  | $\bar{\sigma}_{11}$ | $(L/2, -h/2)$ | 6.4195 | 13% | 5.6406 | $(L/2, -h/2)$ | 9.2047 | 2% | 8.9715 |
|  | $\bar{w}$ | $(L/2, 0)$ | 0.7809 | 0.4% | 0.7847 | $(L/2, 0)$ | 1.2310 | 2% | 1.2617 |
|  | $\bar{u}$ | $(0, h/2)$ | 0.2142 | 1% | 0.2165 | $(0, h/2)$ | 1.0871 | 0.7% | 1.0788 |
| SinRef-c | $\bar{\sigma}_{13}$ direct | $(0, 0)$ | 0.3082 | 0.7% | 0.3061 | $(0, -h/4)$ | 0.5211 | 7% | 0.5602 |
|  | $\bar{\sigma}_{13}$ equiv.eq | $(0, 0)$ | 0.3051 | 0.3% |  | $(0, -h/4)$ | 0.5659 | 1% |  |
|  | $\bar{\sigma}_{11}$ | $(L/2, -h/2)$ | 7.5326 | 33% | 5.6406 | $(L/2, -h/2)$ | 11.8810 | 32% | 8.9715 |
|  | $\bar{w}$ | $(L/2, 0)$ | 0.7969 | 1.5% | 0.7847 | $(L/2, 0)$ | 1.2451 | 1% | 1.2617 |
|  | $\bar{u}$ | $(0, h/2)$ | 0.2181 | 0.7% | 0.2165 | $(0, h/2)$ | 1.1259 | 4% | 1.0788 |

**Table 8.** $S = 4$, with two and three layers, localized pressure.
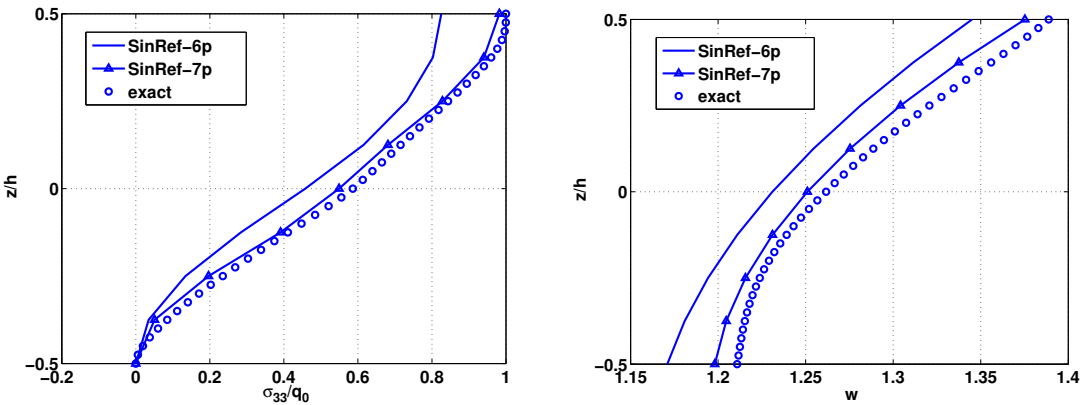


**Figure 14.** Distribution of $\bar{\sigma}_{33}$ and $\bar{w}$ along the thickness, $S = 4$, with two layers $(0°/90°)$, localized pressure.

As in the previous case, the SinRef-7p model improves results issued from the SinRef-6p model, especially for the transverse shear stress in the antisymmetric lay-up.

*Bending analysis of a sandwich beam under uniform pressure.* The test deals with a sandwich beam under uniform pressure with two different boundary conditions. Only the more accurate model, the SinRef-7p model, is used in this severe test. This example is detailed now.

Geometry: The 3-layer sandwich beam has graphite-epoxy faces and a soft core with thicknesses $0.1h$, $0.8h$, $0.1h$ and length to thickness ratios $S = 2.5$, $S = 5$, $S = 10$; half of the beam is meshed.

Boundary conditions: Simply supported or clamped-clamped (C-C) beam under an uniform pressure $q_0$.

Material properties (face): $E_{11} = 131.1$ GPa, $E_{22} = E_{33} = 6.9$ GPa, $G_{12} = 3.588$ GPa, $G_{13} = 3.088$ GPa, $G_{23} = 2.3322$ GPa, $\nu_{12} = \nu_{13} = 0.32$, $\nu_{23} = 0.49$.

Material properties (core): $E_{11} = 0.2208$ MPa, $E_{22} = 0.2001$ MPa, $E_{33} = 2760$ MPa, $G_{12} = 16.56$ MPa, $G_{13} = 545.1$ MPa, $G_{23} = 455.4$ MPa, $\nu_{12} = 0.99$, $\nu_{13} = 0.00003$, $\nu_{23} = 0.00003$.

Mesh: $N = 16$.

Results: The results are presented in nondimensional form as

$$\bar{w} = 100 w Y_0 / h S^4 q_0, \quad \bar{\sigma}_{11} = \sigma_{11}/S^2 q_0, \quad \bar{\tau}_{13} = \tau_{13}/S q_0, \quad Y_0 = 6.9 \text{ GPa}.$$

They are compared with the available 2D exact solution from [Kapuria et al. 2004] and results from a commercial code with a very refined mesh including 3800 DOFs. This choice is justified by the convergence study given in Table 9 for a slenderness ratio $S = 2.5$. The error on the stresses with respect to the reference mesh (61000 DOFs) becomes negligible when the number of DOFs is greater than 3800.

Tables 10 and 11 show that the model is very efficient and accurate, even for the very thick case. Figure 15 gives the distribution of in-plane, transverse shear, and normal stresses through the thickness for the clamped-clamped beam with $S = 2.5$. These stresses are very well estimated, in particular the maximum transverse shear stress in the face and the asymmetrical maximum value due to the thickness and the load.

| | | | | | |
|---|---|---|---|---|---|
| $\bar{\sigma}_{11}(L/2, -h/2)$ | 1% | 0.5% | 0.1% | 0.03% | 2.1000 |
| $\bar{\sigma}_{13\,\text{max}}$ | 12% | 0.7% | 0.7% | 0.0% | 0.8309 |
| DOFs | 700 | 2000 | 3800 | 15000 | 61000 |

**Table 9.** Convergence study (ANSYS), $S = 2.5$, C-C. Reference values are in the last column.

| $S$ | | | error | literature | ANSYS |
|---|---|---|---|---|---|
| 2.5 | $\bar{\sigma}_{13}(0, 0)$ | 0.4773 | 0.1% | | 0.4777 |
| | $\bar{\sigma}_{11}(L/2, h/2)$ | $-3.2370$ | 0.3% | | $-3.2285$ |
| | $\bar{\sigma}_{11}(L/2, -h/2)$ | 3.2686 | 1.1% | | 3.2318 |
| | $\bar{w}(L/2, 0)$ | 25.5916 | 0.1% | | 25.5761 |
| 5 | $\bar{\sigma}_{13}(0, 0)$ | 0.5153 | 0.2% | 0.5144 | 0.5155 |
| | $\bar{\sigma}_{11}(L/2, h/2)$ | $-1.9729$ | 0.2% | $-1.9698$ | $-1.9655$ |
| | $\bar{\sigma}_{11}(L/2, -h/2)$ | 1.9727 | 0.2% | 1.9689 | 1.9655 |
| | $\bar{w}(L/2, 0)$ | 7.8804 | 0.0% | 7.8778 | 7.8925 |
| 10 | $\bar{\sigma}_{13}(0, 0)$ | 0.5346 | 0.1% | 0.5338 | 0.5344 |
| | $\bar{\sigma}_{11}(L/2, h/2)$ | $-1.6466$ | 0.1% | $-1.6451$ | $-1.6441$ |
| | $\bar{\sigma}_{11}(L/2, -h/2)$ | 1.6466 | 0.1% | 1.6449 | 1.6441 |
| | $\bar{w}(L/2, 0)$ | 3.2416 | 0.2% | 3.2486 | 3.2521 |

**Table 10.** Sandwich, uniform pressure, simply supported. Literature values are taken from [Kapuria et al. 2004].

| $S$ | | | error | ANSYS |
|---|---|---|---|---|
| | $\bar{\sigma}_{13}(L/8, 0)$ | 0.3280 | 0.5% | 0.3263 |
| | $\bar{\sigma}_{13}$ max | 0.8038 | 3% | 0.8310 |
| 2.5 | $\bar{\sigma}_{11}(L/2, h/2)$ | $-2.3326$ | 7% | $-2.1610$ |
| | $\bar{\sigma}_{11}(L/2, -h/2)$ | 2.0056 | 4% | 2.1000 |
| | $\bar{w}(L/2, 0)$ | 20.2549 | 1.4% | 20.5340 |
| | $\bar{\sigma}_{13}(L/8, 0)$ | 0.3877 | 0.1% | 0.3880 |
| 5 | $\bar{\sigma}_{11}(L/2, h/2)$ | $-0.9966$ | 4% | $-0.9520$ |
| | $\bar{\sigma}_{11}(L/2, -h/2)$ | 0.9237 | 1.7% | 0.9398 |
| | $\bar{w}(L/2, 0)$ | 6.0218 | 1.1% | 5.9550 |
| | $\bar{\sigma}_{13}(L/8, 0)$ | 0.4120 | 0.1% | 0.4125 |
| 10 | $\bar{\sigma}_{11}(L/2, h/2)$ | $-0.6351$ | 2% | $-0.6224$ |
| | $\bar{\sigma}_{11}(L/2, -h/2)$ | 0.6154 | 0.6% | 0.6193 |
| | $\bar{w}(L/2, 0)$ | 1.8186 | 0.9% | 1.8358 |

**Table 11.** Sandwich, uniform pressure, C-C. The tranverse shear stress is calculated at $x = L/8$ because the 2D finite element solution is not valid at a fixed edge.
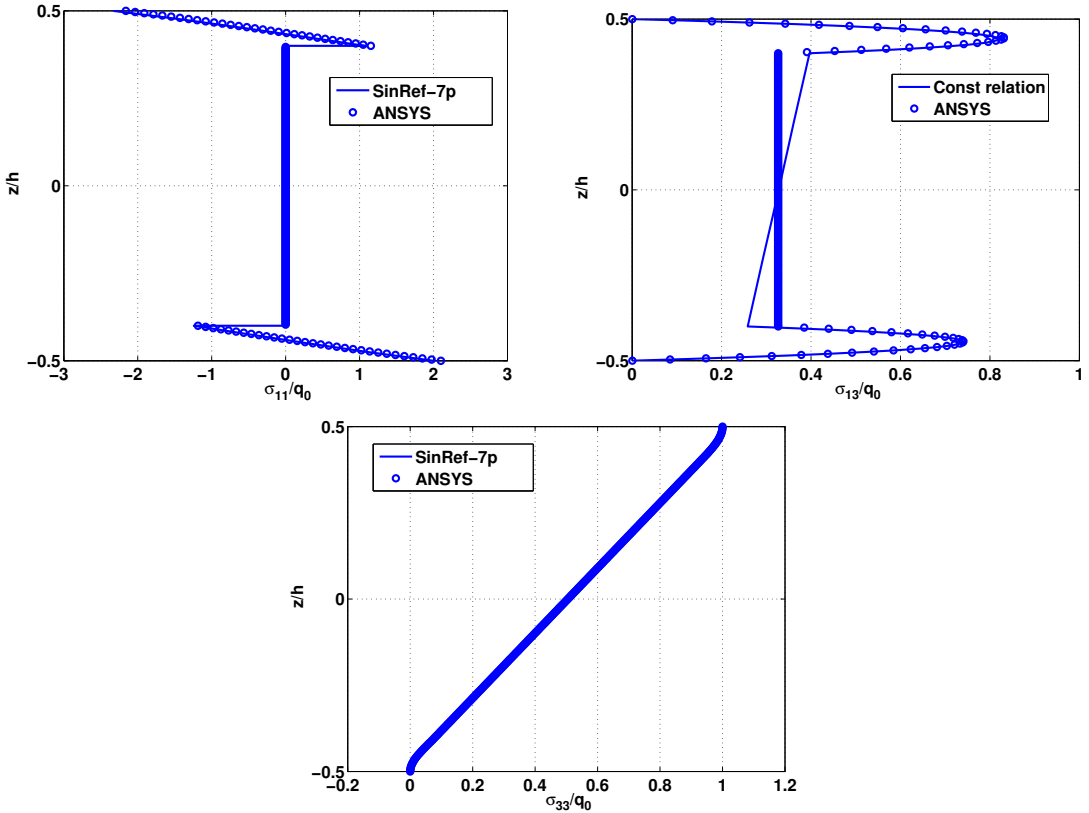


**Figure 15.** Distribution of $\bar{\sigma}_{11}$, $\bar{\sigma}_{13}$ and $\bar{\sigma}_{33}$ along the thickness, $S = 2.5$, sandwich, SinRef-7p, uniform pressure, C-C.

## 4. A thermomechanical problem

In this section, the accuracy of the present theory is assessed in thermomechanical analysis. The results are compared with the exact 2D thermoelasticity solution [Bhaskar et al. 1996]. The problem is described as follows:

Geometry: Composite cross-ply beam $(0°/90°/0°)$ and $(0°/90°)$, slenderness ratio $S$ ranging from 4 to 100; half of the beam is meshed. All layers have the same thickness.

Boundary conditions: Simply supported beam subjected to the temperature field

$$T(x_1, z) = T_{\max} \frac{2z}{h} \sin \frac{\pi x_1}{L}. \qquad (22)$$

It corresponds to a cylindrical bending.

Material properties: Same properties as on page 1136, plus $\alpha_T = 1125\alpha_L$, where $\alpha_L$, $\alpha_T$ are the thermal expansion coefficients in the fiber and normal direction.

Mesh: $N = 8$.

Results: As in reference [Carrera 2000a], we define the dimensionless quantities:

$$\bar{u} = \frac{u_1}{\alpha_L T_{\max} L}, \qquad \bar{w} = \frac{h u_3}{\alpha_L T_{\max} L^2}, \qquad \bar{\sigma}_{11} = \frac{\sigma_{11}}{\alpha_L E_T T_{\max}}, \qquad \bar{\sigma}_{13} = \frac{\sigma_{13}}{\alpha_L E_T T_{\max}}. \qquad (23)$$

The reference results have been obtained upon an extension to the thermomechanical problem of the exact Pagano solution given in [Pagano 1969].

The numerical results for deflection, in-plane displacement, shear stress, and in-plane stress are given in Tables 12–14 and 15–17 for two and three layers, respectively. These examples show clearly the necessity to take into account the transverse normal deformation in the model. In fact, the improvement is significant for the SinRef-6p and SinRef-7p models compared to the SinRef-c one.

| $S$ | SinRef-7p | error | SinRef-6p | error | SinRef-c | error | exact |
|---|---|---|---|---|---|---|---|
| | | | $\bar{u}(0, h/2)$ | | | | |
| 4 | 155.1 | 0.2% | 156.60 | 0.8% | 153.39 | 1% | 155.36 |
| 10 | 114.22 | 0.03% | 114.35 | 0.1% | 111.88 | 2% | 114.18 |
| 50 | 104.50 | < 0.01% | 104.50 | < 0.01% | 101.93 | 2% | 104.50 |
| 100 | 104.18 | 0.01% | 104.18 | < 0.01% | 101.60 | 2% | 104.19 |
| | | | $\bar{w}(L/2, 0)$ | | | | |
| $S$ | SinRef-7p | error | SinRef-6p | error | SinRef-c | error | exact |
| 4 | 42.652 | 0.5% | 41.302 | 3% | 45.882 | 7% | 42.889 |
| 10 | 43.285 | 0.01% | 43.023 | 0.6% | 42.191 | 2% | 43.293 |
| 50 | 43.158 | < 0.01% | 43.146 | 0.03% | 41.314 | 4% | 43.161 |
| 100 | 43.152 | < 0.01% | 43.149 | 0.01% | 41.286 | 4% | 43.155 |

**Table 12.** $\bar{u}(0, h/2)$ and $\bar{w}(L/2, 0)$ for different values of $S$, with two layers $(0°/90°)$.

| | $\bar{\sigma}_{13}(0, -h/4)$ | | | | | | | | | | | |
|---|---|---|---|---|---|---|---|---|---|---|---|---|
| | SinRef-7p | | | | SinRef-6p | | | | SinRef-c | | | |
| $S$ | direct | error | equil.eq | error | direct | error | equil.eq | error | direct | error | equil.eq | error | exact |
| 4 | 136.350 | 3% | 129.610 | 1% | 109.820 | 16% | 134.320 | 2% | 119.600 | 9% | 133.170 | 1% | 131.730 |
| 10 | 68.707 | 1% | 67.422 | 0.8% | 55.351 | 18% | 67.834 | 0.2% | 59.742 | 12% | 68.341 | 0.5% | 67.964 |
| 50 | 14.430 | 0.6% | 14.240 | 0.6% | 11.611 | 18% | 14.244 | 0.6% | 12.519 | 12% | 14.391 | 0.4% | 14.333 |
| 100 | 7.225 | 0.6% | 7.132 | 0.6% | 5.814 | 19% | 7.133 | 0.6% | 6.269 | 12% | 7.207 | 0.3% | 7.179 |

**Table 13.** $\bar{\sigma}_{13}(0, -h/4)$ for different values of $S$, with two layers (0°/90°).

| $S$ | SinRef-7p | error | SinRef-6p | error | SinRef-c | error | exact |
|---|---|---|---|---|---|---|---|
| | $\bar{\sigma}_{11}(L/2, -h/2)$ | | | | | | |
| 4 | 2044.1 | 2% | 2075.4 | 4% | 1774.5 | 11% | 1994.7 |
| 10 | 2142.4 | 0.6% | 2150.1 | 1% | 2115.3 | 0.6% | 2129.0 |
| 50 | 2179.8 | 0.4% | 2180.1 | 0.4% | 2197.1 | 1% | 2170.2 |
| 100 | 2181.1 | 0.4% | 2181.2 | 0.4% | 2199.8 | 1% | 2171.7 |

**Table 14.** $\bar{\sigma}_{11}(L/2, -h/2)$ for different values of $S$, with two layers (0°/90°).

| $S$ | SinRef-7p | error | SinRef-6p | error | SinRef-c | error | exact |
|---|---|---|---|---|---|---|---|
| | $\bar{u}(0, h/2)$ | | | | | | |
| 4 | 7.5399 | 0.9% | 7.5262 | 0.7% | 0.2608 | 96% | 7.4696 |
| 10 | 5.0069 | 0.05% | 5.0013 | 0.1% | 0.7346 | 85% | 5.0095 |
| 50 | 4.4667 | < 0.01% | 4.4665 | 0.01% | 0.8622 | 80% | 4.4670 |
| 100 | 4.4493 | < 0.01% | 4.4492 | < 0.01% | 0.8665 | 80% | 4.4494 |
| | $\bar{w}(L/2, 0)$ | | | | | | |
| $S$ | SinRef-7p | error | SinRef-6p | error | SinRef-c | error | exact |
| 4 | 3.6285 | 0.3% | 3.6272 | 0.3% | 0.2332 | 93% | 3.6156 |
| 10 | 1.8935 | 0.01% | 1.8919 | 0.08% | 0.3762 | 80% | 1.8934 |
| 50 | 2.7924 | < 0.01% | 2.7924 | < 0.01% | 0.5449 | 80% | 2.7924 |
| 100 | 2.8197 | < 0.01% | 2.8197 | < 0.01% | 0.5506 | 80% | 2.8197 |

**Table 15.** $\bar{u}(0, h/2)$ and $\bar{w}(L/2, 0)$ for different values of $S$, with three layers (0°/90°/0°).

| | SinRef-7p | | | | SinRef-6p | | | | SinRef-c | | | |
|---|---|---|---|---|---|---|---|---|---|---|---|---|---|
| $S$ | direct | error | equil.eq | error | direct | error | equil.eq | error | direct | error | equil.eq | error | exact |
| 4 | 21.4280 | 0.04% | 21.7350 | 1.5% | 20.2340 | 5% | 21.7010 | 1.3% | 6.8092 | 68% | 14.3210 | 33% | 21.4178 |
| 10 | 7.1544 | 0.1% | 7.2837 | 2% | 6.2585 | 12% | 7.2771 | 1.8% | 3.7459 | 47% | 6.5851 | 7% | 7.1436 |
| 50 | 1.3522 | 0.1% | 1.3778 | 2% | 1.1538 | 14% | 1.3777 | 2% | 0.8040 | 40% | 1.3629 | 1% | 1.3497 |
| 100 | 0.6748 | 0.1% | 0.6876 | 2% | 0.5753 | 14% | 0.6875 | 2% | 0.4029 | 40% | 0.6822 | 1% | 0.6735 |

**Table 16.** $\bar{\sigma}_{13}(0, 0)$ (max) for different values of $S$, with three layers (0°/90°/0°).

| $\bar{\sigma}_{11}(L/2, -h/2)$ | | | | | | | |
|---|---|---|---|---|---|---|---|
| $S$ | SinRef-7p | error | SinRef-6p | error | SinRef-c | error | exact |
| 4 | 289.17 | 2.8% | 288.10 | 2% | 4.4627 | 98% | 281.11 |
| 10 | 88.63 | 1.4% | 88.19 | 1% | 32.96 | 62% | 87.41 |
| 50 | 45.83 | 2.5% | 45.80 | 2% | 43.0390 | 3% | 44.70 |
| 100 | 44.44 | 2.6% | 44.44 | 2% | 43.3780 | 0.1% | 43.31 |

**Table 17.** $\bar{\sigma}_{11}(L/2, -h/2)$ for different values of $S$, with three layers $(0°/90°/0°)$.

Note that the SinRef-7p results are in excellent agreement with the exact solution. The error is less than 3% regardless of the length to thickness ratio for both displacements and stresses, and even for the transverse shear stress deduced from the constitutive relation. Figures 16–20 show that the distribution of these quantities are similar to the reference solution, in particular for the thick beam.
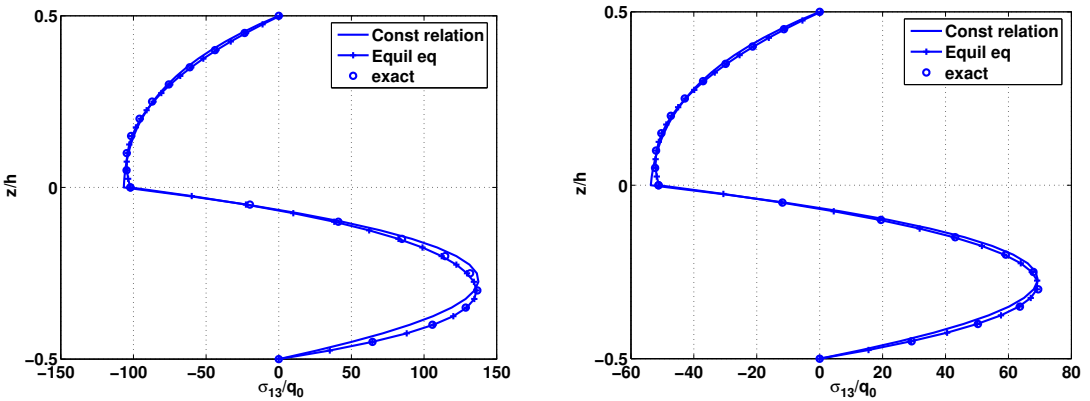


**Figure 16.** Distribution of $\bar{\sigma}_{13}$ along the thickness, $S = 4$ (left) and $S = 20$ (right), with two layers $(0°/90°)$, SinRef-7p model.
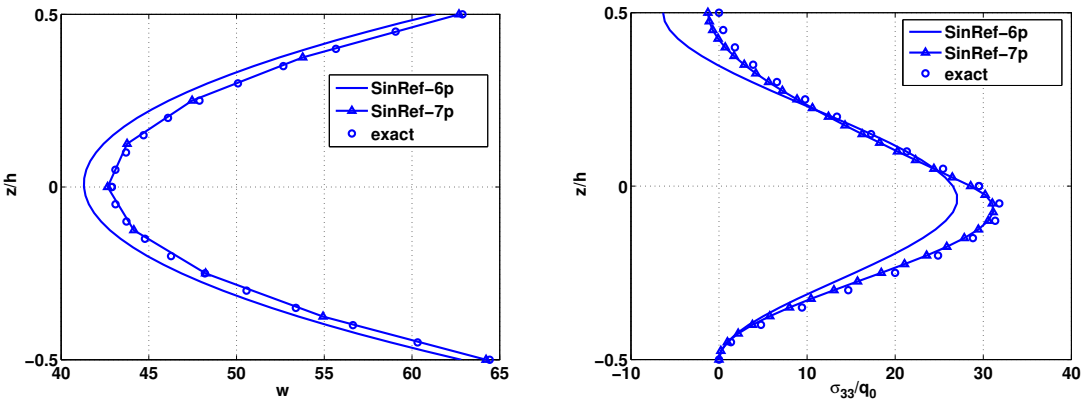


**Figure 17.** Distribution of $\bar{w}$ (left) and $\bar{\sigma}_{33}$ (right) along the thickness, $S = 4$, with two layers $(0°/90°)$.
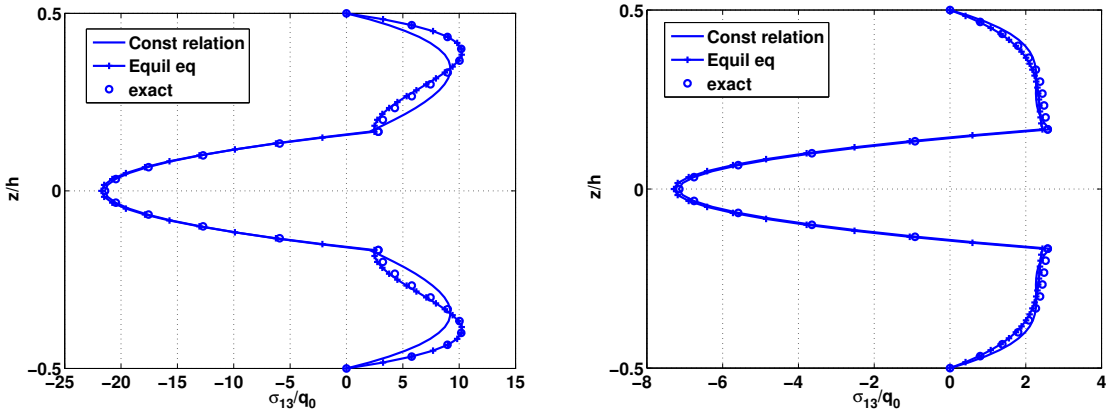
**Figure 18.** Distribution of $\bar{\sigma}_{13}$ along the thickness, $S = 4$ (left) and $S = 10$ (right), with three layers ($0°/90°/0°$), SinRef-7p model.



**Figure 19.** Distribution of $\bar{u}$ (left) and $\bar{w}$ (right) along the thickness, $S = 4$, with three layers ($0°/90°/0°$).



**Figure 20.** Distribution of $\bar{\sigma}_{11}$ (left) and $\bar{\sigma}_{33}$ (right) along the thickness, $S = 4$, with three layers ($0°/90°/0°$).
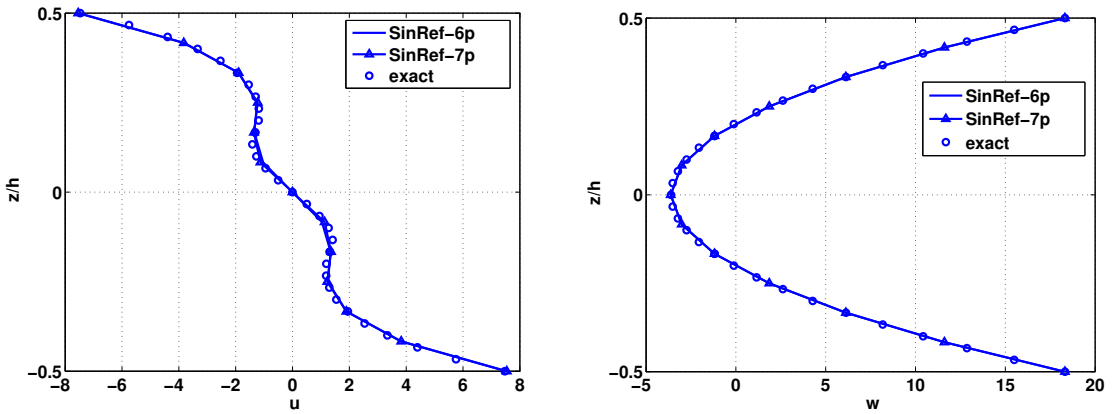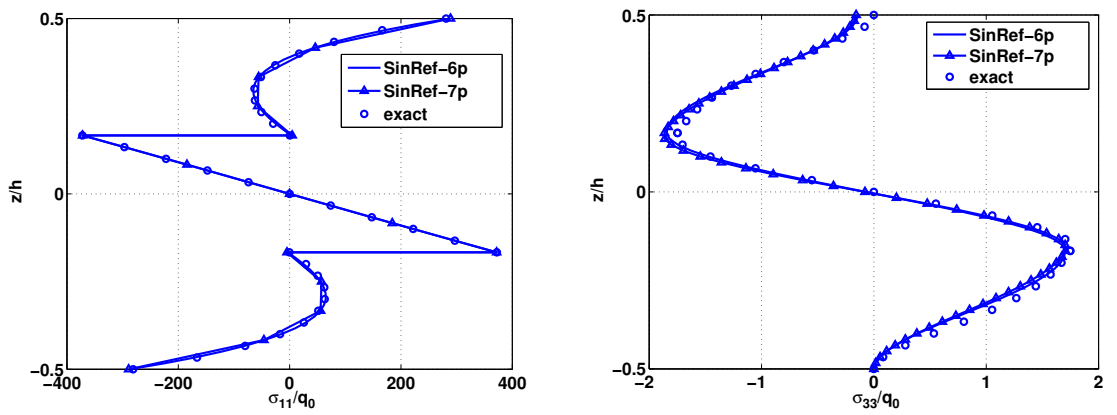
Concerning the SinRef-6p model, the percentage error is close to the previous one except for the transverse shear stress where it is more important. However, notice that only the quantity calculated directly from the constitutive relation is involved. For the thick beam, the distribution of the transverse normal stress is in good agreement with the reference solution for the two cases (Figures 17, right, and 20, right). However, the accuracy of this quantity calculated by the SinRef-7p model is improved (see Figure 17, right). The same holds for the transverse displacement (see Figure 17, left).

## 5. Conclusion

In this article, two new numerical models, denoted SinRef-6p and SinRef-7p, have been presented and evaluated through different benchmarks under mechanical and thermomechanical loading. Special attention is pointed towards the transverse normal stress effect, which plays an important role for thick beams and coupled problems. Each of the two models consists in a three-node multilayered (sandwich and laminated) beam finite element for static analysis with a parabolic distribution of transverse displacement. Based on the sine equivalent single layer model, a third-order kinematic per layer is added, improving the bending description for thick beams. There is no need for transverse shear correction factors and all the interface and boundary conditions are exactly satisfied. So, this approach has a strong physical meaning. Finally, the number of unknowns is independent of the number of layers.

Several numerical evaluations have proved that this model has very good properties in the field of finite elements. Convergence velocity is high and accurate results are obtained for very thick and thin cases. So, these finite elements are simple and efficient for a low cost, compared to layerwise approach or plane elasticity model in commercial software. This study shows the necessity of taking into account the transverse normal effect which cannot be neglected, in particular for coupled thermomechanical problems. This approach allows us to calculate the transverse shear stress directly by the constitutive relation with a very satisfactory accuracy.

Based on these promising results, an extension to plates, shells and piezoelastic coupling will be investigated.

## References

[Aitharaju and Averill 1999]  V. R. Aitharaju and R. C. Averill, "$C^0$ zig-zag finite element for analysis of laminated composite beams", *J. Eng. Mech.* (*ASCE*) **125**:3 (1999), 323–330.

[Ali et al. 1999]  J. S. M. Ali, K. Bhaskar, and T. K. Varadan, "A new theory for accurate thermal/mechanical flexural analysis of symmetric laminated plates", *Compos. Struct.* **45**:3 (1999), 227–232.

[Ambartsumyan 1969]  S. A. Ambartsumyan, *Theory of anisotropic plates*, edited by J. E. Ashton, Technomic, Stamford, CT, 1969. Translated from Russian by T. Cheron.

[Averill and Yip 1996]  R. C. Averill and Y. C. Yip, "Thick beam theory and finite element model with zig-zag sublaminate approximations", *AIAA J.* **34**:8 (1996), 1627–1632.

[Barbero et al. 1990]  E. J. Barbero, J. N. Reddy, and J. Teply, "An accurate determination of stresses in thick laminates using a generalized plate theory", *Int. J. Numer. Methods Eng.* **29**:1 (1990), 1–14.

[Barut et al. 2001]  A. Barut, E. Madenci, J. Heinrich, and A. Tessler, "Analysis of thick sandwich construction by a {3, 2}-order theory", *Int. J. Solids Struct.* **38**:34–35 (2001), 6063–6077.

[Basset 1890]  A. Basset, "On the extension and flexure of cylindrical and spherical thin elastic shells", *Phil. Trans. R. Soc. A* **181** (1890), 433–480.

[Bhaskar and Varadan 1989] K. Bhaskar and T. K. Varadan, "Refinement of higher-order laminated plate theories", *AIAA J.* **27**:12 (1989), 1830–1831.

[Bhaskar et al. 1996] K. Bhaskar, T. K. Varadan, and J. S. M. Ali, "Thermoelastic solutions for orthotropic and anisotropic composite laminates", *Compos. B Eng.* **27**:5 (1996), 415–420.

[Carrera 1999] E. Carrera, "A study of transverse normal stress effect on vibration of multilayered plates and shells", *J. Sound Vib.* **225**:5 (1999), 803–829.

[Carrera 2000a] E. Carrera, "An assessment of mixed and classical theories for the thermal stress analysis of orthotropic multilayered plates", *J. Therm. Stresses* **23**:9 (2000), 797–831.

[Carrera 2000b] E. Carrera, "A priori vs. a posteriori evaluation of transverse stresses in multilayered orthotropic plates", *Compos. Struct.* **48**:4 (2000), 245–260.

[Carrera 2002] E. Carrera, "Theories and finite elements for multilayered, anisotropic, composite plates and shells", *Arch. Comput. Methods Eng.* **9**:2 (2002), 87–140.

[Carrera 2003] E. Carrera, "Historical review of zig-zag theories for multilayered plates and shells", *Appl. Mech. Rev.* (*ASME*) **56**:3 (2003), 287–308.

[Carrera 2004] E. Carrera, "On the use of the Murakami's zig-zag function in the modeling of layered plates and shells", *Comput. Struct.* **82**:7–8 (2004), 541–554.

[Carrera and Brischetto 2008] E. Carrera and S. Brischetto, "Analysis of thickness locking in classical, refined and mixed multilayered plate theories", *Compos. Struct.* **82**:4 (2008), 549–562.

[Chaudhri 1986] R. A. Chaudhri, "An equilibrium method for prediction of transverse shear stresses in a thick laminated plate", *Comput. Struct.* **23**:2 (1986), 139–146.

[Cho and Parmerter 1993] M. Cho and R. R. Parmerter, "Efficient higher order composite plate theory for general lamination configurations", *AIAA J.* **31**:7 (1993), 1299–1306.

[Cook and Tessler 1998] G. M. Cook and A. Tessler, "A {3, 2}-order bending theory for laminated composite and sandwich beams", *Compos. B Eng.* **29**:5 (1998), 565–576.

[Dau et al. 2006] F. Dau, O. Polit, and M. Touratier, "$C^1$ plate and shell finite elements for geometrically nonlinear analysis of multilayered structures", *Comput. Struct.* **84**:19–20 (2006), 1264–1274.

[Flanagan 1994] G. Flanagan, "A general sublaminate analysis method for determining strain energy release rates in composites", pp. 381–389 in *35th AIAA/ASME/ASCE/AHS/ASC Structures, Structural Dynamics, and Materials Conference* (Hilton Head, SC, 1994), AIAA, Reston, VA, 1994. Paper #1994-1356.

[Ganapathi et al. 1999] M. Ganapathi, B. P. Patel, P. Boisse, and O. Polit, "Flexural loss factors of sandwich and laminated composite beams using linear and nonlinear dynamic analysis", *Compos. B Eng.* **30**:3 (1999), 245–256.

[Gaudenzi et al. 1995] P. Gaudenzi, R. Barboni, and A. Mannini, "A finite element evaluation of single-layer and multi-layer theories for the analysis of laminated plates", *Compos. Struct.* **30**:4 (1995), 427–440.

[Gherlone and di Sciuva 2007] M. Gherlone and M. di Sciuva, "Thermo-mechanics of undamaged and damaged multilayered composite plates: a sub-laminates finite approach", *Comput. Struct.* **81**:1 (2007), 125–136.

[Han and Hoa 1993] J. Han and S. V. Hoa, "A three-dimensional multilayer composite finite element for stress analysis of composite laminates", *Int. J. Numer. Methods Eng.* **36**:22 (1993), 3903–3914.

[Heller and Swift 1971] R. Heller and G. Swift, "Solutions for the multilayer Timoshenko beam", Technical Report VPI-E-71-12, Virginia Polytechnic Institute, Blacksburg, VA, 1971.

[Icardi 2001] U. Icardi, "Higher-order zig-zag model for analysis of thick composite beams with inclusion of transverse normal stress and sublaminates approximations", *Compos. B Eng.* **32**:4 (2001), 343–354.

[Kant and Gupta 1988] T. Kant and A. Gupta, "A finite element model for a higher-order shear-deformable beam theory", *J. Sound Vib.* **125**:2 (1988), 193–202.

[Kant and Swaminathan 2000] T. Kant and K. Swaminathan, "Estimation of transverse/interlaminar stresses in laminated composites: a selective review and survey of current developments", *Compos. Struct.* **49**:1 (2000), 65–75.

[Kant and Swaminathan 2002] T. Kant and K. Swaminathan, "Analytical solutions for the static analysis of laminated composite and sandwich plates based on a higher order refined theory", *Compos. Struct.* **56**:4 (2002), 329–344.

[Kant et al. 1997] T. Kant, S. R. Marur, and G. S. Rao, "Analytical solution to the dynamic analysis of laminated beams using higher order refined theory", *Compos. Struct.* **40**:1 (1997), 1–9.

[Kapuria et al. 2003] S. Kapuria, P. C. Dumir, and A. Ahmed, "An efficient higher order zigzag theory for composite and sandwich beams subjected to thermal loading", *Int. J. Solids Struct.* **40**:24 (2003), 6613–6631.

[Kapuria et al. 2004] S. Kapuria, P. C. Dumir, and N. K. Jain, "Assessment of zigzag theory for static loading, buckling, free and forced response of composite and sandwich beams", *Compos. Struct.* **64**:3–4 (2004), 317–327.

[Kärger et al. 2006] L. Kärger, A. Wetzel, R. Rolfes, and K. Rohwer, "A three-layered sandwich element with improved transverse shear stiffness and stresses based on FSDT", *Comput. Struct.* **84**:13–14 (2006), 843–854.

[Kim and Cho 2007] J.-S. Kim and M. Cho, "Enhanced first-order theory based on mixed formulation and transverse normal effect", *Int. J. Solids Struct.* **44**:3–4 (2007), 1256–1276.

[Lee et al. 1992] C.-Y. Lee, D. Liu, and X. Lu, "Static and vibration analysis of laminated composite beams with an interlaminar shear stress continuity theory", *Int. J. Numer. Methods Eng.* **33**:2 (1992), 409–424.

[Li and Liu 1997] X. Li and D. Liu, "Generalized laminate theories based on double superposition hypothesis", *Int. J. Numer. Methods Eng.* **40**:7 (1997), 1197–1212.

[Librescu 1967] L. Librescu, "On the theory of anisotropic elastic shells and plates", *Int. J. Solids Struct.* **3**:1 (1967), 53–68.

[Liu and Soldatos 2002] S. Liu and K. P. Soldatos, "On the prediction improvement of transverse stress distributions in cross-ply laminated beams: advanced versus conventional beam modelling", *Int. J. Mech. Sci.* **44**:2 (2002), 287–304.

[Lo et al. 1977] K. Lo, R. Christensen, and F. Wu, "A higher-order theory of plate deformation, II: Laminated plates", *J. Appl. Mech.* (*ASME*) **44** (1977), 669–676.

[Matsunaga 2002] H. Matsunaga, "Assessment of a global higher-order deformation theory for laminated composite and sandwich plates", *Compos. Struct.* **56**:3 (2002), 279–291.

[Mau 1973] S. Mau, "A refined laminate plate theory", *J. Appl. Mech.* (*ASME*) **40** (1973), 606–607.

[Mindlin 1951] R. Mindlin, "Influence of rotatory inertia and shear on flexural motions of isotropic, elastic plates", *J. Appl. Mech.* (*ASME*) **18** (1951), 31–38.

[Mittelstedt and Becker 2007] C. Mittelstedt and W. Becker, "Free-edge effects in composite laminates", *Appl. Mech. Rev.* (*ASME*) **60**:5 (2007), 217–244.

[Murakami 1986] H. Murakami, "Laminated composite plate theory with improved in-plane responses", *J. Appl. Mech.* (*ASME*) **53** (1986), 661–666.

[Noor and Burton 1990] A. K. Noor and W. S. Burton, "Assessment of computational models for multilayered composite shells", *Appl. Mech. Rev.* (*ASME*) **43**:4 (1990), 67–97.

[Noor and Malik 1999] A. K. Noor and M. Malik, "Accurate determination of transverse normal stresses in sandwich panels subjected to thermomechanical loadings", *Comput. Methods Appl. Mech. Eng.* **178**:3–4 (1999), 431–443.

[Pagano 1969] N. J. Pagano, "Exact solutions for composite laminates in cylindrical bending", *J. Compos. Mater.* **3**:3 (1969), 398–411.

[Pagano 1970] N. J. Pagano, "Exact solutions for rectangular bidirectional composites and sandwich plates", *J. Compos. Mater.* **4**:1 (1970), 20–34.

[Pai and Palazzotto 2001] P. F. Pai and A. N. Palazzotto, "A higher-order sandwich plate theory accounting for 3-D stresses", *Int. J. Solids Struct.* **38**:30–31 (2001), 5045–5062.

[Polit and Touratier 2002] O. Polit and M. Touratier, "A multilayered/sandwich triangular finite element applied to linear and non-linear analysis", *Compos. Struct.* **58**:1 (2002), 121–128.

[Polit et al. 1994] O. Polit, M. Touratier, and P. Lory, "A new eight-node quadrilateral shear-bending plate finite element", *Int. J. Numer. Methods Eng.* **37**:3 (1994), 387–411.

[Rao and Desai 2004] M. K. Rao and Y. M. Desai, "Analytical solutions for vibrations of laminated and sandwich plates using mixed theory", *Compos. Struct.* **63**:3–4 (2004), 361–373.

[Reddy 1984] J. N. Reddy, "A simple higher-order theory for laminated composite plates", *J. Appl. Mech.* (*ASME*) **51**:4 (1984), 745–752.

[Reddy 1989] J. N. Reddy, "On refined computational models of composite laminates", *Int. J. Numer. Methods Eng.* **27**:2 (1989), 361–382.

[Reddy 1997] J. N. Reddy, *Mechanics of laminated composite plates: theory and analysis*, CRC Press, Boca Raton, FL, 1997.

[Robaldo 2006] A. Robaldo, "Finite element analysis of the influence of temperature profile on thermoelasticity of multilayered plates", *Comput. Struct.* **84**:19–20 (2006), 1236–1246.

[Rohwer et al. 2001] K. Rohwer, R. Rolfes, and H. Sparr, "Higher-order theories for thermal stresses in layered plates", *Int. J. Solids Struct.* **38**:21 (2001), 3673–3687.

[Rolfes et al. 1998] R. Rolfes, A. K. Noor, and H. Sparr, "Evaluation of transverse thermal stresses in composite plates based on first-order shear deformation theory", *Comput. Methods Appl. Mech. Eng.* **167**:3–4 (1998), 355–368.

[di Sciuva 1986] M. di Sciuva, "Bending, vibration and buckling of simply supported thick multilayered orthotropic plates: an evaluation of a new displacement model", *J. Sound Vib.* **105**:3 (1986), 425–442.

[di Sciuva and Icardi 2001] M. di Sciuva and U. Icardi, "Numerical assessment of the core deformability effect on the behavior of sandwich beams", *Compos. Struct.* **52**:1 (2001), 41–53.

[Shimpi and Ainapure 2001] R. P. Shimpi and A. V. Ainapure, "A beam finite element based on layerwise trigonometric shear deformation theory", *Compos. Struct.* **53**:2 (2001), 153–162.

[Soldatos and Watson 1997] K. P. Soldatos and P. Watson, "A general theory for the accurate stress analysis of homogeneous and laminated composite beams", *Int. J. Solids Struct.* **34**:22 (1997), 2857–2885.

[Srinivas 1973] S. Srinivas, "A refined analysis of laminated composites", *J. Sound Vib.* **30**:4 (1973), 495–507.

[Subramanian 2001] P. Subramanian, "Flexural analysis of symmetric laminated composite beams using $c^1$ finite element", *Compos. Struct.* **54**:1 (2001), 121–126. Technical note.

[Subramanian 2006] P. Subramanian, "Dynamic analysis of laminated composite beams using higher order theories and finite elements", *Compos. Struct.* **73**:3 (2006), 342–353.

[Swaminathan and Patil 2007] K. Swaminathan and S. Patil, "Higher order refined computational model with 12 degrees of freedom for the stress analysis of antisymmetric angle-ply plates: analytical solutions", *Compos. Struct.* **80**:4 (2007), 595–608.

[Swift and Heller 1974] G. Swift and R. Heller, "Layered beam analysis", *J. Eng. Mech.* (*ASCE*) **100** (1974), 267–282.

[Sze et al. 1998] K. Y. Sze, R. Chen, and Y. K. Cheung, "Finite element model with continuous transverse shear stress for composite laminates in cylindrical bending", *Finite Elem. Anal. Des.* **31**:2 (1998), 153–164.

[Tahani 2007] M. Tahani, "Analysis of laminated composite beams using layerwise displacement theories", *Compos. Struct.* **79**:4 (2007), 535–547.

[Tanigawa et al. 1989] Y. Tanigawa, H. Murakami, and Y. Ootao, "Transient thermal stress analysis of a laminated composite beam", *J. Therm. Stresses* **12**:1 (1989), 25–39.

[Tessler et al. 2001] A. Tessler, M. S. Annett, and G. Gendron, "A {1, 2}-order plate theory accounting for three-dimensional thermoelastic deformations in thick composite and sandwich laminates", *Compos. Struct.* **52**:1 (2001), 67–84.

[Touratier 1991] M. Touratier, "An efficient standard plate theory", *Int. J. Eng. Sci.* **29**:8 (1991), 901–916.

[Touratier 1992a] M. Touratier, "A generalization of shear deformation theories for axisymmetric multilayered shells", *Int. J. Solids Struct.* **29**:11 (1992), 1379–1399.

[Touratier 1992b] M. Touratier, "A refined theory of laminated shallow shells", *Int. J. Solids Struct.* **29**:11 (1992), 1401–1415.

[Vidal and Polit 2006] P. Vidal and O. Polit, "A thermomechanical finite element for the analysis of rectangular laminated beams", *Finite Elem. Anal. Des.* **42**:10 (2006), 868–883.

[Vidal and Polit 2008] P. Vidal and O. Polit, "A family of sinus finite elements for the analysis of rectangular laminated beams", *Compos. Struct.* **84**:1 (2008), 56–72.

[Vidal and Polit 2009] P. Vidal and O. Polit, "Assessment of the refined sinus model for the non-linear analysis of composite beams", *Compos. Struct.* **87**:4 (2009), 370–381.

[Vinayak et al. 1996] R. U. Vinayak, G. Prathap, and B. P. Naganarayana, "Beam elements based on a higher order theory, I: Formulation and analysis of performance", *Comput. Struct.* **58**:4 (1996), 775–789.

[Whitney 1969] J. M. Whitney, "The effect of transverse shear deformation on the bending of laminated plates", *J. Compos. Mater.* **3**:3 (1969), 534–547.

[Whitney and Sun 1973] J. M. Whitney and C. T. Sun, "A higher order theory for extensional motion of laminated composites", *J. Sound Vib.* **30**:1 (1973), 85–97.

[Wu et al. 2005] Z. Wu, R. Chen, and W. Chen, "Refined laminated composite plate element based on global-local higher-order shear deformation theory", *Compos. Struct.* **70**:2 (2005), 135–152.

[Yang et al. 1966] P. C. Yang, C. H. Norris, and Y. Stavsky, "Elastic wave propagation in heterogeneous plates", *Int. J. Solids Struct.* **2**:4 (1966), 665–684.

[Zhang and Kim 2005] Y. X. Zhang and K. S. Kim, "A simple displacement-based 3-node triangular element for linear and geometrically nonlinear analysis of laminated composite plates", *Comput. Methods Appl. Mech. Eng.* **194**:45–47 (2005), 4607–4632.

[Zhang and Yang 2009] Y. X. Zhang and C. H. Yang, "Recent developments in finite elements analysis for laminated composite plates", *Compos. Struct.* **88**:1 (2009), 147–157.

[Zhen and Wanji 2007] W. Zhen and C. Wanji, "Refined global-local higher-order theory and finite element for laminated plates", *Int. J. Numer. Methods Eng.* **69**:8 (2007), 1627–1670.

PHILIPPE VIDAL: philippe.vidal@u-paris10.fr
*LMpX, Université Paris Ouest, 50 rue de Sèvres, 92410 Ville d'Avray, France*

OLIVIER POLIT: olivier.polit@u-paris10.fr
*LMpX, Université Paris Ouest, 50 rue de Sèvres, 92410 Ville d'Avray, France*

# IMPROVED SMEARED AND ZIGZAG THIRD-ORDER THEORIES FOR PIEZOELECTRIC ANGLE-PLY LAMINATED CYLINDRICAL SHELLS UNDER ELECTROTHERMOMECHANICAL LOADS

JAYANTA KUMAR NATH AND SANTOSH KAPURIA

An improved efficient zigzag theory (IZIGT) and an improved third-order theory (ITOT) are presented for hybrid piezoelectric angle-ply composite circular cylindrical shells under electrothermomechanical loading. In both theories, the potential and thermal fields are approximated as piecewise linear across a number of sublayers so that the nonlinear potential field and actual temperature profile across the laminate thickness can be captured to any desired degree of accuracy. The transverse displacement is approximated to explicitly account for the transverse normal strain resulting from thermal and electric fields without introducing additional unknowns. The shear traction free conditions on the top and bottom surfaces in both theories and the continuity of transverse shear stresses at layer interfaces in the IZIGT are satisfied exactly considering coupled constitutive equations. The theories are assessed in comparison with the available exact 3D piezothermoelasticity solution for simply supported angle-ply hybrid cylindrical panels under electrothermomechanical loads. The comparisons for a hybrid test panel, a composite panel, and a sandwich panel establish that the IZIGT is very accurate and the ITOT is an improvement over the conventional third-order theory for thermal loads, which assumes uniform deflection across the laminate thickness.

## 1. Introduction

Research efforts continue to be directed towards the analysis, design, development, and testing of smart piezoelectric composite shell-type structures because of the increasing potential of their use in aerospace, marine, and automobile vehicles. Due to the presence of high layerwise inhomogeneity in mechanical, thermal and electric properties in these so called hybrid laminates, development of an accurate but computationally efficient two-dimensional (2D) shell theory for their analysis is a requirement that poses considerable challenges. Exact three-dimensional (3D) piezothermoelasticity solutions for simply supported finite-length cross-ply hybrid cylindrical shells [Xu and Noor 1996; Kapuria et al. 1997] and for infinite-length angle-ply hybrid cylindrical shells [Dumir et al. 1997] have been presented, against which the accuracy of the 2D theories can be assessed. In 3D solutions, no simplified hypothesis is made on the variations of field variables along the thickness coordinate, whereas in 2D laminate theories, variables are approximated in the thickness direction assuming a priori a given expansion. It is now well understood that:

- The neglect of direct piezoelectric and pyroelectric coupling effects leads to substantial error in predicting structural response [Lee and Saravanos 2000].

---

*Keywords:* cylindrical shell, angle-ply, piezoelectric composite, zigzag theory, thermal load.

- The transverse normal strain (out-of-plane deformation) can not be neglected in presence of thermal and electric fields [Kapuria and Achary 2006].

- The slope discontinuity in the inplane displacements at the layer interfaces, as observed from exact 3D solutions [Kapuria et al. 1997] should be included in the 2D theory for obtaining an accurate response.

- A 2D theory which works well for a shell loaded by an assumed linear or quadratic temperature profile may yield inaccurate results for an actual temperature profile based on the heat conduction equation [Carrera 2002].

These effects should be included in an accurate 2D theory, without enhancing the cost of analysis.

A comprehensive review of the 2D theories for piezoelectric hybrid plates and shells has been presented by Saravanos and Heyliger [1999]. Classical laminate theory (CLT) has been employed for electromechanical static and dynamic response of piezoelectric laminated generic [Jia and Rogers 1990] and circular cylindrical [Sung et al. 1996; Zhang et al. 2008] shells, wherein the two-way electromechanical coupling is not considered (the charge balance equation is not solved). Kapuria et al. [1998b] presented an assessment of uncoupled CLT and first-order shear deformation theory (FSDT) based on Flugge's approximations for electromechanical response of hybrid circular cylindrical shells in direct comparison with the exact 3D piezoelasticity solution. Berg et al. [2004] employed classical shell theory based on Flugge's approximations for the dynamic response of single-layer piezoelectric shells, considering electromechanical coupling. A coupled mixed field approach [Saravanos 1997; Saravanos and Christoforou 2002] with FSDT assumptions for the displacement field and layerwise linear approximation for the electric potential has been employed for doubly curved and cylindrical hybrid shells. Pinto Correia et al. [2002] developed a finite element for active control of axisymmetric hybrid shells based on the coupled third-order theory (TOT) with a sublayerwise linear approximation for electric potential. In this theory, the shear traction conditions at the top (outer) and bottom (inner) surfaces of the shell are not satisfied in presence of nonuniform electric potential on these surfaces. These equivalent single layer (ESL) theories, wherein the displacements are assumed to follow a global variation across the laminate thickness, violate the slope discontinuity in the inplane displacements and continuity of transverse shear stresses at the layer interfaces. The slope discontinuity is incorporated in the displacement field approximations of the layerwise theories (LWT), which yield accurate results [D'Ottavio et al. 2006; Carrera and Brischetto 2007]. However, these are computationally expensive since the number of unknown variables increases with the number of layers, which restricts their applicability in dynamics and control problems. As an efficient alternative to the LWT, zigzag theories (ZIGT) have been proposed, wherein the assumptions of displacements are the same as in the LWT with additional quadratic and cubic or trigonometric global variation across thickness for the inplane displacements. But the number of variables is reduced to that of the corresponding ESL theory by enforcing transverse shear continuity conditions at layer interfaces, and shear traction free conditions at the top and bottom surfaces. Ossadzow-David and Touratier [2004] presented a semicoupled ZIGT for doubly curved hybrid shells under electromechanical loading wherein the continuity and boundary conditions on transverse shear stresses and transverse electric displacement at the layer interfaces and the bounding surfaces (top and bottom) are satisfied using uncoupled constitutive equations. D'Ottavio et al. [2006] and Carrera and Brischetto [2007] also employed ESL models

with additional Murakami zigzag functions for inplane displacements, which do not satisfy the conditions on transverse shear stresses.

Limited literature is available wherein the above theories have been extended to incorporate thermal loading and the implications of the thermal effects on the hybrid shells have been assessed. The uncoupled CLT [Tzou and Bao 1995], coupled mixed field FSDT with layerwise linear potential [Raja et al. 2004], and coupled ZIGT [Kim et al. 2002; Oh and Cho 2007] have been presented for doubly curved shells under assumed temperature profile of linear and cubic variations across the thickness. A finite element model based on the coupled FSDT with layerwise linear temperature profile was presented for doubly curved hybrid shells by Lee and Saravanos [2000]. Kapuria et al. [1998a] extended the uncoupled CLT and FSDT based on Flugge's approximations for hybrid cylindrical shells to the thermal load case with layerwise temperature profile and assessed the theories in direct comparison with the 3D exact piezothermoelasticity solution. Such comparisons are not available for the other advanced 2D theories for hybrid shells under thermoelectric loading.

In this work, two new improved 2D theories are developed, namely, improved zigzag theory (IZIGT) and improved third-order theory (ITOT) for hybrid piezoelectric angle-ply composite cylindrical shells under electrothermomechanical loading. It is an extension an earlier work [Kapuria and Achary 2006; Kumari et al. 2008] for hybrid plates to the case of hybrid cylindrical shells. The temperature field is approximated to be piecewise linear across a number of sublayers across the laminate so as to capture the actual thermal profile based on the heat conduction equation, to any desired accuracy. The electric potential is similarly approximated across the piezoelectric layers, and the deflection is approximated to account for the normal strain along the thickness direction due to thermal and electric fields, without introducing any additional unknown variables. The conditions on transverse shear stresses at the top and bottom and at the layer interfaces (for IZIGT only) are satisfied exactly considering the coupled constitutive equations, and the number of displacement unknowns in both theories is reduced to five. The theories are assessed in direct comparison with the exact piezothermoelasticity solution [Dumir et al. 1997] for simply supported angle-ply infinite-length hybrid cylindrical panels of heterogeneous composite and sandwich laminate configurations under mechanical, electric potential, and thermal loads. The effect of inclusion of transverse normal strain in the approximation of deflection is investigated.

## 2. Displacement, potential and thermal field approximations

Consider a hybrid circular cylindrical shell panel of thickness $h$ and circumferential span angle $\alpha$ as shown in Figure 1, with circumferential axis $\theta$, longitudinal axis $x$, and thickness (radial) axis $z$. It is made of $L$ number of perfectly bonded orthotropic layers with their stiffer principal material axis direction at an angle $\psi$ to the $\theta$-axis. Some of the layers can be of radially polarized piezoelectric materials of orthorhombic class mm2 symmetry [Auld 1973]. The shell is subjected to a thermal load and a transverse mechanical load on the inner (bottom) and the outer (top) surfaces, with actuation potentials applied to some piezoelectric layers. The midsurface of the panel is chosen as the reference surface $z = 0$. The $z$-coordinate of the bottom surface of the $k$-th layer from the bottom is denoted as $z_{k-1}$. Thus, the $z$-coordinates of the bottom and the top surfaces are $z_0$ and $z_L$, respectively, with $z_0 = -h/2$ and $z_L = h/2$. The layer in which the reference surface lies or is at the bottom is denoted as the $k_0$-th layer and its radius is $R$.
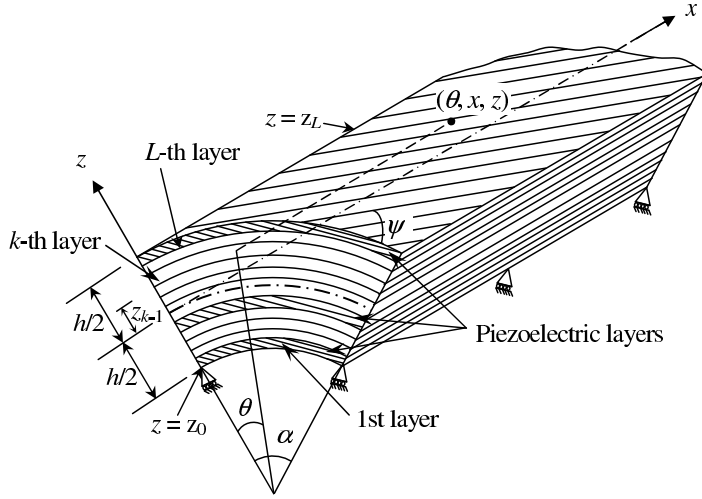
**Figure 1.** Geometry of a hybrid angle-ply cylindrical shell.

The 3D piezothermoelasticity solutions [Kapuria et al. 1997] have revealed that the contribution of the transverse normal stress $\sigma_z$ to the strain energy is much smaller than the contributions of the other stress components. Hence the assumption of $\sigma_z \simeq 0$ made in some 2D shell theories is retained in the present formulation. Using this assumption, the linear constitutive equations for the stresses $\sigma_\theta$, $\sigma_x$, $\tau_{\theta x}$, $\tau_{xz}$, and $\tau_{\theta z}$ and the electric displacements $D_\theta$, $D_x$, and $D_z$ are given by

$$\sigma = \bar{Q}\varepsilon - \bar{e}_3^{\mathrm{T}} E_z - \bar{\beta} T, \qquad \tau = \hat{Q}\gamma - \hat{e}E \qquad D = \hat{e}^{\mathrm{T}}\gamma + \hat{\eta}E, \qquad D_z = \bar{e}_3\varepsilon + \bar{\eta}_{33}E_z + \bar{p}_3 T, \quad (1)$$

where

$$\sigma = \begin{bmatrix} \sigma_\theta \\ \sigma_x \\ \tau_{\theta x} \end{bmatrix}, \qquad \tau = \begin{bmatrix} \tau_{\theta z} \\ \tau_{xz} \end{bmatrix}, \qquad D = \begin{bmatrix} D_\theta \\ D_x \end{bmatrix}, \qquad \varepsilon = \begin{bmatrix} \varepsilon_\theta \\ \varepsilon_x \\ \gamma_{\theta x} \end{bmatrix},$$

$$\bar{Q} = \begin{bmatrix} \bar{Q}_{11} & \bar{Q}_{12} & \bar{Q}_{16} \\ \bar{Q}_{12} & \bar{Q}_{22} & \bar{Q}_{26} \\ \bar{Q}_{16} & \bar{Q}_{26} & \bar{Q}_{66} \end{bmatrix}, \qquad \bar{\beta} = \begin{bmatrix} \bar{\beta}_1 \\ \bar{\beta}_2 \\ \bar{\beta}_6 \end{bmatrix}, \qquad \gamma = \begin{bmatrix} \gamma_{\theta z} \\ \gamma_{xz} \end{bmatrix}, \qquad \hat{Q} = \begin{bmatrix} \bar{Q}_{55} & \bar{Q}_{45} \\ \bar{Q}_{45} & \bar{Q}_{44} \end{bmatrix}, \quad (2)$$

$$E = \begin{bmatrix} E_\theta \\ E_x \end{bmatrix}, \qquad \hat{e} = \begin{bmatrix} \bar{e}_{15} & \bar{e}_{25} \\ \bar{e}_{14} & \bar{e}_{24} \end{bmatrix}, \qquad \hat{\eta} = \begin{bmatrix} \bar{\eta}_{11} & \bar{\eta}_{12} \\ \bar{\eta}_{12} & \bar{\eta}_{22} \end{bmatrix}, \qquad \bar{e}_3 = \begin{bmatrix} \bar{e}_{31} & \bar{e}_{32} & \bar{e}_{36} \end{bmatrix}.$$

Here $\varepsilon$ and $\gamma$ are the inplane and transverse strain components, and $E_\theta$, $E_x$, and $E_z$ are the electric field components. $\bar{Q}_{ij}$, $\bar{e}_{ij}$, $\bar{\eta}_{ij}$, and $\bar{\beta}_i$ are the reduced elastic stiffnesses, piezoelectric stress constants, electric permittivities, and stress-temperature coefficients, respectively. Let $u_\theta$, $u_x$, and $w$ be the inplane and transverse displacements and $\phi$ be the electric potential. Denoting differentiation by a subscript comma, the strain-displacement and electric field-electric potential relations for small strain condition

are given by

$$\varepsilon_\theta = \frac{u_{\theta,\theta} + w}{R + z}, \qquad \gamma_{xz} = u_{x,z} + w_{,x}, \qquad E_\theta = -\frac{\phi_{,\theta}}{R + z},$$

$$\varepsilon_x = u_{x,x}, \qquad \gamma_{\theta z} = u_{\theta,z} + \frac{w_{,\theta} - u_\theta}{R + z}, \qquad E_x = -\phi_{,x}, \qquad (3)$$

$$\varepsilon_z = w_{,z}, \qquad \gamma_{\theta x} = u_{\theta,x} + \frac{u_{x,\theta}}{R + z}, \qquad E_z = -\phi_{,z}.$$

The temperature field $T(\theta, x, z)$ for the hybrid laminated shell can be solved analytically for some geometries or numerically by, say, the finite element method. The temperature field $T$ is approximated piecewise linearly between $n_T$ points at $z_T^l$ ($l = 1, 2, \ldots, n_T$) across the thickness. The potential field is similarly approximated between $n_\phi$ points at $z_\phi^j$ ($j = 1, 2, \ldots, n_\phi$) across the thickness:

$$T(\theta, x, z) = \Psi_T^l(z) T^l(\theta, x), \qquad \phi(\theta, x, z) = \Psi_\phi^j(z) \phi^j(\theta, x), \qquad (4)$$

where $T^l(\theta, x) = T(\theta, x, z_T^l)$ and $\phi^j(\theta, x) = \phi(\theta, x, z_\phi^j)$. Functions $\Psi_T^l(z)$ and $\Psi_\phi^j(z)$ are linear Lagrange interpolation functions for $T$ and $\phi$ respectively. The summation convention is used for repeated indices $l$ and $j$, and for $l'$ and $j'$, used later. For discretisation of $T$ and $\phi$, each layer is divided into a number of sublayers as required by the desired accuracy.

3D exact solutions [Xu and Noor 1996; Kapuria et al. 1997] have revealed that for moderately thick hybrid shells under thermoelectric load, the transverse displacement $w$ has significant variation across the thickness, which is caused by the thickness deformation primarily due to the electric and thermal fields. Hence, in the present IZIGT, $w$ is approximated by neglecting the contributions of stresses in the constitutive equation for $\varepsilon_z$, but retaining the contributions of thermal and electric fields and then integrating the remaining expression for $\varepsilon_z$:

$$\varepsilon_z = w_{,z} \simeq -\bar{d}_{33}\phi_{,z} + \bar{a}_3 T \quad \implies \quad w(\theta, x, z) = w_0(\theta, x) - \bar{\Psi}_\phi^j(z)\phi^j(\theta, x) + \bar{\Psi}_T^l(z)T^l(\theta, x), \quad (5)$$

with

$$\bar{\Psi}_\phi^j(z) = \int_0^z d_{33}\Psi_{\phi,z}^j(z)\,dz, \qquad \bar{\Psi}_T^l(z) = \int_0^z \alpha_3 \Psi_T^l(z)\,dz. \qquad (6)$$

$\bar{\Psi}_\phi^j(z)$ is a piecewise linear function and $\bar{\Psi}_T^l(z)$ is a piecewise quadratic function.

The inplane displacements $u_\theta$ and $u_x$ are approximated as a combination of a global third-order variation in $z$ across the thickness and a layerwise piecewise linear variation:

$$u(\theta, x, z) = \begin{bmatrix} 1 + \dfrac{z}{R} & 0 \\ 0 & 1 \end{bmatrix} u_k(\theta, x) - z w_{0_d} + z\psi_k(\theta, x) + z^2\xi(\theta, x) + z^3\eta(\theta, x) \qquad (7)$$

where

$$u = \begin{bmatrix} u_\theta \\ u_x \end{bmatrix}, \quad u_k = \begin{bmatrix} u_{k_\theta} \\ u_{k_x} \end{bmatrix}, \quad w_{0_d} = \begin{bmatrix} w_{0,\theta}/R \\ w_{0,x} \end{bmatrix}, \quad \psi_k = \begin{bmatrix} \psi_{k_\theta} \\ \psi_{k_x} \end{bmatrix}, \quad \xi = \begin{bmatrix} \xi_\theta \\ \xi_x \end{bmatrix}, \quad \eta = \begin{bmatrix} \eta_\theta \\ \eta_x \end{bmatrix}, \qquad (8)$$

and $u_k$ and $\psi_k$ are the translation and shear rotation variables of the $k$-th layer. Substituting $u_\theta$ and $u_x$ from (7), $w$ from (5) and $\phi$ from (4)$_2$ into (3) and thereafter using (1), the transverse shear stresses $\tau$ are

obtained as

$$\tau = Q_1^k(z)\psi_k + Q_2^k(z)\xi + Q_3^k(z)\eta + Q_{4j}^k(z)\phi_d^j + Q_{5l}^k(z)T_d^l, \tag{9}$$

with

$$Q_1^k(z) = \hat{Q}^k \begin{bmatrix} \dfrac{R}{R+z} & 0 \\ 0 & 1 \end{bmatrix}, \quad Q_{5l}^k(z) = \hat{Q}^k \begin{bmatrix} \dfrac{R}{R+z} & 0 \\ 0 & 1 \end{bmatrix}\bar{\Psi}_T^l(z), \quad Q_2^k(z) = \hat{Q}^k \begin{bmatrix} \dfrac{z^2+2zR}{R+z} & 0 \\ 0 & 2z \end{bmatrix},$$

$$\phi_d^j = \begin{bmatrix} \dfrac{\phi_{,\theta}^j}{R} \\ \phi_{,x}^j \end{bmatrix}, \qquad Q_3^k(z) = \hat{Q}^k \begin{bmatrix} \dfrac{2z^3+3z^2R}{R+z} & 0 \\ 0 & 3z^2 \end{bmatrix}, \qquad T_d^l = \begin{bmatrix} \dfrac{T_{,\theta}^l}{R} \\ T_{,x}^l \end{bmatrix}, \tag{10}$$

$$Q_{4j}^k(z) = \hat{e}^k \begin{bmatrix} \dfrac{R}{R+z} & 0 \\ 0 & 1 \end{bmatrix}\Psi_\phi^j(z) - \hat{Q}^k \begin{bmatrix} \dfrac{R}{R+z} & 0 \\ 0 & 1 \end{bmatrix}\bar{\Psi}_\phi^j(z).$$

The conditions of zero transverse shear stresses $\tau$ at the inner and outer surfaces, and the continuity of $\tau$ and $u$ at the layer interfaces yield

$$\tau(z_0) = 0 \qquad \Longrightarrow \quad Q_1^1(z_0)\psi_1 + Q_2^1(z_0)\xi + Q_3^1(z_0)\eta = -Q_{4j}^1(z_0)\phi_d^j - Q_{5l}^1(z_0)T_d^l, \tag{11}$$

$$\tau(z_k^-) = \tau(z_k^+) \quad \Longrightarrow \quad Q_1^{k+1}(z_k)\psi_{k+1} - Q_1^k(z_k)\psi_k + \hat{Q}_2^k\xi + \hat{Q}_3^k\eta = -\hat{Q}_{4j}^k\phi_d^j - \hat{Q}_{5l}^kT_d^l, \tag{12}$$

$$u(z_k^-) = u(z_k^+) \quad \Longrightarrow \quad \begin{bmatrix} 1+\dfrac{z_k}{R} & 0 \\ 0 & 1 \end{bmatrix}(u_{k+1} - u_k) + z_k\psi_{k+1} - z_k\psi_k = 0, \tag{13}$$

$$\tau(z_L) = 0 \qquad \Longrightarrow \quad Q_1^L(z_L)\psi_L + Q_2^L(z_L)\xi + Q_3^L(z_L)\eta = -Q_{4j}^L(z_L)\phi_d^j - Q_{5l}^L(z_L)T_d^l, \tag{14}$$

where $k = 1, \ldots, L-1$,

$$\hat{Q}_i^k = Q_i^{k+1}(z_k) - Q_i^k(z_k), \quad i = 1, 2, 3, 4, \tag{15}$$

and

$$\hat{Q}_{4j}^k = Q_{4j}^{k+1}(z_k) - Q_{4j}^k(z_k), \qquad \hat{Q}_{5l}^k = Q_{5l}^{k+1}(z_k) - Q_{5l}^k(z_k). \tag{16}$$

Equations (11)–(14) along with $u_{k_0} = u_0$ and $\psi_{k_0} = \psi_0$ are arranged in matrix form for the $2L+2$ unknowns $u_k$, $\psi_k$, $\xi$, and $\eta$:

$$A\bar{x} = B^u u_0 + B^\psi \psi_0 + B_j^\phi \phi_d^j + B_l^T T_d^l, \tag{17}$$

where $A$ is a $(4L+4) \times (4L+4)$ matrix, $B^u$, $B^\psi$, $B_j^\phi$, and $B_l^T$ are matrices of size $(4L+4) \times 2$, and

$$\bar{x} = \begin{bmatrix} u_1^T & \psi_1^T & u_2^T & \psi_2^T & \ldots & u_L^T & \psi_L^T & \xi^T & \eta^T \end{bmatrix}^T. \tag{18}$$

Partitioning the matrices $A$, $B^u$, $B^\psi$, $B^\phi_j$, and $B^T_l$ into $2 \times 2$ submatrices $A(i, j)$, $B^u(i)$, $B^\psi(i)$, $B^\phi_j(i)$, and $B^T_l(i)$, the nonzero submatrices are given by

$$A(1, 2) = Q^1_1(z_0),$$
$$A(1, 2L+1) = Q^1_2(z_0),$$
$$A(1, 2L+2) = Q^1_3(z_0),$$
$$A(2i, 2i) = -Q^i_1(z_i),$$
$$A(2i, 2i+2) = Q^{i+1}_1(z_i),$$
$$A(2i, 2L+2) = \hat{Q}^i_3(z_i),$$
$$A(2i, 2L+1) = \hat{Q}^i_2(z_i),$$
$$A(2i+1, 2i-1) = -\begin{bmatrix} 1+\dfrac{z_i}{R} & 0 \\ 0 & 1 \end{bmatrix},$$

$$A(2L, 2L) = Q^L_1(z_L),$$
$$A(2L, 2L+1) = Q^L_2(z_L),$$
$$A(2L, 2L+2) = Q^L_3(z_L),$$
$$A(2L+1, 2k_0-1) = I_2,$$
$$A(2L+2, 2k_0) = I_2,$$
$$A(2i+1, 2i) = -z_i I_2,$$
$$A(2i+1, 2i+2) = z_i I_2,$$
$$A(2i+1, 2i+1) = \begin{bmatrix} 1+\dfrac{z_i}{R} & 0 \\ 0 & 1 \end{bmatrix},$$

$$B^u(2L+1) = I_2,$$
$$B^\psi(2L+2) = I_2,$$
$$B^\phi_j(1) = -Q^1_{4j}(z_0),$$
$$B^\phi_j(2i) = -\hat{Q}^i_{4j}(z_i),$$
$$B^\phi_j(2L) = -Q^L_{4j}(z_L),$$
$$B^T_l(1) = -Q^1_{5l}(z_0),$$
$$B^T_l(2i) = -\hat{Q}^i_{5l}(z_i),$$
$$B^T_l(2L) = -Q^L_{5l}(z_L),$$

for $i = 1, \ldots, L-1$. Here $I_2$ is the $2 \times 2$ identity matrix. The solution of (17) can be expressed as

$$\bar{x} = C^u u_0 + C^\psi \psi_0 + C^\phi_j \phi^j_d + C^T_l T^l_d, \tag{19}$$

where

$$C^u = A^{-1} B^u, \qquad C^\psi = A^{-1} B^\psi, \qquad C^\phi_j = A^{-1} B^\phi_j, \qquad C^T_l = A^{-1} B^T_l. \tag{20}$$

$C^u$, $C^\psi$, $C^\phi_j$, and $C^T_l$ are partitioned into $2L+1$ submatrices $C^u(i)$, $C^\psi(i)$, $C^\phi_j(i)$, and $C^T_l(i)$ of size $2 \times 2$ each. Since $\xi$, $\eta$, and $\psi_i$ in (11), (12), and (14) can be solved in terms of $\psi_0$, $\phi^j_d$, and $T^l_d$ only, it follows that $C^u(2i) = 0$ for $i = 1, \ldots, L$, and $C^u(2L+1) = C^u(2L+2) = 0$. Moreover, (13) implies that $u_i = u_0 + f(\psi_1, \psi_2, \ldots, \psi_L)$, where $f$ is a function of the $\psi_i$. Thus $C^u(2i-1) = I_2$. Considering these submatrices of $C$, (19) can be explicitly written as

$$\begin{aligned} u_k &= I_2 u_0 + C^\psi(2k-1)\psi_0 + C^\phi_j(2k-1)\phi^j_d + C^T_l(2k-1)T^l_d, \\ \psi_k &= C^\psi(2k)\psi_0 + C^\phi_j(2k)\phi^j_d + C^T_l(2k)T^l_d, \\ \xi &= C^\psi(2L+1)\psi_0 + C^\phi_j(2L+1)\phi^j_d + C^T_l(2L+1)T^l_d, \\ \eta &= C^\psi(2L+2)\psi_0 + C^\phi_j(2L+2)\phi^j_d + C^T_l(2L+2)T^l_d. \end{aligned} \tag{21}$$

These expressions are now substituted in (7) to obtain the final expressions of $u$:

$$u(\theta, x, z) = \begin{bmatrix} 1+\dfrac{z}{R} & 0 \\ 0 & 1 \end{bmatrix} u_0(\theta, x) - z w_{0d}(\theta, x) + R^k(z)\psi_0(\theta, x) + \hat{R}^{kj}(z)\phi^j_d(\theta, x) + \bar{R}^{kl}(z)T^l_d(\theta, x), \tag{22}$$

where

$$\begin{aligned} R^k(z) &= R^k_1 + z R^k_2 + z^2 R_3 + z^3 R_4, \\ \hat{R}^{kj}(z) &= \hat{R}^{kj}_1 + z \hat{R}^{kj}_2 + z^2 \hat{R}^j_3 + z^3 \hat{R}^j_4, \\ \bar{R}^{kl}(z) &= \bar{R}^{kl}_1 + z \bar{R}^{kl}_2 + z^2 \bar{R}^l_3 + z^3 \bar{R}^l_4, \end{aligned} \tag{23}$$

with

$$R_1^k = C^\psi(2k-1), \quad R_2^k = \begin{bmatrix} \frac{1}{R} & 0 \\ 0 & 0 \end{bmatrix} C^\psi(2k-1) + C^\psi(2k), \quad R_3 = C^\psi(2L+1), \quad R_4 = C^\psi(2L+2),$$

$$\hat{R}_1^{kj} = C_j^\phi(2k-1), \quad \hat{R}_2^{kj} = \begin{bmatrix} \frac{1}{R} & 0 \\ 0 & 0 \end{bmatrix} C_j^\phi(2k-1) + C_j^\phi(2k), \quad \hat{R}_3^j = C_j^\phi(2L+1), \quad \hat{R}_4^j = C_j^\phi(2L+2), \quad (24)$$

$$\bar{R}_1^{kl} = C_l^T(2k-1), \quad \bar{R}_2^{kl} = \begin{bmatrix} \frac{1}{R} & 0 \\ 0 & 0 \end{bmatrix} C_l^T(2k-1) + C_l^T(2k), \quad \bar{R}_3^l = C_l^T(2L+1), \quad \bar{R}_4^l = C_l^T(2L+2).$$

For the improved and consistent third-order ESL theory (ITOT), $w$ is approximated by (5) and $u$ is approximated as

$$u(\theta, x, z) = \begin{bmatrix} 1 + \frac{z}{R} & 0 \\ 0 & 1 \end{bmatrix} u_0(\theta, x) - z w_{0_d} + z \psi_0(\theta, x) + z^2 \xi(\theta, x) + z^3 \eta(\theta, x), \quad (25)$$

for which the expression for $\tau$ is obtained as

$$\tau = Q_1^k(z)\psi_0 + Q_2^k(z)\xi + Q_3^k(z)\eta + Q_{4j}^k(z)\phi_d^j + Q_{5l}^k(z)T_d^l. \quad (26)$$

Applying the shear traction-free condition $\tau = 0$ at $z = z_0, z_L$ yields

$$\bar{a}_1\psi_0 + \bar{a}_2\xi + \bar{a}_3\eta + \bar{a}_{4j}\phi_d^j + \bar{a}_{5l}T_d^l = 0, \qquad \bar{b}_1\psi_0 + \bar{b}_2\xi + \bar{b}_3\eta + \bar{b}_{4j}\phi_d^j + \bar{b}_{5l}T_d^l = 0, \quad (27)$$

where

$$\begin{aligned} \bar{a}_1 &= Q_1^1(z_0), & \bar{a}_2 &= Q_2^1(z_0), & \bar{a}_3 &= Q_3^1(z_0), & \bar{a}_{4j} &= Q_{4j}^1(z_0), & \bar{a}_{5l} &= Q_{5l}^1(z_0), \\ \bar{b}_1 &= Q_1^L(z_L), & \bar{b}_2 &= Q_2^L(z_L), & \bar{b}_3 &= Q_3^L(z_L), & \bar{b}_{4j} &= Q_{4j}^L(z_L), & \bar{b}_{5l} &= Q_{5l}^L(z_L). \end{aligned} \quad (28)$$

Equation (27) is solved for $\xi$ and $\eta$ to obtain

$$\xi = R_3\psi_0 + \hat{R}_3^j\phi_d^j + \bar{R}_3^l T_d^l, \qquad \eta = R_4\psi_0 + \hat{R}_4^j\phi_d^j + \bar{R}_4^l T_d^l, \quad (29)$$

where

$$\begin{aligned} R_3 &= \bar{\Delta}^{-1}(\bar{b}_3^{-1}\bar{b}_1 - \bar{a}_3^{-1}\bar{a}_1), & R_4 &= -\bar{a}_3^{-1}(\bar{a}_2 R_3 + \bar{a}_1), \\ \hat{R}_3^j &= \bar{\Delta}^{-1}(\bar{b}_3^{-1}\bar{b}_{4j} - \bar{a}_3^{-1}\bar{a}_{4j}), & \hat{R}_4^j &= -\bar{a}_3^{-1}(\bar{a}_2\hat{R}_3^j + \bar{a}_{4j}), \\ \bar{R}_3^l &= \bar{\Delta}^{-1}(\bar{b}_3^{-1}\bar{b}_{5l} - \bar{a}_3^{-1}\bar{a}_{5l}), & \bar{R}_4^l &= -\bar{a}_3^{-1}(\bar{a}_2\bar{R}_3^l + \bar{a}_{5l}), & \bar{\Delta} &= \bar{a}_3^{-1}\bar{a}_2 - \bar{b}_3^{-1}\bar{b}_2. \end{aligned} \quad (30)$$

Substitution of $\xi$ and $\eta$ from (29) into (25) yields the expression of $u$ for the ITOT to be of the same form as of (22) for the IZIGT with the functions $R^k(z)$, $\hat{R}^{kj}(z)$, and $\bar{R}^{kl}(z)$ for the former given by

$$R^k(z) = z I_2 + z^2 R_3 + z^3 R_4, \qquad \hat{R}^{kj}(z) = z^2 \hat{R}_3^j + z^3 \hat{R}_4^j, \qquad \bar{R}^{kl}(z) = z^2 \bar{R}_3^l + z^3 \bar{R}_4^l. \quad (31)$$

## 3. Strain-displacement relations

The displacements $u$ and $w$ given by (22), (5) and the small virtual displacements $\delta u$, $\delta w$ can be written

$$u = f_1(z)\bar{u}_1 + \bar{R}^{kl}(z)T_d^l, \qquad\qquad w = f_2(z)\bar{u}_2 + \bar{\Psi}_T^l(z)T^l, \qquad (32)$$

$$\delta u = f_1(z)\delta\bar{u}_1 = \delta\bar{u}_1^T f_1^T(z), \qquad \delta w = f_2(z)\delta\bar{u}_2 = \delta\bar{u}_2^T f_2^T(z), \qquad (33)$$

with

$$\bar{u}_1 = \begin{bmatrix} u_0^T & -w_{0_d}^T & \psi_0^T & \phi_d^{jT} \end{bmatrix}^T, \qquad \bar{u}_2 = \begin{bmatrix} w_0 & -\phi^j \end{bmatrix}^T, \qquad I_z = \begin{bmatrix} 1+\dfrac{z}{R} & 0 \\ 0 & 1 \end{bmatrix}, \qquad (34)$$

$$f_1(z) = \begin{bmatrix} I_z & I_2z & R^k(z) & \hat{R}^{kj}(z) \end{bmatrix}, \qquad f_2(z) = \begin{bmatrix} 1 & \bar{\Psi}_\phi^j(z) \end{bmatrix},$$

where the index $j$ indicates a sequence of elements with $j$ ranging from 1 to $n_\phi$. Substituting $u$ and $w$ from (22) and (5) into (3) yields

$$\varepsilon = f_3(z)\bar{\varepsilon}_1 + \bar{f}_2(z)\bar{u}_2 + \bar{\Phi}^{kl}(z)T_{dd}^l + \tilde{I}_1(z)\bar{\Psi}_T^l(z)T^l, \qquad \gamma = f_4(z)\bar{\varepsilon}_2 + \bar{\Phi}_0^{kl}(z)T_d^l, \qquad (35)$$

and hence

$$\delta\varepsilon = f_3(z)\delta\bar{\varepsilon}_1 + \bar{f}_2(z)\delta\bar{u}_2, \quad \delta\gamma = f_4(z)\delta\bar{\varepsilon}_2, \qquad (36)$$

with

$$f_3(z) = \begin{bmatrix} \Phi^0(z) & \Phi(z) & \Phi^k(z) & \Phi^{kj}(z) \end{bmatrix}, \quad f_4(z) = \begin{bmatrix} \Phi_0^k(z) & \Phi_0^{kj}(z) \end{bmatrix}, \quad \bar{f}_2(z) = \frac{1}{R+z}\tilde{I}_1\begin{bmatrix} 1 & \bar{\Psi}_\phi^j(z) \end{bmatrix}, \quad (37)$$

$$\Phi^0(z) = \begin{bmatrix} 1 & 0 & 0 & 0 \\ 0 & 0 & 0 & 1 \\ 0 & 1+\dfrac{z}{R} & \dfrac{1}{1+z/R} & 0 \end{bmatrix}, \qquad\qquad \Phi(z) = \begin{bmatrix} \dfrac{z}{1+z/R} & 0 & 0 & 0 \\ 0 & 0 & 0 & z \\ 0 & z & \dfrac{z}{1+z/R} & 0 \end{bmatrix},$$

$$\Phi^k(z) = \begin{bmatrix} \dfrac{R_{11}^k}{1+z/R} & 0 & \dfrac{R_{12}^k}{1+z/R} & 0 \\ 0 & R_{21}^k & 0 & R_{22}^k \\ \dfrac{R_{21}^k}{1+z/R} & R_{11}^k & \dfrac{R_{22}^k}{1+z/R} & R_{12}^k \end{bmatrix}, \qquad \Phi^{kj}(z) = \begin{bmatrix} \dfrac{R_{11}^{kj}}{1+z/R} & 0 & \dfrac{R_{12}^{kj}}{1+z/R} & 0 \\ 0 & R_{21}^{kj} & 0 & R_{22}^{kj} \\ \dfrac{R_{21}^{kj}}{1+z/R} & R_{11}^{kj} & \dfrac{R_{22}^{kj}}{1+z/R} & R_{12}^{kj} \end{bmatrix},$$

$$\Phi_0^k(z) = \begin{bmatrix} R_{11,z}^k - \dfrac{R_{11}^k}{R+z} & R_{12,z}^k - \dfrac{R_{12}^k}{R+z} \\ R_{21,z}^k & R_{22,z}^k \end{bmatrix}, \qquad \bar{\Phi}^{kl}(z) = \begin{bmatrix} \dfrac{\bar{R}_{11}^{kl}}{1+z/R} & 0 & \dfrac{\bar{R}_{12}^{kl}}{1+z/R} & 0 \\ 0 & \bar{R}_{21}^{kl} & 0 & \bar{R}_{22}^{kl} \\ \dfrac{\bar{R}_{21}^{kl}}{1+z/R} & \bar{R}_{11}^{kl} & \dfrac{\bar{R}_{22}^{kl}}{1+z/R} & \bar{R}_{12}^{kl} \end{bmatrix}, \qquad (38)$$

$$\Phi_0^{kj}(z) = \begin{bmatrix} R_{11,z}^{kj} - \dfrac{R_{11}^{kj}+R\bar{\Psi}_\phi^j}{R+z} & R_{12,z}^{kj} - \dfrac{R_{12}^{kj}}{R+z} \\ R_{21,z}^{kj} & R_{22,z}^{kj} - \bar{\Psi}_\phi^j \end{bmatrix}, \qquad \bar{\Phi}_0^{kl}(z) = \begin{bmatrix} \bar{R}_{11,z}^{kl} - \dfrac{\bar{R}_{11}^{kl}-R\bar{\Psi}_T^l}{R+z} & \bar{R}_{12,z}^{kl} - \dfrac{\bar{R}_{12}^{kl}}{R+z} \\ \bar{R}_{21,z}^{kl} & \bar{R}_{22,z}^{kl} + \bar{\Psi}_T^l \end{bmatrix},$$

$$
\bar{\varepsilon}_1 = \begin{bmatrix} u_{0d} \\ -w_{0dd} \\ \psi_{0d} \\ \phi_{dd}^j \end{bmatrix}, \qquad \bar{\varepsilon}_2 = \begin{bmatrix} \psi_0 \\ \phi_d^j \end{bmatrix}, \qquad \bar{I}_1 = \begin{bmatrix} 1 \\ 0 \\ 0 \end{bmatrix}, \qquad \tilde{I}_1(z) = \begin{bmatrix} \dfrac{1}{R+z} \\ 0 \\ 0 \end{bmatrix},
$$

$$
w_{0d} = \begin{bmatrix} w_{0,\theta}/R \\ w_{0,x} \end{bmatrix}, \quad w_{0dd} = \begin{bmatrix} w_{0,\theta\theta}/R^2 \\ w_{0,\theta x}/R \\ w_{0,x\theta}/R \\ w_{0,xx} \end{bmatrix}, \quad u_{0d} = \begin{bmatrix} u_{0\theta,\theta}/R \\ u_{0\theta,x} \\ u_{0x,\theta}/R \\ u_{0x,x} \end{bmatrix}, \quad \psi_{0d} = \begin{bmatrix} \psi_{0\theta,\theta}/R \\ \psi_{0\theta,x} \\ \psi_{0x,\theta}/R \\ \psi_{0x,x} \end{bmatrix}, \tag{39}
$$

$$
\phi_d^j = \begin{bmatrix} \phi_{,\theta}^j/R \\ \phi_{,x}^j \end{bmatrix}, \quad \phi_{0dd}^j = \begin{bmatrix} \phi_{,\theta\theta}^j/R^2 \\ \phi_{,\theta x}^j/R \\ \phi_{,x\theta}^j/R \\ \phi_{,xx}^j \end{bmatrix}, \quad T_d^l = \begin{bmatrix} T_{,\theta}^l/R \\ T_{,x}^l \end{bmatrix}, \quad T_{0dd}^l = \begin{bmatrix} T_{,\theta\theta}^l/R^2 \\ T_{,\theta x}^l/R \\ T_{,x\theta}^l/R \\ T_{,xx}^l \end{bmatrix}.
$$

## 4. Equilibrium equations and boundary conditions

The variational principle for the piezoelectric shell is given by

$$
\int_V (\sigma_{ij}\delta\varepsilon_{ij} + D_i\delta\phi_{,i})\,dV - \int_\Gamma (T_i^n\delta u_i + D_n\delta\phi)\,d\Gamma - \sum_{i=1}^{n_\phi} \int_{A^{ji}} q_{j_i}\delta\phi^{ji}\,dA^{ji} = 0 \tag{40}
$$

(see [Tiersten 1969]), where $V$ and $\Gamma$ denote the volume and the surface area of the shell; $A^{ji}$ is an internal surface area at $z = z_\phi^{ji}$ where $\phi^{ji}$ is prescribed and $q_{j_i}$ is the jump in electric displacement $D_z$ at this interface; the total number of such prescribed potentials is $\bar{n}_\phi$; and $D_n$, $T_i^n$ denote the electric displacement vector and surface traction vector on a surface with outward normal vector $\bar{n}$.

Let $p_z^1$ and $p_z^2$ be the normal forces per unit area, and $D_z^1$ and $D_z^2$ be the surface charge density applied on the bottom and top surfaces of the shell. Using the notation

$$
\langle \dots \rangle = \sum_{k=1}^{L} \int_{z_{k-1}^+}^{z_k^-} (\dots)\,dz
$$

for integration across the thickness, the variational equation (40) for the laminated piezoelectric cylindrical shell panel of length $a$ and span angle $\alpha$ can be expressed as

$$
\begin{aligned}
\int_0^a \int_0^\alpha &\left( \left\langle \left(1 + \frac{z}{R}\right)\left\{\sigma_\theta\delta\varepsilon_\theta + \sigma_x\delta\varepsilon_x + \tau_{\theta x}\delta\gamma_{\theta x} + \tau_{\theta z}\delta\gamma_{\theta z} + \tau_{xz}\delta\gamma_{xz} + \frac{D_\theta\delta\phi_{,\theta}}{R+z} + D_x\delta\phi_{,x} + D_z\delta\phi_{,z}\right\}\right\rangle \right. \\
&- p_z^1\left(1 + \frac{z_0}{R}\right)\delta w(x,\theta,z_0) + D_z^1\left(1 + \frac{z_0}{R}\right)\delta\phi^1 \\
&\left. - p_z^2\left(1 + \frac{z_L}{R}\right)\delta w(x,\theta,z_L) - D_z^2\left(1 + \frac{z_L}{R}\right)\delta\phi^{n_\phi} - q_{j_i}\left(1 + \frac{z_\phi^{j_i}}{R}\right)\delta\phi^{ji}\right)R\,d\theta\,dx \\
&- \int_0^a \langle \sigma_\theta\delta u_\theta + \tau_{\theta x}\delta u_x + + \tau_{\theta z}\delta w + D_\theta\delta\phi \rangle \Big|_0^\alpha dx \\
&- \int_0^\alpha \left\langle \left(1 + \frac{z}{R}\right)(\tau_{\theta x}\delta u_\theta + \sigma_x\delta u_x + \tau_{xz}\delta w + D_x\delta\phi) \right\rangle \Big|_0^a R\,d\theta = 0,
\end{aligned} \tag{41}
$$

for all $\delta u_0$, $\delta w_0$, $\delta \psi_0$, and $\delta \phi^j$. This variational equation is expressed in terms of $\delta u_0$, $\delta w_0$, $\delta \psi_0$, and $\delta \phi^j$ to yield the governing equations of equilibrium for the shell and its variationally consistent boundary conditions.

Using (36), the strain energy terms in (41) can be expressed as

$$\left\langle \left(1+\frac{z}{R}\right)[\delta \varepsilon^{\mathrm{T}} \sigma + \delta \gamma^{\mathrm{T}} \tau] \right\rangle = \delta u_{0_d}^{\mathrm{T}} \hat{N} - \delta w_{0_{dd}}^{\mathrm{T}} M + \delta \psi_{0_d}^{\mathrm{T}} P + \delta \psi_{dd}^{j\mathrm{T}} S^j + \frac{\delta w_0 N_\theta}{R} - \frac{\delta \phi^j \hat{S}_\theta^j}{R} + \delta \psi_0^{\mathrm{T}} Q + \delta \phi_d^{j\mathrm{T}} \bar{Q}^j,$$

where

$$\hat{N} = \begin{bmatrix} N_\theta + M_\theta/R \\ N_{x\theta} + M_{x\theta}/R \\ N_{\theta x} \\ N_x \end{bmatrix} = \left\langle \left(1+\frac{z}{R}\right)\Phi^{0\mathrm{T}}(z)\sigma \right\rangle, \qquad M = \begin{bmatrix} M_\theta \\ M_{x\theta} \\ M_{\theta x} \\ M_x \end{bmatrix} = \left\langle \left(1+\frac{z}{R}\right)\Phi^{\mathrm{T}}(z)\sigma \right\rangle,$$

$$P = \begin{bmatrix} P_\theta \\ P_{x\theta} \\ P_{\theta x} \\ P_x \end{bmatrix} = \left\langle \left(1+\frac{z}{R}\right)\Phi^{k\mathrm{T}}(z)\sigma \right\rangle, \qquad \text{and} \qquad S^j = \begin{bmatrix} S_\theta^j \\ S_{x\theta}^j \\ S_{\theta x}^j \\ S_x^j \end{bmatrix} = \left\langle \left(1+\frac{z}{R}\right)\Phi^{kj\mathrm{T}}(z)\sigma \right\rangle$$

(42)

are stress resultants of the inplane stress components $\sigma$ (and likewise $\hat{S}^j$, defined analogously), and

$$Q = \begin{bmatrix} Q_\theta \\ Q_x \end{bmatrix} = \left\langle \left(1+\frac{z}{R}\right)\Phi_0^{k\mathrm{T}}(z)\tau \right\rangle \qquad \text{and} \qquad \bar{Q}^j = \begin{bmatrix} \bar{Q}_\theta^j \\ \bar{Q}_x^j \end{bmatrix} = \left\langle \left(1+\frac{z}{R}\right)\Phi_0^{kj\mathrm{T}}(z)\tau \right\rangle \qquad (43)$$

are the stress resultants of the shear stress $\tau$. In these formulas $N_\theta = \langle \sigma_\theta \rangle$, $N_{x\theta}$, $N_{\theta x} = \langle \tau_{\theta x} \rangle$, and $N_x$ are inplane force resultants; $M_\theta$, $M_{x\theta}$, $M_{\theta x}$, and $M_x$ are moment resultants; $P_\theta$, $P_{x\theta}$, $P_{\theta x}$, $P_x$, $S_\theta^j = \langle \bar{\phi}^j(z)\sigma_\theta \rangle$, $S_{x\theta}^j$, $S_{\theta x}^j$, and $S_x^j$ are higher-order moment resultants; and $Q_\theta$, $Q_x$, $\bar{Q}_\theta^j$, and $\bar{Q}_x^j$ are higher-order transverse shear resultants.

The electrical enthalpy terms in (41) can be expressed as

$$\left\langle \left(1+\frac{z}{R}\right)\left(\frac{D_\theta \delta\phi_{,\theta}}{R+z} + D_x \delta\phi_{,x} + D_z \delta\phi_{,z}\right) \right\rangle = \frac{H_\theta^j \delta\phi_{,\theta}^j}{R} + H_x^j \delta\phi_{,x}^j + G^j \delta\phi^j, \qquad (44)$$

where the shell electric resultants $H_\theta^j$, $H_x^j$, and $G^j$ of electric displacements $D_\theta$, $D_x$, and $D_z$ are defined by

$$H^j = \begin{bmatrix} H_\theta^j \\ H_x^j \end{bmatrix} = \begin{bmatrix} \langle \Psi_\phi^j(z)D_\theta \rangle \\ \left\langle \left(1+\frac{z}{R}\right)\Psi_\phi^j(z)D_x \right\rangle \end{bmatrix} = \left\langle \Psi_\phi^j(z) \begin{bmatrix} 1 & 0 \\ 0 & 1+\frac{z}{R} \end{bmatrix} D \right\rangle, \quad G^j = \left\langle \left(1+\frac{z}{R}\right)\Psi_{\phi,z}^j(z)D_z \right\rangle. \quad (45)$$

The electromechanical loading terms in (41) can be expressed as $-(F_3 \delta w_0 + F_6^j \delta\phi^j)$ where $F_3$ and $F_6^j$ are the mechanical and electrical loads respectively, defined by

$$F_3 = \left(1+\frac{z_0}{R}\right)p_z^1 + \left(1+\frac{z_L}{R}\right)p_z^2.$$

$$F_6^j = -\left(1+\frac{z_0}{R}\right)p_z^1 \bar{\Psi}_\phi^j(z_0) - \left(1+\frac{z_L}{R}\right)p_z^2 \bar{\Psi}_\phi^j(z_L) + \left(1+\frac{z_L}{R}\right)D_z^2 \delta_{jn_\phi} - \left(1+\frac{z_0}{R}\right)D_z^1 \delta_{j1} + \left(1+\frac{z_\phi^{j_i}}{R}\right)q_{j_i} \delta_{jj_i}.$$

(46)

The boundary terms in (41) are similarly expressed in terms of the stress and electric resultants and its area integral is expressed in terms of $\delta u_{0_\theta}$, $\delta u_{0_x}$, $\delta w_0$, $\delta\psi_{0_\theta}$, $\delta\psi_{0_x}$, and $\delta\phi^j$ by applying Green's theorem, wherever required, to yield the following $5 + n_\phi$ equations of equilibrium:

$$\frac{N_{\theta,\theta}}{R} + \frac{M_{\theta,\theta}}{R^2} + N_{x\theta,x} + \frac{M_{x\theta,x}}{R} = 0, \qquad \frac{M_{\theta,\theta\theta}}{R^2} + \frac{(M_{x\theta} + M_{\theta x}),_{x\theta}}{R} + M_{x,xx} - \frac{N_\theta}{R} + F_3 = 0,$$

$$N_{x,x} + \frac{N_{\theta x,\theta}}{R} = 0, \qquad \frac{P_{\theta,\theta}}{R} + P_{x\theta,\theta} - Q_\theta = 0, \qquad \frac{P_{\theta x,\theta}}{R} + P_{x,x} - Q_x = 0, \qquad (47)$$

$$\frac{\bar{Q}^j_{\theta,\theta}}{R} + \bar{Q}^j_{x,x} - \left( \frac{S^j_{\theta,\theta\theta}}{R^2} + \frac{S^j_{\theta x,\theta x}}{R} + \frac{S^j_{x\theta,x\theta}}{R} + S^j_{x,xx} \right) + \frac{H^j_{\theta,\theta}}{R} + H^j_{x,x} - G^j + \frac{\hat{S}^j_\theta}{R} + F^j_6 = 0,$$

and boundary conditions which consist of prescribed values of one of the factors of each of the following products at $\theta = 0, \alpha$:

$$u_{0_\theta}\left(N_\theta + \frac{M_\theta}{R}\right), \qquad u_{0_x}N_{\theta x}, \qquad w_0\left(M_{x\theta,x} + \frac{M_{\theta,\theta}}{R} + M_{\theta x,x}\right), \qquad w_{0,\theta}M_\theta,$$

$$\psi_{0_\theta}P_\theta, \qquad \psi_{0_x}P_{\theta x}, \qquad \phi^j\left(\bar{Q}^j_\theta + H^j_\theta - \frac{S^j_{\theta,\theta}}{R} - S^j_{x\theta,x} - S^j_{\theta x,x}\right), \qquad \phi^j_{,\theta}S^j_\theta, \qquad (48)$$

and at $x = 0, a$:

$$u_{0_\theta}\left(N_{x\theta} + \frac{M_{x\theta}}{R}\right), \qquad u_{0_x}N_x, \qquad w_0\left(M_{x,x} + \frac{M_{\theta x,\theta}}{R} + \frac{M_{x\theta,\theta}}{R}\right), \qquad w_{0,x}M_x,$$

$$\psi_{0_\theta}P_{x\theta}, \qquad \psi_{0_x}P_x, \qquad \phi^j\left(\bar{Q}^j_x + H^j - \frac{S^j_{x\theta,\theta}}{R} - \frac{S^j_{\theta x,\theta}}{R} - S^j_{x,x}\right), \qquad \phi^j_{,x}S^j_x. \qquad (49)$$

The first term of each product corresponds to the essential boundary condition and the second term corresponds to the natural boundary condition.

We now turn to the shell constitutive equations, which are the relations between shell stress resultants and electric displacement resultants defined in (42), (43) and (45) with the generalised shell mechanical strains and electric potential entities. They are obtained by substituting the expressions of $\sigma$, $\tau$, $D$, and $D_z$ from (1) into (42), (43) and (45):

$$F_1 = \left[\hat{N}^{\mathrm{T}} \; M^{\mathrm{T}} \; P^{\mathrm{T}} \; S^{j\mathrm{T}}\right]^{\mathrm{T}} = A\bar{\varepsilon}_1 + \beta^{j'}\phi^{j'} + A^l T^l_{dd} + (\tilde{A}^l - \gamma^l)T^l + \hat{A}\bar{u}_2,$$

$$F_2 = \left[Q^{\mathrm{T}} \; \bar{Q}^{j\mathrm{T}}\right]^{\mathrm{T}} = \bar{A}\bar{\varepsilon}_2 + \bar{\beta}^{j'}\phi^{j'}_d + \bar{A}^l T^l_d,$$

$$\bar{F}_2 = \left[N_\theta/R \; \hat{S}^j_\theta/R\right]^{\mathrm{T}} = \hat{A}^{\mathrm{T}}\bar{\varepsilon}_1 + \hat{A}^*\bar{u}_2 + \hat{\beta}^{j'}\phi^{j'} + \hat{A}^l T^l_{dd} + (A^{*l} - \hat{\gamma}^l)T^l, \qquad (50)$$

$$H^j = \bar{\beta}^{j\mathrm{T}}\bar{\varepsilon}_2 - \bar{E}^{jj'}\phi^{j'}_d + \bar{\beta}^{jl}T^l_d, \qquad G^j = \beta^{j\mathrm{T}}\bar{\varepsilon}_1 + \hat{\beta}^{j\mathrm{T}}\bar{u}_2 - E^{jj'}\phi^{j'} + \beta^{jl}T^l_{dd} + (\tilde{\gamma}^{jl} + \gamma^{jl})T^l,$$

where $A$, $\bar{A}$, $\hat{A}$, and $\hat{A}^*$ are the shell stiffnesses; $A^l$, $\bar{A}^l$, and $\hat{A}^l$ are the shell thermomechanical coefficients; $\beta^{j'}$, $\bar{\beta}^{j'}$, and $\hat{\beta}^j$ are the shell electromechanical coupling matrices; $\beta^{jl}$, $\bar{\beta}^{jl}$, $\gamma^l$, $\hat{\gamma}^l$, $\tilde{A}^l$, $A^{*l}$, and $\tilde{\gamma}^{jl}$ are the shell electrothermal matrices; $\gamma^{jl}$ is the shell pyroelectric matrix; and $E^{jj'}$ and $\bar{E}^{jj'}$ are the shell

dielectric matrices. These are defined in terms of material constants by

$$[A, A^l, \tilde{A}^l] = \left\langle \left(1 + \frac{z}{R}\right) f_3^{\mathrm{T}}(z)\bar{Q}[f_3(z), \bar{\Phi}^{kl}(z), \tilde{I}_1(z)\bar{\Psi}_T^l(z)]\right\rangle,$$

$$[\bar{A}, \bar{A}^l] = \left\langle \left(1 + \frac{z}{R}\right) f_4^{\mathrm{T}}(z)\hat{Q}[f_4(z), \bar{\Phi}_0^{kl}(z)]\right\rangle, \qquad \hat{A} = \left\langle \frac{f_3^{\mathrm{T}}(z)\bar{Q}_1^{\mathrm{T}} f_2(z)}{R}\right\rangle,$$

$$\hat{A}^* = \left\langle \frac{f_2^{\mathrm{T}}(z)\bar{Q}_{11} f_2(z)}{R(R+z)}\right\rangle, \qquad A^{*l} = \left\langle \frac{f_2^{\mathrm{T}}(z)\bar{Q}_{11}\bar{\Psi}_T^l(z)}{R(R+z)}\right\rangle,$$

$$\hat{A}^l = \left\langle \frac{f_2^{\mathrm{T}}(z)\bar{Q}_1\bar{\Phi}^{kl}(z)}{R}\right\rangle, \qquad \beta^{j'} = \left\langle \left(1 + \frac{z}{R}\right) f_3^{\mathrm{T}}(z)\bar{e}_3^{\mathrm{T}}\Psi_{\phi,z}^{j'}(z)\right\rangle,$$

$$\bar{\beta}^{j'} = \langle f_4^{\mathrm{T}}(z)\hat{e}I_z^*(z)\Psi_\phi^{j'}(z)\rangle, \qquad \hat{\beta}^{j'} = \left\langle \frac{f_2^{\mathrm{T}}(z)\bar{e}_{31}\Psi_{\phi,z}^j(z)}{R}\right\rangle, \qquad (51)$$

$$\beta^{jl} = \left\langle \left(1 + \frac{z}{R}\right)\Psi_{\phi,z}^j(z)\bar{e}_3\bar{\Phi}^{kl}(z)\right\rangle, \qquad \bar{\beta}^{jl} = \langle I_z^*(z)\Psi_\phi^j(z)\hat{e}^{\mathrm{T}}\bar{\Phi}_0^{kl}(z)\rangle,$$

$$\gamma^l = \left\langle \left(1 + \frac{z}{R}\right) f_3^{\mathrm{T}}(z)\bar{\beta}\Psi_T^l(z)\right\rangle, \qquad \hat{\gamma}^l = \left\langle \frac{f_2^{\mathrm{T}}(z)\bar{\beta}_1\Psi_T^l(z)}{R}\right\rangle,$$

$$E^{jj'} = \left\langle \left(1 + \frac{z}{R}\right)\bar{\eta}_{33}\Psi_{\phi,z}^j(z)\Psi_{\phi,z}^{j'}(z)\right\rangle, \qquad \bar{E}^{jj'} = \langle I_z^*(z)\hat{\eta}C_1(z)\Psi_\phi^j(z)\Psi_\phi^{j'}(z)\rangle,$$

$$\gamma^{jl} = \left\langle \left(1 + \frac{z}{R}\right)\bar{p}_3\Psi_{\phi,z}^j(z)\Psi_T^l(z)\right\rangle, \qquad \tilde{\gamma}^{jl} = \left\langle \frac{\Psi_{\phi,z}^j(z)\bar{e}_{31}\bar{\Psi}_T^l(z)}{R}\right\rangle,$$

with

$$\bar{Q}_1 = \begin{bmatrix} Q_{11} & Q_{12} & Q_{16} \end{bmatrix}, \qquad I_z^*(z) = \begin{bmatrix} 1 & 0 \\ 0 & 1 + \frac{z}{R} \end{bmatrix}. \qquad (52)$$

## 5. Angle-ply shell under cylindrical bending

Consider an angle-ply circular cylindrical shell panel of infinite length for which the applied thermoelectromechanical loading and hence all response entities are independent of $x$. The governing field equations, the boundary conditions, and the shell constitutive equations for such a shell under cylindrical bending are obtained by setting $(\ )_{,x} = 0$ in (47), (48), (49), and (50) for general bending of shell. Substituting the expressions of the resultants into the governing equations for the case of cylindrical bending yields the following coupled electromechanical equations in terms of the primary variables $u_{0\theta}$, $u_{0x}$, $w_0$, $\psi_{0\theta}$, $\psi_{0x}$, and $\phi^j$:

$$L\bar{U} = \bar{P}, \qquad (53)$$

where

$$\bar{U} = \begin{bmatrix} u_{0\theta} & u_{0x} & w_0 & \psi_{0\theta} & \psi_{0x} & \phi^1 & \phi^2 & \dots & \phi^{n_\phi} \end{bmatrix}^{\mathrm{T}},$$

$$\bar{P} = \begin{bmatrix} P_1 & P_2 & P_3 & P_4 & P_5 & P_6^1 & P_6^2 & \dots & P_6^{n_\phi} \end{bmatrix}^{\mathrm{T}}. \qquad (54)$$

$L$ is a symmetric matrix of linear differential operators in $\theta$, whose elements are given by

$$L_{11} = \frac{-A_{11}(\,)_{,\theta\theta}}{R^2}, \qquad L_{12} = \frac{-A_{13}(\,)_{,\theta\theta}}{R^2}, \qquad L_{13} = \frac{A_{15}(\,)_{,\theta\theta\theta}}{R^3} - \frac{\hat{A}_{11}(\,)_{,\theta}}{R}, \qquad L_{14} = \frac{-A_{19}(\,)_{,\theta\theta}}{R^2},$$

$$L_{15} = \frac{-A_{1,11}(\,)_{,\theta\theta}}{R^2}, \qquad L_{1,5+j'} = \frac{-A_{1,13}^{j'}(\,)_{,\theta\theta\theta}}{R^3} + \frac{(\hat{A}_{12}^{j'} - \beta_1^{j'})(\,)_{,\theta}}{R}, \qquad L_{22} = \frac{-A_{33}(\,)_{,\theta\theta}}{R^2},$$

$$L_{23} = \frac{A_{35}(\,)_{,\theta\theta\theta}}{R^3} - \frac{\hat{A}_{31}(\,)_{,\theta}}{R}, \qquad L_{24} = \frac{-A_{39}(\,)_{,\theta\theta}}{R^2}, \qquad L_{25} = \frac{-A_{3,11}(\,)_{,\theta\theta}}{R^2},$$

$$L_{2,5+j'} = \frac{-A_{3,13}^{j'}(\,)_{,\theta\theta\theta}}{R^3} + \frac{(\hat{A}_{32}^{j'} - \beta_3^{j'})(\,)_{,\theta}}{R}, \qquad L_{33} = -\hat{A}_{11}^* - \frac{A_{55}(\,)_{,\theta\theta\theta\theta}}{R^4} + \frac{(\bar{A}_{11} + 2\hat{A}_{51})(\,)_{,\theta\theta}}{R^2},$$

$$L_{34} = \frac{A_{59}(\,)_{,\theta\theta\theta}}{R^3} + \frac{(\bar{A}_{13} - \hat{A}_{91})(\,)_{,\theta}}{R}, \qquad L_{35} = \frac{A_{5,11}(\,)_{,\theta\theta\theta}}{R^3} + \frac{(\bar{A}_{14} - \hat{A}_{11,1})(\,)_{,\theta}}{R},$$

$$L_{3,5+j'} = \frac{(\beta_5^{j'} - \hat{A}_{52}^{j'} - \hat{A}_{13,1}^{j'} + \bar{A}_{15}^{j'} + \bar{\beta}_{11}^{j'})(\,)_{,\theta\theta}}{R^2} + \frac{A_{5,13}^{j'}(\,)_{,\theta\theta\theta\theta}}{R^4} + \hat{A}_{12}^{*j'} - \hat{\beta}_1^{j'}, \quad L_{44} = \bar{A}_{33} - \frac{A_{99}(\,)_{,\theta\theta}}{R^2},$$

$$L_{45} = \bar{A}_{34} - \frac{A_{9,11}(\,)_{,\theta\theta}}{R^2}, \qquad L_{4,5+j'} = \frac{-A_{9,13}^{j'}(\,)_{,\theta\theta\theta}}{R^3} + \frac{(\bar{A}_{35}^{j'} + \bar{\beta}_{31}^{j'} - \beta_9^{j'} + \hat{A}_{92}^{j'})(\,)_{,\theta}}{R},$$

$$L_{55} = \bar{A}_{44} - \frac{A_{11,11}(\,)_{,\theta\theta}}{R^2}, \qquad L_{5,5+j'} = \frac{-A_{11,13}^{j'}(\,)_{,\theta\theta\theta}}{R^3} + \frac{(\bar{A}_{45}^{j'} + \bar{\beta}_{41}^{j'} - \beta_{11}^{j'} + \hat{A}_{11,2}^{j'})(\,)_{,\theta}}{R},$$

$$L_{5+j,5+j'} = \frac{(\bar{A}_{55}^{jj'} - \beta_{13}^{jj'} - \beta_{13}^{j'j} + \bar{\beta}_{51}^{jj'} + \bar{\beta}_{51}^{j'j} - \bar{E}_{11}^{jj'} + \hat{A}_{13,2}^{jj'} + \hat{A}_{13,2}^{j'j})(\,)_{,\theta\theta}}{R^2} - \frac{A_{13,13}^{jj'}(\,)_{,\theta\theta\theta\theta}}{R^4}$$
$$+ E^{jj'} - \hat{A}_{22}^{*jj'} + \hat{\beta}_2^{jj'} + \hat{\beta}_2^{j'j},$$

for $(j, j') = 1, \ldots n_\phi$. The elements of the load vector $\bar{P}$ are

$$P_1 = \frac{A_{11}^l T_{,\theta\theta\theta}^l}{R^3} + \frac{(\tilde{A}_1^l - \gamma_1^l)T_{,\theta}^l}{R}, \qquad P_2 = \frac{A_{31}^l T_{,\theta\theta\theta}^l}{R^3} + \frac{(\tilde{A}_3^l - \gamma_3^l)T_{,\theta}^l}{R},$$

$$P_3 = \frac{(\gamma_5^l - \tilde{A}_5^l + \hat{A}_{11}^l - \bar{A}_{11}^l)T_{,\theta\theta}^l}{R^2} - F_3 - \frac{A_{51}^l T_{,\theta\theta\theta\theta}^l}{R^4} + (A_1^{*l} - \hat{\gamma}_1^l)T^l,$$

$$P_4 = \frac{A_{91}^l T_{,\theta\theta\theta}^l}{R^3} - \frac{(\gamma_9^l - \tilde{A}_9^l + \bar{A}_{31}^l)T_{,\theta}^l}{R}, \qquad P_5 = \frac{A_{11,1}^l T_{,\theta\theta\theta}^l}{R^3} - \frac{(\gamma_{11}^l - \tilde{A}_{11}^l + \bar{A}_{41}^l)T_{,\theta}^l}{R},$$

$$P_6^j = -F_6^j - \frac{(\bar{A}_{51}^{jl} + \bar{\beta}_{11}^{jl} - \beta_1^{jl} + \gamma_{13}^{jl} - \tilde{A}_{13}^{jl})T_{,\theta\theta}^l}{R^2} + (\gamma^{jl} + \tilde{\gamma}^{jl})T^l + \frac{A_{13,1}^{jl} T_{,\theta\theta\theta\theta}^l}{R^4} + (\hat{\gamma}_2^{jl} - A_2^{*jl})T^l - \frac{\hat{A}_{21}^{jl} T_{,\theta\theta}^l}{R^2}.$$

To assess the accuracy of the theories developed herein, a Fourier series solution is obtained for simply supported angle-ply shell panels of span angle $\alpha$ for the following boundary conditions at $\theta = 0, \alpha$:

$$N_\theta + \frac{M_\theta}{R} = 0, \quad N_{\theta x} = 0, \quad w_0 = 0, \quad M_\theta = 0, \quad P_\theta = 0, \quad P_{\theta x} = 0, \quad \phi^j = 0, \quad S_\theta^j = 0, \quad (55)$$

for $j = 1, \ldots, n_\phi$. The load parameters and the solution are expanded in Fourier series, satisfying the boundary conditions, as:

$$(u_{0_\theta}, u_{0_x}, \psi_{0_\theta}, \psi_{0_x}, Q_x, Q_\theta, \bar{Q}_\theta^j, H_\theta^j) = \sum_{m=1}^{\infty} (u_{0_\theta}, u_{0_x}, \psi_{0_\theta}, \psi_{0_x}, Q_x, Q_\theta, \bar{Q}_\theta^j, H_\theta^j)_m \cos(\bar{m}\theta),$$

$$(w_0, \phi^j, N_\theta, M_\theta, N_{\theta x}, P_\theta, P_{\theta x}, S_\theta^j, G^j, \hat{S}_\theta^j) = \sum_{m=1}^{\infty} (w_0, \phi^j, N_\theta, M_\theta, N_{\theta x}, P_\theta, P_{\theta x}, S_\theta^j, G^j, \hat{S}_\theta^j)_m \sin(\bar{m}\theta),$$

$$(p_i, \phi_i, D_i, T_i, \Phi_i, q_i) = \sum_{m=1}^{\infty} (p_i, \phi_i, D_i, T_i, \Phi_i, q_i)_m \sin(\bar{m}\theta),$$

with $\bar{m} = \dfrac{m\pi}{\alpha}$. Substituting these in (53) yields for the $m$-th Fourier component

$$K\bar{U}^m = \bar{P}^m. \tag{56}$$

$\bar{U}$ is partitioned into a set of five mechanical displacement variables $U$, a set of unknown output voltages $\Phi_s$ at $z_\phi^j$ where $\phi$ is not prescribed, and a set of known input actuation voltages $\Phi_a$ at the actuated surfaces. $\bar{P}$ is also partitioned accordingly. Equation (56) is then solved for the unknown variables $U$ and $\Phi_s$. The transverse shear stresses $\tau$ and normal stress $\sigma_z$ are obtained by integrating the 3D equations of equilibrium.

## 6. Assessment of the theories

The IZIGT and ITOT developed herein are assessed for accuracy by comparison with the exact 3D piezothermoelasticity solution by Dumir et al. [1997] for simply supported hybrid angle-ply cylindrical shell panels in cylindrical bending. The exact 3D results for various laminate configurations have been generated using the computer program developed by the same authors for their numerical study.

Three laminate configurations (a), (b), and (c) as shown in Figure 2 are considered for the assessment. The orientation of the principal material direction is mentioned with respect to $\theta$-axis. Laminate (a), which has been devised as a benchmark test case, has an elastic substrate of five plies of materials 1/2/3/1/3 having highly inhomogeneous properties for tensile and shear stiffnesses, coefficients of thermal expansion, as well as thermal conductivities. A piezoelectric layer of PZT-5A is bonded to the top (outer) surface of the substrate. Laminate (b) has a four-ply graphite-epoxy composite substrate of material 4 and
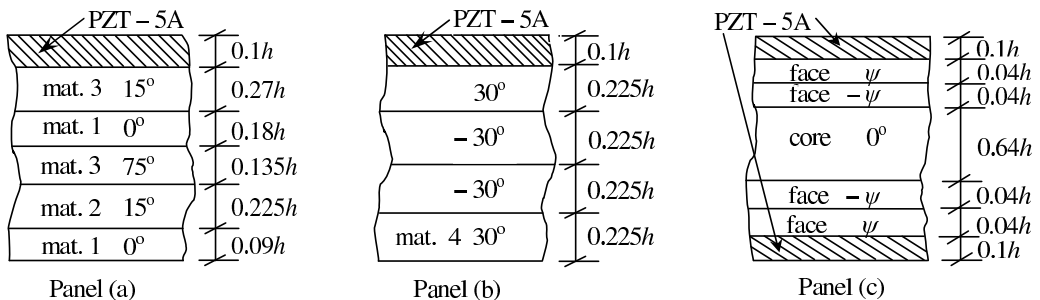


**Figure 2.** Configurations of hybrid cylindrical panels.

a PZT-5A layer bonded to its top surface. Laminate (c) has a sandwich substrate with two-ply composite faces and a soft core, and two layers of PZT-5A bonded to its top and bottom surfaces. The span angle is taken as 120° and the fibre orientation angle for the sandwich panel (c) is taken as 30° unless otherwise mentioned. The interfaces between the substrates and the piezoelectric layers are grounded. The outer surfaces of all the panels are in a close circuit condition with the prescribed electric potentials, while the inner surface of panel (c) is in an open circuit condition with the prescribed charge density and unknown electric potential.

Material constants and thermal conductivities, along with properties of PZT-5A, are given in Table 1. The following mechanical, potential, and thermal load cases are considered:

(1) Pressure load $p_z^2 = -p_0 \sin(\pi\theta/\alpha)$ applied on the top surface.

(2) Potential load $\phi^{n\phi} = \phi_0 \sin(\pi\theta/\alpha)$ applied on the top surface.

(3) Thermal load $T(\theta, -h/2) = T_0 \sin(\pi\theta/\alpha)$, $T(\theta, h/2) = 0$.

The results for the three load cases are nondimensionalised as shown in Table 2.

The 3D thermal problem is solved as in [Dumir et al. 1997], by analytically solving the heat conduction equation for all layers and satisfying the thermal boundary conditions and the continuity conditions at layer interfaces for temperature and heat flow. The distributions of temperature across the thickness for load case 3 is shown in Figure 3. It has been found from convergence studies that converged results

| | $Y_1$ | $Y_2$ | $Y_3$ | $G_{23}$ | $G_{13}$ | $G_{12}$ |
|---|---|---|---|---|---|---|
| Material 1 | 6.9 | 6.9 | 6.9 | 2.76 | 2.76 | 2.76 |
| Material 2 | 224.25 | 6.9 | 6.9 | 1.38 | 56.58 | 56.58 |
| Material 3 | 172.5 | 6.9 | 6.9 | 1.38 | 3.45 | 3.45 |
| Material 4 | 181.0 | 10.3 | 10.3 | 2.87 | 7.17 | 7.17 |
| Face | 131.1 | 6.9 | 6.9 | 2.3322 | 3.588 | 3.588 |
| Core | $2.208\times10^{-4}$ | $2.001\times10^{-4}$ | 2.76 | 0.4554 | 0.5451 | 0.01656 |
| PZT-5A | 61.0 | 61.0 | 53.2 | 21.1 | 21.1 | 22.6 |

| | $\nu_{12}$ | $\nu_{13}$ | $\nu_{23}$ | $\alpha_1$ | $\alpha_2$ | $\alpha_3$ | $k_1$ | $k_2$ | $k_3$ |
|---|---|---|---|---|---|---|---|---|---|
| Material 1 | 0.25 | 0.25 | 0.25 | 35.6 | 35.6 | 35.6 | 0.12 | 0.12 | 0.12 |
| Material 2 | 0.25 | 0.25 | 0.25 | 0.25 | 35.6 | 35.6 | 7.2 | 1.44 | 1.44 |
| Material 3 | 0.25 | 0.25 | 0.25 | 0.57 | 35.6 | 35.6 | 1.92 | 0.96 | 0.96 |
| Material 4 | 0.28 | 0.28 | 0.33 | 0.02 | 22.5 | 22.5 | 1.5 | 0.5 | 0.5 |
| Face | 0.32 | 0.32 | 0.49 | 0.0225 | 22.5 | 22.5 | 1.5 | 0.5 | 0.5 |
| Core | 0.99 | $3\times10^{-5}$ | $3\times10^{-5}$ | 30.6 | 30.6 | 30.6 | 3.0 | 3.0 | 3.0 |
| PZT-5A | 0.35 | 0.38 | 0.38 | 1.5 | 1.5 | 2.0 | 1.8 | 1.8 | 1.8 |

| | $d_{31}$ | $d_{32}$ | $d_{33}$ | $d_{24}$ | $d_{15}$ | $\eta_{11}$ | $\eta_{22}$ | $\eta_{33}$ | $p_3$ |
|---|---|---|---|---|---|---|---|---|---|
| PZT-5A | $-171$ | $-171$ | 374 | 584 | 584 | 15.3 | 15.3 | 15.0 | 0.0007 |

**Table 1.** Material constants $Y_1$, $Y_2$, $Y_3$, $G_{23}$, $G_{13}$, $G_{12}$ (GPa); $\nu_{12}$, $\nu_{13}$, $\nu_{23}$; $\alpha_1$, $\alpha_2$, $\alpha_3$ ($10^{-6}\,\text{K}^{-1}$); and thermal conductivities $k_1$, $k_2$, $k_3$ (W/m K). Other properties of PZT-5A $d_{31}$, $d_{32}$, $d_{33}$, $d_{24}$, $d_{15}$ (pm/V); $\eta_{11}$, $\eta_{22}$, $\eta_{33}$ (nF/m); and $p_3$ (C/m$^2$K).

Pressure load case:     $(\bar{u}_\theta, \bar{w}) = (u_\theta, w)\dfrac{Y_0}{hS^4 p_0},$     $\bar{D}_z = \dfrac{D_z}{10S^2 p_0 d_0},$

$$(\bar{\sigma}_\theta, \bar{\sigma}_x, \bar{\sigma}_z, \bar{\tau}_{\theta x}, \bar{\tau}_{xz}, \bar{\tau}_{\theta z}) = \left(\dfrac{\sigma_\theta}{S}, \dfrac{\sigma_x}{S}, \sigma_z, \dfrac{\tau_{\theta x}}{S}, \tau_{xz}, \tau_{\theta z}\right)\dfrac{1}{10Sp_0}.$$

Potential load case:     $(\bar{u}_\theta, \bar{w}) = \dfrac{(u_\theta, w)}{10S^2 \phi_0 d_0},$     $\bar{D}_z = \dfrac{D_z h}{1000\phi_0 d_0^2 Y_0},$

$$(\bar{\sigma}_\theta, \bar{\sigma}_x, \bar{\sigma}_z, \bar{\tau}_{\theta x}, \bar{\tau}_{xz}, \bar{\tau}_{\theta z}) = (\sigma_\theta, \sigma_x, \sigma_z S, \tau_{\theta x}, \tau_{xz}S, \tau_{\theta z}S)\dfrac{h}{10\phi_0 d_0 Y_0}.$$

Thermal load case: $(\bar{u}_\theta, \bar{w}) = \dfrac{10(u_\theta, w)}{hS^2 \alpha_0 T_0},$     $\bar{D}_z = \dfrac{D_z}{\alpha_0 T_0 Y_0 d_0},$     $\bar{\phi} = \dfrac{1000\phi d_0}{\alpha_0 T_0 h},$

$$(\bar{\sigma}_\theta, \bar{\sigma}_x, \bar{\sigma}_z, \bar{\tau}_{\theta x}, \bar{\tau}_{xz}, \bar{\tau}_{\theta z}) = (10\sigma_\theta, \sigma_x, 100\sigma_z S, \tau_{\theta x}, S\tau_{xz}, S\tau_{\theta z})\dfrac{1}{\alpha_0 T_0 Y_0}.$$

**Table 2.** Nondimensional magnitudes in the loading cases considered. Parameters in the formulas: $S = R/h$, $Y_0 = 6.9$ GPa for panels (a) and (c), $Y_0 = 10.3$ GPa for panel (b); $\alpha_0 = 35.6 \times 10^{-6}$ K$^{-1}$ for panel (a), $\alpha_0 = 22.5 \times 10^{-6}$ K$^{-1}$ for panels (b) and (c); and $d_0 = 374 \times 10^{-12}$ pm/V for all panels.

are obtained by approximating the exact temperature distributions across the thickness by the present sublayerwise linear distribution with 8 equal sublayers in the core of sandwich panel and 4 equal sublayers for all other laminas. For the distribution of electric potential, converged results are obtained by dividing each piezoelectric layer into 4 equal sublayers.

The exact 3D results and the percent errors in the results of the present 2D theories IZIGT and ITOT for displacements, predominant inplane normal stresses $\sigma^e$ in the elastic substrate and $\sigma^p$ in the piezoelectric layer, shear stresses, $D_z$ and $\phi$ at typical points across the thickness, where they are large, are given in Tables 3–5 for panels (a), (b), and (c) for the pressure and potential load cases. The $z$-locations of the entities are mentioned within brackets. In order to investigate the influence of the thermoelectric
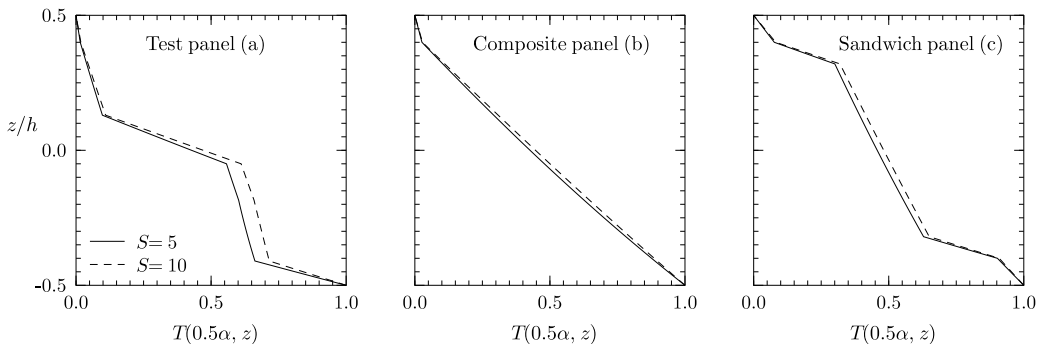


**Figure 3.** Temperature distributions in hybrid angle-ply cylindrical panels (a), (b), and (c).

| | | Load case 1 | | | Load case 2 | | | | | |
|---|---|---|---|---|---|---|---|---|---|---|
| $S$ | Entity | Exact | IZIGT | ITOT | Entity | Exact | IZIGT | ZIGT | ITOT | TOT |
| 5 | $\bar{u}_\theta$ | –0.57137 | –4.56 | –23.8 | $\bar{u}_\theta$ | 0.13464 | –2.60 | –3.76 | –5.63 | –7.53 |
| 10 | $(-0.5h)$ | –0.40342 | –1.62 | –8.07 | $(-0.5h)$ | 0.12403 | –0.69 | –1.39 | –1.55 | –2.46 |
| 20 | | –0.35424 | –0.49 | –2.27 | | 0.12020 | –0.16 | –0.54 | –0.39 | –0.83 |
| 5 | $\bar{w}$ | –0.77787 | –4.57 | –24.7 | $\bar{w}$ | 0.18944 | –2.58 | –3.71 | –5.66 | –7.55 |
| 10 | $(0)$ | –0.57234 | –1.66 | –8.30 | $(0)$ | 0.18020 | –0.69 | –1.39 | –1.56 | –2.47 |
| 20 | | –0.51595 | –0.51 | –2.31 | | 0.17744 | –0.16 | –0.54 | –0.39 | –0.83 |
| 5 | $\bar{\sigma}_\theta^e$ | 0.98562 | –0.10 | –8.05 | $\bar{\sigma}_\theta^e$ | 2.9186 | –3.63 | –4.40 | –4.02 | –5.22 |
| 10 | $(-0.41h^+)$ | 0.84048 | 0.10 | –2.00 | $(0.4h^-)$ | 2.8458 | –0.82 | –1.41 | –0.93 | –1.64 |
| 20 | | 0.78939 | 0.10 | –0.43 | | 2.8290 | –0.12 | –0.47 | –0.15 | –0.53 |
| 5 | $\bar{\sigma}_\theta^p$ | –0.35624 | –3.83 | –9.47 | $\bar{\sigma}_x^p$ | –5.7276 | 1.29 | 1.07 | 1.35 | 1.17 |
| 10 | $(0.5h)$ | –0.33133 | –1.23 | –2.85 | $(0.4h^+)$ | –5.7419 | 0.56 | 0.47 | 0.58 | 0.49 |
| 20 | | –0.32473 | –0.45 | –0.87 | | –5.7440 | 0.24 | 0.20 | 0.25 | 0.20 |
| 5 | $\bar{\tau}_{\theta x}$ | –0.14333 | –3.48 | –3.23 | $\bar{\tau}_{\theta x}$ | 0.69887 | –3.15 | –3.86 | –3.27 | –4.44 |
| 10 | $(0.4h^-)$ | –0.13794 | –1.14 | –1.10 | $(0.4h^-)$ | 0.68701 | –0.48 | –1.06 | –0.51 | –1.21 |
| 20 | | –0.13588 | –0.40 | –0.39 | | 0.68492 | 0.07 | –0.28 | 0.07 | –0.32 |
| 5 | $\bar{\tau}_{\theta z}$ | –0.20590 | 0.72 | 2.35 | $\bar{\tau}_{\theta z}$ | 0.20268 | 4.78 | 2.50 | 5.40 | 3.42 |
| 10 | $(-0.05h)$ | –0.19841 | 0.26 | 0.65 | $(-0.21h)$ | 0.20421 | 1.67 | 0.66 | 1.84 | 0.91 |
| 20 | | –0.19363 | 0.10 | 0.20 | | 0.20360 | 0.65 | 0.17 | 0.69 | 0.24 |
| 5 | $\bar{D}_z$ | 0.18698 | –0.64 | –4.18 | $\bar{D}_z$ | –0.19026 | –0.66 | 0.18 | –0.74 | 0.08 |
| 10 | $(0.5h)$ | 0.17955 | 0.42 | –0.57 | $(0.5h)$ | –0.19101 | –0.27 | 0.15 | –0.29 | 0.13 |
| 20 | | 0.17727 | 0.74 | 0.48 | | –0.19154 | –0.11 | 0.10 | –0.11 | 0.09 |

**Table 3.** Exact 3D results and percent errors of 2D theories for hybrid test panel (a) under load cases 1 and 2.

transverse normal strain, the results for the potential load case and the thermal load case (presented later) are also compared with the particular cases of the present theories wherein $w$ is considered uniform across the thickness. The latter theories are referred to herein as the ZIGT and TOT. It is observed from these tables that the IZIGT yields accurate results for all response entities for both pressure and electric potential load cases even for thick hybrid panels with $S = 5$, having highly inhomogeneous lay-up. The ITOT with the same number of unknowns yields far inferior results with large error in the deflection and predominant inplane stress for the inhomogeneous test case and the sandwich panel under pressure loading. For the potential load case, the ITOT is quite accurate although inferior to IZIGT. For this load case, the IZIGT and ITOT are in general superior to their respective counterparts the ZIGT and TOT with uniform deflection approximation. The improvement is not restricted to $w$ only, but holds well also for $u_\theta$, $\sigma_\theta$, and $\tau_{\theta x}$. Similar results for the thermal load case are presented in Tables 6 and 7 for hybrid cylindrical panels (a), (b), and (c). It is revealed from these results that inclusion of layerwise terms in the approximation of inplane displacements has far less effect on the results than the incorporation of the

| | | Load case 1 | | | Load case 2 | | | | | |
|---|---|---|---|---|---|---|---|---|---|---|
| $S$ | Entity | Exact | IZIGT | ITOT | Entity | Exact | IZIGT | ZIGT | ITOT | TOT |
| 5 | $\bar{u}_\theta$ | −0.79418 | −2.81 | −4.62 | $\bar{u}_\theta$ | 0.14747 | −0.91 | −2.14 | −1.80 | −3.07 |
| 10 | $(-0.5h)$ | −0.62329 | −0.86 | −1.41 | $(-0.5h)$ | 0.13644 | −0.07 | −0.78 | −0.31 | −1.05 |
| 20 | | −0.56802 | −0.24 | −0.39 | | 0.13229 | 0.08 | −0.30 | 0.02 | −0.37 |
| 5 | $\bar{w}$ | −1.0772 | −2.98 | −4.81 | $\bar{w}$ | 0.20551 | −1.15 | −2.30 | −2.08 | −3.31 |
| 10 | $(0)$ | −0.88373 | −0.92 | −1.47 | $(0)$ | 0.19697 | −0.10 | −0.81 | −0.36 | −1.08 |
| 20 | | −0.82736 | −0.26 | −0.40 | | 0.19462 | 0.07 | −0.31 | 0.01 | −0.38 |
| 5 | $\bar{\sigma}_\theta^e$ | 0.62386 | 0.08 | −0.63 | $\bar{\sigma}_\theta^e$ | 1.5160 | −1.75 | −2.76 | −2.14 | −3.42 |
| 10 | $(-0.5h)$ | 0.56103 | 0.06 | −0.12 | $(0.4h^-)$ | 1.5042 | −0.31 | −0.97 | −0.41 | −1.14 |
| 20 | | 0.53462 | 0.03 | −0.01 | | 1.5028 | 0.00 | −0.37 | −0.03 | −0.42 |
| 5 | $\bar{\sigma}_\theta^p$ | −0.37858 | −2.22 | −2.84 | $\bar{\sigma}_x^p$ | −3.8409 | 1.15 | 2.62 | 1.35 | 1.16 |
| 10 | $(0.5h)$ | −0.35979 | −0.57 | −0.75 | $(0.4h^+)$ | −3.8496 | 0.51 | 0.41 | 0.57 | 0.47 |
| 20 | | −0.35532 | −0.20 | −0.24 | | −3.8504 | 0.22 | 0.17 | 0.23 | 0.19 |
| 5 | $\bar{\tau}_{\theta x}$ | 0.30147 | 0.15 | −0.19 | $\bar{\tau}_{\theta x}$ | 0.73238 | −0.35 | −1.41 | 0.05 | −1.29 |
| 10 | $(-0.5h)$ | 0.27576 | 0.10 | 0.02 | $(0.4h^-)$ | 0.73872 | 0.38 | −0.29 | 0.49 | −0.26 |
| 20 | | 0.26415 | 0.06 | 0.03 | | 0.74212 | 0.34 | −0.04 | 0.36 | −0.03 |
| 5 | $\bar{\tau}_{\theta z}$ | −0.20207 | 0.26 | 0.11 | $\bar{\tau}_{\theta z}$ | −0.43799 | 1.75 | 0.04 | 2.66 | 0.99 |
| 10 | $(0)$ | −0.19365 | 0.05 | 0.01 | $(0.4h)$ | −0.45551 | 0.65 | −0.18 | 0.90 | 0.08 |
| 20 | | −0.18926 | 0.00 | 0.00 | | −0.46292 | 0.27 | −0.14 | 0.33 | −0.08 |
| 5 | $\bar{D}_z$ | 0.20302 | 0.66 | 0.33 | $\bar{D}_z$ | −0.12744 | −0.57 | 0.26 | −0.71 | 0.11 |
| 10 | $(0.5h)$ | 0.19631 | 0.97 | 0.87 | $(0.5h)$ | −0.12797 | −0.24 | 0.18 | −0.28 | 0.14 |
| 20 | | 0.19445 | 0.95 | 0.93 | | −0.12834 | −0.10 | 0.12 | −0.11 | 0.11 |

**Table 4.** Exact 3D results and percent errors of 2D theories for hybrid composite panel (b) under load cases 1 and 2.

layerwise terms in the transverse displacement. While the difference between the IZIGT and ITOT or between the ZIGT and TOT is not significant, the IZIGT and ITOT exhibit very significant improvement over their respective conventional counterparts the ZIGT and TOT, respectively. For the given load case, the reduction in error in the improved theories is over 70% for the deflection $\bar{w}$ and predominant inplane stress $\bar{\sigma}_\theta$. For the hybrid test and composite panels (a) and (b), the improved theories predict the deflection $\bar{w}$ with significant error (9–10%) even for thin panels with $S = 20$.

The through-the-thickness distributions of $\bar{u}_\theta$, $\bar{w}$, $\bar{\sigma}_\theta$, and $\bar{\tau}_{\theta z}$ predicted by the present 2D theories, the IZIGT and ITOT, are compared with the exact 3D solutions in Figures 4–8 for panels (a), (b), and (c). It is observed that even though the ITOT yields erroneous distributions for $\bar{u}_\theta$ and $\bar{w}$ for thick panels with $S = 5$, the distributions for $\bar{\sigma}_\theta$ and $\bar{\tau}_{\theta z}$ predicted by it are accurate for both load cases except for some error in the distributions in stiffer layers for $\bar{\sigma}_\theta$ for hybrid test panel (a) and sandwich panel (c) under pressure load. The IZIGT predicts more accurate distributions of these entities in all cases.

| | | Load case 1 | | | Load case 2 | | | | | |
|---|---|---|---|---|---|---|---|---|---|---|
| $S$ | Entity | Exact | IZIGT | ITOT | Entity | Exact | IZIGT | ZIGT | ITOT | TOT |
| 5 | $\bar{u}_\theta$ | −1.3080 | −3.17 | −19.9 | $\bar{u}_\theta$ | 0.24821 | −0.05 | −1.58 | −3.84 | −4.94 |
| 10 | $(-0.5h)$ | −0.82100 | −1.22 | −7.61 | $(-0.5h)$ | 0.23618 | 0.08 | −0.73 | −0.94 | −1.64 |
| 20 | | −0.68738 | −0.36 | −2.22 | | 0.23187 | 0.07 | −0.34 | −0.19 | −0.58 |
| 5 | $\bar{w}$ | −1.8181 | −3.08 | −20.6 | $\bar{w}$ | 0.36134 | −0.02 | −1.55 | −3.85 | −4.94 |
| 10 | $(0)$ | −1.1709 | −1.25 | −7.87 | $(0)$ | 0.34907 | 0.08 | −0.73 | −0.94 | −1.64 |
| 20 | | −1.0024 | −0.37 | −2.27 | | 0.34524 | 0.07 | −0.34 | −0.19 | −0.57 |
| 5 | $\bar{\sigma}_\theta^e$ | −0.54675 | −0.02 | 1.63 | $\bar{\sigma}_\theta^e$ | 3.8462 | 0.27 | −1.23 | 0.60 | −0.93 |
| 10 | $(0.4h^-)$ | −0.55914 | −0.06 | 0.34 | $(0.4h^-)$ | 3.8267 | 0.16 | −0.63 | 0.26 | −0.54 |
| 20 | | −0.56060 | −0.04 | 0.06 | | 3.8146 | 0.09 | −0.31 | 0.12 | −0.29 |
| 5 | $\bar{\sigma}_\theta^p$ | 0.93850 | −1.97 | −8.23 | $\bar{\sigma}_x^p$ | −5.0918 | 0.53 | 0.66 | 0.47 | 0.61 |
| 10 | $(-0.5h)$ | 0.77239 | −0.93 | −2.62 | $(0.4h^+)$ | −5.0862 | 0.22 | 0.29 | 0.20 | 0.28 |
| 20 | | 0.71722 | −0.60 | −1.03 | | −5.0832 | 0.06 | 0.10 | 0.06 | 0.09 |
| 5 | $\bar{\tau}_{\theta x}$ | −0.28170 | −0.66 | 1.01 | $\bar{\tau}_{\theta x}$ | 1.9572 | 0.94 | −0.58 | 1.34 | −0.21 |
| 10 | $(0.4h^-)$ | −0.28768 | −0.47 | −0.07 | $(0.4h^-)$ | 1.9543 | 0.50 | −0.29 | 0.62 | −0.18 |
| 20 | | −0.28794 | −0.27 | −0.17 | | 1.9515 | 0.26 | −0.14 | 0.29 | −0.11 |
| 5 | $\bar{\tau}_{\theta z}$ | −0.17733 | 0.12 | 0.84 | $\bar{\tau}_{\theta z}$ | −0.37320 | 0.67 | −0.84 | 0.98 | −0.57 |
| 10 | $(-0.32h)$ | −0.16068 | 0.04 | 0.21 | $(0.4h)$ | −0.38334 | 0.28 | −0.50 | 0.36 | −0.42 |
| 20 | | −0.15238 | 0.01 | 0.06 | | −0.38824 | 0.12 | −0.27 | 0.14 | −0.25 |
| 5 | $\bar{D}_z$ | 0.35811 | 1.94 | −1.43 | $\bar{D}_z$ | −0.20263 | −0.31 | 0.27 | −0.34 | 0.24 |
| 10 | $(0.5h)$ | 0.34826 | 1.17 | 0.26 | $(0.5h)$ | −0.20368 | −0.13 | 0.17 | −0.14 | 0.16 |
| 20 | | 0.34504 | 0.95 | 0.71 | | −0.20426 | −0.03 | 0.12 | −0.04 | 0.11 |
| 5 | $\bar{\phi}$ | 21.149 | 0.41 | −3.70 | $\bar{\phi}$ | −0.010942 | 1.29 | 0.68 | 0.07 | −1.08 |
| 10 | $(-0.5h)$ | 18.686 | 0.31 | −0.75 | $(-0.5h)$ | −0.010343 | 0.62 | 0.23 | 0.30 | −0.22 |
| 20 | | 17.727 | 0.18 | −0.08 | | −0.010086 | 0.32 | 0.10 | 0.23 | −0.02 |

**Table 5.** Exact 3D results and percent errors of 2D theories for hybrid sandwich panel (c) under load cases 1 and 2.
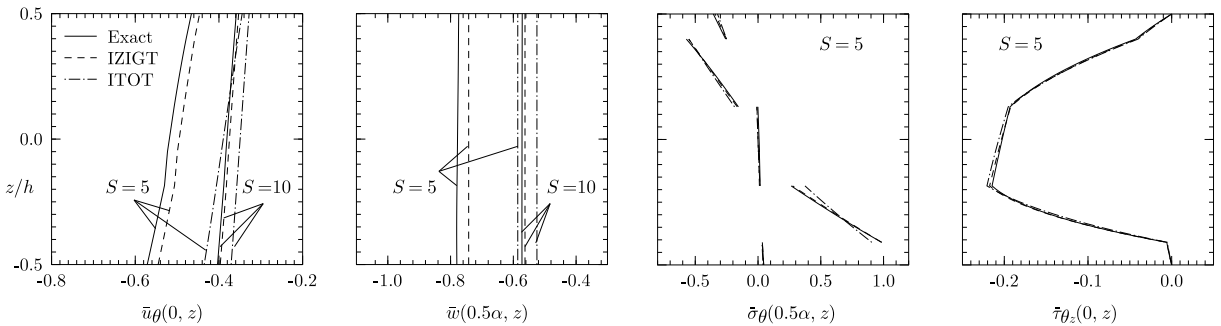


**Figure 4.** Through-the-thickness distributions of $\bar{u}_\theta$, $\bar{w}$, $\bar{\sigma}_\theta$, and $\bar{\tau}_{\theta z}$ for hybrid test panel (a) under load case 1.
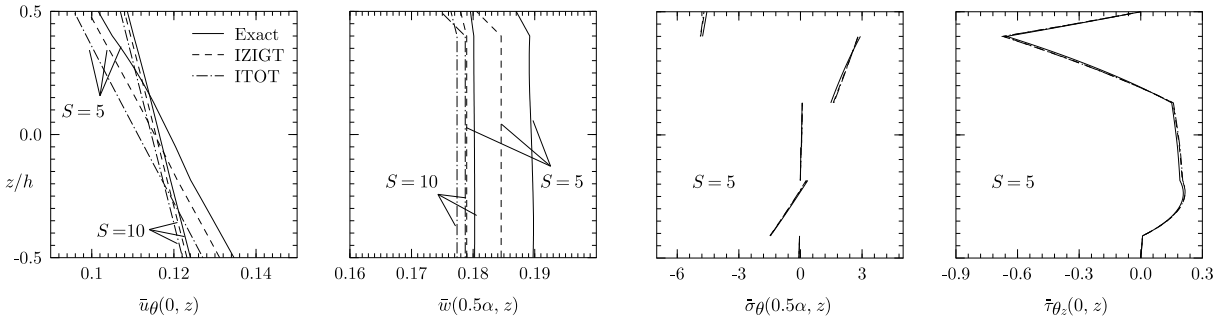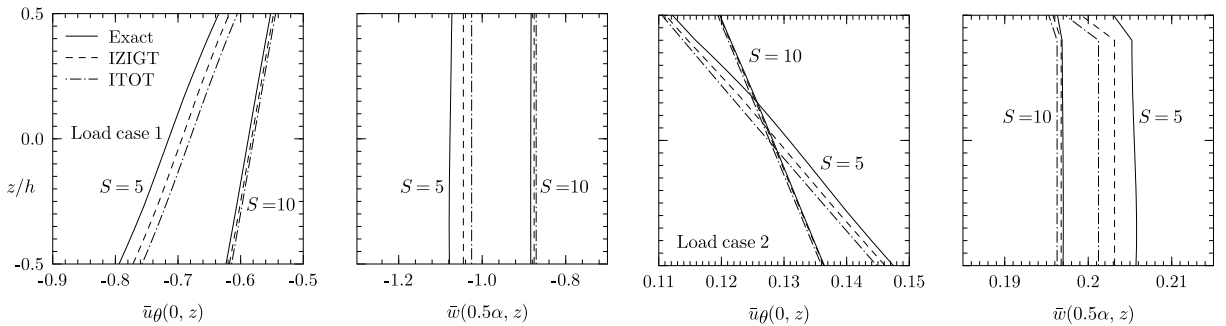
**Figure 5.** Through-the-thickness distributions of $\bar{u}_\theta$, $\bar{w}$, $\bar{\sigma}_\theta$, and $\bar{\tau}_{\theta z}$ for hybrid test panel (a) under load case 2.



**Figure 6.** Through-the-thickness distributions of $\bar{u}_\theta$ and $\bar{w}$ for hybrid composite panel (b) under load cases 1 and 2.
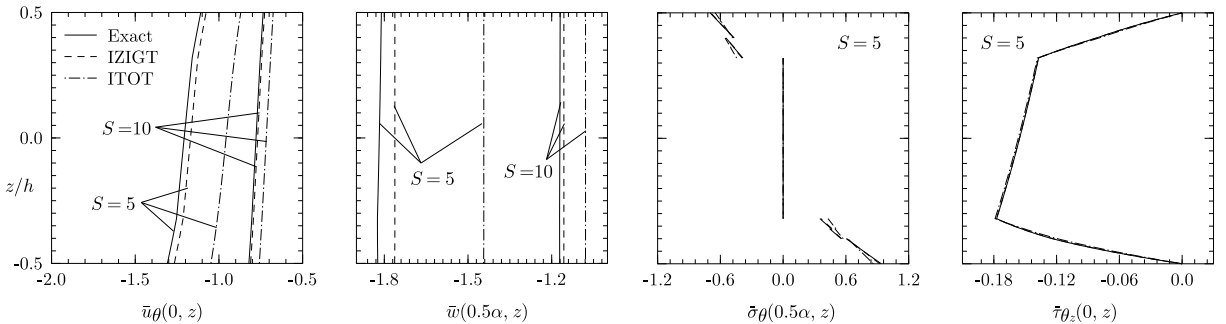


**Figure 7.** Through-the-thickness distributions of $\bar{u}_\theta$, $\bar{w}$, $\bar{\sigma}_\theta$, and $\bar{\tau}_{\theta z}$ for hybrid sandwich panel (c) under load case 1.

It is seen in Tables 6 and 7 that results of the IZIGT and ITOT do not show any significant difference for load case 3. To investigate the effect of inclusion of transverse normal strain, the through-the-thickness distributions of $\bar{u}_\theta$, $\bar{w}$, $\bar{\sigma}_\theta$, and $\bar{\tau}_{\theta z}$ obtained from the IZIGT and ZIGT, are compared with the exact 3D solutions in Figures 9–11 for panels (a), (b), and (c). The distributions of $\bar{\sigma}_z$ across the thickness, obtained by postprocessing from the 3D equilibrium equations, are shown in Figure 12. It is revealed that the assumption of uniform deflection in the conventional ZIGT causes erroneous distributions not only for the deflection $\bar{w}$, but also for inplane displacements and stresses for hybrid test and composite
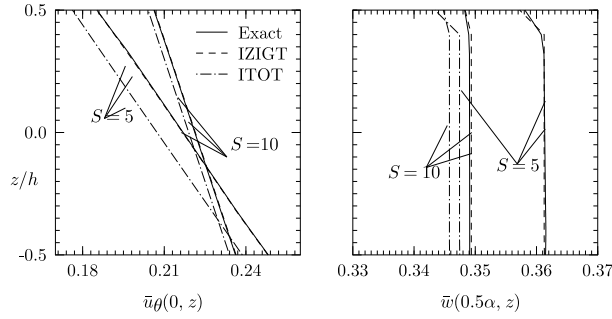
**Figure 8.** Through-the-thickness distributions of $\bar{u}_\theta$ and $\bar{w}$ for hybrid sandwich panel (c) under load case 2.

| | | | Panel (a) | | | | | | Panel (b) | | |
|---|---|---|---|---|---|---|---|---|---|---|---|
| $S$ | Entity | Exact | IZIGT | ZIGT | ITOT | TOT | Entity | Exact | IZIGT | ZIGT | ITOT | TOT |
| 5 | $\bar{u}_\theta$ | −0.97476 | −16.1 | −62.5 | −18.2 | −64.5 | $\bar{u}_\theta$ | −1.0501 | −17.1 | −69.4 | −17.6 | −69.9 |
| 10 | $(-0.5h)$ | −0.63749 | −12.3 | −48.2 | −13.2 | −48.9 | $(-0.5h)$ | −0.63504 | −13.5 | −55.4 | −13.7 | −55.6 |
| 20 | | −0.46207 | −8.33 | −32.7 | −8.65 | −33.0 | | −0.43876 | −9.53 | −39.2 | −9.60 | −39.2 |
| 40 | | −0.37548 | −5.06 | −19.9 | −5.16 | −20.0 | | −0.34405 | −6.00 | −24.7 | −6.02 | −24.7 |
| 5 | $\bar{w}$ | −1.3929 | −17.7 | −68.0 | −19.8 | −70.0 | $\bar{w}$ | −1.5229 | −18.0 | −73.8 | −18.5 | −74.3 |
| 10 | $(-0.5h)$ | −0.91058 | −13.3 | −51.7 | −14.2 | −52.5 | $(-0.5h)$ | −0.91930 | −14.2 | −58.4 | −14.4 | −58.6 |
| 20 | | −0.66701 | −8.80 | −34.4 | −9.13 | −34.7 | | −0.63899 | −9.90 | −40.8 | −9.98 | −40.8 |
| 40 | | −0.54930 | −5.23 | −20.5 | −5.33 | −20.6 | | −0.50578 | −6.15 | −25.3 | −6.17 | −25.3 |
| 5 | $\bar{\sigma}_\theta^e$ | −12.923 | −0.51 | −1.54 | −0.44 | −1.47 | $\bar{\sigma}_x^e$ | −0.73423 | −1.63 | −5.94 | −1.49 | −5.81 |
| 10 | $(-0.5h)$ | −12.821 | −0.31 | −0.91 | −0.29 | −0.89 | $(-0.5h)$ | −0.71242 | −0.86 | −3.34 | −0.83 | −3.31 |
| 20 | | −12.762 | −0.16 | −0.48 | −0.16 | −0.48 | | −0.70050 | −0.44 | −1.77 | −0.43 | −1.76 |
| 40 | | −12.732 | −0.09 | −0.25 | −0.09 | −0.25 | | −0.69431 | −0.22 | −0.91 | −0.22 | −0.91 |
| 5 | $\bar{\tau}_{\theta x}$ | −0.090954 | −2.90 | −6.43 | −1.59 | −5.21 | $\bar{\sigma}_\theta^p$ | −1.0225 | −14.0 | −59.4 | −14.2 | −60.3 |
| 10 | $(0.4h^+)$ | −0.10173 | −1.09 | −2.89 | −0.69 | −2.55 | $(0.4h^+)$ | −0.79055 | −14.4 | −48.7 | −14.6 | −49.1 |
| 20 | | −0.10588 | −0.45 | −1.39 | −0.35 | −1.29 | | −0.63965 | −13.1 | −35.8 | −13.2 | −35.9 |
| 40 | | −0.10755 | −0.20 | −0.68 | −0.18 | −0.66 | | −0.55613 | −11.7 | −25.1 | −11.7 | −25.2 |
| 5 | $\bar{\tau}_{\theta z}$ | −0.15346 | 2.99 | 7.68 | 3.29 | 8.03 | $\bar{\tau}_{\theta x}$ | 0.46301 | 4.45 | 15.4 | 4.07 | 15.0 |
| 10 | $(-0.185h)$ | −0.16911 | 1.40 | 4.00 | 1.47 | 4.08 | $(-0.5h)$ | 0.49989 | 2.03 | 7.72 | 1.95 | 7.63 |
| 20 | | −0.17489 | 0.66 | 2.02 | 0.68 | 2.04 | | 0.51953 | 0.97 | 3.85 | 0.95 | 3.83 |
| 40 | | −0.17717 | 0.32 | 1.01 | 0.33 | 1.02 | | 0.52962 | 0.47 | 1.92 | 0.47 | 1.92 |
| 5 | $\bar{D}_z$ | 0.096015 | −22.3 | −75.4 | −23.5 | −76.9 | $\bar{\tau}_{xz}$ | −0.15942 | 1.07 | 2.55 | 0.92 | 2.42 |
| 10 | $(0.5h)$ | 0.070628 | −21.0 | −64.7 | −21.5 | −65.3 | $(-0.275h)$ | −0.16049 | 0.43 | 1.34 | 0.39 | 1.31 |
| 20 | | 0.052848 | −19.2 | −50.7 | −19.4 | −50.9 | | −0.16052 | 0.19 | 0.69 | 0.18 | 0.68 |
| 40 | | 0.042949 | −17.7 | −37.6 | −17.7 | −37.7 | | −0.16042 | 0.09 | 0.35 | 0.09 | 0.35 |
| 5 | | | | | | | $\bar{D}_z$ | 0.17730 | −11.2 | −38.0 | −11.4 | −38.5 |
| 10 | | | | | | | $(0.5h)$ | 0.15998 | −10.2 | −27.6 | −10.3 | −27.7 |
| 20 | | | | | | | | 0.14759 | −9.0 | −19.1 | −9.1 | −19.2 |
| 40 | | | | | | | | 0.14048 | −8.2 | −13.7 | −8.2 | −13.7 |

**Table 6.** Exact 3D results and percent errors of 2D theories for hybrid panels (a) and (b) under load case 3.

|  |  | Panel (c) | | | | | Panel (c) | | | | |
| S | Entity | Exact | IZIGT | ZIGT | ITOT | TOT | Entity | Exact | IZIGT | ZIGT | ITOT | TOT |
|---|---|---|---|---|---|---|---|---|---|---|---|---|
| 5 | $\bar{u}_\theta$ | –2.8779 | –1.52 | –24.7 | –4.04 | –26.9 | $\bar{\tau}_{\theta x}$ | 1.7026 | 0.41 | 2.32 | 0.79 | 2.60 |
| 10 | $(-0.5h)$ | –2.2940 | –0.82 | –15.2 | –1.61 | –15.9 | $(-0.4h^+)$ | 1.7444 | 0.19 | 1.06 | 0.29 | 1.13 |
| 20 |  | –2.0141 | –0.43 | –8.50 | –0.66 | –8.68 |  | 1.7616 | 0.09 | 0.50 | 0.12 | 0.52 |
| 40 |  | –1.8781 | –0.23 | –4.51 | –0.29 | –4.56 |  | 1.7692 | 0.04 | 0.24 | 0.05 | 0.25 |
| 5 | $\bar{w}$ | –3.7519 | –1.98 | –27.7 | –4.78 | –30.2 | $\tau_{\theta z}$ | 0.26651 | 0.65 | 2.29 | 1.27 | 2.79 |
| 10 | $(-0.5h)$ | –3.1537 | –0.97 | –16.4 | –1.81 | –17.1 | $(0.4h)$ | 0.26441 | 0.17 | 0.86 | 0.31 | 0.97 |
| 20 |  | –2.8760 | –0.48 | –8.87 | –0.71 | –9.07 | – | 0.26246 | 0.05 | 0.37 | 0.09 | 0.39 |
| 40 |  | –2.7442 | –0.24 | –4.62 | –0.30 | –4.67 | – | 0.26128 | 0.03 | 0.17 | 0.03 | 0.18 |
| 5 | $\bar{\sigma}_\theta^e$ | 23.442 | 1.32 | 4.07 | 1.80 | 4.42 | $D_z$ | 0.60796 | –4.61 | –8.00 | –4.93 | –8.37 |
| 10 | $(-0.4h^+)$ | 24.247 | 0.63 | 1.87 | 0.75 | 1.96 | $(0.5h)$ | – 0.64232 | –5.05 | –6.99 | –5.14 | –7.09 |
| 20 |  | 24.591 | 0.31 | 0.90 | 0.34 | 0.92 | – | 0.65673 | –5.25 | –6.29 | –5.28 | –6.31 |
| 40 |  | 24.747 | 0.15 | 0.44 | 0.16 | 0.44 | – | 0.66318 | –5.35 | –5.89 | –5.36 | –5.89 |
| 5 | $\bar{\sigma}_x^p$ | –3.5722 | 0.39 | 1.95 | 0.75 | 2.21 | $\bar{\phi}$ | –58.181 | 1.39 | 0.29 | 1.49 | 0.35 |
| 10 | $(-0.5h)$ | –3.6373 | –0.03 | 0.66 | 0.05 | 0.72 | $(-0.5h)$ | –58.563 | 0.65 | 0.13 | 0.67 | 0.14 |
| 20 |  | –3.6638 | –0.20 | 0.13 | –0.18 | 0.14 |  | –58.711 | 0.31 | 0.06 | 0.32 | 0.06 |
| 40 |  | –3.6757 | –0.27 | –0.11 | –0.26 | –0.11 |  | –58.775 | 0.15 | 0.03 | 0.15 | 0.03 |

**Table 7.** Exact 3D results and percent errors of 2D theories for hybrid sandwich panel (c) under load case 3.
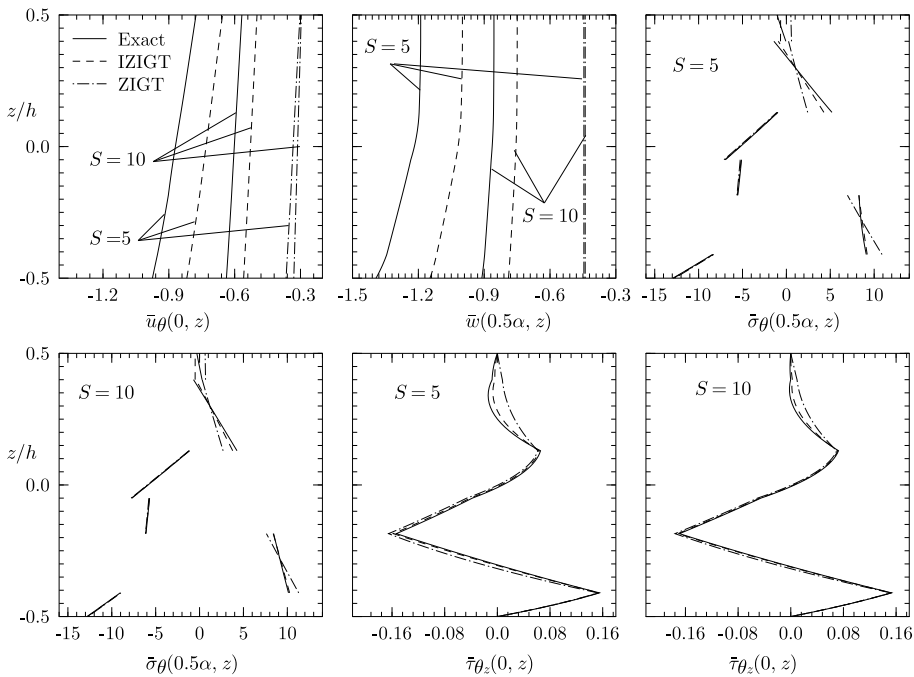


**Figure 9.** Through-the-thickness distributions of $\bar{u}_\theta$, $\bar{w}$, $\bar{\sigma}_\theta$, and $\bar{\tau}_{\theta z}$ for hybrid test panel (a) under load case 3.
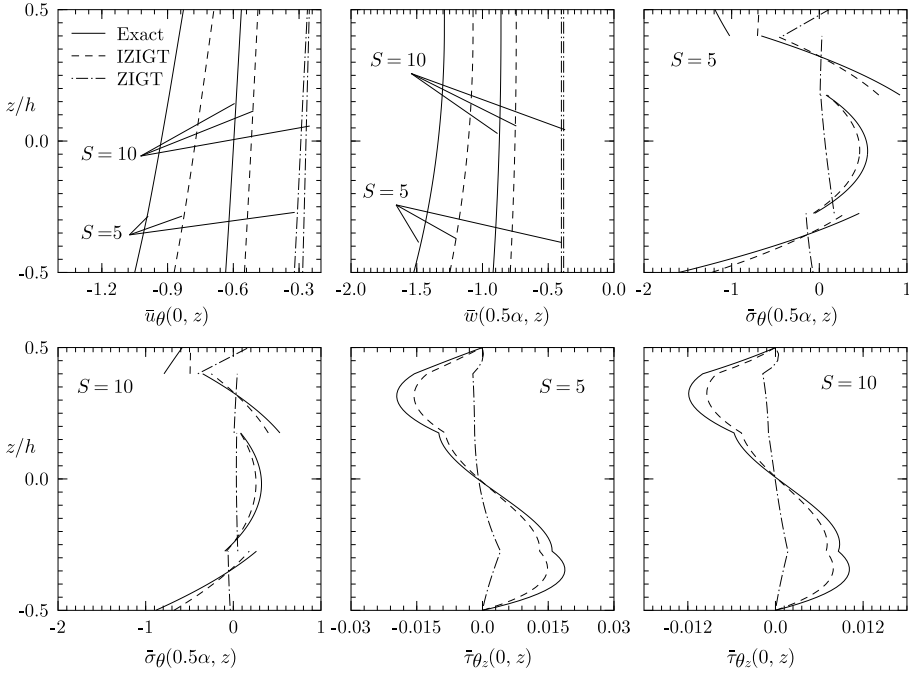
**Figure 10.** Through-the-thickness distributions of $\bar{u}_\theta$, $\bar{w}$, $\bar{\sigma}_\theta$, and $\bar{\tau}_{\theta z}$ for hybrid composite panel (b) under load case 3.
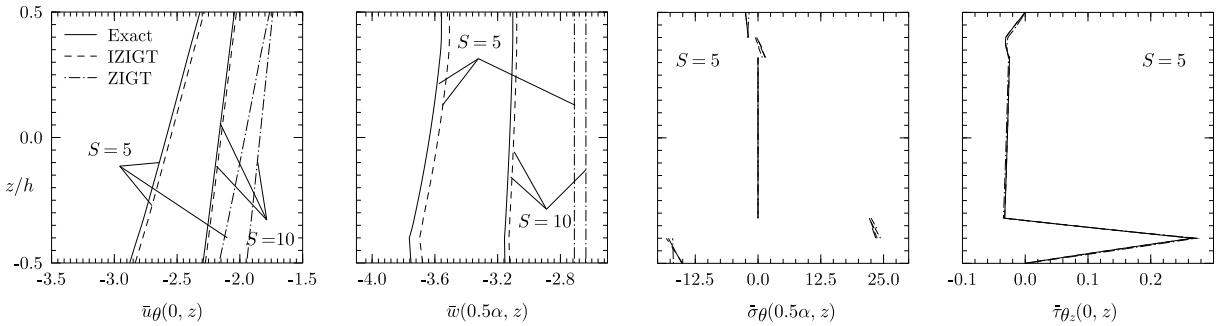


**Figure 11.** Through-the-thickness distributions of $\bar{u}_\theta$, $\bar{w}$, $\bar{\sigma}_\theta$, and $\bar{\tau}_{\theta z}$ for hybrid sandwich panel (c) under load case 3.

panels. These distributions show significant improvement for the IZIGT. The percent error in $\bar{w}$ and $\bar{\sigma}_\theta^e$ in the substrate is plotted in Figure 13 against the fibre axis angle $\psi$ of the face layers of the sandwich panel (c) with span angle $\alpha = 2\pi/3$ and $S = 10$. The error in $\bar{w}$ for the ITOT and ZIGT (for the thermal load case) increases with the decrease in the ply angle $\psi$ for all load cases, but the same does not hold well for $\bar{\sigma}_\theta^e$. For the IZIGT, the same trend is valid for $\bar{w}$ only for load case 1.

The effect of span angle $\alpha$ on the response is shown by plotting the % error in $\bar{w}$ and $\bar{\sigma}_\theta^e$ against the span angle in Figure 14 for the hybrid sandwich panel with $S = 10$ and $\psi = 30°$ under load cases 1–3. It is observed that the error in the ITOT and ZIGT (for the thermal load case) increases with the decrease in the span angle for all load cases. The same is not always true for the IZIGT for which the error is small.
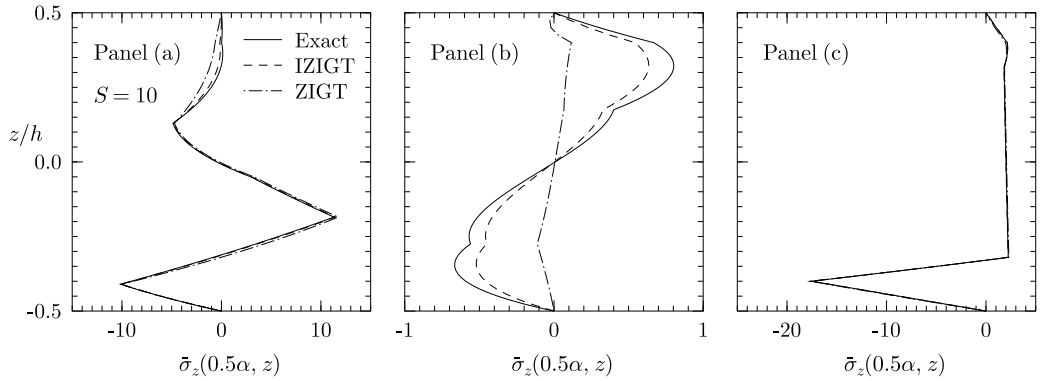
**Figure 12.** Through-the-thickness distributions of $\bar{\sigma}_z$ for panels (a), (b), and (c) under load case 3.
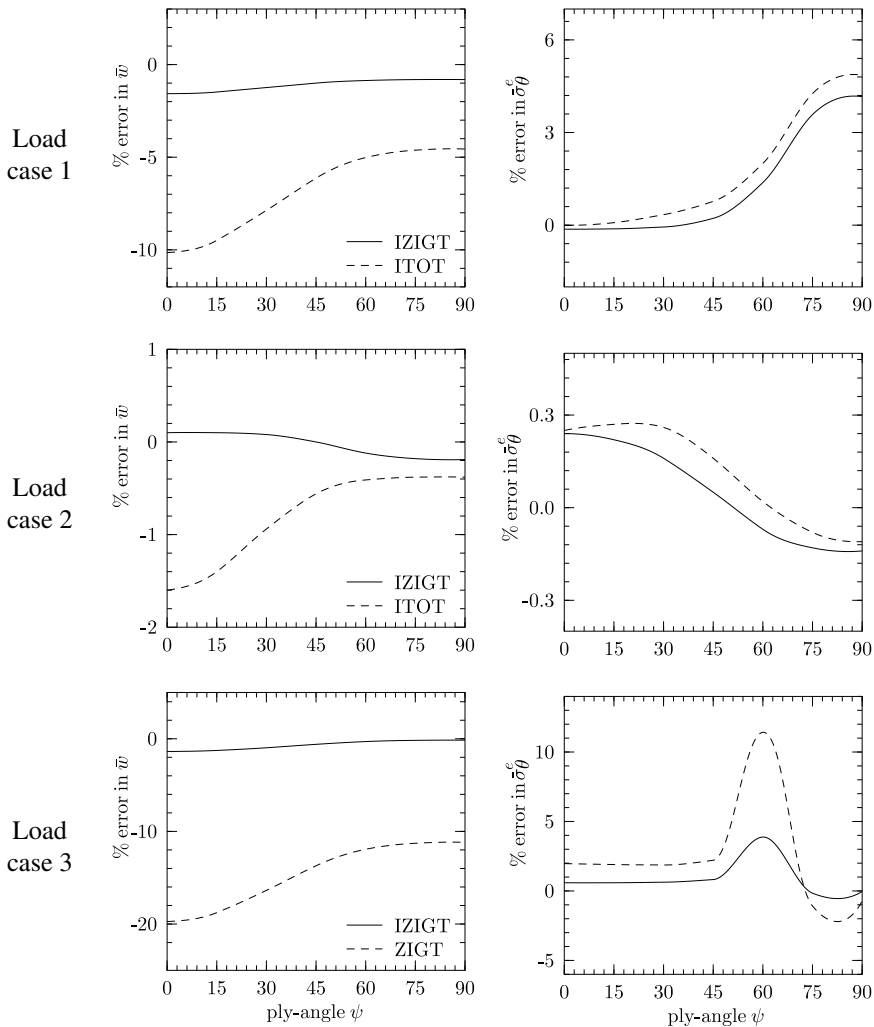


**Figure 13.** Effect of ply angle on percent error of $\bar{w}$ and $\bar{\sigma}_\theta^e$ for hybrid panel (c).
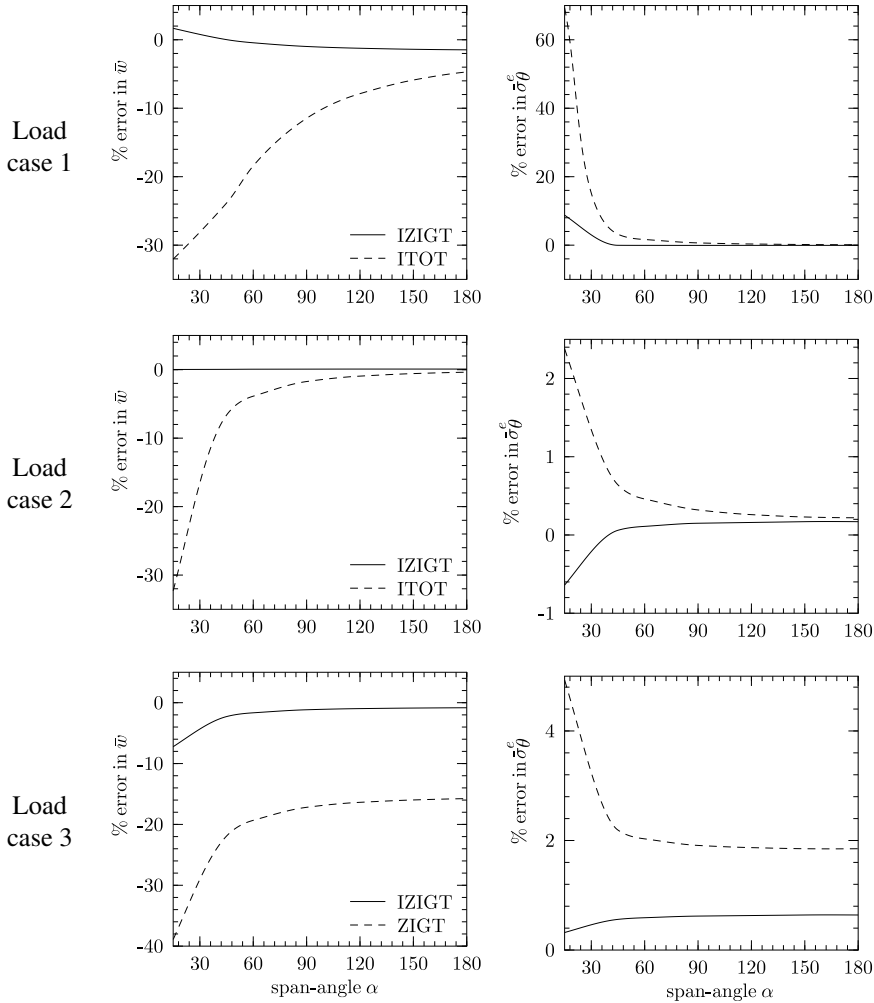
**Figure 14.** Effect of span-angle on percent error of $\bar{w}$ and $\bar{\sigma}_\theta^e$ for hybrid panel (c).

## 7. Conclusions

An improved third-order zigzag theory and an improved third-order theory have been presented for the electrothermomechanical response of hybrid angle-ply circular cylindrical shells. The accuracy of the theories has been assessed in direct comparison with the 3D exact piezothermoelasticity solution for simply supported infinite-length angle-ply cylindrical panels under pressure, electric potential, and thermal loads. The assessment is made for hybrid shell panels with highly inhomogeneous test, composite, and sandwich substrates. Based on the assessment of maximum values of entities and their distributions across the thickness, it is concluded that the IZIGT with the same number of unknowns as the ITOT yields accurate results and is a significant improvement over the ITOT for all laminate configurations for mechanical and potential loads. This improvement is due to the inclusion of layerwise terms in the approximation of inplane displacements in the IZIGT. However, the IZIGT and ITOT do not show any

significant differences for the thermal loading case. Both the theories, however, show significant improvements over their counterparts with uniform $w$ across the thickness for thermal loads. The inclusion of the transverse normal strain in the approximation of $w$ in the 2D theories improves not only the predicted deflection but all other response entities. In general, the error in the ITOT increases with the decrease in ply angle and span angle. The same does not hold well for the IZIGT for which the error itself is small.

# References

[Auld 1973] B. A. Auld, *Acoustic fields and waves in solids*, vol. I, John Wiley, New York, 1973.

[Berg et al. 2004] M. Berg, P. Hagedorn, and S. Gutschmidt, "On the dynamics of piezoelectric cylindrical shells", *J. Sound Vib.* **274**:1–2 (2004), 91–109.

[Carrera 2002] E. Carrera, "Temperature profile influence on layered plates response considering classical and advanced theories", *AIAA J.* **40**:9 (2002), 1885–1896.

[Carrera and Brischetto 2007] E. Carrera and S. Brischetto, "Reissner mixed theorem applied to static analysis of piezoelectric shells", *J. Intell. Mater. Syst. Struct.* **18**:10 (2007), 1083–1107.

[D'Ottavio et al. 2006] M. D'Ottavio, D. Ballhause, B. Kroplin, and E. Carrera, "Closed-form solutions for the free-vibration problem of multilayered piezoelectric shells", *Comput. Struct.* **84**:22–23 (2006), 1506–1518.

[Dumir et al. 1997] P. C. Dumir, G. P. Dube, and S. Kumar, "Piezothermoelastic solution for angle-ply laminated cylindrical panel", *J. Intell. Mater. Syst. Struct.* **8**:5 (1997), 452–464.

[Jia and Rogers 1990] J. Jia and C. A. Rogers, "Formulation of a laminated shell theory incorporating embedded distributed actuators", *J. Mech. Des.* (*ASME*) **112**:4 (1990), 596–604.

[Kapuria and Achary 2006] S. Kapuria and G. G. S. Achary, "Electromechanically coupled zigzag third-order theory for thermally loaded hybrid piezoelectric plates", *AIAA J.* **44**:1 (2006), 160–170.

[Kapuria et al. 1997] S. Kapuria, P. C. Dumir, and S. Sengupta, "Nonaxisymmetric exact piezothermoelastic solution for laminated cylindrical shell", *AIAA J.* **35**:11 (1997), 1792–1795.

[Kapuria et al. 1998a] S. Kapuria, P. C. Dumir, and S. Sengupta, "Assessment of shell theories for hybrid piezoelectric cylindrical shell under thermoelectric load", *J. Therm. Stresses* **21**:5 (1998), 519–544.

[Kapuria et al. 1998b] S. Kapuria, S. Sengupta, and P. C. Dumir, "Assessment of shell theories for hybrid piezoelectric cylindrical shell under electromechanical load", *Int. J. Mech. Sci.* **40**:5 (1998), 461–477.

[Kim et al. 2002] H. S. Kim, X. Zhou, and A. Chattopadhyay, "Interlaminar stress analysis of shell structures with piezoelectric patch including thermal loading", *AIAA J.* **40**:12 (2002), 2517–2525.

[Kumari et al. 2008] P. Kumari, J. K. Nath, S. Kapuria, and P. C. Dumir, "An improved third order theory and assessment of efficient zigzag theory for angle-ply flat hybrid panels", *Compos. Struct.* **83**:2 (2008), 226–236.

[Lee and Saravanos 2000] H. J. Lee and D. A. Saravanos, "A mixed multi-field finite element formulation for thermopiezoelectric composite shells", *Int. J. Solids Struct.* **37**:36 (2000), 4949–4967.

[Oh and Cho 2007] J. Oh and M. Cho, "Higher order zig-zag theory for smart composite shells under mechanical-thermo-electric loading", *Int. J. Solids Struct.* **44**:1 (2007), 100–127.

[Ossadzow-David and Touratier 2004] C. Ossadzow-David and M. Touratier, "A multilayered piezoelectric shell theory", *Compos. Sci. Technol.* **64**:13–14 (2004), 2121–2137.

[Pinto Correia et al. 2002] I. F. Pinto Correia, C. M. Mota Soares, C. A. Mota Soares, and J. Herskovits, "Active control of axisymmetric shells with piezoelectric layers: a mixed laminated theory with a high order displacement field", *Comput. Struct.* **80**:27–30 (2002), 2265–2275.

[Raja et al. 2004] S. Raja, P. K. Sinha, G. Prathap, and D. Dwarakanathan, "Thermally induced vibration control of composite plates and shells with piezoelectric active damping", *Smart Mater. Struct.* **13**:4 (2004), 939–950.

[Saravanos 1997] D. A. Saravanos, "Mixed laminate theory and finite element for smart piezoelectric composite shell structures", *AIAA J.* **35**:8 (1997), 1327–1333.

[Saravanos and Christoforou 2002] D. A. Saravanos and A. P. Christoforou, "Low-energy impact of adaptive cylindrical piezoelectric-composite shells", *Int. J. Solids Struct.* **39**:8 (2002), 2257–2279.

[Saravanos and Heyliger 1999] D. A. Saravanos and P. R. Heyliger, "Mechanics and computational models for laminated piezoelectric beams, plates and shells", *Appl. Mech. Rev.* (*ASME*) **52**:10 (1999), 305–320.

[Sung et al. 1996] C. K. Sung, T. F. Chen, and S. G. Chen, "Piezoelectric modal sensor/actuator design for monitoring/generating flexural and torsional vibrations of cylindrical shells", *J. Vib. Acoust.* (*ASME*) **118**:1 (1996), 48–55.

[Tiersten 1969] H. F. Tiersten, *Linear piezoelectric plate vibrations: elements of the linear theory of piezoelectricity and the vibrations of piezoelectric plates*, Plennum Press, New York, 1969.

[Tzou and Bao 1995] H. S. Tzou and Y. Bao, "A theory on anisotropic piezothermoelastic shell laminates with sensor/actuator applications", *J. Sound Vib.* **184**:3 (1995), 453–473.

[Xu and Noor 1996] K. Xu and A. K. Noor, "Three-dimensional analytical solutions for coupled thermoelectroelastic response of multilayered cylindrical shells", *AIAA J.* **34**:4 (1996), 802–812.

[Zhang et al. 2008] Y. H. Zhang, S. L. Xie, and X. N. Zhang, "Vibration control of a simply supported cylindrical shell using a laminated piezoelectric actuator", *Acta Mech.* **196**:1–2 (2008), 87–101.

JAYANTA KUMAR NATH: jkniter@gmail.com
*Department of Applied Mechanics, Indian Institute of Technology Delhi, New Delhi 110016, India*

SANTOSH KAPURIA: kapuria@am.iitd.ac.in
*Department of Applied Mechanics, Indian Institute of Technology Delhi, New Delhi 110016, India*
http://web.iitd.ac.in/~am/

# SUBMISSION GUIDELINES

## ORIGINALITY

Authors may submit manuscripts in PDF format on-line. Submission of a manuscript acknowledges that the manuscript is *original and has neither previously, nor simultaneously, in whole or in part, been submitted elsewhere.* Information regarding the preparation of manuscripts is provided below. Correspondence by email is requested for convenience and speed. For further information, consult the Web site at http://www.jomms.org or write to

jomms.steele@stanford.edu

## LANGUAGE

Manuscripts must be in English. A brief abstract of about 150 words or less must be included. The abstract should be self-contained and not make any reference to the bibliography. Also required are keywords and subject classification for the article, and, for each author, postal address, affiliation (if appropriate), and email address if available. A home-page URL is optional.

## FORMAT

Authors are encouraged to use LaTeX and the standard article class, but submissions in other varieties of TeX, and, exceptionally in other formats, are acceptable. Electronic submissions are strongly encouraged in PDF format only; after the refereeing process we will ask you to submit all source material.

## REFERENCES

Bibliographical references should be listed alphabetically at the end of the paper and include the title of the article. All references in the bibliography should be cited in the text. The use of BibTeX is preferred but not required. Tags will be converted to the house format (see a current issue for examples), however, in the manuscript, the citation should be by first author's last name and year of publication, e.g. "as shown by Kramer, et al. (1994)". Links will be provided to all literature with known web locations and authors are encouraged to provide their own links on top of the ones provided by the editorial process.

## FIGURES

Figures prepared electronically should be submitted in Encapsulated PostScript (EPS) or in a form that can be converted to EPS, such as GnuPlot, Maple, or Mathematica. Many drawing tools such as Adobe Illustrator and Aldus FreeHand can produce EPS output. Figures containing bitmaps should be generated at the highest possible resolution. If there is doubt whether a particular figure is in an acceptable format, the authors should check with production by sending an email to:

production@mathscipub.org

Each figure should be captioned and numbered so that it can float. Small figures occupying no more than three lines of vertical space can be kept in the text ("the curve looks like this:"). It is acceptable to submit a manuscript with all figures at the end, if their placement is specified in the text by means of comments such as "Place Figure 1 here". The same considerations apply to tables.

## WHITE SPACE

Forced line breaks or page breaks should not be inserted in the document. There is no point in your trying to optimize line and page breaks in the original manuscript. The manuscript will be reformatted to use the journal's preferred fonts and layout.

## PROOFS

Page proofs will be made available to authors (or to the designated corresponding author) at a web site in PDF format. Failure to acknowledge the receipt of proofs or to return corrections within the requested deadline may cause publication to be postponed.